Fabrication and Mechanical Properties of Magnesium Alloy Composites Reinforced with TiC and Ti_2AlC Particles

A Thesis

Submitted to the Faculty

of

Drexel University

by

Babak Anasori

in partial fulfillment of the

requirements for the degree

of

Doctor of Philosophy

September 2014

© Copyright 2014
Babak Anasori. All Rights Reserved

Dedicated to

My wife, Bita Alizadehtazi,
whose love, endless support and understanding helped me along my undergraduate and graduate studies.

My parents, Ashraf and Ezat,
for their unconditional love and support and teaching me about life.

My nieces, Rozhin and Viana,
for their love.

Acknowledgments

I would like to express my gratitude to the many individuals who have supported and helped to make possible the research presented in this dissertation.

First and foremost, I would like to thank my advisor, Prof. Michel W. Barsoum; a great mentor who wants his students to live up to their full potential and succeed. He is a true scientist who is passionate and enthusiastic about what he is doing and inspires his students with endless ideas. Without his tireless support, motivation and numerous constructive discussions none of the success I achieved could have been possible. In fact, I know I have been very fortunate to work with an advisor who always makes himself available for his students and is willing to discuss and help. His confidence in me helped me along the path to become an independent researcher. There are no words to fully express my gratitude, so all I can say is thank you.

I would also like to thank my thesis committee members for their great suggestions and time. A great deal of thanks to Prof. Roger Doherty for very helpful, constructive and educational discussions. He fueled my enthusiasm for science and showed me how humble a true scientist can be. I am grateful for reading my thesis very carefully and giving me great feedback. I would like to thank Prof. Antonios Zavaliangos, Prof. Mitra Taheri and Prof. Antonios Kontsos for individual discussions and their suggestions. I would also like to thank my external committee Prof. Suveen Mathaudhu for all the great discussions and encouragement in all aspects of my research.

I would like to thank my colleagues in the MAX Phases and MXene research group for their nonstop help whenever I needed them. I really enjoyed working with them. Special thanks to Dr. Shahram Amini and his wife Dr. Sara Pourshahriari, who

welcomed me and my wife and helped us in our first days in Philadelphia. Shahram introduced me to Drexel University and helped me to start my research. I am thankful to Mohammed Shamma, Ismail Albayrak, Charles B. Spencer Jr., Justin Griggs, Grady Bentzel, Joseph Halim, Matthias Agne, Michael Ghidiu, Matt Nelson, Dr. Yungsoo Chung, Dr. Sandip Basu, Prof. Aaron Sakulich and Prof. Alexander Moseson. A very special thanks to Dr. Nina Lane, Dr. Michael Naguib, Darin Tallman for all the countless help. Extra special thanks to Dr. El'ad Caspi, who graciously helped me with analyzing data, specifically X-ray diffraction data. We had many helpful discussions regarding my research.

Many thanks to the members of Prof. Kontsos's and Prof. Taheri's research groups, especially Dr. Kavan Hazeli, Dr. Greg Vetterick and Christopher Barr. Greg did hours of TEM right before his PhD defense and I really appreciate his time and effort. I would also like to thank Majid Sharifi in Dr. Palmese's group in Chemical Engineering department for helping me with tensile measurements.

Thanks to Prof. Volker Presser for helping me with analyzing X-ray diffraction data and completing the 2 dimensional X-ray diffraction.

Thank you to Dr. Troy Topping and Prof. Enrique Lavernia at University of California, Davis, for conducting extrusion on the composites of this study.

I would like to thank the faculty in the Materials Science and Engineering department at Drexel, notably Prof. Richard Knight, Prof. Yury Gogotsi and Prof. Jonathan Spanier. A special thank you to the MSE staff: Keiko Nakazawa, Yenneeka Long, Dorilona Rose, Sarit Kunz, Leslie Anastasio and Andrew Marx for always being helpful and making such a great environment in the department. Also, I would like to

thank Drexel's Centralized Research Facilities staff: Dr. Edward Basgall, Dr. Craig Johnson and Dr. Dmitri Barbash for their unconditional help and training me on different equipment. A big thank you to the Office of Graduate Studies at Drexel, specifically Dr. Teck-Kah Lim and Taz Kwok for their nonstop help and support along all the steps in my Ph.D. study. Also, the help from the Drexel's Machine shop, specifically Mark Shiber, is greatly appreciated.

I am grateful for funding support from the Army Research Office for my PhD. I also would like to thank Thixomat Company, specifically Ray Decker, for providing Mg alloys for this study.

I owe my existence to my family. My lovely mom, who so patiently took the best care of me every nanosecond of my childhood. She always encourages me to achieve the best I can. She has been the best teacher in my life. My dad, who taught me how to face different challenges and make the best out of them. My amazing brothers, Pourya and Arash, for their endless support. I would also like to thank my parents-in-law, Nazi and Abbas, my sisters-in-law, Naghmeh, Rita and Mahdis, my brother-in-law and my best friend, David, for their love and support.

Last but not least, a gigantic thank you to my lovely wife, Bita, who has been my best friend since I was 17. She has given me unconditional support throughout my entire studies and for her understating of all the extra time I dedicated to this work. I owe her every success I achieved.

Babak Anasori
Philadelphia
September 2014

Table of contents

List of Tables

List of Figures

Abstract

Fabrication and Mechanical Properties of Magnesium Alloy Composites Reinforced with TiC and Ti_2AlC Particles

Babak Anasori

Advisor: Prof. Michel W. Barsoum

Herein we report on the fabrication and mechanical properties of Mg composites fabricated by pressureless melt infiltration of Mg and Mg alloys into porous preforms of TiC and Ti_2AlC. The latter is a member of the MAX phases - viz. layered machinable ternary carbides and nitrides - some of which are relatively light and stiff. In this study, pure Mg and three, commercially available, aluminum-containing Mg alloys - AZ31, AZ61 and AZ91 - were used as matrices at a loading of ≈ 50 vol.%. For the most part, increasing the Al content enhanced the elastic moduli, Vickers hardness values and yield and ultimate compressive strengths. Reducing the particle sizes of the TiC and Ti_2AlC particulate reinforcements also had a large impact on the mechanical properties. At 1028±5 MPa, the ultimate compressive strength of a TiC-AZ61 composite, in which the TiC particle size distribution is Lorentzian and centered at, d_c = 0.41±0.01 μm, was ≈ 40% higher than that of the same composite with coarser TiC particles with bimodal size distributions centered around d_c=1.6±0.1 μm, and 5.8±0.3 μm. In addition, the elastic modulus and Vickers hardness of the former composite were measured to be 174±5 GPa and 3.4±0.3 GPa, respectively. For the Ti_2AlC reinforced composites, the best properties were obtained when AZ61 was reinforced with Ti_2AlC particles with d_c = 0.51±0.01 μm. The enhancements in elastic and mechanical properties are attributed to finer grained Mg-

matrices, the presence of Al in the matrices which enhances the wetting of TiC and Ti_2AlC by Mg to create a strong interface and finer reinforcement particle sizes. The latter two attributes, in turnlead to better mechanical interlocking.

For the composites studied herein better elastic and mechanical properties, were obtained at the expense of damping. The TiC-reinforced Mg matrix composites despite their high mechanical properties, have very small energy dissipation capabilities. However, by using Ti_2AlC, which inherently dissipates mechanical energy, it is possible to achieve higher damping while simultaneously enhancing the mechanical properties almost to the same levels as for the TiC reinforced composites. Using Mg alloys instead of pure Mg and reducing the reinforcement particle sizes also reduced the damping capabilities of these composites.

There is a threshold stress below which the damping capacities of the Ti_2AlC reinforced composites are comparable to those of their TiC reinforced counterparts. This was ascribed to the negligible damping of Ti_2AlC below the threshold stress ($\approx$ 200 MPa).

The Ti_2AlC composites are slightly lighter and can be fabricated at lower temperature than comparable TiC composites; the former are also readily machinable but more expensive.

Chapter 1: Introduction

This chapter describes a brief history of composites and explains how common they are. Then talks about the modern composite, specifically metal matrix composites. The outline of this work will be also presented at the end.

1.1. Composites

Composite materials are solids, in which two or more different materials with different properties are used to enhance the composite properties. The constituent materials usually keep their individual properties as they do not dissolve or blend into each other. The goal of fabricating composite is to enhance the properties by combining the component qualities without accentuating their shortcomings.

Composites can be found in the nature. Wood, or even celery, and bone are the most common examples. The former is a composite of long cellulose fibers (a polymer, also found in cotton), which is embedded in a much weaker material called lignin. The combination of these two weak materials leads to the formation of wood. Bones are composites of a soft protein called collagen, which is reinforced with hard calcium phosphate.

The mankind has been making composites for millenniums. In fact, composites were the first material mankind used after stones. Mud brick is the first known manmade composite, which the oldest discovered evidence goes back to the Pre-Pottery Neolithic A, approximately 11500 years ago [1]. Mud bricks can be made by mixing mud, stone and water and letting them dry either in the sun or baking them. The resulting brick has

high compressive strengths with very low tensile strengths and breaks by bending. Later on, straws or rice husks were used in the bricks to fabricate a better composite and improve brick tensile strengths.

1.2. Metal matrix composites

Composites usually consist of reinforcing phase dispersed in a matrix and have superior properties compare to their individual components. When a metal is used as the matrix, the composite is called metal matrix composites, MMCs. The latter are custom made composites in which properties are tailored to fulfill the desired requirements. The first scientifically fabricated metal matrix composite can be dated back to 1924, when Schimd consolidated mixture of aluminum and aluminum oxide powder as a dispersion hardened system and achieved higher hardness values than that of as cast aluminum [2].

The next step in MMCs development was high interest in the continuously reinforced metal composite in 1960s, in which high vol.% of the reinforcement (40-80 vol.%) was used. The role of matrix is mostly transferring the applied load to reinforcement and the latter is the load-bearing component. The main disadvantages of these composites were high cost and limitations of fabrication.

In 1980s discontinuously reinforced composites gained interests mostly by developing Al composite reinforced with SiC and Al_2O_3 particles. The reinforcement fraction is usually in the range of 5- 40 vol.%, which means matrix and reinforcement both contribute in load bearing. These composite become the most commercially attractive system due to their low cost, good workability and uniform properties compare to continuously reinforced composites.

1.3. Magnesium, its alloys and composites

Magnesium is the lightest structural metal and sixth abundant element on earth. Mg engineering applications goes back to 1920s when Mg parts were used in racing cars and one of its first commercially applications was in 1930s in Volkswagen Beetle, in which more than 20 kg of Mg alloy was used [3]. Although it has been almost a century since its first applications, Mg was not the material of choice for many applications due to its high cost till about two decades ago. However, the increasing demand for reducing the weight in many products, especially to reduce energy consumption, industries are constantly searching for new, lighter and advanced materials. Currently, there are many different applications for Mg alloys such as automotive, aerospace, medical, sports, electronic applications.

Mg alloys have relatively low elastic moduli, strengths and hardness values compared to other structural metals. One method to overcome these limitations is to fabricate Mg matrix composites. Among different reinforcement materials, ceramic reinforcements are most commonly used in Mg composites. Of all the ceramic reinforcements, SiC particulates is one of the most widely reinforcement in Mg and Mg alloys, which is due to its thermodynamically stability in many Mg alloys and good wettability with Mg [3]. TiC is the second mostly used carbide in Mg matrix composites, which is one of the interests of this study. A review of TiC and SiC reinforced Mg composites will be presented in chapter 2.

In 2009, Amini et al. were the first to use Ti_2AlC, a MAX phases, to reinforce pure Mg composites and were able to achieve very high strengths [4]. This work is a follow up on the work by Amini et al. and to further develop this family of composites.

1.4.Outline

In chapter 2, previously reported results on Mg composites reinforced with SiC, TiC and Ti_2AlC will be reviewed and the goals of this study will be explained.

Since, the composites fabricated herein are capable of energy dissipation and in the previous work damping was related to a specific type of damping known as kinking non-linear elasticity, the latter will be discussed in details in chapter 3 and a new hypothesis on this type of damping will be presented.

In chapters 4 and 5 experimental methods and all the measured mechanical properties and microstructural characterizations will be presented. Chapter 6 will discuss the damping properties of all the composites fabricated in this work.

To further understand these composites, many short experiments had been done, each of which can be the beginning of a future study and will be presented in chapter 7. Summary and conclusions will be presented in chapter 8.

Appendices A provide information on the topics that are slightly outside of the scope of this thesis. Appendices A1 and A2 are about deformation under nanoindentation and A3 is about high temperature oxidation of Ti_2GeC, a MAX phase, in air.

Chapter 2: Background

In this chapter, a short review on previously reported Mg composites reinforced with TiC and SiC is presented. Since this is a follow up on earlier work, previously reported pure Mg composites reinforced with MAX phases are discussed and the important conclusions are presented.

2.1. Introduction

Magnesium, Mg, alloys have attracted a great deal of interest over the past decades in the aerospace, automotive and electronics industries mostly due to their lightweight and high specific strengths, damping capacity and superior machinability [5-7]. However, Mg alloys have relatively low elastic moduli, strengths and hardness values compared to other structural metals. One method to compensate for these limitation is to incorporate ceramic particles in Mg matrices [8].

Discontinuously reinforced composites, such as particulates, short whiskers and fibers, gained more attraction due to their availability at lower cost and scalable fabrication methods [9]. The subject of this thesis is particulate reinforced Mg-matrix composites.

Different processing methods have been used to fabricate particulate reinforced Mg matrix composites. They can be divided into three major categories: solid phase, semi solid and liquid phase processing. Solid phase processing such as powder metallurgy [10, 11] and mechanical alloying are methods to fabricate composites with very low to moderate reinforcement volume fractions. However, usually secondary processing steps are needed to fabricate the final product.

Liquid phase processing includes stir casting [12, 13], squeeze casting [14, 15], melt deposition [16-18], in-situ synthesis [19, 20], pressureless melt infiltration, MI, [21-23]. In all of these processing techniques molten Mg is in contact with ceramic particulates, which can enhance any reactions between them at the matrix/reinforcement interface. In general, the latter is one of the most critical aspects of composites and achieving any strengthening in composites is usually dependent on the strength of these interfaces. Weak interfaces can fail before any load transfer occurs between matrix and reinforcement and can even reduce the overall matrix strengths. Consequently, strong interfacial bonds are desirable [24].

2.2. Mg reactions with reinforcements

To date, the two major binary carbides used to reinforce Mg matrix composites have been SiC and TiC. Mg readily wets SiC forming a strong interface. Mg_2Si is potentially a reaction product between Mg and Si reported in some of studies on Mg-SiC composites. However, the reported results are not in agreement. Based on scanning electron microscopy, SEM, results, Saravanan *et al.* concluded that no reactions occurred between pure Mg and SiC after fabrication via stir casting at 700ºC followed by hot extrusion, [13]. Conducting transmission electron microscopy, TEM, Zheng *et al*. also reported no evidence of Mg_2Si at the interfaces of a squeezed cast 20 vol.% SiC whisker reinforced AZ91 alloy [14]. Kevorkijan also reported no SEM evidence of a reaction between Mg alloys and SiC at processing temperatures of 730±10ºC [23]. Poddar *et al*. rheocast 15 vol.% SiC reinforced AZ91 composites at 584±2ºC, and again showed by X-ray diffraction, XRD, and SEM that no evidence for a reaction between the matrix and reinforcement phase [25]. In contrast, Gupta *et al.* and Reddy *et al.*, reported Mg_2Si

formation in pure Mg composites reinforced with SiC fabricated via disintegrated melt deposition, DMD. In both studies, only XRD results showed the presence of Mg_2Si reaction product. No evidence of the latter was observed in SEM micrographs at the matrix and interface [16-18].

In contradistinction to SiC, Mg does not react with TiC [21, 26], an observation that is consistent with the fact that no intermetallics exist in the Mg-Ti system. Furthermore, MgC_2 is not stable at temperatures higher than 680 ºC. Contreras *et al.*, using a sessile drop technique, reported a contact angle of ≈ 120º for pure Mg on TiC substrates at 850 ºC. Holding for 30 min at 850 °C, however, reduced the contact angle to ≈ 90º. Further holding did not further change the contact angle. Pure Al showed similar wetting behavior as Mg initially, however, by holding at 850°C, the Al spreading radius increased and the contact angle was reduced to ≈ 50º after 90 min [26]. This result suggests that Al-containing Mg alloys may lead to better wetting and better interfaces in Mg-TiC composites. It is important to note that improving the wetting at the interface by using Al-containing Mg alloys does not necessarily result from a chemical reaction with TiC. In fact, one of the methods used to fabricate Mg-TiC composites is to start with Ti and C elemental powder mixtures in molten Mg. In those cases, no reaction between Mg and elemental Ti or C is observed. Chen *et al*. reported on TiC-AZ91 composites via melt infiltration of Mg into a preform made of a Ti and C powder mixture at 800ºC for 1h. It was confirmed by XRD that TiC formation is the only reaction occurring during this process [20]. In separate studies, Wang *et al*. and Cao *et al* also fabricated TiC-AZ91 composites via in-situ reaction of Ti and C in molten Mg at 800 ºC [19, 27]. More recently, Shamekh *et al*. infiltrated a preform of Ti-B_4C powder with AZ91 in order to

fabricate Mg composites reinforced with TiC-TiB_2 by in-situ reaction of Ti and B_4C in the molten AZ91 in the 700 ºC to 950 ºC temperature range [28, 29]. Although, different reaction products between Mg-B and Ti-B such as MgB_2, TiB_2, TiB, Ti_3B_4 and even TiC and Ti_2AlC were detected, no evidence of a reaction between Mg and Ti or C was reported. Contreras *et al.* fabricated 56 vol.% TiC-Mg composites via MI of pure Mg into porous TiC preforms under flowing Ar at temperatures of 850 ºC, 900 ºC and 950 ºC. Here again, no Mg/TiC reaction was observed even at 950 ºC [21]

2.3. Previously reported Mg composites reinforced with TiC or SiC

There are many studies on Mg and its alloys reinforced with TiC or SiC particulates at low reinforcement loadings. However, there are limited number of studies on Mg composites with high volume fraction of SiC or TiC (≈ 50 vol. %) in the literature. Table 2.1 summarizes the properties of some of the Mg composites reinforced with SiC or TiC with moderate or high reinforcement volume fractions..

At 878±20 MPa, the highest ultimate compressive strength, UCS, to our knowledge, for Mg composites was reported for 60 vol.% AZ91 reinforced with TiC and TiB_2 [29]. As explained earlier, this composite was made via in-situ reaction of Ti and B_4C inside molten AZ91 and other phases were detected such as TiB, Ti_3B_4, MgB_2 and B_4C. In other words, the resulting composite had many different intermetallic or carbide phases in it. At 620±20 MPa, the highest ultimate tensile strength, UTS, for Mg composites was observed for 50 vol.% SiC-AZ80 composites, which will henceforth be referred to as 50-SiC-AZ80 [23]. In general in this thesis, the number that comes before the reinforcement represents the vol. % of the reinforcement. In 50-SiC-AZ80 composite, 1 wt.% Si was mixed with SiC prior to MI to enhance the Mg/SiC wetting and ≈ 0.8 MPa

nitrogen gas pressure was applied during MI. When almost no pressure was applied, the UTS of the composite was measured to be 580±30 MPa [23]. At 136 GPa, the highest elastic modulus, E, to our knowledge, was reported for a 56-TiC-Mg composite, which was fabricated via pressureless MI at 950 ºC; reducing the latter to 850ºC, reduced the E to 123 GPa [21]. The enhancement in mechanical properties was attributed to better Mg wetting of the TiC at higher temperatures. Wang *et al.* fabricated 42.1 vol. % TiC-AZ91 composites by reactive MI of AZ91 into Ti/C preform at 800 ºC and reported UTS value of the order of 200 MPa [19].

Most of the reinforcing TiC and SiC particle sizes have been used in Mg composites are smaller than 50 μm. Vaidya *et al.* studied the effect of SiC particle size on the mechanical properties of 25- and 20-SiC-AZ91 composites and reported that reducing the average SiC size from 52 μm to 15 μm, enhanced the YSs and UTSs but did not change E (Table 2.1).

In addition, we can extract the following information about previously reported Mg composites reinforced with TiC and SiC from Table 2.1:

(i) Increasing the vol. % of the reinforcement enhances E, strengths and hardness at the expense of elongation.

(ii) The final mechanical properties, specifically strengths, are processing method dependent; changing the latter can significantly affect the properties. This comment is also applicable to monolithic Mg alloys.

(iii) The MI temperature is usually in the range of 730 ºC to 950 ºC. Increasing the MI temperature improves the wetting of TiC and SiC by Mg and in general enhances the mechanical properties.

(iv) Applying a secondary processing step such as extrusion enhances the final mechanical properties.

Table 2.1. Mechanical properties of Mg and Mg alloys composites reported in the literature. The numbers before the carbide phases represent their vol %.

Materials	Reinforcement particle size (µm)	Processing	E (GPa)	Yield strength (MPa)	UTS (MPa)	Elongation (%)	Vickers Hardness (HV)
56-TiC-Mg [21]	1.2	MI 850ºC	123	–	172	–	183-191
56-TiC-Mg [21]	1.2	MI 900ºC	130	–	200	–	194-197
56-TiC-Mg [21]	1.2	MI 950ºC	136	–	233	–	205-212
42-TiC-AZ91 [19] [20]	–	in situ-r MI 800ºC		–	203	1.5	–
40-(TiC-TiB_2)-AZ91 [29]	–	in situ-r MI 900ºC	195±16	–	UCS:¥ 878±20	0.66	–
(45-B_4C-5-Ti)-Mg [22]	44 & 0.8§	MI 850ºC	108±3	364±25	535±7	0.9	–
50-SiC-AZ80 [23] †	50	MI-730ºC	103	525±15	580±20	0.5	287±5
50-SiC-AZ80 [23] †	50	Ps/MI 730ºC	103	560±10	620±20	0.5	291 ± 5
30-SiC-Mg [13]	40	Stir-Hot Ex	59	229	258	2	–
20-SiCw-AZ91[14]	††	Sq	77±2	202±3	314±11	1.29	174±8
20-SiCw-AZ91[14]	††	Sq+binder $Al(PO_3)_3$	85±3	220±4	355±9	1.38	175±10
20-SiC-(Mg-6wt.%Zn) [12]	18	Stir-HT	62-73	260-383	306-427	1.2-3.4	–
15-SiC-AZ91[25]	150	Rheo-T4	–	155	169	1.6	–
15-SiC-AZ91 [25]	15	Rheo-T4	–	182	192	1.8	–
15-SiC-AZ91 [10]	6	PM/Sq+Ex	65-75	~350	400	~1	–

¥ The ultimate compressive strength was reported.
† 1 wt. % Si powder was added to SiC powder mixture.
†† SiC whiskers with a diameter of 0.1–1.0 µm and length of 30–100 µm.
§ bimodal mixture of coarse (d_{50}=44µm) and fine (d_{50}=0.8µm) B_4C particulates were used.
MI: Melt infiltration, Ex: extruded, in-situ-r: in situ reactive, Sq: squeeze cast, Ps/MI: Pressured melt infiltration, Rheo: Rheocast, PM: powder metallurgy, Stir: stir cast, HT: heat treated, DMD: Disintegrated melt deposition.

Table 2.1. Cont. Mechanical properties of Mg and Mg alloys composites reported in the literature. The numbers before the carbide phases represent their vol. % in composites.

Materials	Reinforcement particle size (µm)	Processing	E (GPa)	Yield strength (MPa)	UTS (MPa)	Elongation (%)	Vickers Hardness (HV)
10-SiC-AZ91 [11]	15	PM+Hot Ex (400ºC)	44.5	120	135	0.47	–
10-SiC-AZ91 [11]	50	PM+Hot Ex (400ºC)	49.8	105	110	0.23	–
25-SiC-AZ91 [15]	15	Sq+ Hot Ex	78	310	330	0.8	–
25-SiC-AZ91 [15]	52	Sq+ Hot Ex	79	290	340	1.1	–
20-SiC-AZ91 [15]	15	Sq+ Hot Ex	71	330	390	1.3	–
20-SiC-AZ91 [15]	52	Sq+ Hot Ex	72	270	320	1.1	–
5.8-SiC-Mg [16]	25	DMD-Ex	41±2	127±7	195±7	6±2	–
9.3-SiC-Mg [16]	25	DMD-Ex	44±2	120±5	181±6	4.7	–
12.8-SiC-Mg [16]	25	DMD-Ex	50±3	128±1.9	176±4	1.4	–
2.7-SiC-Mg [17]	0.6	DMD	46	182±2	219±2	2.1	53±1
5.8-SiC-Mg [17]	0.6	DMD	47	171±3	211±14	1.5	55±1
9-SiC-Mg [17]	0.6	DMD	48	155±1	207±9	1.4	56±2
9-SiC-Mg [18]	0.6	DMD-Ex-HT		168±5	213±4	3.57	–
AZ31 as cast [30]	–	cast	–	152	275	22.0	–
AZ61 as cast [30]	–	cast	–	175	320	19.8	–
AZ61 [31]	–	Hot work+HT	–	–	<300	20	–
AZ91 [32]	–	PM-HP-Ex	40±2	232±6	315±5	14	–
AZ91 [33]	–	Cast	46	102	205	6	–
AZ91 [33]	–	T4	46	87	189	8.14	
AZ91 [14]	–	Sq	45±1	87±1	189±2	8.14	54±2
AZ91 [15]	–	–	42	204	360	9.9	–

MI: Melt infiltration, Ex: extruded, in-situ-r: in situ reactive, Q: quenched, Sq: squeeze cast, Ps/MI: Pressured melt infiltration, PM: powder metallurgy, Stir: stir cast, HT: heat treated, DMD: Disintegrated melt deposition.

2.4. Mg composites reinforced with Ti_2AlC and Ti_3SiC_2

In addition to TiC and SiC, more recently, Ti_2AlC and Ti_3SiC_2 were used as Mg-reinforcements. The latter belong to a large, 60+, family of ternary carbides with a general formula $M_{n+1}AX_n$, (MAX) where n = 1, 2, 3 etc., M is an early transition metal, A is an A-group element (mostly groups 13 and 14) and X is either carbon and/or nitrogen [34-37]. MAX phases are layered hexagonal solids with two formula units per unit cell,

in which layers of edge shared M_6X octahedrons are interleaved with layers of the A-group elements. Figure 2.1 shows two series of MAX phases, M_2AX and M_3AX_2 in which, a single block of octahedrons (3 atoms thick) and two octahedron blocks, respectively, are interleaved with one layer of the A element.

The MAX phases combine some of the best attributes of metals and ceramics. Like metals, they are electrically and thermally conductive, most readily machinable [37-39], not susceptible to thermal shock, plastic at high temperatures and exceptionally damage tolerant [40]. Like ceramics, some of them are elastically rigid (Young's moduli > 300 GPa), lightweight (≈ 4 Mg/m^3) and maintain their strengths to high temperatures. Ti_2AlC is also creep, fatigue and oxidation resistant [41-43].

Due to their high c/a ratio, the MAX phases are hugely plastically anisotropic in that dislocations are confined to the basal planes at all temperatures. Consequently, one of their more common deformation modes is the formation of kink bands. It is believed that prior to the formation the latter, these solids form incipient kink bands or IKBs [44], that upon cyclic loading, nucleate and grow on the easy slip planes; during unloading they shrink and annihilate [44-46]. IKBs and their effect on damping are discussed in chapter 3.

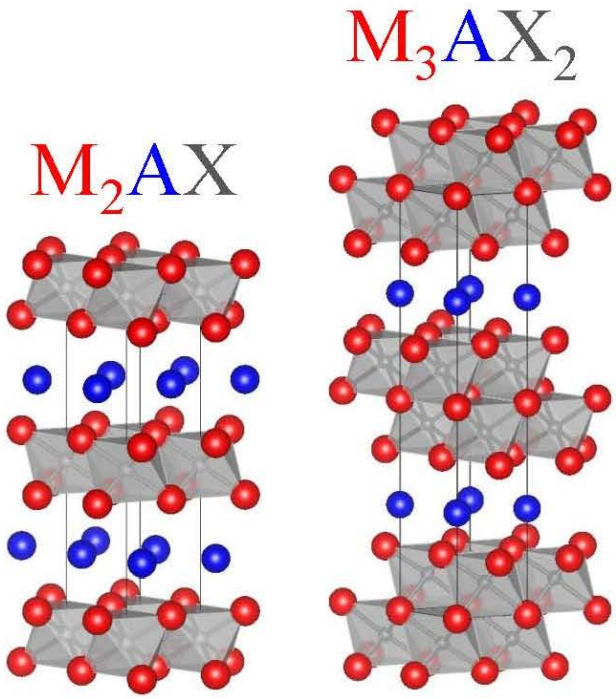

Fig. 2.1. Schematic of the unit cells of the M_2AX and M_3AX_2 phases.

In 2009, Amini *et al.* were the first to fabricate pure Mg composite reinforced with ~ 50 vol.% Ti_2AlC or Ti_3SiC_2, two commercially available MAX phases [4]. Two methods were applied to fabricate these composites. The first method was MI, which was used only for the 50-Ti_2AlC-Mg composite. Before MI, the Ti_2AlC preforms were made by uniaxial cold pressing of the powder at 45 MPa. For the purpose of MI, pure Mg chunks were placed on the top of the preforms, which in turn were placed in alumina crucibles covered with alumina lids and placed in a vacuum furnace under a vacuum of 10^{-2} torr and held at 750 ºC for 1 h, before furnace cooling.

The second method was to use a hot press, HP, to fabricate 50-Ti_2AlC- and 50-Ti_3SiC_2-Mg composites. For the HPed samples, the carbide powder, Ti_2AlC or Ti_3SiC_2, was mixed with Mg powder and ball milled for 12 h and dried in a mechanical vacuum

furnace at 150 ºC for 24 h. The dried powder mixtures were poured and wrapped in graphite foil that, in turn was placed in a graphite die and HPed in a graphite heated vacuum HP, heated at 10 ºC/min to 750 ºC and held at the target temperature for 1 h, again before furnace cooling. A load corresponding to a stress of ~ 45 MPa was applied when the temperature reached 500 ºC and maintained thereafter [47].

Although fully dense monolithic Ti_3SiC_2 has higher stiffness than fully dense monolithic Ti_2AlC, when they were used as the reinforcing phases, the mechanical properties of the resulting composites, in which Ti_2AlC were used as the reinforcement were higher than the Ti_3SiC_2-Mg composites. At 800±25 and 700±10 MPa the UCSs of the HP-50-Ti_2AlC-Mg and MI-50-Ti_2AlC-Mg composites were 41 % and 33 %, respectively, higher than that of HP-50-Ti_3SiC_2-Mg composites. For the sake of comparison, HP-50-SiC-Mg composites were also made. However, the UCS of the latter was measured to be 500±25 MPa, which is much lower than its Ti_2AlC counterpart [47]. The high strengths in 50-Ti_2AlC-Mg were ascribed to the presence of nano-crystalline, nc-, Mg grains, which was only observed in the 50-Ti_2AlC-Mg composites [4, 47].

The presence of nano size Mg grains was confirmed by XRD, TEM and differential scanning calorimetry, DSC, each of which will be explained briefly here. The XRD results showed Mg peaks broadening only when Ti_2AlC was used as the reinforcement. However, no Mg peak broadening was observed in HP-50-Ti_3SiC_2-Mg or the HP-50-SiC-Mg composites [4]. By measuring the full width at half maximum, FWHM, of the Mg peaks and applying Scherrer formula [48], the Mg grain size in the 50-Ti_2AlC-Mg composite was reported to be 35±15 nm [4].

The second proof for the presence of nc-Mg was the TEM images, that nc-Mg

were only observed next to Ti_2AlC particles [4]. However, before proceeding, the following needs to be noted: i) according to all the micrographs, nano grain clusters were only observed in the porous regions, an example of which is shown in Fig. 2.2(a) [4]; ii) there were some regions that showed no evidence of nano grains such as Fig. 2.2(b), a selected area electron diffraction, SAED, was needed on those regions to confirm whether they were single large grains or multiple nano grains; iii) the presence of oxygen in nc-Mg regions was confirmed by energy dispersive X-ray spectroscopy, EDS, in a TEM. It was also assumed that MgO exists and it is in a form of thin layers that cover the nc-Mg grains [4, 47].

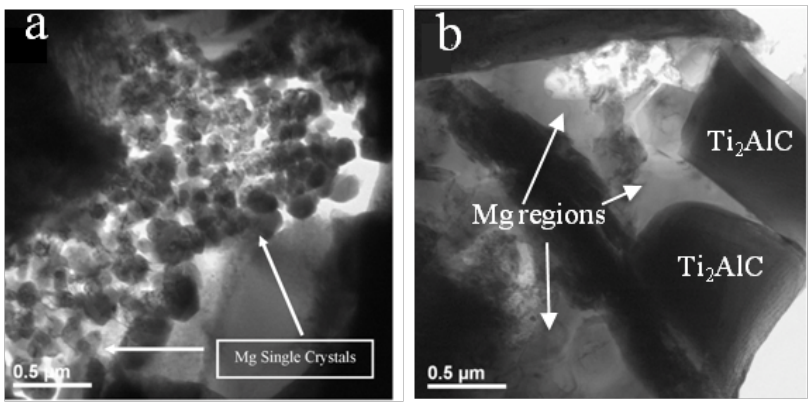

Fig. 2.2. TEM micrographs of MI-50-Ti_2AlC-Mg published in [4], (a) nc-Mg clusters in the porous region, (b) Mg regions with no evidence of nc-grains.

The third proof was DSC. Composites were heated 3 times to 700 ºC in order to measure any changes in the onset of the melting, T_m, and solidification, T_s, of the matrix Mg. At about 601±2 ºC and 633±1 ºC the T_m and T_s of Mg, respectively, in MI-50-Ti_2AlC-Mg composite was reported to be 45 ºC and 13 ºC lower than those of pure Mg. These depressions were explained by the presence of nc-Mg grains. However, when the

50-Ti_3SiC_2-Mg was heated to the same temperature, T_m and T_s of Mg were reported to be 638±1 ºC and 640±1 ºC, respectively. The small depressions observed for 50-Ti_3SiC_2-Mg composite were assumed to be due to the large Ti_3SiC_2/Mg interface area and/or the fact that the Mg was no longer pure.

Before we proceed further, it is worth revisiting the Mg-Si and Mg-Al phase diagrams shown in Figs. 2.3(a) and (b), respectively. Based on the Mg-Si phase diagram, Si has 1.16 at.% solubility in Mg at 637.6ºC, below which it becomes negligible (top inset in Fig. 2.2(a)). This can explain the melting point depression in the 50-Ti_3SiC_2-Mg composite. Following the same arguments, if one draws a line on the Mg-Al phase diagram that intersects the liquidus line at ~ 633 ºC (top inset in Fig. 2.2 (b)), the same line intersects the solidus at ~ 600 ºC. In other words, high temperature solubility of Si and/or Al in Mg, can simply explain the T_m and T_s depressions observed in the DSC results. As discussed later in this thesis, quite bafflingly, there is no evidence for such solubility in the Ti_2AlC case, within the resolution of our instruments.

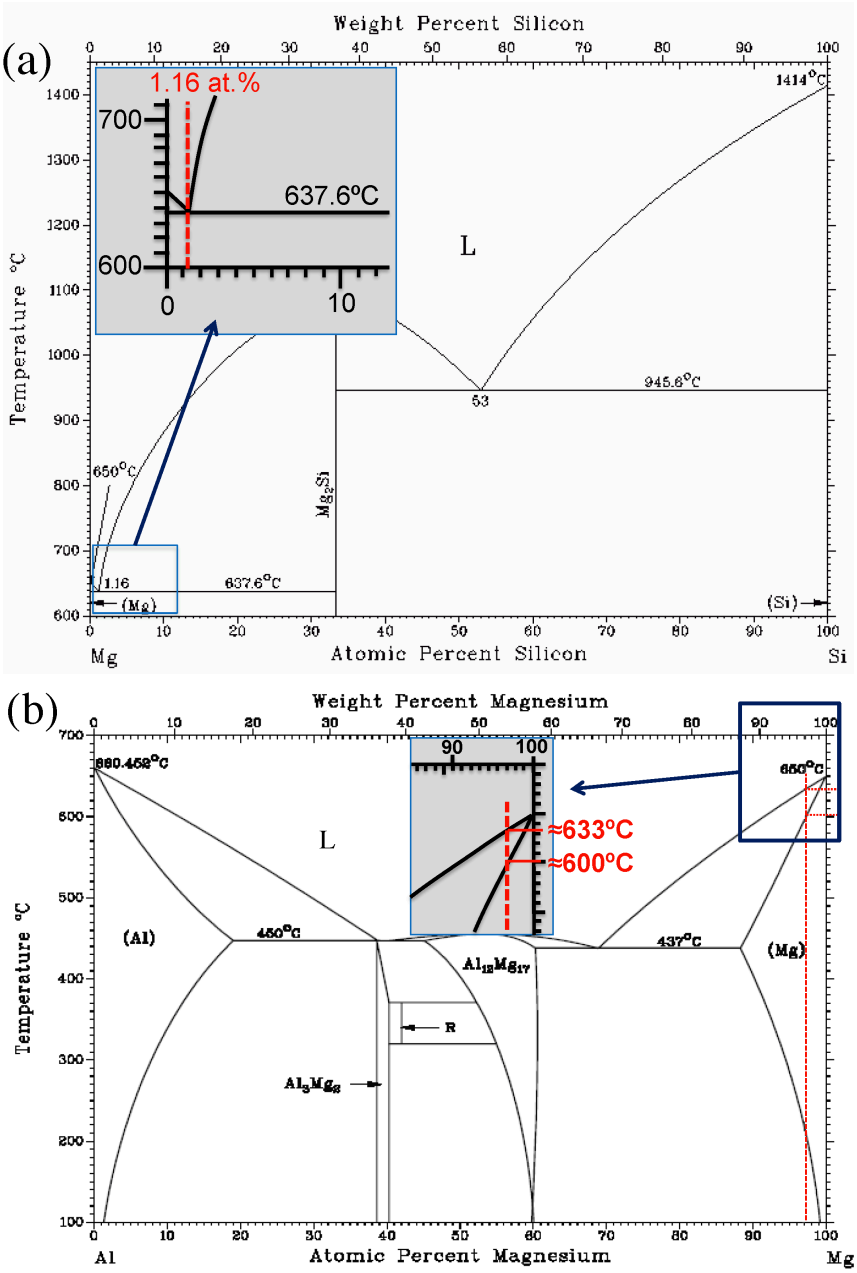

Fig. 2.3. Phase diagram of, (a) Mg-Si, (b) Mg-Al. The insets show the Mg rich regions [49].

2.5. Damping properties

High damping materials are important in structural applications in which reducing mechanical vibration and noise are needed. However, most metals and their alloys usually have low damping properties. Metal matrix composites, MMC, have been used as an alternative to the latter in order to improve the damping properties and at the same

time enhance the mechanical properties such as stiffness and strengths.

It is possible to tailor the damping properties of MMCs firstly by applying reinforcements with high damping capacities and/or controlling their volume fractions and geometries, and secondly by modifying the matrix microstructure to create sources for energy dissipation, such as defects. The damping capacities of MMCs were mostly ascribed to the presence of large numbers of defects [50, 51]. In general, the presence of a second phase can create two types of defects: large interfacial areas between the composite components [52, 53] and high dislocation densities in the regions adjacent to the interfaces, that can form during processing or deformation [51]. Interfacial damping can also result from frictional energy loss caused by sliding at the reinforcement/matrix interfaces. In general weak interfaces can lead to more energy dissipation [53, 54]. Among different shapes of reinforcement used in MMCs, one of the highest damping improvement was reported when particulate reinforcements were used [53].

Residual thermal strain, as a result of the large coefficient of thermal expansion, CTE, mismatch between matrix and reinforcement, can result in high densities of dislocations in the former [50]. In the case of MMCs reinforced with ceramics particulates, the CTE values of the metal matrix can be approximately $25x10^{-6}$ K^{-1} and those for the ceramic reinforcement can be 1 to $10x10^{-6}$ K^{-1} [9, 51]. This large CTE difference can result in a high density of dislocations induced during cooling from processing temperatures.

By using reinforcements with high damping capabilities themselves, it is also possible to further enhance the MMCs damping capacities, which in turn can be controlled by varying the reinforcement volume fraction, size and shape. Zhang *et al.*

reported that 1 vol.% SiC-Al alloy composite, fabricated via spray deposition, had the same damping properties as a monolithically spray deposited Al alloy. However, when 1 vol.% of graphite particulates were used instead of SiC, the damping capacity of the composite was doubled, which was attributed to the inherent damping of graphite [53].

In contrast to Al, the hexagonal close-packed metals, Ti, Mg, Co, Zr and Zn, inherently have good damping capabilities. Zhou *et al.* showed that when polycrystalline Co [55], Mg [56] or Ti [57], samples are cyclically loaded in simple compression, fully reversible loops formed above a threshold stress, σ_t. The size and shape of these loops was found to be a strong function of grain size; large grained samples had significantly larger damping capacities. The size of the loops was also a function of pre-strain that was attributed to the fact that increasing the deformation strain reduced the grain sizes, which in turn increased σ_t and ultimately reduced damping. In these studies, the damping behavior of these hexagonal metals was explained by a dislocation-based model and they were all classified as kinking non-linear elastic, KNE, solids [55-57]. The KNE model will be discussed in chapter 3.

Among all the structural metallic materials, pure cast Mg has the highest damping capability [58]. That was explained by the large average grain size of as-cast Mg and also by the low concentration of alloying elements, both of which, lead to longer and easier dislocation movements on the basal planes and easier twin formation [56, 59].

In general, the elastic and mechanical properties of pure Mg and Mg-alloys are relatively low for structural materials. One approach to enhancing these properties is to fabricate Mg matrix composite. However, since Mg damping is strongly grain size dependent [46, 56], and fabricating Mg-matrix composites reduces its grain size, in

almost all reports on the latter, typically improvements in mechanical properties come at the expense of lower damping capabilities [60, 61].

One approach, to enhance the damping properties in MMCs, is to use reinforcements that exhibit high damping capabilities themselves. As mentioned in section 2.4, the MAX phases are ternary carbides and nitrides with relatively high damping properties. Amini *et al.* showed that in pure Mg matrix composites reinforced with 50 vol.% ceramic particulates, changing the reinforcement type from SiC to Ti_2AlC or Ti_3SiC_2 can double the damping properties, due to the inherent damping capacities of the MAX phases. It is important to note that although at 500±25 MPa, the UCS of the 50 vol.% SiC-Mg was ≈ 30% lower than that of the Ti_2AlC reinforced composite, the damping capacity of the latter was almost double of that of the former, which was ascribed to the inherent damping of Ti_2AlC [62].

In a previous study by Amini *et al.*, it was concluded that in the Ti_2AlC 50 vol.%-Mg composite, energy dissipation mainly comes from the to and fro motion of basal dislocation loops in the Ti_2AlC and that Mg does not contribute to the energy dissipation due to the fact that it was assumed to be at nano scale. However, when Ti_3SiC_2 was used as the reinforcement damping was reported to be due to both Mg and Ti_3SiC_2. These conclusions were made based on outcomes of the KNE model, in which the calculated critical resolved shear stress, CRSS, in the 50-Ti_2AlC-Mg composites was the same as monolithic Ti_2AlC. However, the CRSS of the 50-Ti_3SiC_2-Mg was measured to be the average of the Mg and Ti_3SiC_2 values [62].

The main purpose of this study was to develop and understand the structure-property-composition relationships a new family of Mg-based composites. To investigate

the matrix composition effects, pure Mg and three Al-containing Mg alloys, viz. AZ31, AZ61 and AZ91, were used. To study the effect of reinforcement composition, TiC, Ti_2AlC and Ti_3AlC_2 were tested. To examine the effect of reinforcement particle size, two different particle sizes of each reinforcement phase (TiC and Ti_2AlC) were used. Careful XRD and SEM and TEM studies were carried out to shed light on the morphology of the grains in the Mg-matrices. In carrying out the characterization we specifically looked for evidence for nc-Mg in the Ti_2AlC-Mg composites. The mechanical properties were also characterized.

The last purpose of this thesis is to report on the damping properties of these composites. The effects of matrix and reinforcement compositions and particle size on the damping properties are elucidated. To investigate the effect of reinforcement volume fraction, pure Mg matrix reinforced with 5 and 20 vol.% reinforcements - Ti_2AlC and TiC - were fabricated and their damping properties measured.

Chapter 3: Modification of microscale modeling of kinking nonlinear elastic solids

This chapter revisits the kinking nonlinear elastic model and modifies it based on dislocation and kinking theories.

3.1. Introduction

The history of kinks in nonmetallic crystals is quite old. Mugge in 1898 was apparently the first to explain the nature of kink bands in mineral crystals [63]. However, Orowan in 1942 was the first to suggest kinking as a new type of deformation in metals in addition to slip and twinning. Orowan discovered kink bands when he axially compressed Cd single crystals, almost parallel to their basal (0001) planes. Single crystal Cd wires are typically quite soft; however, when their basal planes are parallel to the loading axis – such that glide mechanisms are not activated - they can be as hard as polycrystalline wires. Consequently, by increasing the load, the Cd wires suddenly collapsed forming kink bands with sharp ridges [64].

In 1949, Hess and Barrett studied Zn single crystal rods under uniaxial compression and also observed kink band formation. However, in contrast to Orowan's suggestion that kink formed abruptly like a twin, they suggested progressive basal glides which lead to the gradual development of kink bands [65]. Hess and Barrett explained kink band formation by the qualitative model shown in Fig. 3.1. In their model, they assumed that by loading along the basal planes, elastic bending creates a region of maximum shear stress in the center of columns (Figs. 3.1(a) and (b)). Above a critical shear stress value, dislocation pairs of opposite sign are nucleated and move in opposite

directions in the volume that is to become the kink band (Fig. 3.1(c)). The final result is two kink boundaries, each of which is made of many edge dislocations of one sign, which in turn cause the lattice rotation observed at BC and DE in Fig. 3.1(d). The combination of two kink boundaries and the region confined between them defines a kink band, KB.

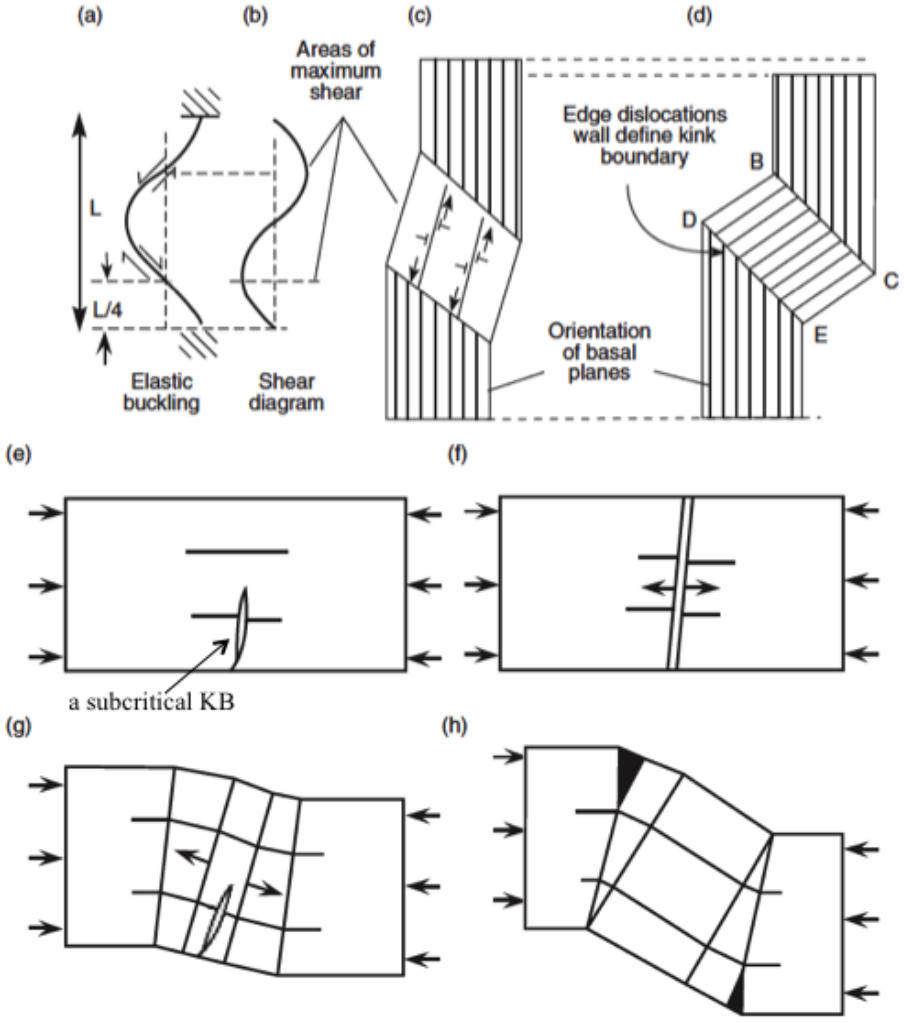

Fig. 3.1.Schematic of kink band formation: (a) elastic buckling; (b) corresponding shear diagram; (c) initiation of pairs of dislocations in areas of maximum shear; (d) kink band and kink boundaries comprised of edge dislocations of one sign giving rise to the signature stove-pipe configuration. (e–h) Adapted from Frank and Stroh [66] (e) initiation of subcritical KB; (f) intersection of subcritical KB with free surface removes the attractive energy between the walls and allows them to separate and move in opposite directions; and (g, h) repetition of same process to create more dislocation walls that ultimately become kink boundaries.

In 1952 Frank and Stroh, F&S, mathematically explained kinking theory and the essential difference between slip and kinking in term of dislocations. They explained that slip occurs by the successive generation of many dislocations all in the same slip plane, while kinking occurs by the generation of dislocation pairs on many parallel slip planes with an atomic distance, D, separating them (Fig. 3.2). They considered a subcritical KB as a region between two tilt edge dislocation walls of opposite sign in a crystal, transverse to a slip direction. The applied stress forces the walls away from each other, but the walls edges attract each other to form an elliptic cylinder. They then calculated the stress field and the energy of such a subcritical KB; a schematic of which is shown in Fig. 3.1(e). F&S showed that if a subcritical KB extends to a free surface the attraction between the edges of the dislocation tilt walls disappears and they become two separated parallel dislocation walls (Fig. 3.1(f)). A continuing stress forces the walls further apart. It follows that the same source can initiate a second subcritical KB (Fig. 3.1(g)) and by increasing the stress, the latter in turn grows to the free surfaces and separates into two walls. They explained these subcritical KBs as the precursors of the experimentally observed KBs, in which a successive generation of the subcritical KBs inside each other, from the same source, produce a KB as shown in Fig. 3.1(h) [66].

As noted above, F&S considered a subcritical KB as an infinite elliptic cylinder, whose generator is parallel to the y-axis and the cross section of the ellipse is

$$\frac{x^2}{\beta^2} + \frac{z^2}{\alpha^2} = 1 \qquad \alpha \gg \beta \tag{3.1}$$

A schematic of such a kink band is shown in Fig. 3.2. It is important to note that in the F&S model the kink length is assumed to be infinity and 2α is not limited to the

grain height. F&S postulated that a subcritical KB can grow by producing new dislocations pairs at its edges and/or shrink by annihilation of dislocation pairs. F&S derived the critical kinking angle (or shear strain) as

$$\gamma_c = \frac{b}{D} \approx \frac{3\sqrt{3}(1-\nu)\tau_{loc}}{2G} \tag{3.2}$$

where D is the distance between dislocations along 2α (Fig. 3.2), G and ν are the shear modulus and Poisson's ratio, respectively. τ_{loc} is the local shear stress needed to form a dislocation pair. In metals, if τ_{loc} is assumed to be ≈ G/30, then $\gamma_c \approx 3.5°$. It is important to note here that in that case the dislocation core width, w, is equal to the Burgers vector, b [46, 57].

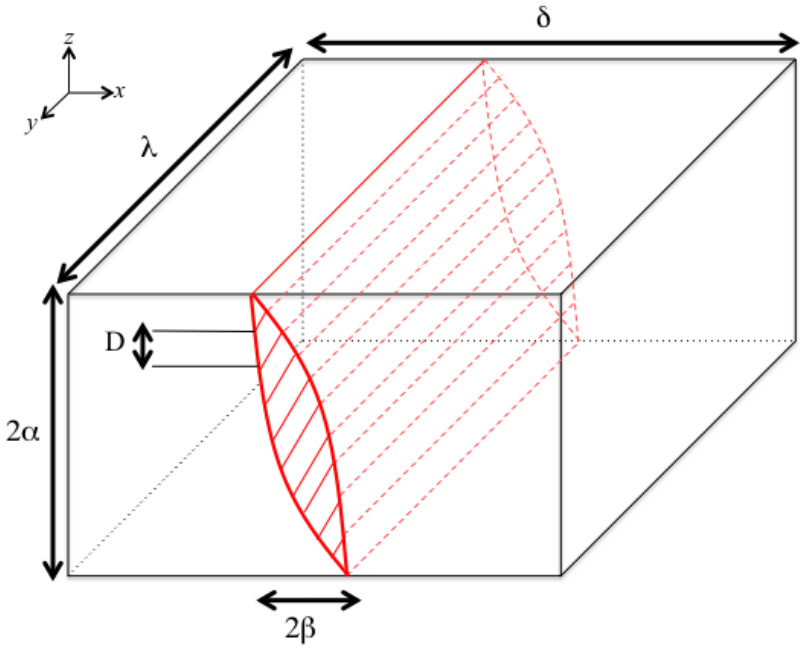

Fig. 3.2. An elliptic cylinder IKB.

Using a Griffith-like approach, F&S showed that at a critical shear stress

$$\tau_c \approx \sqrt{\frac{4G^2 b\gamma_c}{\pi^2 2\alpha} \ln \frac{b}{w\gamma_c}} \tag{3.3}$$

a subcritical kink band (Fig. 3.1(e)) becomes critical and would autocatalytically grow. More details about the F&S model will be discussed in section 3.2.

Gilman in 1954 studied kink band formation in Zn single crystals. He observed no kinking when the Zn basal planes were parallel to the loading direction. However, slight misalignment, in the range of 2.5º, induced kinking and by increasing the misalignment angle, the kink widths increased. Gilman, in contrast to Hess and Barrett, observed kinking in Zn even when the specimen ends were free to rotate during the compression test [67].

Roberts and Brown in 1960 carried out a carful study on micro and macroyielding of 99.994% purity Zn single crystals [68]. They oriented the specimens in a way that only basal slip can occur in tension tests. Microyielding started at stresses very close to zero and hysteresis stress-strain loops were observed in the microyielding region but only after an initial pre-strain. In other words, the hysteresis loops were not observed during initial loading of the annealed specimens, but once the specimen was given a small permanent strain, it began to show hysteresis loops, at or below the maximum stress level reached, in the microyielding region. They attributed the closed loops, in the microyielding region, to the bowing of dislocation networks in Zn.

A linear correlation between the area of the closed hysteresis loops, W_d, and the nonlinear strain was observed and the slope of the curve was equated to the frictional stresses of the moving dislocations. The frictional stress was found to be a function of the

interaction energy between dislocations and solute atoms, e.g., a Zn single crystal with 0.01 wt.% Cd, had almost 3 times higher frictional stresses than pure Zn [68].

By increasing the stress, an almost abrupt transition from micro to macroyielding was observed. They associated this sudden macroyielding to abrupt dislocations generation and/or their sudden movement over long distances. A nonlinear strain was also observed during unloading even after macroyielding and was correlated to both unbowing of the dislocations and the backward movement of the dislocations generated at the macroyielding point. After macroyielding, a *non-linear* correlation between W_d and non-linear strain, ε_{NL}, was observed [68].

In 1997, Barsoum and coworkers showed that the MAX phases are layered ceramics, which deform plastically by kinking [69, 70]. In order to study the deformation mechanisms in Ti_3SiC_2, the first MAX phase characterized in Barsoum's research group, highly oriented samples with grain sizes of the order of 1 to 2 mm were made and deformed at room temperature with the basal planes oriented, i) parallel to and, ii) at 65º with respect to the loading direction [71]. In the latter, shear bands were the only macroscopically observed deformation mechanism. However, when the basal planes were loaded edge on, KBs were observed in addition to shear bands. These kink bands were similar to those reported by Orowan, Hess and Barrett and others in hexagonal metals [71]. TEM micrographs of the same Ti_3SiC_2 sample revealed clear evidence of dislocation walls and KBs [72, 73].

In 2003, it was shown that it is possible to obtain full reversible hysteresis stress strain loops by cyclic compression of Ti_3SiC_2 polycrystalline samples up to stress levels as high as 1 GPa [44]. The stress-strain loops were not a function of strain rate. The same

loops sizes and shapes were obtained when the strain rates were 10^{-3} to 10^{-5} s^{-1}. In order to eliminate microcracking as a mechanism of energy dissipation, a fine-grained Ti_3SiC_2 sample was cycled 100 times to 700 MPa. When the first and the last loops were compared, the last loop was found to be slightly stiffer, which eliminated microcracking as the source of the hysteresis loops.

When samples were loaded to a maximum stress, followed by cycling to progressively lower stresses, nested loops were obtained and by measuring the area of such loops, the energy dissipated per unit volume per cycle, W_d, at each stress was calculated. In the same paper [44] along with a nanoindentation study on Ti_3SiC_2 [74], the idea of incipient kink bands, IKBs, was introduced for the first time as a possible reason for energy dissipation. In these two papers, the IKB was defined as an elliptic cylinder, similar to what F&S defined as sub-critical KBs (Fig. 3.2).

In 2004, the idea of energy dissipation due to the growing and annihilation of IKBs was proposed for different materials such as mica and graphite single crystals [75, 76] and it was concluded that plastically anisotropic solids (with high c/a ratios), can dissipate energy during cyclic loading, provided they did not twin, and thus deformed solely by kinking. Consequently, this family of solids was labeled kinking nonlinear elastic, KNE, solids; kinking because they deform by kinking, nonlinear because they show nonlinear behavior upon loading and unloading, and elastic because there is no permanent deformation observed during cyclic loading. A typical hysteresis stress-strain loop for a KNE solid during cyclic loading is shown in Fig. 3.3, in which W_d and ε_{NL} are defined.

In 2005, a KNE microscale model was introduced [77]. In this model, in contrast

to what F&S assumed as a subcritical KB and to what the previous papers called IKBs, the shape of the latter was changed to prolate spheroids that were made of parallel and coaxial basal dislocation loops as shown in Fig. 3.4(a). In the following, the KNE model based on the later definition of IKB will be discussed.

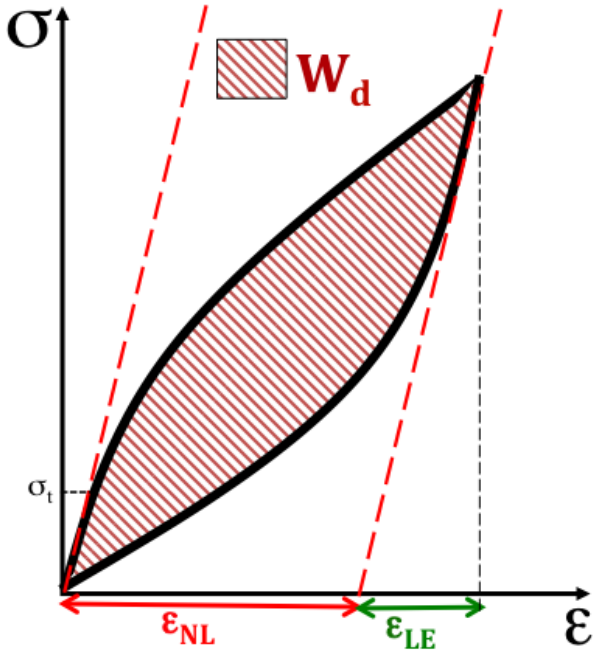

Fig. 3.3. Typical stress-strain curve for a KNE solid and definitions of non-linear strain, ε_{NL}, and energy dissipated per cycle, W_d.

3.2. KNE microscale model based on prolate spheroid IKBs

In the KNE model, IKBs were assumed to be prolate spheroids, PS, (i.e. the shape of an American football) shown schematically in Fig. 3.4(a), with 2α as the polar diameter (or height) and 2β as the equatorial diameter.

Eq. 3.3 was used in the KNE model and was modified for polycrystalline materials by defining $\tau_c = \sigma_t/M$, in which σ_t is a critical remote axial threshold stress (Fig. 3.3) and M is the Taylor factor. In Eq. 3.3, 2α was assumed to be the grain dimension along [0001] [55]. Interestingly, this implies σ_t is proportional to $1/\sqrt{}$ grain size, i.e. it follows a Hall-Petch-like relationship. In addition, in the KNE model, it was mostly assumed that $w = 5b$ [56, 57, 78], and as a result $\gamma_c = 0.7^o$ (Eqs. 3.2 and 3)

As noted above, an PS IKB consists of multiple parallel dislocation loops (Fig. 3.4(a)). As a first approximation, each loop was assumed to be made up of two edge and two screw dislocation segments with lengths of $2\beta_x$ and $2\beta_y$, respectively. The latter were related to the applied stress and 2α following the F&S model by:

$$2\beta_x \approx \frac{2\alpha(1-\nu)}{G\gamma_c}\frac{\sigma}{M} \qquad\qquad 2\beta_y \approx \frac{2\alpha}{G\gamma_c}\frac{\sigma}{M} \tag{3.4}$$

In general the formation of an IKB can be divided into two stages: nucleation and growth. The KNE model only discuss the growth from a critical size $2\beta_{xc}$ and $2\beta_{yc}$ to $2\beta_x$ and $2\beta_y$, respectively. The former were assumed to either preexist, or form during pre straining.

When $\sigma > \sigma_t$, the IKBs grow and the strain induced by these IKBs is

$$\varepsilon_{IKB} = \frac{\Delta V.\gamma_c N_k}{k} = \frac{4\pi\alpha(\beta_x\beta_y - \beta_{xc}\beta_{yc})\gamma_c N_k}{3k} \tag{3.5}$$

where ΔV is change in the volume as the IKBs grow from their critical size at σ_t to their size at σ and N_k is the number of IKB per unit volume. k represents a factor that relates the IKB shear strain at the grain level to the measured uniaxial macro-scale strain. This factor depends on various microstructural parameters that would control the orientations of the IKBs with respect to the loading axis, e.g., the texture in the sample and is of the order of 1 to 2 [46, 56, 57].

Combining Eqs. 3.4 and 3.5 leads to

$$\varepsilon_{IKB} = \frac{4\pi(1-\nu)\alpha^3 N_k}{3kG^2\gamma_c M^2}(\sigma^2 - \sigma_t^2) = m_1(\sigma^2 - \sigma_t^2) \quad (3.6)$$

This equation predicts that the non-linear strain due to IKBs should be linearly proportional to stress squared. m_1 is a coefficient that can be determined experimentally, i.e. it the slope of the ε_{NL} vs. σ^2 curves. Once m_1 is determined and since the other factors are known, N_k can be estimated.

The energy dissipated per unit volume per cycle, W_d, resulting from the growth of the IKBs from β_{ic} to β_c was assumed to be [46]

$$W_d = 2\,\pi\,(\beta_x\beta_{y-}\beta_{xc}\beta_{yc})N_k\,\frac{2\alpha}{D}\Omega \quad (3.7)$$

where 2α/D and Ω represent the number of dislocation loops per PS and the energy dissipated by a dislocation line sweeping a unit area, respectively. Combing Eqs. 3.4 and 3.7 results in

$$W_d = \frac{4\pi(1-\nu)N_k\alpha^3\Omega}{G^2 b\gamma_c M^2}(\,\sigma^2 - \sigma_t^2) = m_2(\,\sigma^2 - \sigma_t^2) \quad (3.8)$$

where m_2 is another coefficient that can be experimentally determined from the slopes of the W_d vs. σ^2 curves. The linear correlation between W_d and σ^2, at stresses above σ_t, was explained by the fact that IKBs keep their lengths (2α) and only grow along β_x and β_y. It is this 2-D growth of IKB dislocations in the basal planes, that gives rise to the dependence of W_d on σ^2.

Combining Eqs. 3.6 and 3.8 yields

$$W_d = 3k\,\frac{\Omega}{b}\,\varepsilon_{IKB} \quad (3.9)$$

which is another result of this model and predicts that W_d has a linear correlation with nonlinear strain due to the growth of the IKBs. Note that Ω/b is the critical resolved shear stress (CRSS) of a basal dislocation loop.

Presence of 3k in Eq. 3.9 is due to the fact that the IKB was assumed to be a PS in the ε_{IKB} calculations (Eqs. 3.5 and 3.6) and as a cylinder in the W_d calculations (Eqs. 3.7 and 8). If IKB are assumed to be PS in the W_d calculations as well, then $\beta_{average}$ has to be used in Eq. 3.7, because 2β changes over the height of the spheroid. A simplified averaging is to assume a linear change in 2β along the spheroid height, which leads to $\beta_{average}=\beta/2$. Applying $\beta/2$ in W_d calulations changes Eq. 3.9

$$W_d = \frac{3k}{4}\frac{\Omega}{b}\,\varepsilon_{IKB} \tag{3.10}$$

This modification has no effect on the concept of Ω/b and can only change its value. A more detailed discussion of Ω/b will be presented in section 3.5.

Over the past decade, it has been shown that a large number of seemingly unrelated solids such as C-plane ZnO [79], $BaTiO_3$ [80], sapphire [81], $LiNbO_3$ [82], $LiTaO_3$ [83], Mg, Co, Ti, Zn [55, 57], graphite [75], mica [76, 84] and the MAX phases [45, 77, 78] among others, trace fully reversible hysteretic stress-strain loops upon cyclic loading. In all cases, the results were fitted to the KNE model leading to reasonable results for Ω/b and other parameters.

Before moving forward, it is critical to note that the KNE model is a microscale model based on IKBs, which have been never observed experimentally due to the fact that they are small and only appear under load and disappear when the load is removed.

Furthermore, the concomitant shear is quite small, in the range of 0.7º.

In the following a slightly different IKB dislocation configuration is proposed. No new experiments have been carried out. The goal was to achieve a better understanding of the model and possible IKB shape and to better describe what type of defect configurations to look for in order to observe IKBs.

3.3. KNE microscale model based on different dislocation configurations

It is crucial to note that in the existing KNE model, as well as, in all the calculations here, it was assumed that the strain is uniformly distributed in all the grains, which experimentally is not the case. However, this simplification does not affect the basis of the calculations.

For the first hypothesis, the IKBs are assumed to be PS (Fig. 3.4(a)) of parallel dislocation loops as was assumed in the existing KNE model. One of the best methods to check if such an IKB definition is valid, is to calculate how many IKBs are needed per grain for a measured ε_{NL}. This can be done for all the data that have been published on the KNE model. In this study, only the results for the maximum applied stress on coarse grain-, CG-, and fine grain-, FG-, Ti_3SiC_2 [77] and CG-Ti_2AlC [45] are reanalyzed at the reported maximum applied stress, ε_{NL} and the grain dimensions. Since in both studies, the MAX phase are shown to be elongated grains along $[10\bar{1}0]$, 2α is assumed as the smallest grain dimension (along [0001]), then 2β is calculated from Eq. 3.4. N_k is calculated from Eq. 4.5 assuming all the experimentally measured ε_{NL} is due to the PSs, i.e. making the same assumption as in the original studies [45, 77]. The number of PSs per grain, $N_{k/grain}$ is calculated by multiplying N_k by the average grain volume. Grain

dimensions for Ti_3SiC_2 were reported in the original study [77], however, for Ti_2AlC only the grain size along [0001] was reported as 18 μm [45]. Considering the Ti_2AlC grain shape depicted in the original study, a grain aspect ratio of ≈ 3.3 can be assumed, conaequently, the averge grain dimension can be assumed to be ≈ 60x60x18 μm^3.

The number of PS for the CG- and FG-Ti_3SiC_2 and CG-Ti_2AlC are calculated to be ≈ 5245, 298, 638 per grain, respectively, as shown in Table 3.1. These $N_{k/grain}$ values are clearly too high, considering they are all dislocation loops that do not interact, and have to annihilate upon unloading of the stress (Fig. 3.4(b)). For instance, in the case of FG-Ti_3SiC_2 with $N_{k/grain}$= 298, the maximum number of PS with a diameter of 2β = 0.38 μm can be fitted in a 8x8x3 μm^3 grain is only ≈ 450, assuming the spheroids are close packed. This shows how close the PS have to be in order to reach the reqired N_k. The same is true for CG-Ti_3SiC_2 [77] and CG-Ti_2AlC [45].

Aside from the fact that the PSs are too small and too numerous, all permanet KBs that have been observed experimentaly go through the entire grain and i..e. they do not disapear inside the grains or pentrate partially through a grain. In order words, if the PSs (Fig. 3.4(b)) resulted in the KBs, the latter would change its path along the grain and a kinked grain would have several KBs that only extended across a portion of the grain, similar to what is shown in Fig. 3.4(c), which, to our knowledge, has never been observed.

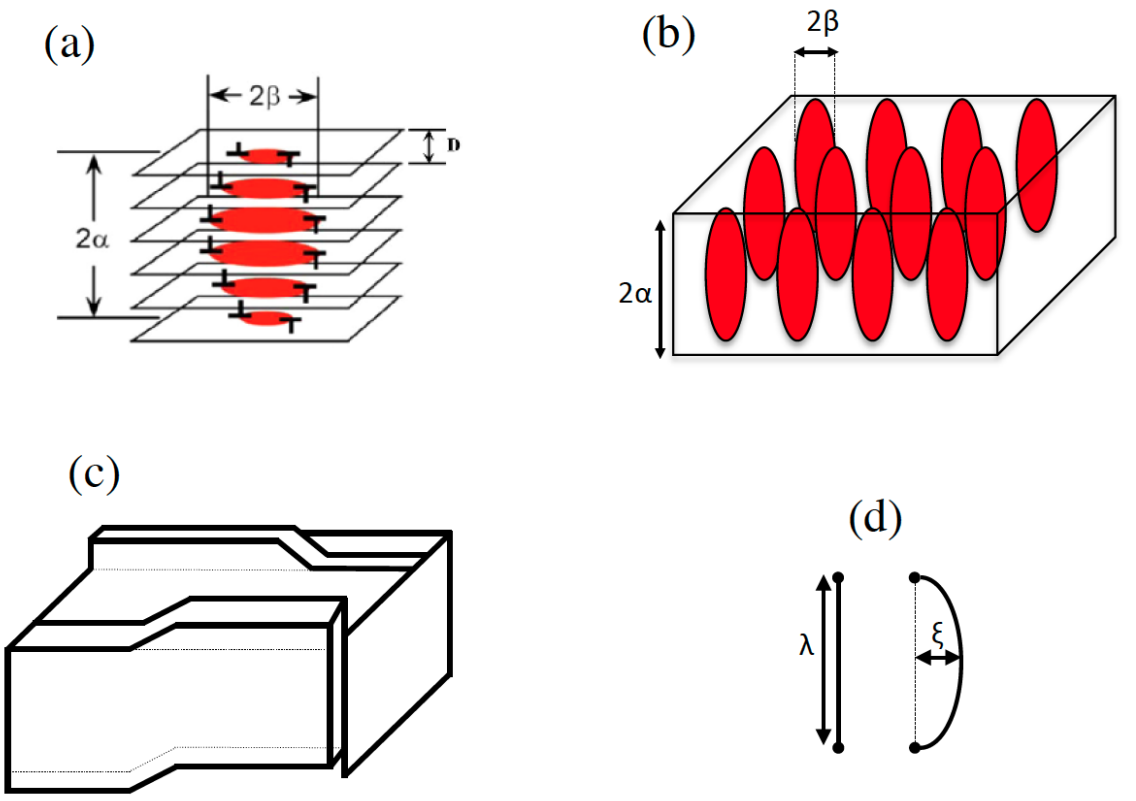

Fig. 3.4. (a) a prolate spheroid IKB; (b) several prolate spheroid IKBs needed in a grain to reach the calculated N_k; (c) a possible kinked grain if IKBs were prolate spheroids; (d) a dislocation of λ length that bows out ξ.

The second possible IKB shape is be the elliptic cylinder, EC, that F&S assumed to be a subcritical KB (see Fig. 3.2). Such an EC is made of two tilt walls of edge dislocations going through the entire grain length (λ). One way to rationalize such an IKB is to assume basal dislocation loops with edge and screw segments form and as a result of repulsion between the screw components, the latter run towards the grain boundaries and only the edge components remain. As a result, Eq. 3.5 can be re-written as

$$\varepsilon_{IKB} = \frac{\Delta V.\gamma_c N'_k}{k} = \frac{\pi\alpha\beta\lambda\gamma_c N'_k}{k} = \frac{\pi\beta\gamma_c N'_{k/grain}}{2k\delta} \qquad (3.11)$$

where N'_k and $N'_{k/grain}$, are the number of ECs per unit volume and per grain, respectively. λ and δ are the grain length and diameter, respectively (Fig. 3.2).

Table 3.1. compares $N'_{k/grain}$ to $N_{k/grain}$. Clearly $N'_{k/grain}$ is a much more reasonable number and can be fitted in a grain. For instance, at 1 GP, only 9 ECs are needed to account for the measured ε_{NL} in the FG-Ti_3SiC_2 sample (Table 3.1).

In Eq. 3.11, however, if Eq. 3.4 is assumed to be valid, then:

$$\varepsilon_{IKB} = \frac{\Delta V.\gamma_c N'_k}{k} = \frac{\pi\alpha\beta\lambda\gamma_c N'_k}{k} = \frac{\pi\alpha^2\lambda N'_k(1-\nu)\sigma}{kMG} \quad (3.12)$$

and ε_{IKB} would be independent of γ_c and only depend on the grain dimensions and the applied stress. This reveals that Eq. 3.4 cannot be applicable, which leads to two unknowns in Eq. 3.11: β and $N'_{k/grain}$ for any measured ε_{NL}.

Table 3.1. ρ_m, $N_{k/grain}$, $N'_{k/grain}$, $\bar{x}$, ξ are calculated based on the different hypotheses. σ and ε_{NL} and grain dimensions are from the papers referenced. 2β was calculated from Eq. 4 assuming 2α is the smallest grain dimension. N_k was calculated using Eq. 5, assuming γ_c =0.012. Multiplying N_k by the grain volume gives $N_{k/grain}$. $N'_{k/grain}$ is calculated from Eq. 11. The average grain diameter and length of the CG-Ti_2AlC is estimated to be 60 μm, assuming the aspect ratio of ≈ 3.3. $\bar{x}$ and ξ are calculated from Eqs. 3.13 and 3.14, respectively. M and k are assumed to be 3 and 2, respectively [45, 77].

Material	Grain dimensions (μm^3)	σ (MPa)	ε_{NL}	2β (μm)	(PS IKB) $N_{k/grain}$	(PS IKB) ρ_m (m^{-2})	(EC IKB) ρ_m (m^{-2})	(EC IKB) $N'_{k/grain}$	$\bar{x}$ (μm)	ξ (μm)
FG-Ti_3SiC_2**[77]**	8 × 8× 3	845	0.0022	0.38	298	2.24×10^{14}	9.5×10^{13}	9.5	0.09	0.06
CG-Ti_3SiC_2**[77]**	42 ×42 ×11	246	0.0016	0.41	5245	1.53×10^{14}	6.5×10^{13}	34	0.10	0.042
CG-Ti_2AlC **[45]**	60 ×60 ×18	336	0.00071	1.12	638	2.54×10^{13}	1.1×10^{13}	7.9	0.27	0.115

To avoid such a problem and as for the third hypothesis, we can start from dislocation theory and calculate the dislocation density (ρ_m) required for the experimentally measured ε_{NL}. For this hypothesis, we need to speculate that the hysteresis loops are only observed after a pre-loading to the maximum stress, which causes a plastic strain at least comparable to ε_{NL}, if not larger. The pre-strain requirement has been observed for metals in different studies [55-57, 68] but not necessarily for the MAX phases. Consequently, it is reasonable to assume at least the same number of dislocations are created during the first loading cycle to the maximum stress. In other words, it is assumed that N_k' of IKBs are created during the first cycle and upon cyclic loading they only move back and forth in the β direction.

In general the shear strain, γ, due to the movement of ρ_m dislocations can be calulated assuming [85]

$$\gamma = b\bar{x}\rho_m \tag{3.13}$$

where $\bar{x}$ is the average dislocation movement in response to the applied shear stress, and $\gamma = 2\varepsilon(1+\nu)/M$ [86]. For Ti_3SiC_2 and Ti_2AlC, one can assume $\nu = 0.2$ and $M = 3$ and the relationship between axial and shear strains is $\varepsilon = 1.25\gamma$. If we assume ε_{NL} is only due to the back and forth movements of dislocations of the IKB tilt walls, it is possible to calculate $\bar{x}$ from Eq. 3.13 for any measured ε_{NL}. Note that, ρ_m and the corresponding N_k' values are calculated from Eq. 3.11. The $\bar{x}$ values listed in Table 3.1 are calculated based on these assumptions.

The fourth and last hypothesis is to assume that the preexisting dislocations, which were created during the first loading cycle, or even during fabrication, bow out and un-bow during cycling loading. As discussed below it is doubtful that only bow out and

unbowing can cause such large energy dissipation. Moreover, if bow and unbowing was the primary source of energy dissipation should have been observed in FCC metals and other non KNE solids.

To test this hypothesis it is worthwhile to carry out a back of envelope calculation to estimate the bowing radius required for dislocations for any measured strain. If we assume the preexisting dislocation density to be the same as the ones assumed above and further assuming:

$$\varepsilon = 1.25\, bn\bar{A} \tag{3.14}$$

where n and $\bar{A}$ are the total number of dislocations per unit volume and the average area swept by a dislocation, respectively, the bowing out of dislocations can be calculated. If a dislocation with length λ bows out to ξ (Fig. 3.4(d)), then $\bar{A}$ can be approximated to be the area of half an ellipse or $\frac{\pi}{2}\lambda\xi$. The values of ξ needed to obtain the experimentally measured ε_{NL} values can be thus calcualted from Eq. 3.14 and are listed in Table 3.1.

As shown herein, these three new hypotheses, namely: i) growing and annihilation of ECs, ii) the back and forth movement of IKB dislocations as the growing and shrinking of preexisting ECs (but no annihilation) and, iii) even bowing and unbowing of dislocations, can possibly explain the results that have been observed for KNE solids to date. In fact, it is shown here, that only ρ_m and the average dislocation movement distance, $\bar{x}$ are crucial. The actual dislocation configuration, whether it is an IKB or not, is not that critical.

However, since random dislocation configurations cannot lead to the permanent KBs observed experimentally in most studies on KNE solids, and since KBs are symmetrical and two kink boundaries with the same angle are usually observed in a given

KB, it is difficult to conceive how the KBs would form from random dislocations. A source, such as an IKB cylinder, is needed to create these walls in two opposite directions in order to create a symmetrical KB. Said otherwise, something has to be nucleating repeatedly in a given volume that ultimately leads to the formation of two symmetric kink boundaries. Note that some kink boundaries can be quite sharp and thus can only form from the accumulation of many mobile dislocation walls, MDWs.

Based on all the hypotheses presented here, IKBs are probably not PSs that exist only under maximum stress with a shear angle of 0.7º. If the new hypothesis is correct, a TEM study on cyclically deformed grains of a KNE solid, such as Ti_3SiC_2 or Ti_2AlC, might show the presence of two tilt walls of opposite dislocation signs. Also, for the third hypothesis, back and forth movement of preexisting dislocations, it is speculated that a pre-strain is always needed to create such loops. If this is true, the configuration of dislocations at the pre-strain range can be figured out by a TEM study, to shed light on the shape of the IKBs.

3.4. Nonlinear strain (ε_{NL}) and maximum applied stress (σ) correlation

In most previous studies on KNE solids, a linear correlation between ε_{NL} and σ^2 was found. This was explained by assuming that the basal dislocation loops of the PSs increased in two dimension: β_x and β_y. N_k on the other hand was assumed to be constant over the entire stress range, e.g. up to 1 GPa [77].

In the new model proposed herein, the EC dislocations are only assumed to move in one direction (β_x) and consequently, σ only increases β in Eq. 3.11 and the relationship between ε_{NL} and σ would be linear, which is not observed. It follows that to reconcile model and theory, herein we assume the number of IKBs increase with increasing σ. In

other words, the number of mobile dislocations contributing to ε_{IKB} (N_k') also increases linearly with increasing applied stress. Consequently, there are still two variables (β and N_k'), both of which are stress dependent, which in turn can lead to the ε_{NL}-σ^2 correlation observed experimentally. Figure 3.5 shows ε_{NL} versus σ^2 for the results for some MAX phases presented in references [45, 77].

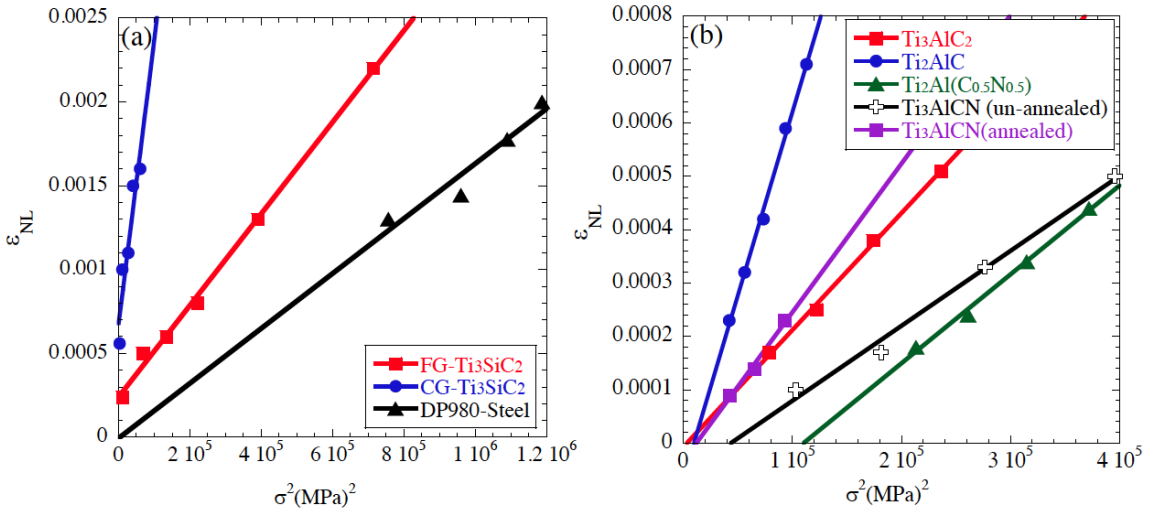

Fig. 3.5. ε_{NL} vs. σ^2 plots for (a) FG- and CG-Ti_3SiC2 [77], (b) Ti_3AlC_2, Ti_2AlC and Ti_3AlCN [45]. The results for dual phase steel (DP980) loaded in tension up to 1 GPa [87] are plotted in (a).

3.5. Nonlinear strain (ε_{NL}) and energy dissipation (W_d) correlation

According to Eq. 3.9, there is a linear correlation between W_d and ε_{NL} with a slope of $\frac{3k}{4}\frac{\Omega}{b}$, in which Ω/b is the CRSS for basal slip. In other words, $\frac{\partial W_d}{\partial \varepsilon_{NL}}$ versus σ should result in a constant value, 3kΩ/4b, over the entire σ range. Figure 3.6 plots $\frac{\partial W_d}{\partial \varepsilon_{NL}}$

versus σ for select MAX phases and pure Mg studied in Refs. [45, 56, 77]. Clearly, $\frac{\partial W_d}{\partial \varepsilon_{NL}}$ increases with increasing the σ. Since, in 3kΩ/4b the only variable is Ω, these results imply that the energy dissipated by the dislocation lines sweeping a unit area is not a constant but is a function of σ.

In order to achieve a better understanding of Eq. 3.9 and the correlation between W_d and ε_{NL}, we can start from the following relationship

$$W_d = 2n\bar{A}\Omega \tag{3.15}$$

in which it is assumed that W_d is due to dislocation motion and that each dislocation line sweeps an average area $\bar{A}$; n is the total number of dislocations per unit volume. It is multiplied by a factor of 2, due to the back and forth dislocations movement, i.e. doing loading and unloading. Combing Eqs. 3.14 and 3.15 leads

$$W_d = 1.6\frac{\Omega}{b}\,\varepsilon_{IKB} \tag{3.16}$$

which is similar to Eq. 3.10. According to Eqs. 3.10 and 3.16, if Ω remains constant over the entire test, plots of $\frac{\partial W_d}{\partial \varepsilon_{NL}}$ vs. σ or non-lineara strain (Figs. 3.6(a) to (c)) should all result in horizontal lines, which is not the case. In the case of Zn single crystal, Roberts and Brown, observed a linear correlation between W_d vs. γ_{NL} only in the microyielding regime, which deviated from linear after microyielding [68]. One possible explanation for increasing Ω after the macroyield point can be the dislocation interactions with other

dislocations or defects. Such an interaction can pin the dislocations, and higher applied resolved shear stresses would then be needed to overcome the obstacle strengths. This comment notwithstanding, more work is needed to understand these results.

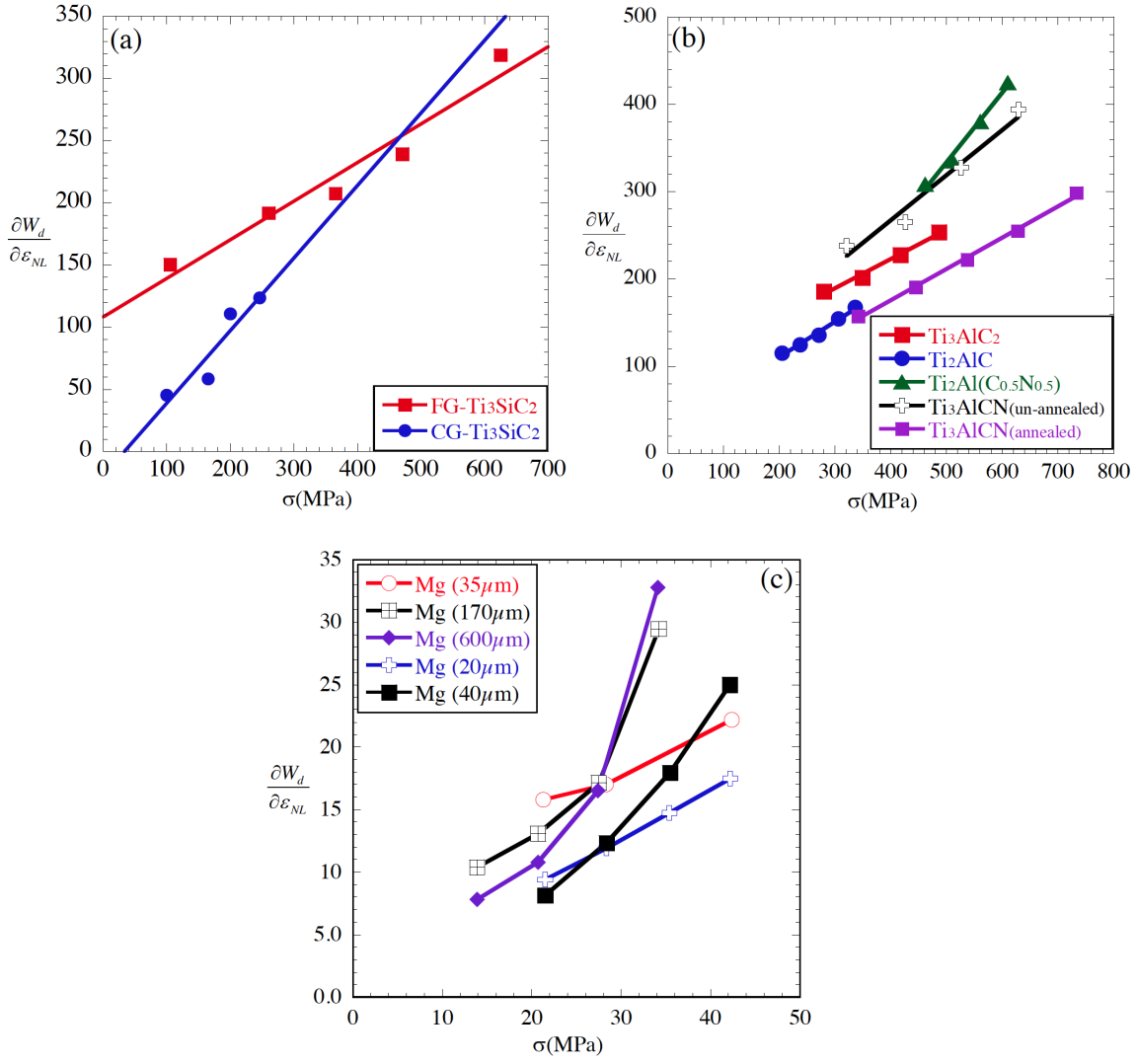

Fig. 3.6. $\frac{\partial W_d}{\partial \varepsilon_{NL}}$ vs. σ plots for (a) FG- and CG-Ti_3SiC2 [77], (b) Ti_3AlC_2, Ti_2AlC and Ti_3AlCN [45], (c) pure Mg with different grain size [56]. The numbers in parantheses respresent Mg grain size.

According to Fig. 3.6(a), Ω increases more rapidly for the CG-Ti_3SiC_2 than the FG. To further understand the effect of grain size, the results for cyclic compression of pure Mg with different grain size, from 20 μm to 600 μm, by Zhou *et al.* are plotted in Fig. 3.6(c) [56], which shows a higher dependency of $\frac{\partial W_d}{\partial \varepsilon_{NL}}$ to stress for larger grain sizes. The reason for state of affairs is not clear at this time. One possible explanation can be the presence of longer dislocation lines in the CG materials that increases the chance of dislocations interacting with defects and other dislocations. The presence of more obstacles would need higher stress to overcome them. Here again more work is needed to understand this dependency.

3.6. Conclusions

At the end of this chapter, it is reasonable to conclude that the shape of IKBs is most probably not prolate cylinders, since the N_k needed for the measured ε_{NL} would be too high to fit within the grains. In addition, the presence of several PSs such as what is shown in Fig. 3.4(b), leads to KBs that change their path through the grains such as Fig. 3.4(c). However, experimental observation showed KBs always go through the entire grains and does not stop in the middle of the grains.

A possible modification is to define IKBs as ECs that extend across the entire grain length. Such an IKB is made of two tilt walls as F&S explained in their kinking theory. By increasing the applied stress, the IKBs dissociate into two mobile dislocation walls of opposite sign. As noted by us and others, it is the accumulation of these walls over a narrow region that creates a symmetric KB. Observation of symmetrical KBs makes it more evident that an IKB source is needed to create two similar dislocation

walls of opposite sign and angles that are almost identical.

Finally, it is worth mentioning that energy dissipation has been observed in materials with hard grains next to soft grains. That is why plastic anisotropy was assumed to be a requirement for non-linear elasticity. However, if a material contains hard and soft grains, it does not necessarily need to be a plastically anisotropic solid. For instance, Sun *et al.* observed hysteresis loops in dual phase steel (DP980), during loading and unloading in tension up to 1 GPa [87]. For the sake of comparison, ε_{NL} vs. σ^2 for dual phase steel is shown in Fig. 3.5(a). This can be explained by the presence of soft ferrite matrix and hard matensite and high dislocation denisty at their interfaces during deformation.

Chapter 4: Material and Procedures

In this chapter, the procedure for fabricating all the composites for this study and testing them are discussed.

4.1. Material

The following composites – all at ≈ 50 vol. % loading - were fabricated: Ti_2AlC-Mg, Ti_2AlC-AZ31, Ti_2AlC-AZ61, Ti_2AlC-AZ91, Ti_3AlC_2-Mg and TiC-Mg, TiC-AZ31, TiC-AZ61 and TiC-AZ91. In addition, Ti_2AlC-Mg and TiC-Mg composites were fabricated with 5 and 20 vol.% of the reinforcement.

Pure Mg (99.8% pure), AZ31B (3 wt.% Al, 1 wt.% Zn) both purchased from Alfa Aesar (Ward Hill, MA) and AZ61L (6 wt.% Al, 1 wt.% Zn, low Mn) and AZ91D (9 wt.% Al, 1 wt.% Zn) both supplied by Thixomat (Livonia, MI) were used. Two TiC powders (Alfa Aesar, Ward Hill, MA) were used; one with coarse grains, the other with fine grains. Similarly, two Ti_2AlC powders (Kanthal, Sweden) were used as reinforcements; one with coarse grains, the other with fine grains.

In general, Ti_3AlC_2 is commonly found in commercially obtained Ti_2AlC powders. The as-received Ti_2AlC powder used herein contained ≈ 20 wt.% Ti_3AlC_2. In order to investigate the effect of the presence of this impurity phase, pure Ti_3AlC_2 was fabricated following the method reported earlier [88], milled and sieved to produce a –325 mesh powder. Composites were then made using the sieved powder.

4. 2. Processing

4.2.1 Preparation of ≈ 50 vol.% dense carbide preforms

Two types of porous (52±2 vol.% dense) Ti_2AlC preforms were fabricated: random and oriented. The former were fabricated by cold pressing Ti_2AlC powders in a steel mold, with a load, corresponding to a stress of 45 MPa. To make oriented preforms Ti_2AlC powders were poured into a graphite die and manually vibrated for ~ 15 min in an attempt to orient the flake-like particles perpendicular to the pressing direction [89]. The porous preforms were then hot pressed (HPed) in a graphite heated, vacuum-atmosphere HP (Series 3600, Centorr Vacuum Industries, Somerville, MA). The preforms were heated at 10 ºC/min to 900 ºC and held at that temperature for 1 h under ≈ 10 Pa vacuum, after which the HP was turned off and the samples were furnace cooled. When the temperature reached 700 ºC, a load, corresponding to a stress of 20 MPa, was applied and maintained thereafter. This step was introduced to enhance the green strengths of the porous performs to prevent their fracture during the MI step.

The Ti_3AlC_2 preform was fabricated in the same method. In this case no attempt was made to orient the powders.

The porous TiC preforms (54±2 vol.% dense) were HPed at 1050 ºC for 1 h, using a load corresponding to a stress of 20 MPa. No manual vibration was applied.

4.2.2. Pressureless melt infiltration

For the purpose of MI, the preforms were placed in alumina crucibles (AdValue Technology, Tucson, AZ), the insides of which were lined with graphite foil to avoid reaction between Mg and alumina. Chunks of Mg or Mg alloys were placed on the top of

the preforms. Alumina disks were used as lids to cover the crucibles that, in turn, were placed in a graphite-heated vacuum (≈10 Pa) furnace and heated at a rate of 10°C/min up to 750°C for the Ti_2AlC and Ti_3AlC_2 preforms and 850ºC for the TiC preforms. Due to high vapor pressure of Mg inside the alumina crucible, it condensed between the alumina lid and crucible and sealed the gap between them. The assembly was held for 1 h at the designated temperature before furnace cooling. A schematic of the MI setup is shown in Fig. 4.1. For comparison purposes, chunks of monolithic AZ61L and pure Mg samples – with no preform - were also molten, at 750 °C for 1 h and furnace cooled. Composites fabricated with ≈ 50 vol.% Ti_2AlC or TiC will henceforth be referred to as 50-Ti_2AlC- or 50-TiC- composites, respectively. In general in this thesis, the number that comes before the reinforcement represents the vol.% of the reinforcement.

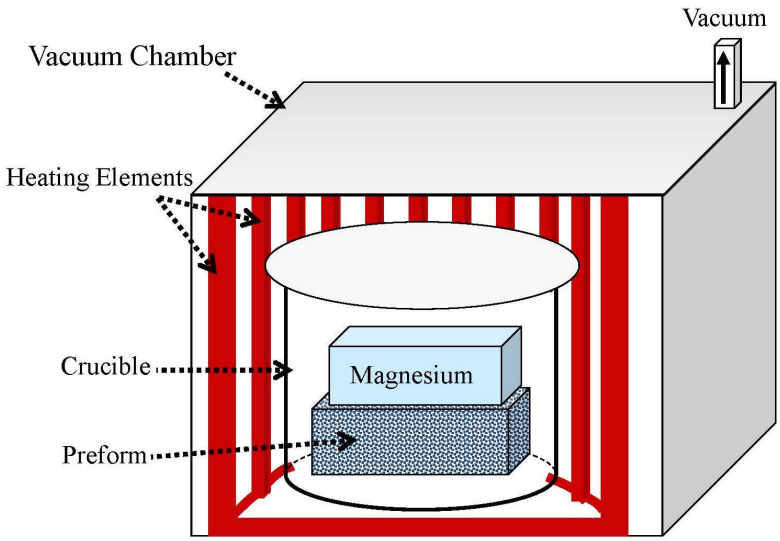

Fig. 4.1. Schematic of melt infiltration setup for fabricating 50 vol.% reinforced composites.

4.2.3. Fabrication of composites with 20 and 5 vol.% reinforcement

The 20±2 and 5±1 vol.% reinforced composites were made via powder metallurgy using Ti_2AlC or TiC as reinforcements. In this case only pure Mg powder was used as the matrix. The proper mixture of reinforcement particles, Mg powder and zirconia milling balls were sealed in a plastic jar and the latter was sealed in a steel can inside a glove box filled with argon, Ar, gas. The mixtures were then removed from the glove box and ball-milled for 12 h, and then cold pressed with a load corresponding to a stress of 50 MPa into rectangular bars (1.3 x 1.3 x 70 mm^3). The porous bars were then placed in alumina crucibles, the insides of which were lined with graphite foil to avoid reaction between Mg and alumina. The crucibles were in turn covered with alumina lids and placed in a graphite-heated vacuum-atmosphere furnace, heated at 10°C/min to 750°C, held at that temperature for 1 h, after which the furnace was turned off and the samples were allowed to cool in the furnace. Composites fabricated with 20±2 and 5±1 vol.% Ti_2AlC will henceforth be referred to as 20-Ti_2AlC-Mg and 5-Ti_2AlC-Mg composites, respectively. Composites with similar volume fractions of TiC as the reinforcement will be referred to as 20-TiC-Mg and 5-TiC-Mg.

4.3. Microstructural characterization

The composite samples were cross-sectioned, mounted and polished down to 1 μm with diamond slurries. The polished and fractured surfaces were imaged using a SEM, (Zeiss Supra 50VP, Germany) equipped with an energy-dispersive spectroscope (EDS) (Oxford Inca X-Sight, Oxfordshire, UK). XRD was carried out on a diffractometer (Rikagu Smartlab, Japan), using step scans of 0.02º in the range of 5°–120° 2 theta and a

step time of 7 s with a 10x 10mm^2 window slit. Scans were made with Cu Kα radiation (40 KV and 30 mA). The accuracy of the diffractometer in determining lattice parameters, and its instrumental peak-shape function parameters, were found using Si (X-ray Diffraction Accessories, State College, PA), and LaB_6 (NIST 660B) standards. The reason for the long acquisition times and the large 2 theta range was to try and identify any minority phases that may have formed as a result of reactions between the reinforcements and matrices.

All diffractograms were analyzed by the Rietveld refinement method, using the FULLPROF code [90, 91]. A systematic shift of - 0.06% was found in the lattice parameters' evaluation of the aforementioned standards as compared to their reported value and corrected. The Thompson-Cox-Hastings pseudo-Voigt model was used to refine the peak shapes of each phase's reflections. Lattice strain, and particle size were also estimated assuming isotropic Gaussian and Lorentzian contributions to the peak shape function, respectively [92].

In previous work, nano sized Mg grains was reported in the matrix of 50-Ti_2AlC-Mg composite [47]. To further investigate whether Mg grains in the matrix are at the nano scale, 2-dimensional, 2-D, XRD was carried out on the 50-Ti_2AlC-Mg using a Bruker D8 Discover XRD^2 microdiffractometer (Bruker, Germany) with CoKα radiation, an area sensitive Hi-Star detector (GADDS) and monocapillary optics ($Ø_{beam}$ ~ 300 μm; Institue for Scientific Instruments GmbH, Berlin, Germany)[1]. For more details about the 2-D XRD see Berthold *et al.* [93].

[1] The 2-D XRD scans and analysis were carried out in Eberhard-Karls-Universität, Tübingen by Prof. Volcker Presser.

A careful measurement of the grain sizes of the composite particles was carried out on SEM micrographs using an image-processing program (ImageJ, National Institutes of Health, Bethesda, MD).

TEM samples were prepared first by cutting ~ 300 μm thick slices from the bulk samples with a low speed diamond saw. Small 3 mm diameter disks were then produced using an ultrasonic disk cutter (Model 170, Fischione, Export, PA). Both sides were polished with a dimpling grinder (Model 200, Fischione, Export, PA) using 3 μm, 1 μm and 0.1 μm diamond pastes successively. The disk thicknesses after dimpling were ≈ 25 μm. Final perforation was made with an ion mill (Model 1010 Fischione, Export, PA) at 5 kV.

TEM characterization was performed using a field emission TEM (JEOL JEM-2010F, Akishima, Japan) operating at 200 kV. Images were collected with a multi-scan CCD digital camera. EDS analysis in the TEM was carried out with an attached ultra-thin window X-ray EDS (EDAX, Mahwan, NJ).

4.4. Hardness measurements

The microhardness measurements were performed using a Vickers microindenter (LECO Corp., St. Joseph, MI) at a load of 10 N held for 15 s. The microhardness values reported are the average of at least 5 indentations for each sample.

4.5. Compression and tension tests

Tensile and compression specimens were electro-discharge machined (EDMed) from the as fabricated samples. In the case of the oriented samples, compression cylinders were EDMed both parallel and normal to the pressing direction.

The samples loaded such the basal planes were normal (edge on) to the compressive loading direction, will henceforth be referred to with a "N" suffix. Conversely when the basal planes were parallel to the loading direction, the samples will be referred to with a "P" suffix. Randomly oriented samples will be referred to with a "R" suffix.

The room temperature ultimate compressive strengths (UCSs) were measured using an electromechanical testing machine (Instron 5600, Norwood, MA) on small (4x4x4 mm^3) cubes that were EDMed. Six cubes of each microstructure were tested.

EDMed cylinders, 9.7 mm in diameter and 31 mm high, were used to measure the elastic moduli in compression and to carry out cyclic uniaxial compression tests. In all cases, the samples' macroscopic strains were measured using an extensometer (2620-603 Instron, 10 mm gauge length with a 10 % full range) directly attached to the sample.

The UTSs were measured using a hydraulic mechanical testing machine (Instron 8800, Norwood, MA) following ASTM standard E8. The tensile specimens were flat, with a gage length and thickness of 14 mm and 1.5 mm, respectively.

To measure the damping properties, cyclic compression experiments, carried out as follows: each sample was loaded to a maximum load of ~ 75% of its UCS for two consecutive cycles before cyclically loading it by 50 MPa decrements from the maximum load during each cycle for the 50 vol.% reinforced composites and by 20 MPa decrements for the 20 and 5 vol.% reinforced composites and pure AZ61 alloy. The cyclic loading and damping properties will be discussed in chapter 6.

Chapter 5: Microstructural and Mechanical Characterization

In this chapter, the results of this study are presented, which includes all the microstructural characterization and mechanical properties, except damping. The latter will be discussed in the next chapter.

5.1. Results

5.1.1. Microstructural observation and density results

The microstructures of all the composites revealed a homogenous distribution of the reinforcement in the composites. Figures 5.1(a) to (b), respectively, show the microstructures of the polished surfaces of 20-Ti_2AlC-Mg and 5-Ti_2AlC-Mg. The darker regions correspond to Mg and the brighter regions correspond to the carbides. The microstructures of the 20- and 5-TiC-Mg composites are shown in Figs 5.1(c) and (d), respectively.

Figures 5.2(a) and (b) show typical microstructures of polished surfaces of AZ61 reinforced with 50 vol.% Ti_2AlC particles. Higher magnification SEM images of all polished surfaces also show the presence of small particles in the matrices (insets in Figs. 5.2(a) to (d)). The top insets in Figs. 5.2(a) and (b) show that some Ti_2AlC particles are delaminated and microcracked. A typical example can be seen in the inset of Fig. 5.2(a), in which a large Ti_2AlC particle, denoted by white arrow, is clearly microcracked. EDS across different Ti_2AlC grains (Fig. 5.3(a) and (b)) showed the presence of Mg even in cracks/delaminations of the order of a few nm (Fig. 5.3(b)).

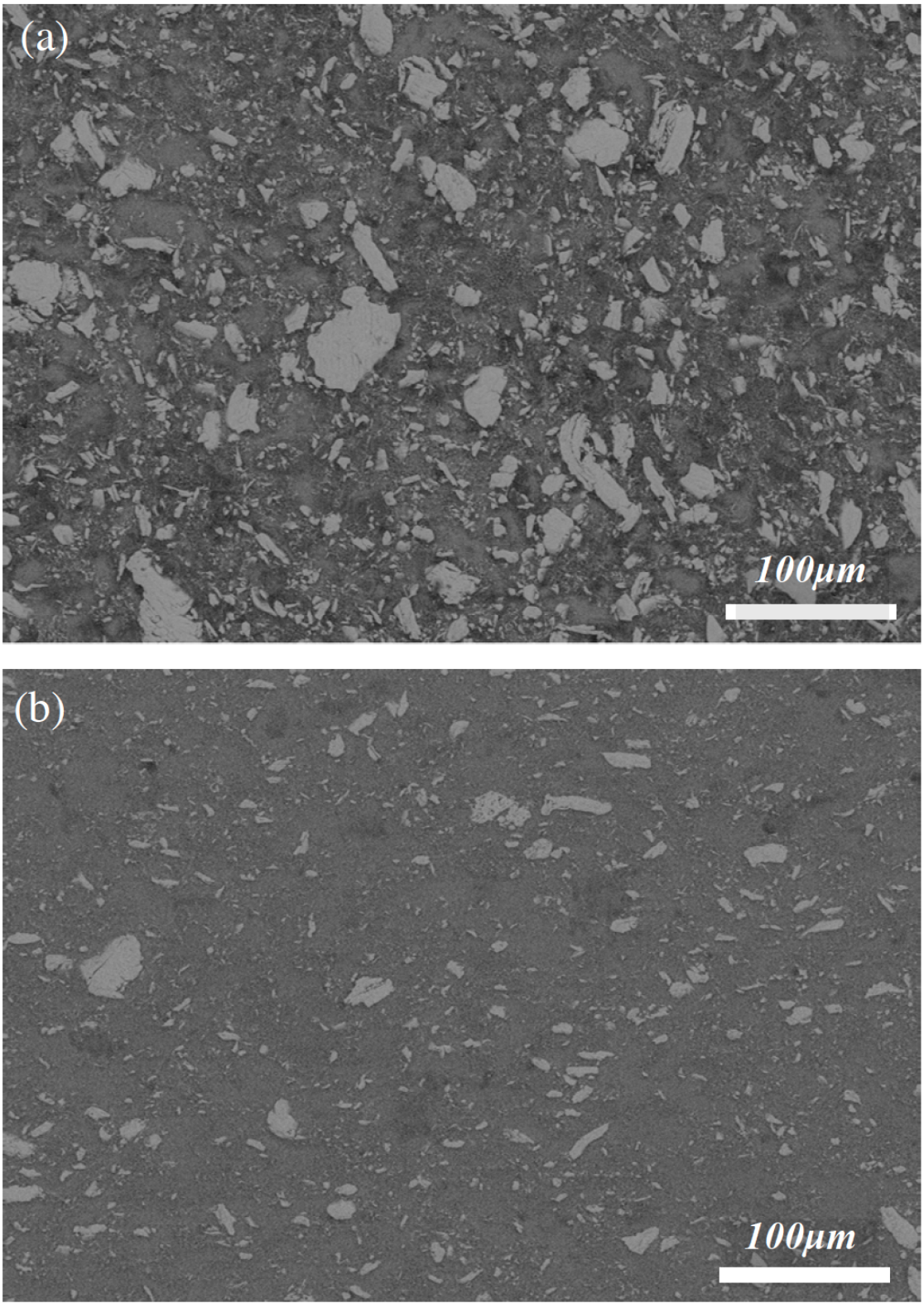
(a)
100μm
(b)
100μm

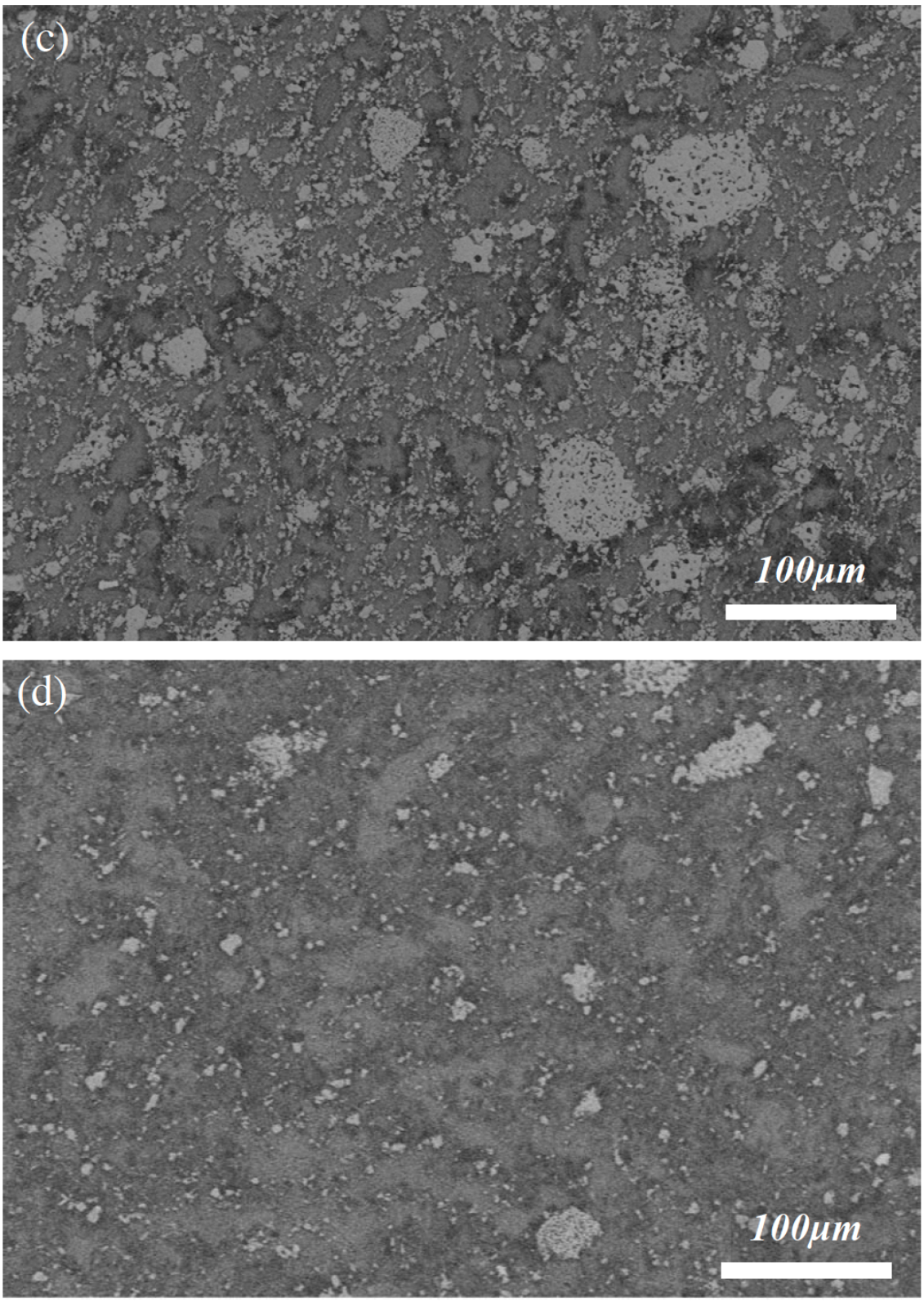

Fig. 5.1.Backscatter SEM micrographs of polished surfaces of: (a) 20-Ti_2AlC-Mg, (b) 5-Ti_2AlC-Mg, (c) 20-TiC-Mg, (d) 5-TiC-Mg composites.

Lorentzian distributions were fit to the particle sizes (obtained from image analysis) of the microstructure shown in Fig. 5.2. The distributions are shown in Fig. 5.4 and Table 5.1. For the coarser Ti_2AlC grains (Fig. 5.2(a)) two, almost equally weighted, Lorentzian distributions were needed to describe the results. The first Lorentzian with ~ 49% of the particles' population, is centered at $d_c = 0.9 \pm 0.1$ μm and has a width of 1.1 ± 0.1 μm. The second, with ~ 51% of the particles' population had a $d_c = 2.0 \pm 0.3$ μm with $w = 3.2 \pm 0.4$ μm (Fig. 5.4; Table 5.1). The finer Ti_2AlC particle population (Fig. 5.2(b)) can be described using one Lorentzian distribution with $d_c = 0.51 \pm 0.01$ μm and $w = 0.65 \pm 0.05$ μm (Fig. 5.4; Table 5.1). Composites fabricated with these particles will henceforth be referred to as coarse grained, CG50-Ti_2AlC and fine grained, FG50-Ti_2AlC composites, respectively.

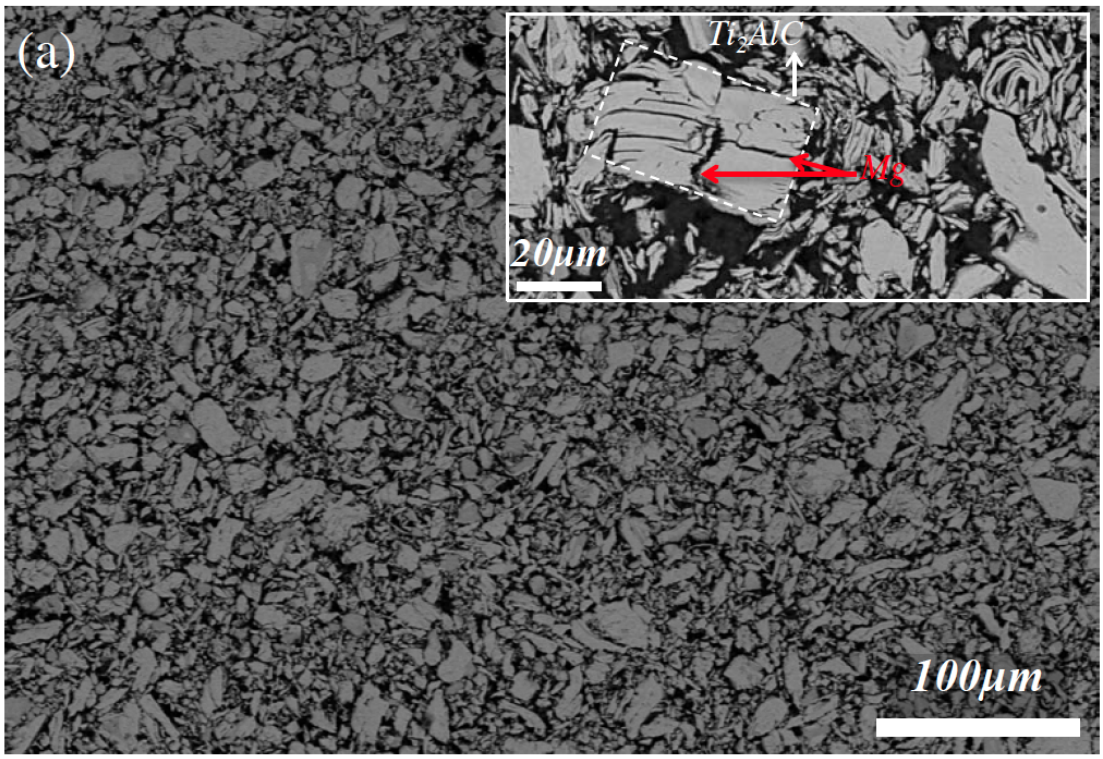
(a)
Ti_2AlC
Mg
20μm
100μm

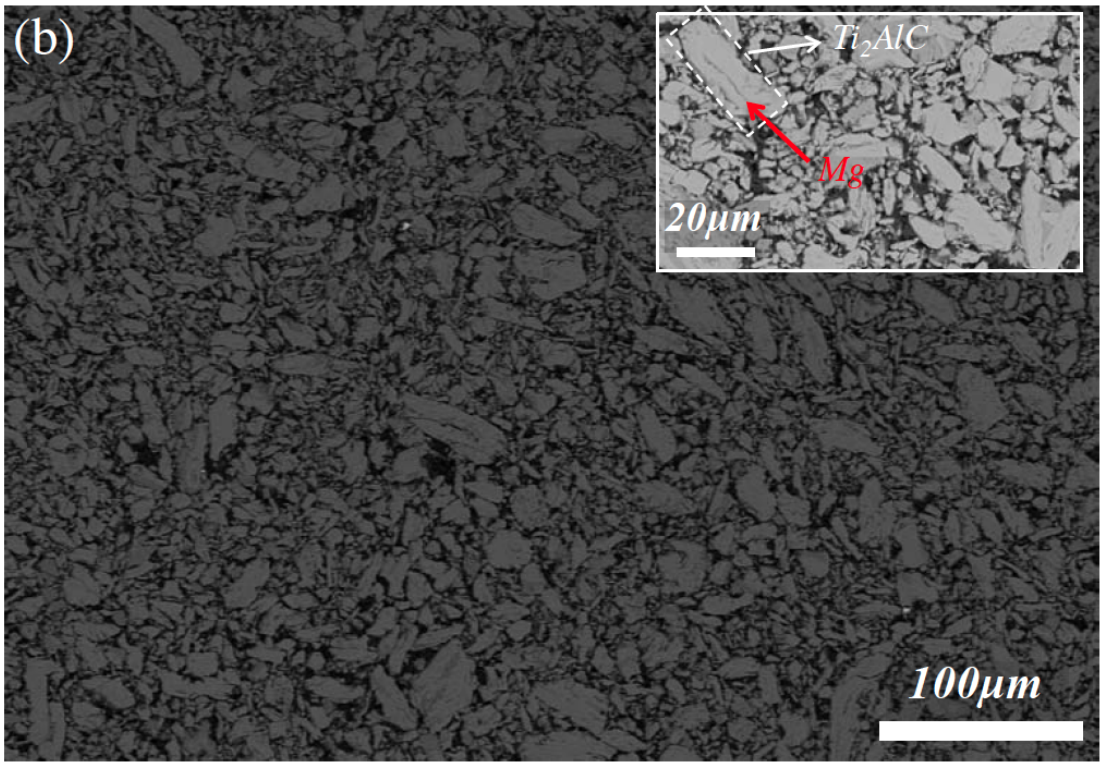
(b)
Ti_2AlC
Mg
20μm
100μm

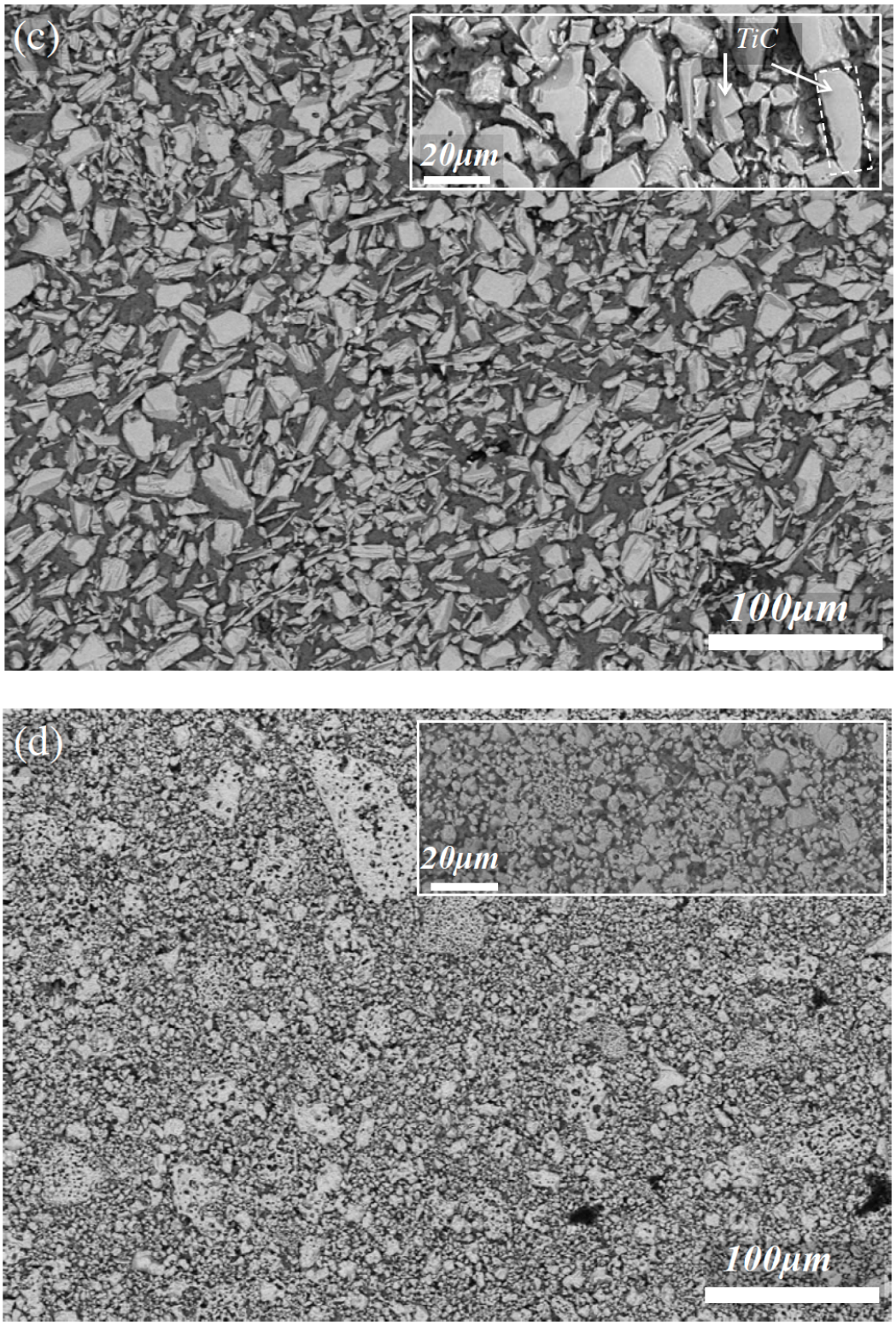

Fig. 5.2. Backscatter SEM micrographs of polished surfaces of: (a) CG50-Ti_2AlC-AZ61, (b) FG50-Ti_2AlC-AZ61, (c) CG50-TiC-AZ61, (d) FG50-TiC-AZ61 composites.

Table 5.1. Peak centers and widths of Lorentzian grain size distribution of Ti_2AlC and TiC powders. Peak area fraction is the area of the peak compared to the total area under the grain size distribution in Fig. 5.2.

Material	First peak center (μm)	First peak width (μm)	First peak area fraction (%)	Second peak center (μm)	Second peak width (μm)	Second peak area fraction (%)
CG50-Ti_2AlC	0.9(1)	1.1(1)	49	2.0(3)	3.2(4)	51
FG50-Ti_2AlC	0.51(1)	0.65(5)	100	-	-	-
CG50-TiC	1.6(1)	0.73(7)	26	5.8(2)	7.2(7)	74
FG50-TiC	0.41(1)	0.49(1)	100	-	-	-

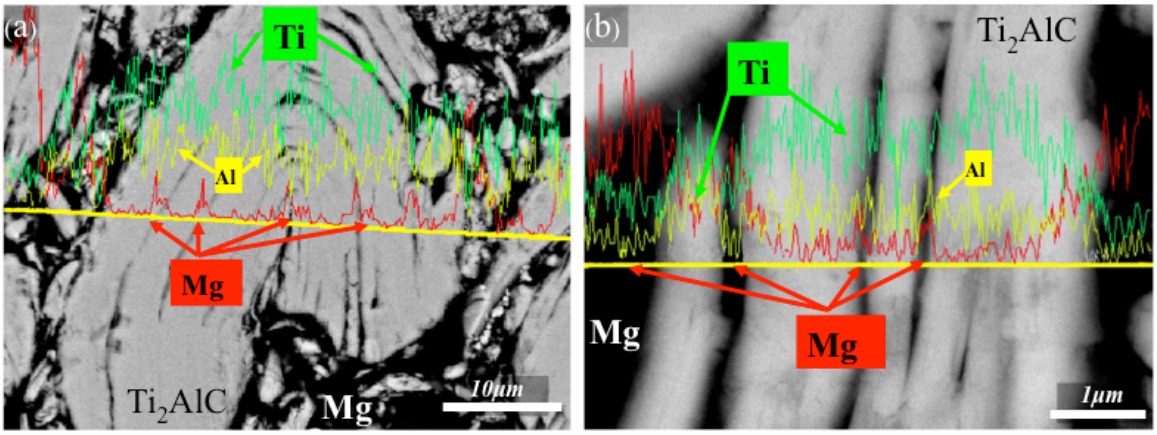

Fig. 5.3. (a) Backscatter SEM micrographs of a CG50-Ti_2AlC-Mg polished surface superimposed with elemental line scans (yellow solid line) showing the presence of Mg in between delaminations in individual Ti_2AlC grains, (b) same as a, but at higher magnification. In these maps, red represents Mg, green Ti and yellow Al.

Figures 5.2(c) and (d) show typical polished surfaces of AZ61 composites reinforced with 50 vol.% TiC particles. Similar to the above described Ti_2AlC case, the TiC powder with the coarser particles' population (Fig. 5.2(c)) is described using two Lorentzian distributions. The first Lorentzian, with ~ 26% of the particles' population, is centered at $d_c = 1.6 \pm 0.1$ μm and with a $w = 0.73 \pm 0.07$μm. The second with ~ 74% of the particles' population had a $d_c = 5.8 \pm 0.2$ μm and a $w = 7.2 \pm 0.7$μm (Table 5.1). The finer TiC particle population (Fig. 5.2(d)) can be described using one Lorentzian distribution with $d_c = 0.41 \pm 0.01$ μm and $w = 0.49 \pm 0.01$ μm (Fig. 5.4; Table 5.1). Composites fabricated with these particles will henceforth be referred to as coarse grained, CG50-TiC and fine grained, FG50-TiC composites, respectively.

Given the importance of knowing the grain size of the Mg in the matrices to understanding the mechanical properties, significant efforts were devoted to measuring their size. Careful mechanical polishing, with different polishing forces and media were carried out. In all cases and most probably due to the presence of the hard carbide particles next to the soft Mg regions, the latter were pulled out and achieving a smooth surface for the Mg matrix was not possible. A second approach was to use focused ion milling together with electron backscatter diffraction (EBSD) to determine the Mg grain size. Here again, the resulting surface was not smooth enough for EBSD. More work is required to understand the reason for these difficulties.

However, in all cases, the carbide particles were well-polished and clearly visible in the SEM after mechanical polishing. Given that the Mg grain size cannot be larger than the distance between the two adjacent carbide particles, the latter were carefully measured and plotted as the maximum possible Mg grain size (see inset in Fig. 5.4). Not

surprisingly, and in most cases, the distributions in Mg grain size were quite similar to the reinforcement particle size distributions. The only exception is the Mg size in CG-TiC, in which larger Mg grains than TiC particles were measured. This can be due to the larger distance between the CG-TiC particles (Fig. 5.2(c)).

At 2.95 ± 0.02 Mg/m^3, the densities of the 50-Ti_2AlC composites were about 99 % of theoretical. At 3.4±0.1 Mg/m^3, those of the 50-TiC composites were about 98% of theoretical. To calculate the theoretical densities, the densities of the preforms prior to MI (52% and 54% for Ti_2AlC and TiC, respectively), were first measured. The densities of Mg, Ti_2AlC and TiC were assumed to be 1.74 Mg/m^3, 4.11 Mg/m^3 [94] and 4.93 Mg/m^3, respectively.

Rietveld refinement analysis of the XRD data of the as-received Ti_2AlC powder revealed the existence of ~ 20 wt.% Ti_3AlC_2, and ~ 1 wt.% TiC. These impurities' phase fractions were the same for all the Ti_2AlC composite samples.

The refined lattice parameter values for Mg and TiC and as-received Ti_2AlC, as well as, the Ti free position in Ti_2AlC, z, are all consistent with previously published data (Table 5.2) [95]. Interestingly, for all Ti_2AlC-composites, the *c* lattice parameters of the Ti_2AlC were slightly lower than their value in the as-received Ti_2AlC (Table 5.2). Rietveld analysis also confirmed the ~ 1:1 volume ratio between matrix and reinforcement for all XRD studied composites. Due to the similarities of all the XRD plots only the Rietveld refinement of the XRD data of CG50-Ti_2AlC(N)-AZ61 is shown in Fig. 5.5(a). All the refinement information is presented in Table 5.2.

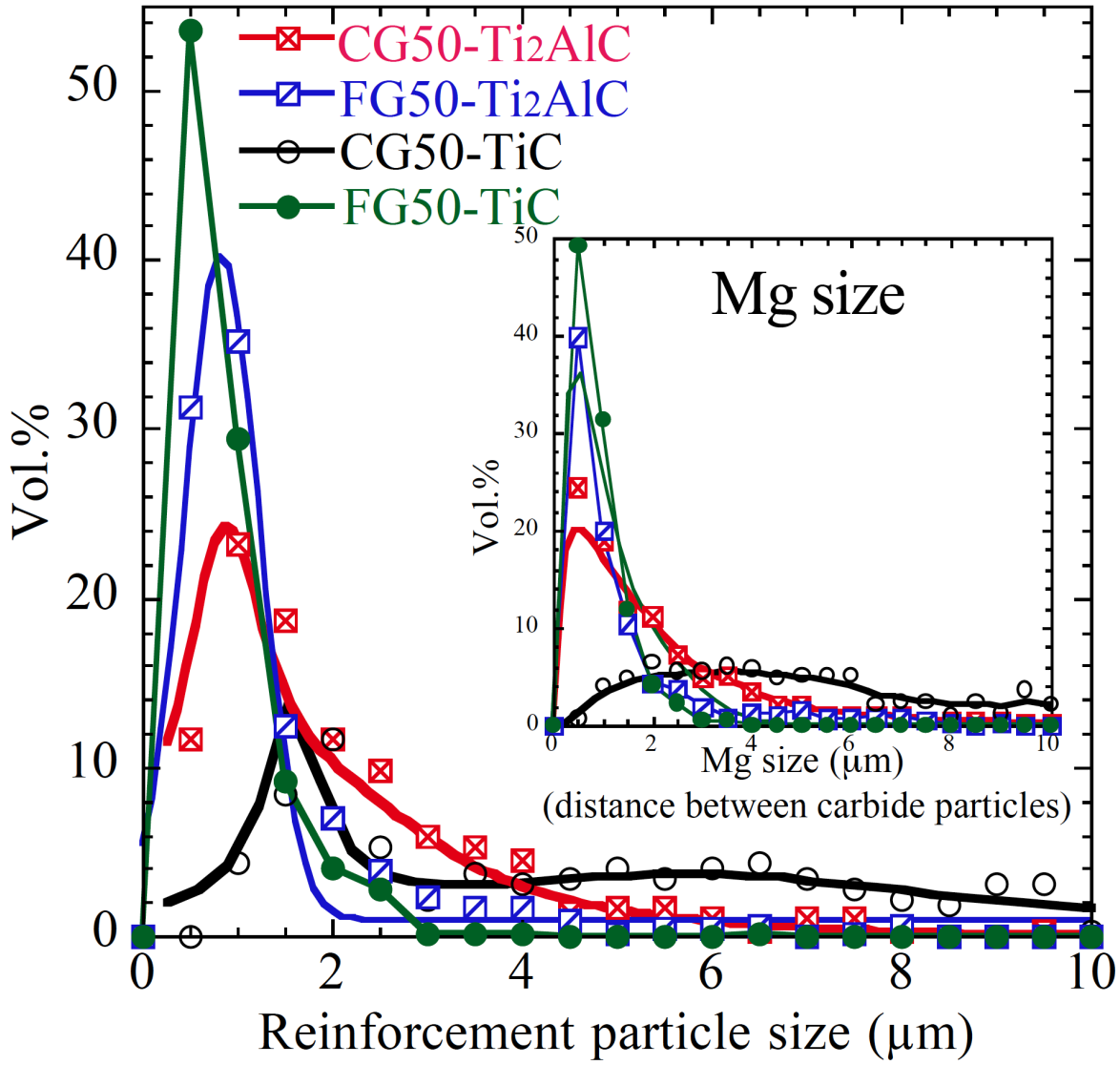

Fig. 5.4. Particle size distributions of the Ti_2AlC and TiC reinforcing particles in the Mg-matrices. The inset shows the maximum possible Mg grain size in each family of composites.

The Ti_2AlC XRD peak intensities in the CG50-Ti_2AlC-AZ61 in R, P and N composites are compared in Fig. 5.5(b). In the top left inset, the peak intensities of the (0002) basal planes are compared; those for the $(10\bar{1}0)$ planes are compared in the top right inset. Table 5.3 compares the ratios of these two peak intensities in the 3 composites to the ones reported in the literature for Ti_2AlC [95].

A 2-D XRD diffraction image of a CG50-Ti_2AlC-Mg sample is shown in Fig. 5.6(a). The Ti_2AlC ring is more complete and less spotty than the Mg ring. The faint Mg rings show there are some Mg at the nano scale and has some large grains with preferred orientation. However, the presence of faint rings in the case of Mg can be due to the nano size Mg that infiltrated the existing cracks in Ti_2AlC, similar to what was explained for Fig. 5.3. The Ti_2AlC ring is in agreement with the peak broadening observed in regular XRD peaks of Ti_2AlC in the composites as well as in the as-received powder (Table 5.2). A SEM image of the as received Ti_2AlC is shown in Fig. 5.6(b). Submicron and nano grains are observed at higher magnifications (right insets in Fig. 5.6(b))

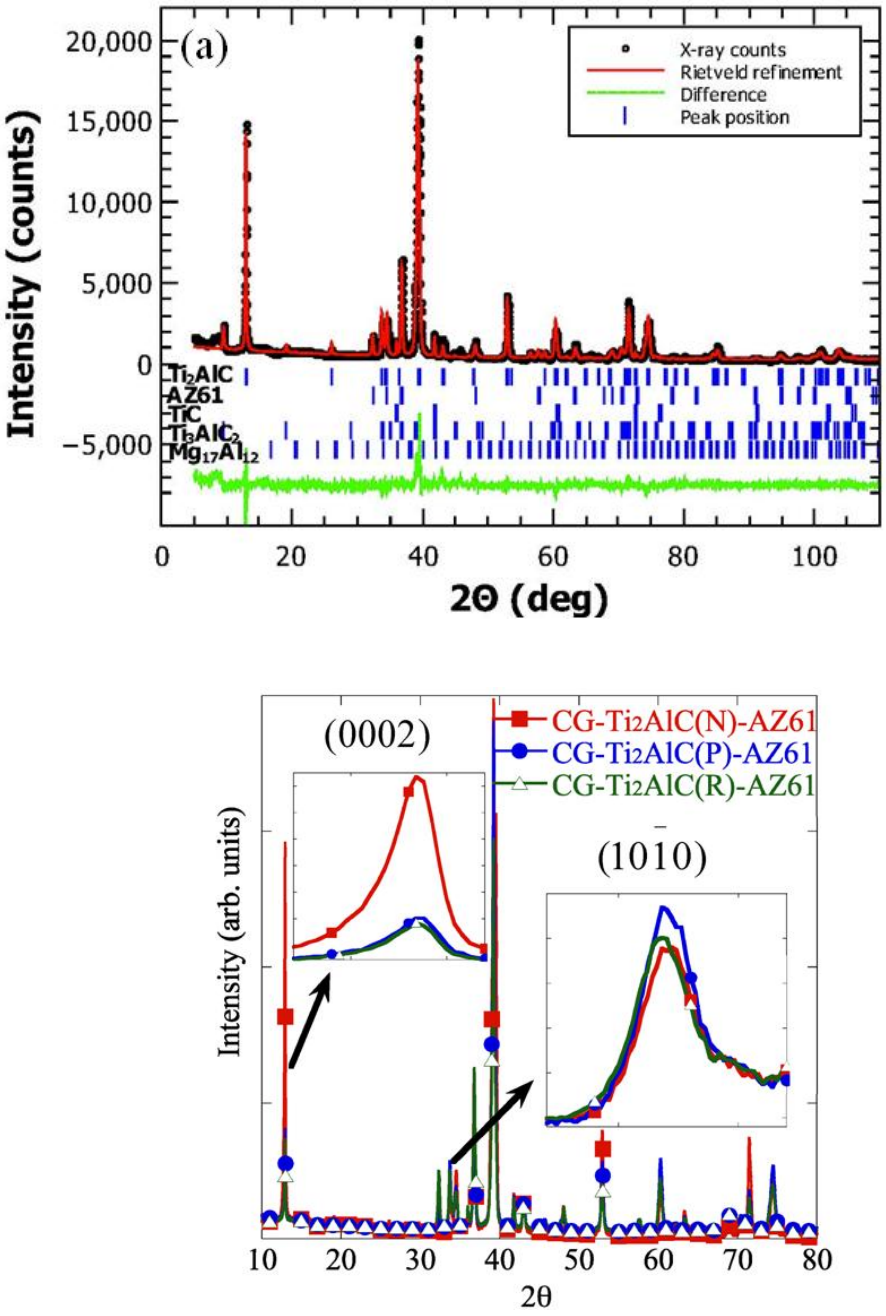

Fig. 5.5. (a) Rietveld analysis of the XRD data of the CG50-Ti_2AlC-AZ61 composite. Open circles, solid line, and dashed line in the bottom, represent the measured data, refined model, and the difference between the two, respectively. The five rows of vertical tags represent the calculated Bragg reflections' positions of the Ti_2AlC (1st row), AZ61 (2nd), TiC (3rd), Ti_3AlC_2 (4th) and $Mg_{17}Al_{12}$ (5th) phases, (b) XRD diffractograms of CG50-Ti_2AlC(R)-AZ61, CG50-Ti_2AlC(N)-AZ61 and CG50-Ti_2AlC(P)-AZ61composites. The top insets compare the (0002) and (10$\bar{1}$0) peak intensities in Ti_2AlC for all 3 composites.

Table 5.2. Lattice parameters of and residual strains in the matrices and reinforcements of the Ti_2AlC-Mg and Ti_2AlC-AZN1 (N=3, 6, or 9), and TiC-Mg, and TiC-AZN1 composites calculated by Rietveld refinement analysis of XRD data. Also listed are the values for pure Mg and AZ61 subjected to the same heat treatment as the composite samples. The strains were evaluated using an isotropic Gaussian model. Numbers in parentheses are the uncertainties (±) on the last digit.

Material	Reinforcement (Ti_2AlC or TiC)				Matrix (Mg or Mg alloy)		
	a (Å)	c (Å)	Z_{Ti}	Strain (%)	a (Å)	c (Å)	Strain (%)
Mg	-	-	-	-	3.2117(1)	5.2095(2)	0.19(1)
AZ61	-	-	-	-	3.1925(1)	5.1845(3)	0.96(1)
CG-Ti_2AlC-as rec	3.0623(1)	13.6784(6)	0.0848(2)	0.62(1)	-	-	-
CG50-Ti_2AlC-Mg	3.06163(5)	13.6667(4)	0.0870(2)	0.57(1)	3.2062(1)	5.2027(3)	0.81(1)
CG50-Ti_2AlC-AZ31	3.06451(8)	13.6680(4)	0.0869(2)	0.58(1)	3.2016(1)	5.1964(4)	1.16(1)
CG50-Ti_2AlC(R)-AZ61	3.06764(7)	13.6689(4)	0.0880(2)	0.77(1)	3.1946(1)	5.1835(3)	0.86(1)
CG50-Ti_2AlC(N)-AZ61	3.06551(6)	13.6674(3)	0.0868(1)	0.61(1)	3.1957(1)	5.1888(3)	0.83(2)
CG50-Ti_2AlC(P)-AZ61	3.06644(7)	13.6678(5)	0.0879(2)	0.72(1)	3.1961(1)	5.1874(3)	0.71(2)
CG50-Ti_2AlC-AZ91	3.06366(6)	13.6583(4)	0.0873(2)	0.50(1)	3.1860(1)	5.1738(3)	1.41(1)
CG50-TiC-Mg	4.32718(5)	-	-	0.00	3.2103(2)	5.2112(5)	0.62(2)
CG50-TiC-AZ61	4.32800(2)	-	-	0.11(1)	3.18549(9)	5.1737(3)	1.07(1)
FG50-TiC-Mg	4.3272(1)	-	-	0.00	3.2103(2)	5.2112(5)	0.48(9)
FG50-TiC-AZ31	4.3263(1)	-	-	0.15(1)	3.2031(2)	5.2012(5)	1.18(9)
FG50-TiC-AZ61	4.3263(1)	-	-	0.12(1)	3.1936(3)	5.1856(7)	1.0(1)
FG50-TiC-AZ91	4.3257(1)	-	-	0.12(1)	3.1919(1)	5.1828(4)	0.8(1)

Table 5.3. The ratio of XRD peak intensities of (0002) planes to $(10\bar{1}0)$ planes of Ti_2AlC obtained from Fig. 5.5(b) compared with those reported in literature for an un-oriented (U) powder, which is expected to be random [95]. Numbers in parentheses are the uncertainties on the last digit.

Intensity	CG50-Ti_2AlC(R)-AZ61	CG50-Ti_2AlC(P)-AZ61	CG50-Ti_2AlC(N)-AZ61	Ti_2AlC(U)
$I(0002)/I(10\bar{1}0)$	0.86(4)	0.71(2)	3.25(7)	2.5 [95]

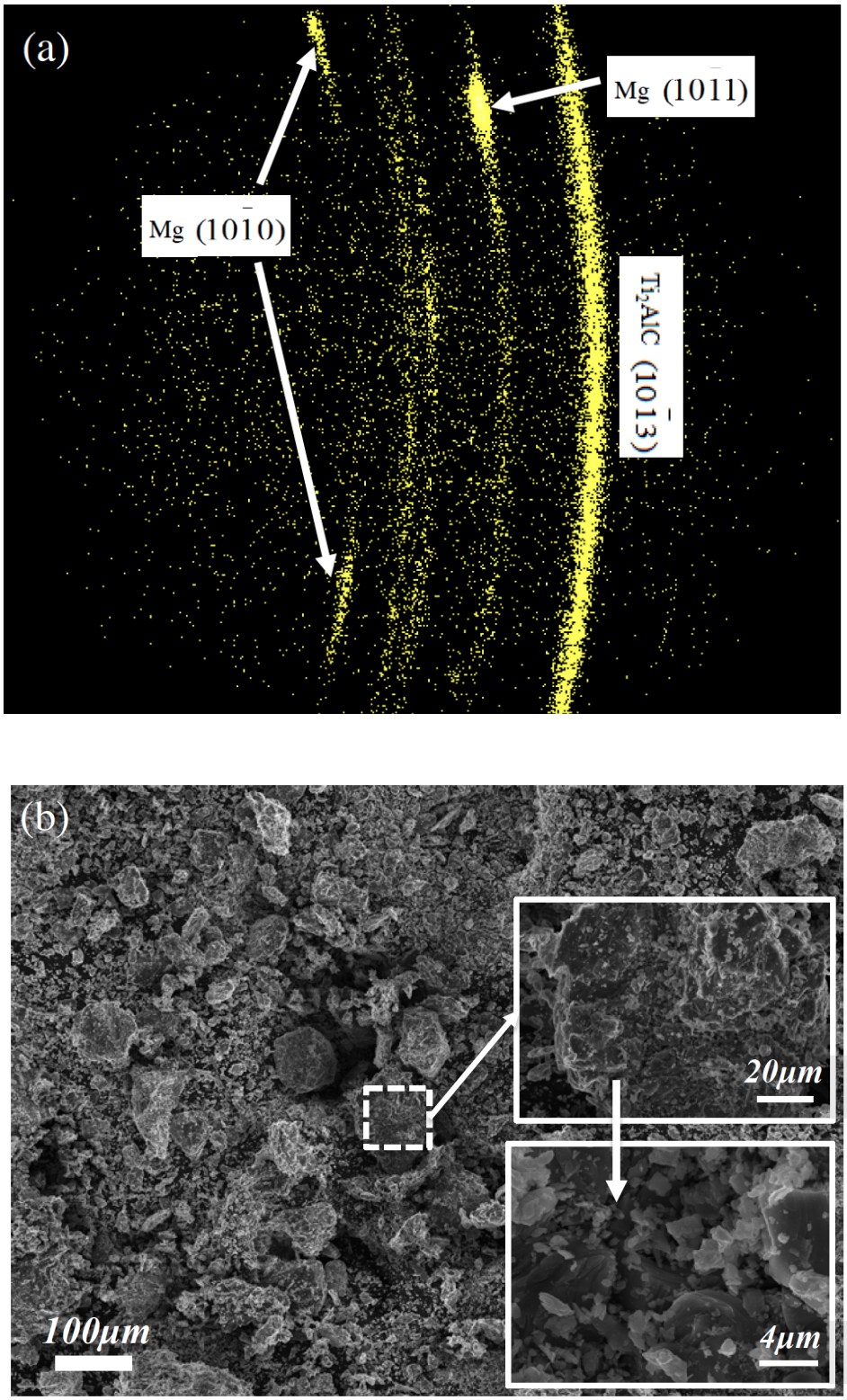

Fig. 5.6. (a) 2-D XRD of a CG50-Ti_2AlC(R)-Mg composite sample. (b) Secondary electron SEM micrograph of the as-received Ti_2AlC powder.

5.1.2. Tensile and compressive properties

Table 5.4 compares the 0.2 % yield strengths, YSs, UCSs, UTSs and the Vickers microhardness values, V_H, of pure AZ61 and the composites fabricated in this study. The compressive stress-strain curves for the first cycle of all the 50 vol.% composites and pure AZ61 tested herein are plotted in Fig. 5.7(a); all the 5 and 20 vol.% composites are shown Fig. 5.7(b).

Table 5.4. Elastic moduli measured from the stress-strain curves at a stress of 100 MPa (E*), average effective elastic moduli ($E_{f(av)}$) measured by averaging least squares fit of each stress-strain loop at different stresses, 0.2% yield strengths (YS), ultimate tensile strengths (UTS), ultimate compression strengths (UCS) and Vickers hardness, V_H, values for the composites studied here. E* is the slope of the stress-strain curves up to 100 MPa. Numbers in parentheses are the uncertainties on the last digit.

Material	E^* (GPa)	$E_{f(av)}$ (GPa)	0.2%YS (MPa)	UCS (MPa)	UTS (MPa)	V_H (GPa)
AZ61‡	45(1)	37(7)	59(4)	220(20)	-	0.5(1)
CG50-Ti_2AlC-Mg	73(2)	67(4)	285(4)	600(10)	345(40) [42]	1.5(1)
CG50-Ti_2AlC-AZ31	106(4)	89(11)	285(4)	662(8)	–	1.7(1)
CG50-Ti_2AlC(R)-AZ61	112(3)	100(8)	331(6)	719(7)	–	2.0(1)
CG50-Ti_2AlC(N)-AZ61	120(3)	107(8)	416(4)	730(15)	420(40)	2.1(1)
CG50-Ti_2AlC(P)-AZ61	123(2)	112(8)	545(3)	755(10)	430(40)	2.1(1)
CG50-Ti_2AlC-AZ61-Ex	133(3)	119(3)	490(12)	830(2)	633(9)	2.1(1)
CG50-Ti_2AlC-AZ91	110(4)	97(4)	321(6)	705(12)	-	1.9(1)
CG50-Ti_3AlC_2-Mg	71(2)	66(5)	254	606(14)	-	1.5(1)
FG50-Ti_2AlC-Mg	109(4)	95(3)	349(3)	688(18)	-	1.7(1)
FG50-Ti_2AlC-AZ31	124(4)	104(4)	346(4)	773(7)	-	1.8(1)
FG50-Ti_2AlC-AZ61	136(6)	114(4)	426(5)	760(9)	-	2.1(1)
FG50-Ti_2AlC-AZ91	123(5)	106(4)	408(4)	768(11)	-	2.2(1)
CG50-TiC-Mg	123(6)	108(10)	258(4)	500(10)	–	2.6(2)
CG50-TiC-AZ31	140(6)	122(9)	311(5)	560(14)	–	2.8(3)
CG50-TiC-AZ61	163(8)	134(13)	382(5)	740(6)	400(50)	3.1(3)
FG50-TiC-Mg	143(5)	131(4)	421(10)	705(10)	-	2.9(3)
FG50-TiC-AZ31	169(7)	149(4)	479(14)	963(7)	-	3.1(3)
FG50-TiC-AZ61	174(5)	157(4)	523(8)	1028(5)	-	3.4(3)
FG50-TiC-AZ91	184(5)	162(5)	557(8)	1013(12)	-	3.4(2)
20-Ti_2AlC-Mg‡	55(3)	51(2)	122(1)	336(7)	-	0.9(1)
5-Ti_2AlC-Mg‡	54(2)	49(2)	128(2)	339(21)	-	0.9(1)
20-TiC-Mg‡	57(3)	52(2)	140(2)	285(5)	-	0.9(1)
5-TiC-Mg‡	42(2)	38(2)	123(1)	337(16)	-	0.88(2)

‡ Measured at 50 MPa.

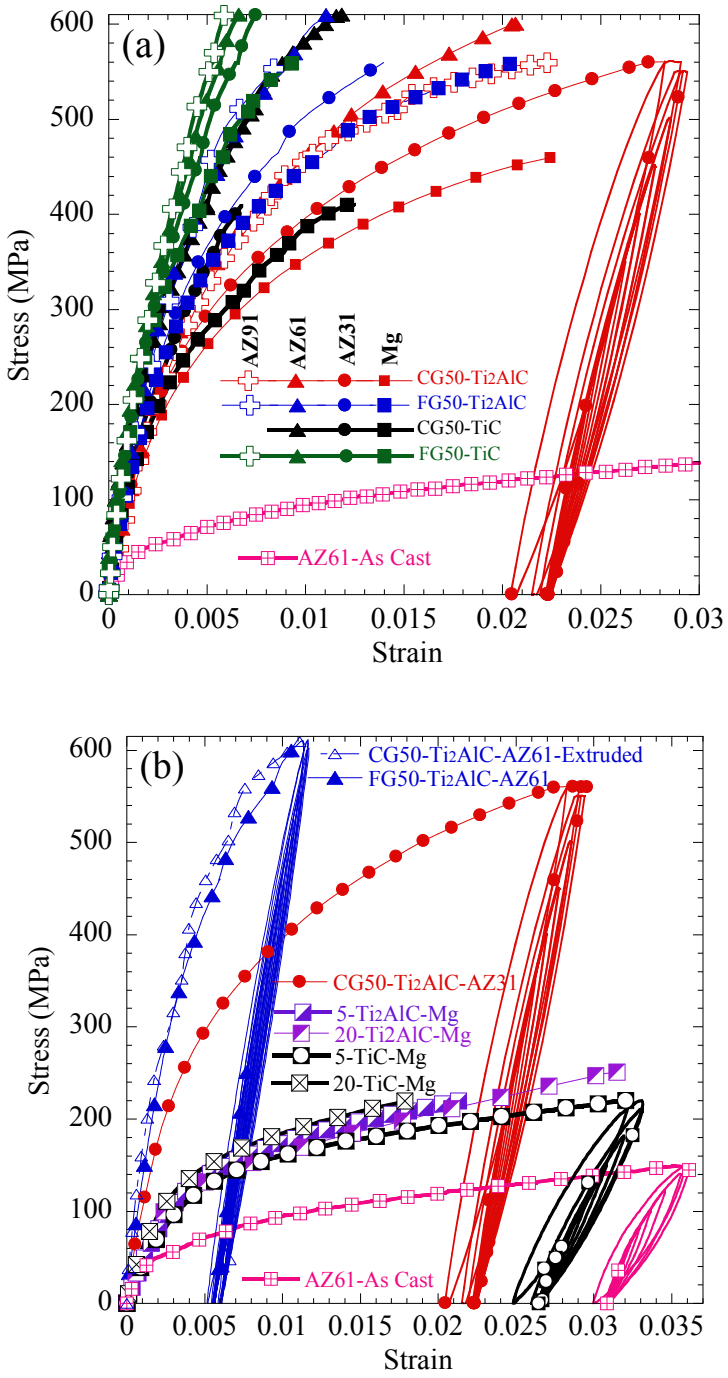

Fig. 5.7. First compressive stress–strain cycles of, (a) all 50 vol.% reinforced composites, (b) 20 and 5 vol.% reinforced composites. A complete cyclic compressive stress–strain curve for a CG50-Ti_2AlC-AZ31 sample is shown in (a); for the sake of comparison a complete cyclic compressive stress–strain for a FG50-Ti_2AlC-AZ61 sample, 5-TiC-Mg and as cast AZ61 are shown in (b).

5.1.3. Elastic moduli

As noted above, cyclic compression tests were performed herein. Typical complete cyclic compression tests - two cycles to the maximum stress followed by the decremental loading - for a CG50-Ti_2AlC-AZ31 sample are shown in Fig. 5.7(a) and for FG50-Ti2AlC-AZ61, 5-TiC-Mg and pure AZ61 in Fig. 5.7(b) (see stress-strain curve with loops in Figs. 5.7(a) and (b)).

Clearly, the first cycles are open, registering small plastic strains of the order of 0.5-3% (Fig. 5.7), after which, all subsequent cycles at stresses lower than the maximum stress are fully reversible and closed. The hysteresis loops and concomitant damping are discussed in the next chapter. Note that these loops are only observed at stresses higher than 100 MPa for the 50 vol.% reinforced composites; below 100 MPa, the loops are absent and the stress-strain curves are straight lines. An example of such loops is presented in the next chapter in Fig. 6.2(k). In the case of 20 and 5 vol.% reinforced composites and pure AZ61, this threshold stress was ≈ 50 MPa. The elastic moduli values reported herein are the slopes of the stress-strain curves at stresses of 100 MPa or 50 MPa, depending on type of the composite - and will henceforth be referred to as E* (see Table 5.4). In addition, for the cyclic tests at different stresses, effective elastic moduli, E_f, were also measured. To do so, least squares fits of the entire data set – that resulted in the diagonal lines bisecting the stress-strain loops – were carried out at each stress. The E_f values are discussed in the next chapter.

The experimental results for the Ti_2AlC and TiC composites were also compared with predicted values from the rule of mixture (ROM) and the Halpin-Tsai models [96] in Figs. 5.8(a) and (b), respectively. The ROM for the E of the composites

$$E_c = E_m V_m + E_r V_r \tag{5.1}$$

where E_c is the modulus of the composite and E_m, E_r, V_m and V_r are the moduli and volume fractions of the matrix and reinforcement particles, respectively. The results of the ROM model are depicted by red dotted lines in Figs. 5.8(a) and (b).

Typically, Eq. 5.1 is more applicable to continuous fiber-reinforced composites. Halpin-Tsai [96] modified the expression for discontinuous reinforced composites to:

$$E_c = \frac{E_m(1+2sqV_r)}{1-qV_r} \tag{5.2}$$

where s is the particles' aspect ratio and q is given by

$$q = \frac{(E_r/E_m - 1)}{(E_r/E_m)+2s} \tag{5.3}$$

To calculate E_c using the Halpin-Tsai model, the particles' aspect ratio, s, was assumed to be 5 or 1 for both reinforcements and the results are plotted as dashed blue lines and solid green lines, respectively, in Figs. 5.8(a) and (b).

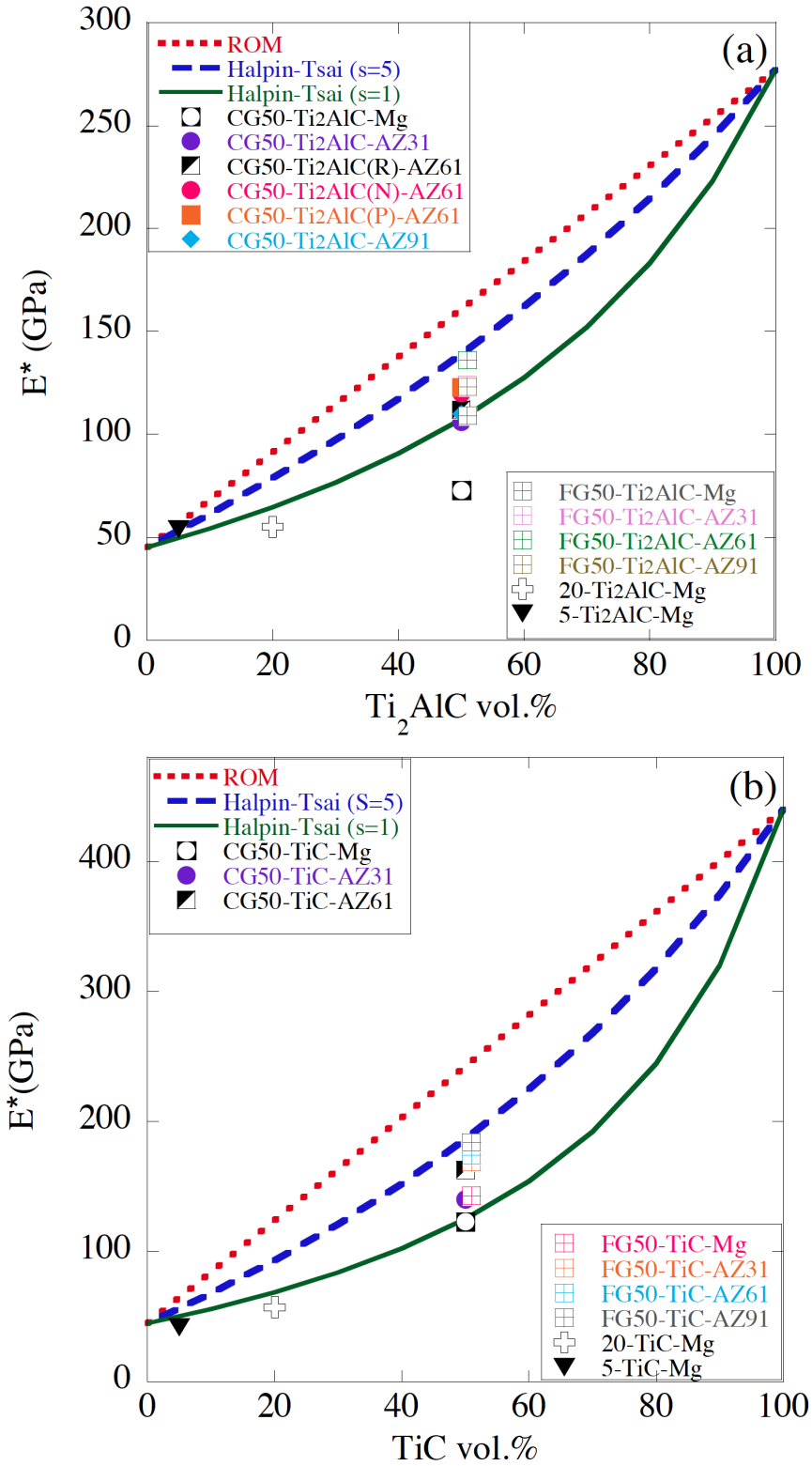

Fig. 5.8. Plots of E* vs. reinforcement volume fraction in, (a) Ti_2AlC composites and, (b) TiC composites. The lines represent the calculated E values from ROM (dotted red line), and the Halpin-Tsai model assuming s = 1 (solid green lines) and s = 5 (dashed blue lines). Uncertainties are smaller than symbol sizes.

5.1.4. Tensile fracture surfaces

In order to characterize the fracture surfaces, both secondary electron, SE, and backscatter electron, BSE, SEM micrographs of the same fractured area were taken (Figs. 5.9 and 5.10). In each figure, the image shown on the left was taken in SE mode; the one on the right in BSE mode. The CG50-Ti_2AlC-Mg and CG50-Ti_2AlC-AZ61 fracture surfaces are shown in Figs. 5.9(a) and (b), respectively. The fracture surfaces of the CG50-TiC-Mg and CG50-TiC-AZ61 are compared in Figs 5.10(a) and (b), respectively.

To further analyze the type of fracture, two opposing surfaces of a CG50-Ti_2AlC-AZ61 fractured tensile specimen (see inset between Figs. 5.11(a) and (b)) imaged in a SEM are shown in Fig. 5.11. The corresponding SEM images for a CG50-TiC-AZ61 fractured surface are shown in Fig. 5.12.

In order to better understand the role of Al content in the Mg alloys on properties, E*, YS, V_H and UCS for the Ti_2AlC and TiC composites are plotted vs. Al content in Figs. 5.13(a), (b), (c), (d), respectively.

5.1.5. TEM observation of the Ti_2AlC-Mg interface

To further explore if any chemical reactions occurred between the Mg and Ti_2AlC, a region - wherein Mg penetrated a pre-existing crack in a Ti_2AlC particle in a Mg-Ti_2AlC composite - was imaged in the TEM (Fig. 5.14). Selected area electron diffractions (SAED) of a Ti_2AlC grain (about 150 nm away from the interface), Mg-Ti_2AlC interface and a Mg grain are shown as top insets in Fig. 5.14.

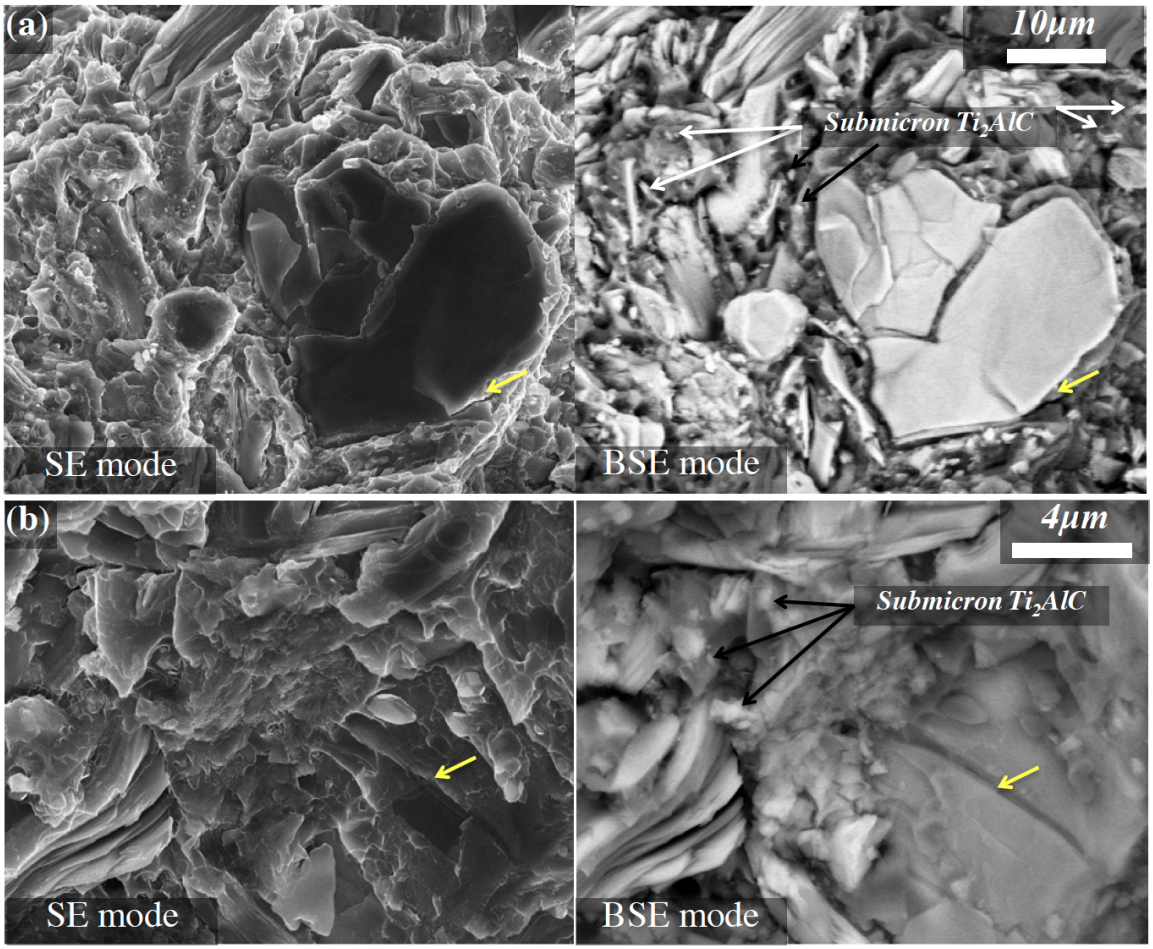

Fig. 5.9. Secondary (left) and backscatter electron SEM micrographs (right) of, (a) CG50-Ti_2AlC-Mg and, (b) CG50-Ti_2AlC-AZ61 surfaces. The arrows in, (a) show a matrix fracture next to the interface, (b) show how Mg filled a pre-existing microcrack in a Ti_2AlC particle (yellow arrow).

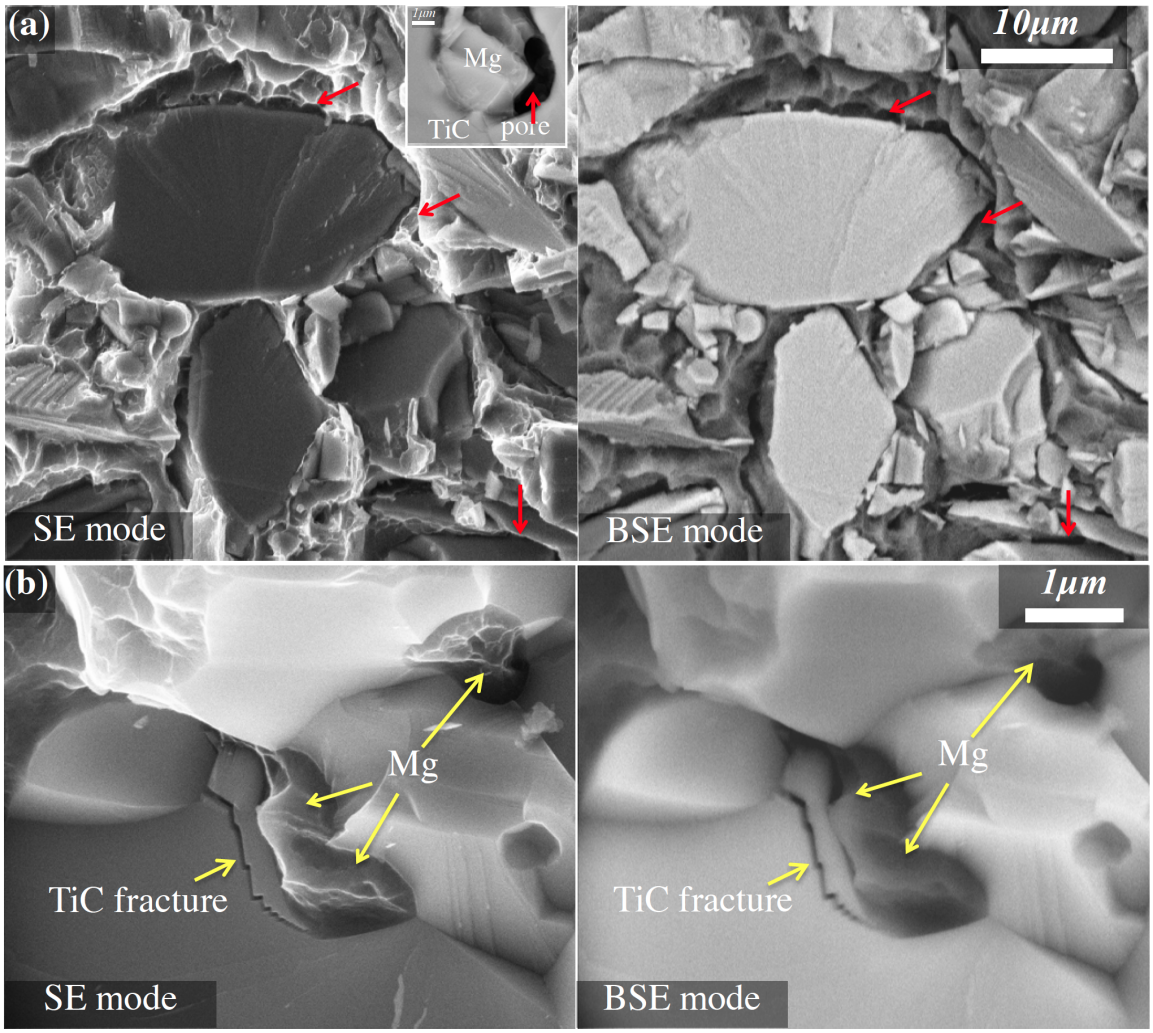

Fig. 5.10. Secondary (left) and backscatter electron SEM micrographs (right) of, (a) CG50-TiC-Mg and, (b) CG50-TiC-AZ61 fractured surfaces. The arrows in, (a) show 4.7-TiC-Mg interface debonding, and (b) show AZ61 infiltrated small pores in the TiC preform and also reinforcement fractured next to the matrix-reinforcement interface. Top inset in (a) shows that Mg was not able to fill all the pores in the TiC composite.

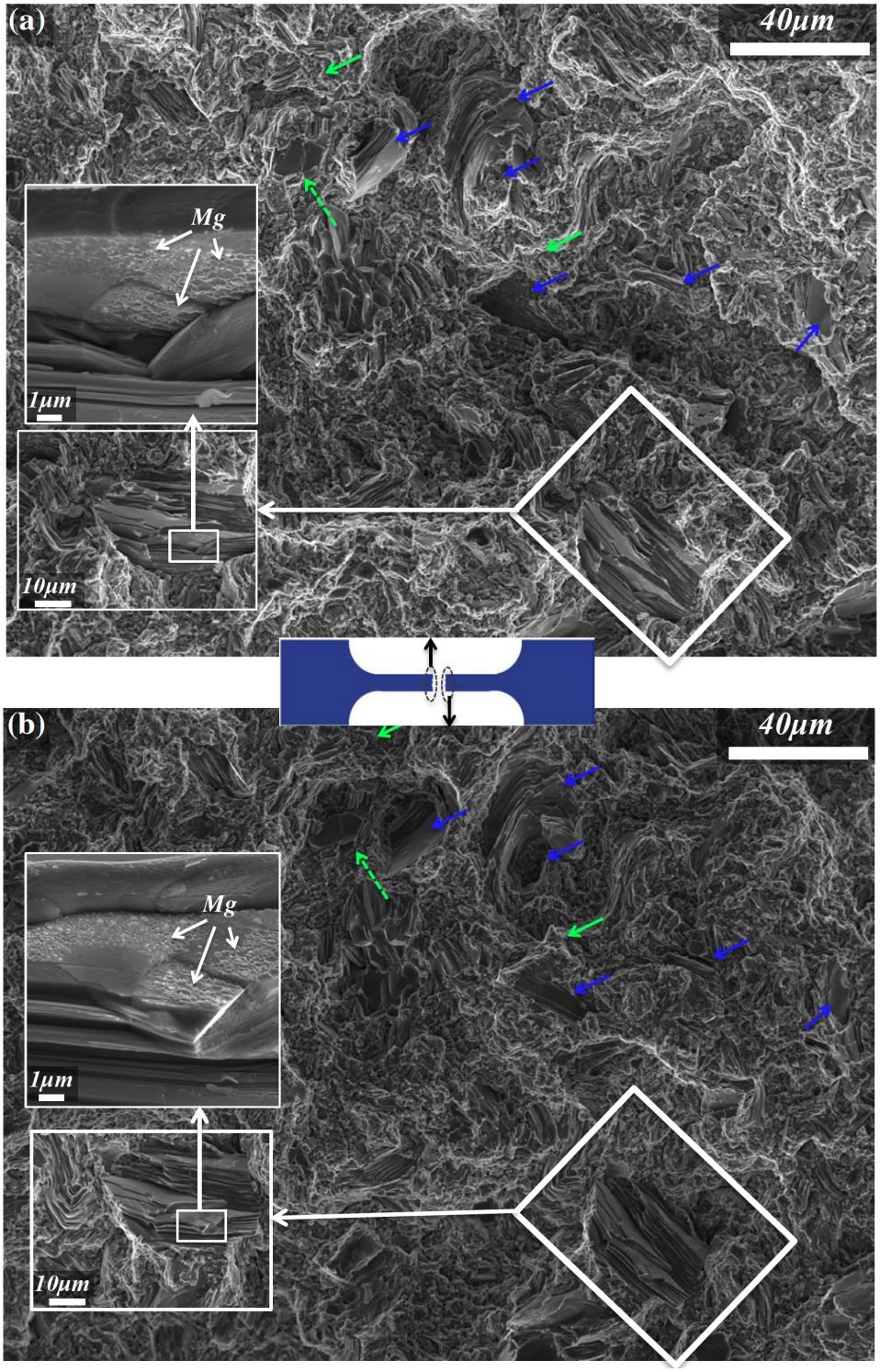

Fig. 5.11. Secondary electron SEM images, (a) and (b), of both surfaces of a fractured CG50-Ti_2AlC-AZ61 tensile specimen. Bottom left insets are a fractured Ti_2AlC particle. The top left insets are the same Ti_2AlC particle at higher magnification and the white arrows point to the areas covered with Mg. The blue and green arrows point to Ti_2AlC and matrix fractures, respectively.

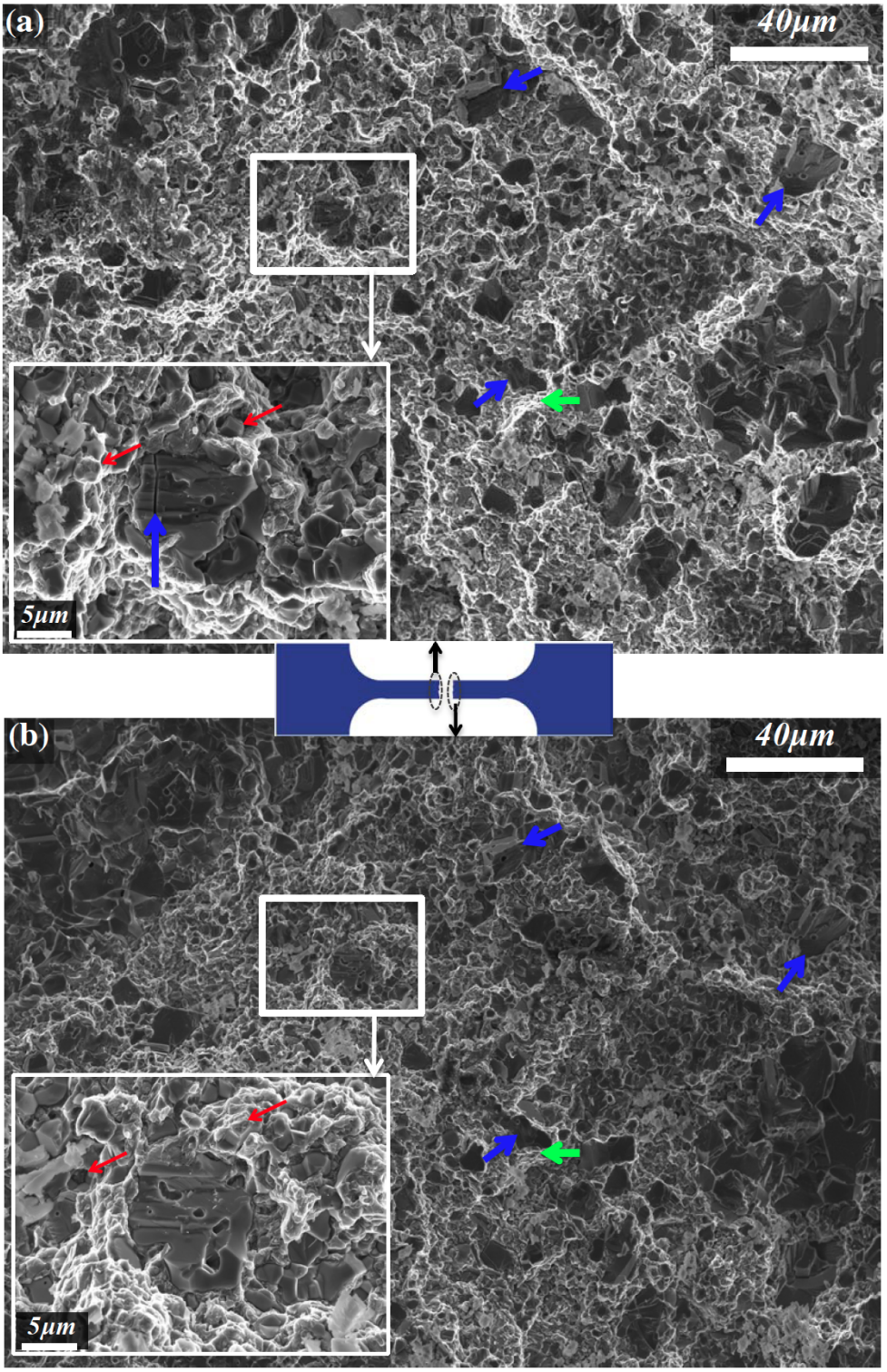

Fig. 5.12. Secondary electron SEM images, (a) and (b), of both surfaces, of a fractured CG50-TiC-AZ61 tensile specimen. Bottom left insets are a fractured TiC particle (blue arrow) surrounded with some matrix/interface debonding (red arrows). The blue and green arrows show TiC and matrix fractures, respectively.

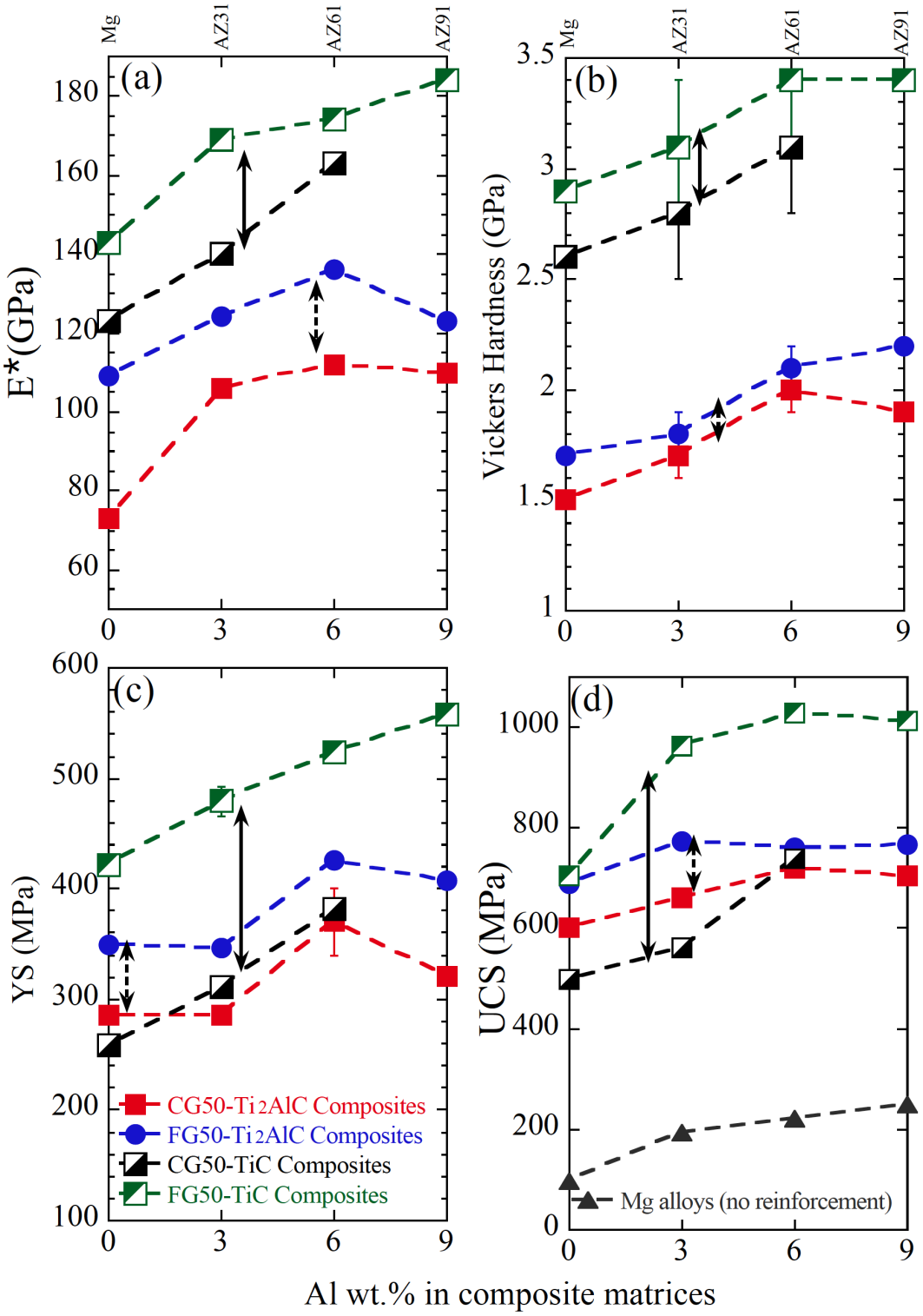

Fig. 5.13. Effect of Al in Mg matrices on, (a) elastic moduli (E*), (b) yield strengths (YS), (c) Vickers hardness values (V_H) and, (d) ultimate compression strengths (UCS) of Ti_2AlC and TiC composites. Lines between points are guides to the eye. The black arrows show the effect of reinforcement particle size refinement. When error bars are not shown, the uncertainties are smaller than symbols sizes.

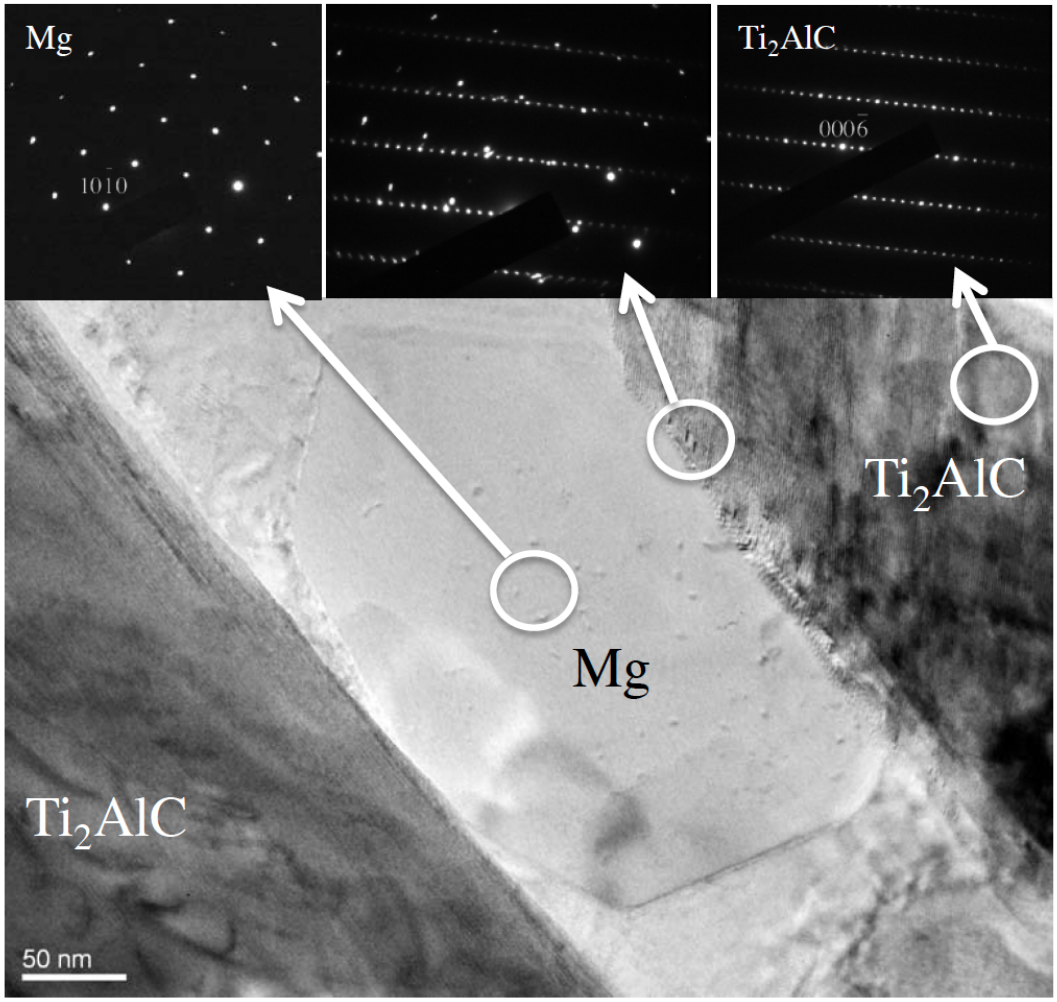

Fig. 5.14. TEM micrograph of Ti_2AlC-Mg interface. The top insets are SADs of the Ti_2AlC particle, the interface and the Mg in between the Ti_2AlC particles.

5.1.6. Machinability

Similar to their components [38, 97], all the MAX-reinforced composites were readily machinable, even with a manual hacksaw, with no lubrication or cooling required. The TiC-Mg composites, on the other hand, were not as readily machinable. However, it was possible to EDM all composites fabricated in this study.

5.2. Discussion

The discussion in this chapter will mainly focus on the results of the 50 vol.% composites. In general, most of the 50 vol.% reinforced composites fabricated herein combine high stiffness and hardness values, low densities, machinability (at least with EDM), high UCSs and UTSs, high damping and excellent fatigue resistance. Their damping and fatigue resistance will be discussed in chapter 6. With an E*, YS, UCS and V_H, of 184±5 GPa, 557 ± 8 MPa and 1013 ± 12 MPa and 3.4 ± 0.2 GPa, respectively, the properties of the FG50-TiC-AZ91 composite are truly noteworthy. As far as we are aware these values are some of the highest ever reported for Mg-matrix composites in general, and ones fabricated by MI, in particular.

As shown in Fig. 5.13, all the properties are functions of two major parameters: i) reinforcement particle size and, ii) Al content in the Mg matrices. For the Ti_2AlC-composites, the properties appear to peak at ≈ 6 wt.%. The situation for the TiC-composites is less clear since E* and YS do not appear to have saturated, while the UCS and V_H values appear to have.

In the following sections each of these properties is discussed and the case is made that these results can be explained by invoking two ideas: the effect of interfacial strengths and reinforcement particle size that, in turn, reduces the grain size of the Mg matrices and creates more obstacles for dislocations motion.

5.2.1. Elastic moduli

Both the 50-Ti_2AlC- and 50-TiC-composites fabricated herein possess high E* values. With the notable exception of the CG50-Ti_2AlC-Mg composite, the E* of all the 50 vol.% composites tested herein exceeded 100 GPa. The highest value obtained was

184±5 GPa for the FG50-TiC-AZ91 composite; for the 50-Ti_2AlC based composites, the highest value was 136±6 GPa (Table 5.4).

Table 5.4 and Fig. 5.13(a) make it amply clear that the presence of Al in the matrix alloy is needed if stiff composites are desired. The increasing trend for all four series of 50 vol.% reinforced composites shown in Fig. 5.13(a) clearly reveals that Al contents of ≥ 6 wt.% significantly improve E*. This increasing trend can also be observed by comparing the results with previous work. At 120±3 GPa and 123±2 GPa the E*'s of the CG50-Ti_2AlC(N)-AZ61 and CG50-Ti_2AlC(P)-AZ61 composites, respectively, tested herein are significantly higher than ≈ 85 GPa reported previously for oriented 50-Ti_2AlC composites with unalloyed Mg [62].

These results clearly reveal the importance of Al, as an alloying element in the Mg matrices for increased load transfer from the matrices to the reinforcement. It is well established that such load transfer is needed to enhance the elastic properties [14]. Based on our results it is reasonable to conclude that an interfacial interaction - the nature of which is unclear at this time - involving Al, results in stronger interfaces. If an interfacial layer forms it must be quite thin indeed since no trace of it in SEM and/or TEM micrographs, even at the highest magnifications, was found (Fig. 5.14). Furthermore, since even XRD results, with long acquisition times, did not identify any trace of reaction in these composites, it is fair to assume that the interfacial interactions are less chemical and more mechanical, in the form of wetting of the Mg and its alloys due to the presence of Al. In other words, Al mostly enhances the wettability in these composites.

Note that while the presence of Al is important, it also appears that it is more effective when present in both matrix and reinforcement. This is best evidenced when

Figs. 5.8(a) and (b) are compared, where it is obvious that the E* values of the 50-Ti_2AlC composites (Fig. 5.8(a)) are closer to the ROM predictions than those for the 50-TiC composites (Fig. 5.8(b)). This result is consistent with the presence of better matrix/reinforcement interfaces in the case of the Ti_2AlC composites.

The results shown in Fig. 5.8 are significant for another important reason: they can be used to check the validity of the various models that have been proposed in the literature for calculating the moduli of composites from the elastic properties of their constituents and check whether these models can be applied to E*. It is important to emphasize here that the E* values reported are not the true elastic moduli of the composites because they are a function of reinforcement particle size (see Fig. 5.13(a)) and texture (Table 5.4). Said otherwise, despite the fact that no hysteresis loops are observed in the stress-strain curves at 100 MPa and that the stress-strain curves trace straight lines within the accuracy of our measurement, one has to conclude that plastic deformation is nonetheless occurring at stresses lower than 100 MPa.

For the 50-Ti_2AlC composites, E* of both the 50-Ti_2AlC-AZ31 and 50-Ti_2AlC-AZ91 composite samples - for both particle sizes- are comparable but are slightly lower than those of the Ti_2AlC-AZ61 composites (Fig. 5.13(a)). Since the only difference between them is the Al content, it appears that the optimum Al content in the Mg matrices to form strong interfaces, at least in the Ti_2AlC composites, is ~ 6 wt.%. The reason why the oriented CG50-Ti_2AlC(N)-AZ61 and CG50-Ti_2AlC(P)-AZ61 composites have higher elastic moduli than the random ones is not entirely clear at this stage. More work is required to understand these differences.

Figure 5.13(a) clearly shows the effect of reinforcement particle size on the enhancements in E* (arrows in Fig. 5.13(a)). As mentioned above, some plastic deformation is occurring even at 100 MPa. It is reasonable to assume that a higher population of finer (nano size) reinforcing particles act as obstacles for plastic deformation at low stresses [98], which in turn leads to higher E* for the finer reinforced composites (Fig. 5.13(a)). This observation indirectly confirms that plastic deformation is occurring, even at 100 MPa. Note that such microyielding that was not associated with reversible stress-strain loops was observed in cyclic loading of polycrystalline Co [55].

The E* value for the 50-Ti_3AlC_2-Mg composites, is quite comparable to that of their 50-Ti_2AlC-Mg counterparts (Table 5.4). Furthermore, all the other mechanical properties reported in Table 5.4 for the 50-Ti_3AlC_2-Mg composite are comparable to their 50-Ti_2AlC-Mg counterparts. Therefore, it is reasonable to conclude that the presence of 20 wt.% Ti_3AlC_2 in the initial Ti_2AlC powders would not alter any of the conclusions reached in this work.

5.2.2. Vickers hardness (V_H)

At 1.5 ± 0.1 GPa, V_H of the CG50-Ti_2AlC-Mg composite is comparable to the one reported by Amini et al. [62]. At 2.1 ± 0.1 GPa, however, the V_H values of the FG50-Ti_2AlC-AZ61 and FG50-Ti_2AlC-AZ91 composites are the highest ever reported for Mg or Mg alloy composites reinforced with Ti_2AlC (Fig. 5.13(b)). For the TiC-Mg alloy composites, the highest value was 3.4 ± 0.3 GPa for the FG50-TiC-AZ91 composite (Table 5.4 and Fig. 5.13(b)).

The differences in V_H between the TiC and Ti_2AlC-reinforced composites can be

traced back to their intrinsic hardness values. The binary carbide, with a V_H 32 ± 3 GPa [99], is a hard brittle ceramic with no active slip systems at room temperature. For the ternary carbide, on the other hand, basal slip is operative at room temperatures, which is why its V_H is significantly lower in the composites reinforced with Ti_2AlC than with TiC. The V_H for Ti_2AlC was reported to be 5.0±0.5 GPa in [69, 100] and 3.0±0.3 GPa in Refs. [62, 78]. It is worth noting that the MAX phases are particularly ductile in single crystal form, especially when loaded in compression [34].

At 2.6 ± 0.2 GPa, the V_H of the CG50-TiC-Mg composite is higher than the ≈ 1.8 GPa reported by Contreras et al. for a 56 vol.% TiC-Mg composite fabricated via MI at 850 ºC, with a TiC average particle size of 1.2 μm and a density ≈ 97 % of theoretical [21]. The reason why our values are higher is not clear but could, in part, be due to the fact that the composites fabricated here are less porous. Furthermore, at 2.9 ± 0.3 GPa, V_H of the FG50-TiC-Mg composite was enhanced due to the presence of the finer TiC particles.

In general, the increase in the hardness of the composites compared to those of pure Mg or Mg alloys can be credited to the presence of the reinforcing particles in the matrices. On the other hand, the increase in V_H with increasing Al content can be related to the presence of stronger interfaces, which, in turn, lead to higher constraints on localized matrix deformation. The increase in the load transfer to the elastically stiffer reinforcement particles must also play an important role.

In the case of CG50-Ti_2AlC composites, the slight reduction in V_H due to replacing AZ61 with AZ91 might be due to the presence of a stronger interface in the

former case.

5.2.3. Yield strengths (YS)

Since for the most part for metals, the 0.2 % YS is proportional to V_H, the same arguments made to explain the changes in V_H can be used to understand the changes in YSs. Here again, based on the results shown in Fig. 5.13(c) and Table 5.4, it is clear that increasing the Al content enhances the YS. However, and in contrast to E* and V_H, changing the matrix from pure Mg to AZ31 in the 50-Ti_2AlC-composites has no discernible effect on YS. Further increasing the Al content to 6 wt.%, however for both Ti_2AlC particle size composites, leads to a ≈ 20% improvement in the YS. Since the YSs of the CG50-Ti_2AlC-AZ61 and FG50-Ti_2AlC-AZ61 composites are higher than their AZ91 matrix counterparts (Fig. 5.13(c)), the optimum Al content can again be considered to be ≈ 6 wt.%. For the 50-TiC-composites' case, increasing the Al content, in both TiC particle size composites, enhances the YS (Fig. 5.13(c) and Table 5.4).

The 0.2% YS is the stress that is needed to operate dislocation sources and it depends on the number and size of obstacles that can hinder dislocation motion in the matrix [86]. The general increase in YSs of the composites compared to monolithic Mg and its alloys can thus be explained by the presence of a large number of small reinforcing particles in the Mg-matrices that, in addition to reducing the matrix grain size, can also act as obstacles to dislocation movement. It follows that the presence of submicron and micron sized particles in all composites (Fig. 5.4) leads to the enhancements in YS.

The arrows in Fig. 5.13(c) show the effect of reinforcement particle size reduction

on the YSs in both the Ti_2AlC and TiC-based composites. At 523±8 MPa, the YS of FG50-TiC-AZ61 was measured to be ≈ 27% higher than that in CG50-TiC-AZ61 composites. Further, the YS enhancements in the TiC-composites are larger than those of the Ti_2AlC-composites, which can be due to the higher TiC particle size reduction in the TiC-composites (Table 5.1). Smaller reinforcing particles reduce the Mg matrix grain size and also can be more effective in hindering dislocation motion.

In addition, the increase in the YSs of the AZ61 and AZ91 matrix composites as compared to the pure Mg and AZ31 matrix composites can be due to stronger interfaces and better matrix bonding with the elastically rigid reinforcement. As a result, the reinforcement will carry more of the applied load and reduces the applied stress on the matrix.

The third factor to be considered are the residual thermal stresses – due to coefficient of thermal expansion (CTE) mismatches [101] – that could, in principle, generate high dislocation densities in the vicinity of the matrix/reinforcement [9, 50]. The CTEs of Ti_2AlC are 7.1±0.3× 10^{-6} K^{-1} and 10.5±0.5 × 10^{-6} K^{-1} in *a*- and *c*-directions, respectively [100]; those for TiC are between 7 and 8.4×10^{-6} K^{-1} [102, 103]. At 26×10^{-6} K^{-1}, the CTE of Mg is significantly larger than either reinforcing particles. The residual thermal strain can be crudely estimated assuming [104]

$$\varepsilon = \Delta\alpha . \Delta T \tag{5.4}$$

where $\Delta\alpha$ is the difference between the CTE of the reinforcement and matrix and ΔT is temperature change during matrix solidification. Herein ΔT is assumed to be 500 °C and by substituting the Mg and reinforcements CTE values in Eq. 5.4, residual thermal strains

at the Ti_2AlC/Mg and TiC/Mg interfaces of the order of ≈ 0.9±0.1 % are predicted. These strains, in turn, can result in compressive stresses in the reinforcement particles and tensile stresses in the matrices. The estimated stresses in the Mg matrices corresponding to these strains are in the range of 353 to 425 MPa, which are higher than the YSs of pure Mg or Mg alloys. As a result, it is reasonable to assume some plastic deformation occurs in the Mg matrices close to the interface that can lead to the nucleation of dislocations and concomitant strengthening.

The residual strains in the composites' components - estimated by the Rietveld analysis of the XRD data, assuming Gaussian XRD peak broadening - are shown in Table 5.2. However, and for reasons that are not entirely clear, the peak widths of the as received Ti_2AlC powders and the re-melted bulk AZ61 alloy are as broad as those in the composites. Consequently, no conclusions can be reached about the presence, or lack thereof, of residual strains in either the Ti_2AlC powders or the Mg-alloy matrices. Peak broadening in Ti_2AlC is most probably related to the method used to mill the powders. Note that the 2-D XRD results (Fig. 5.6(a)) that show a ring for Ti_2AlC, can be ascribed to the presence of nano Ti_2AlC grains in the 50-Ti_2AlC-Mg composite. This conclusion is consistent with the peak broadening observed in the powder diffraction peaks. These conclusions are also confirmed by the morphologies of many of the as-received particles that appear to be highly deformed (e.g. Figs. 5.6(b))

However, XRD peak broadening in the re-melted pure Mg was also observed. For the sake of simplicity, in the Rietveld analysis, the latter was assumed to be only due to the residual strain. The calculated residual strain from the pure Mg peak broadening was calculated to be ≈ 0.19 ± 0.01, which is lower than those estimated for the Mg matrices in

the composites (compare row 1 in Table 5.2 to rows 4, 10 and 12). Furthermore, comparing the Mg strain values in the CG50-Ti_2AlC-Mg with CG50-TiC-Mg and FG50-TiC-Mg composites (rows 10 and 12 in Table 5.2) shows that the Mg residual strains in the latter two are the lowest, a conclusion consistent with the presence of stronger interfaces in the Ti_2AlC-Mg composites. This conclusion is based on the reasonable assumption that less residual stresses would accrue if the interfaces are weak.

Since no peak broadening, due to residual strains, was observed for the TiC in the CG50-TiC-Mg and FG50-TiC-Mg composites (rows 10 and 12 in Table 5.2), it is again reasonable to conclude that the interfaces are weak in these two composites. In sharp contradistinction, the TiC residual strains in the TiC-AZ61 composites are of the order of 0.11±0.01%, which corresponds to a residual stress of ≈ 480 MPa. Here again, a conclusion that is consistent with the presence of a strong interface due to the presence of Al.

At 545 ± 3 MPa, the YSs of CG50-Ti_2AlC(P)-AZ61 composite was at least 25% higher than that of their CG50-Ti_2AlC(N)-AZ61 or CG50-Ti_2AlC(R)-AZ61 counterparts. In the former, according to Table 5.3 and Fig. 5.5(b), the orientation of the Ti_2AlC flake-like particles are more aligned parallel to the loading direction compared to the latter composites. The reason why the oriented CG50-Ti_2AlC(P)-AZ61 composites has a higher YS is not entirely clear at this stage, but again, is most probably related to the fact that the Taylor factors are highest in the oriented microstructures [62].

5.2.4. Ultimate compressive (UCS) and tensile (UTS) strengths

The crucial role Al plays on the UCSs can also be seen in Table 5.4 and Fig. 5.13(d), in which an increasing trend can be observed by increasing the Al content. In order to better understand the effect of Al content on the UCSs, the latter for monolithic Mg and Mg-alloys, fabricated in this study, are plotted in Fig. 5.13(d). Based on these results, and given that the slopes of the monolithic results and the composites are comparable, enhancements in the UCSs of the composites can be related to enhancements in UCSs of the matrices.

The UCSs of the pure Mg composites reinforced with FG-TiC and FG-Ti_2AlC are comparable, despite the fact that the TiC particles have higher UCSs than their Ti_2AlC counterparts – in which basal slip is operative However, the UCSs of both CG-TiC and FG-TiC-composites increase more rapidly with Al content and become higher than those of their Ti_2AlC counterparts. In other words, the increasing UCS trend for the FG-TiC family is faster than that for the monolithic Mg alloys and other composites when matrix changes from pure Mg to AZ-alloys. The reason for this state of affairs is unclear at this time.

At 1028 ± 5 MPa, the UCS of the FG50-TiC-AZ61 composite was ≈ 30% higher than that of the FG50-TiC-Mg composite. The UCS of the former is also about 26% higher than that of FG50-Ti_2AlC-AZ61 composites. These values are noteworthy and, as far as we aware, are the highest ever reported for Mg-based composites. In addition, the presence of finer-reinforcing particles leads to higher UCS values. Changing the TiC particle size from coarse to fine for the same Mg matrices increased the UCSs at least 30% which is consistent with previous conclusions (solid line arrow in Fig. 5.10(d)).

The UTSs of as-cast AZ61 is reported to be 240 MPa [105]. The UTSs of the MAX phases, are generally below 300 MPa [106]. It follows that at 420 ± 40 MPa and 430 ± 40 MPa the UTSs of the CG50-Ti_2AlC(N)-AZ61and CG50-Ti_2AlC(P)-AZ61 composites are higher than their end members.

When Mg infiltrates the porous Ti_2AlC preform, the former not only fills the pores between the particles in the preform, but as importantly, it also fills in any pre-existing delaminations and microcracks in the initial Ti_2AlC particles and bonds them together and to the matrices (a reference to a fig here would be usefuk). In other words, the Mg acts like a tenacious, ductile glue not only between Ti_2AlC particles – i.e. the Mg breaks up any large weak Ti_2AlC agglomerates into much smaller stronger ones – but between the matrices and the particles. Said otherwise, when the Mg penetrates the Ti_2AlC particles it must also form strong, ductile mechanical interlocks that should greatly aid load transfer between matrix and reinforcement . Furthermore, any cracks that form in the brittle reinforcement during tension can be blunted in the matrix (dashed line green arrows in Fig. 5.11). Note that the presence of Mg in between the microcracks and fissures of the Ti_2AlC particles can also partially explain the conclusion that nanometer Mg grains exist in these composites [4, 47, 62, 107, 108].

Lastly, the fact that the UCSs reported herein are higher than their UTSs is not too surprising given the relatively large volume fraction of brittle or quasi-brittle reinforcements. The fact that the thermal residual strains in the matrices are tensile could also play a role in the fact that the UTSs are lower than the UCSs [9, 101].

5.2.5. Tensile fracture surfaces

The effect of interfacial strength and mechanical interlocking in transferring the load to the reinforcement is clear in the tensile fractographs. In the CG50-Ti_2AlC-Mg and CG50-Ti_2AlC-AZ61 composites almost no interfacial failure was observed (Figs. 5.9 and 5.11). The fracture plane went through the ceramic particles or the Mg matrices (depicted by arrows in Figs. 5.9 and 5.11). In Fig. 5.9(a), the SE image on the left shows a crack next to a Ti_2AlC particle and the BSE image, on the right, shows that the crack went through the matrix. In other words, within the resolution of our SEM, no obvious interface debonding was observed. Comparing the two SEM mode fractographs, it is possible to determine what type of fracture led to failure. The SE fractograph of a Ti_2AlC-AZ61 surface (Fig. 5.9(b)) shows that it is mostly covered with ductile Mg matrix fracture features. The BSE image on the left in Fig. 5.9(b) reveals that a Mg thin layer covered the Ti_2AlC particles (bright gray particles) and even filled a pre-existing microcrack present in the initial Ti_2AlC particle (arrows in Figs. 5.9(b)).

The bottom left insets in Figs. 5.11(a) and (b) show a fractured Ti_2AlC particle. EDS analysis evidenced the presence of Mg on the fractured Ti_2AlC particles (white arrows on the top left insets). This is clear evidence that Mg infiltrated the pre-existing microcracks in the Ti_2AlC particles and presumably glued the latter. As importantly the Mg also created a strong interlock between matrix and reinforcement, which in turn resulted in higher fracture stresses. These results are in agreement with Fig. 5.3 that Mg infiltrates all the small microcracks in Ti_2AlC [108].

In the case of the TiC composites, a combination of interface debonding, matrix fracture, particle cracking and fracture are observed. Interface debonding (arrows in Fig.

5.10(a)) is dominant in the CG50-TiC-Mg composite in which Al is absent. Furthermore, the presence of small pores in the latter composite (top inset in Fig. 5.10(a)) shows that pure Mg does not infiltrate all the small pores in the TiC preforms.

In contrast, a typical CG50-TiC-AZ61 fracture surface (Fig. 5.10(b)) shows strong interface bonding which led to reinforcement fracture. This can be due to the presence of Al in the matrix, which improves the wetting. However, when two opposing sides of the same CG50-TiC-AZ61 composite fracture surface are compared (Figs. 5.12(a) and (b)), three types of fracture were observed: interface debonding (red arrows), matrix fracture (green arrows) and particle cracking and fracture (blue arrows). This being said, no evidence of porosity can be observed in this fractured surface, which can be ascribed to the better wetting of AZ61 as compared to pure Mg.

In general, comparing Figs. 5.9 to 5.12 confirms that the Ti_2AlC/Mg interface is stronger than the TiC/Mg interface.

5.2.5. TEM observation of the Ti_2AlC-Mg interface

When the Ti_2AlC composite samples were imaged in a TEM (Fig. 5.14), thin Mg layers were observed in between the Ti_2AlC layers confirming the SEM observations. SAED of the interface (center top inset in Fig. 5.14) clearly shows it to be comprised of a combination of Mg and Ti_2AlC diffraction spots. Comparing the SAED of pure Ti_2AlC (right top inset) and Ti_2AlC at the interface showed no changes in lattice parameters. The same was observed for Mg. These results confirm that both components maintain their structure at, or near, the interfaces.

5.3. Comparison with literature results

Lastly, it is important to compare the mechanical properties of this new family of composites with other materials and composites. Figure 15.15 plots the specific stiffness of different materials versus density. The blue shaded region in Fig. 15.15 represent the specific stiffness of all the composites fabricated in this study. At ≈ 55 GPa/g/cm^3, the specific stiffness of the FG50-TiC-AZ91 composite is the highest. Clearly, it is possible to tune the specific stiffness values, by varying the vol. % of the reinforcement and Al content of the Mg alloys.

The elastic moduli and hardness values of the composites fabricated herein are compared with some of the composites reported in the literature. For the sake of simplicity, only the values of the best composites of each family (FG50-Ti_2AlC-AZ61 and FG50-TiC-AZ91) are shown. The highest elastic moduli and hardness values of the Mg-matrix composite reinforced with TiC or SiC reported in the literature, to our knowledge, are also plotted versus reinforcement vol.% in Fig. 15.16. Based on these results it is obvious that at 184±5 GPa, the elastic modulus of the FG50-TiC-AZ61 composite is the highest value ever reported for Mg matrix composites (Fig. 15.16(a)). Even the 50-Ti_2AlC-AZ61 possesses higher E values than the 50-SiC-AZ80 reported in the literature [23], despite the fact that SiC is significantly stiffer than Ti_2AlC. This observation demonstrates the critical role the matrix/reinforcement interface plays.

At 3.4±2 GPa, the hardness of the FG50-TiC-AZ91 is also the highest value reported to Mg matrix composites to our knowledge. However, the hardness of the FG50-Ti_2AlC-AZ61 is lower than that of a 50-SiC-AZ80, which is not too surprising given that that SiC is significantly harder than Ti_2AlC.

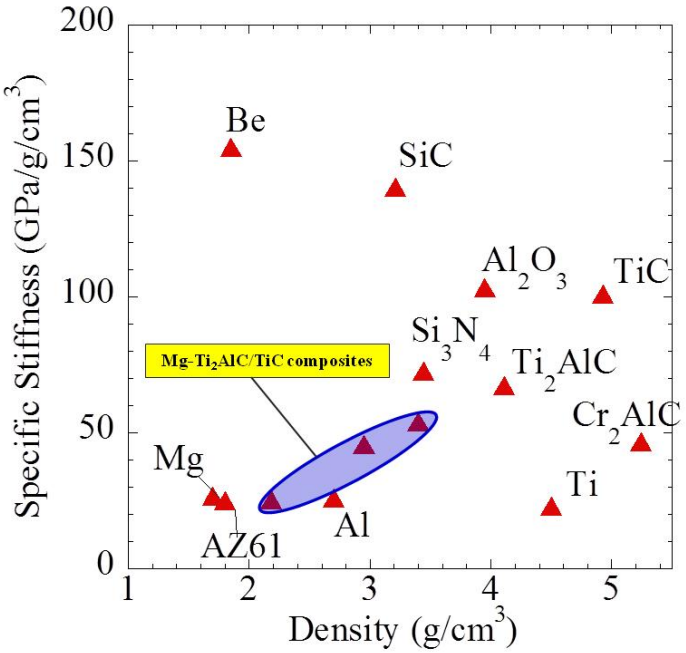

Fig. 5.15. Specific stiffness versus density of different materials. The blue oval represent the specific stiffness of all the composites fabricated herein which reinforced with either Ti_2AlC or TiC. E* is used to calculate the specific stiffness of the composites in this study.

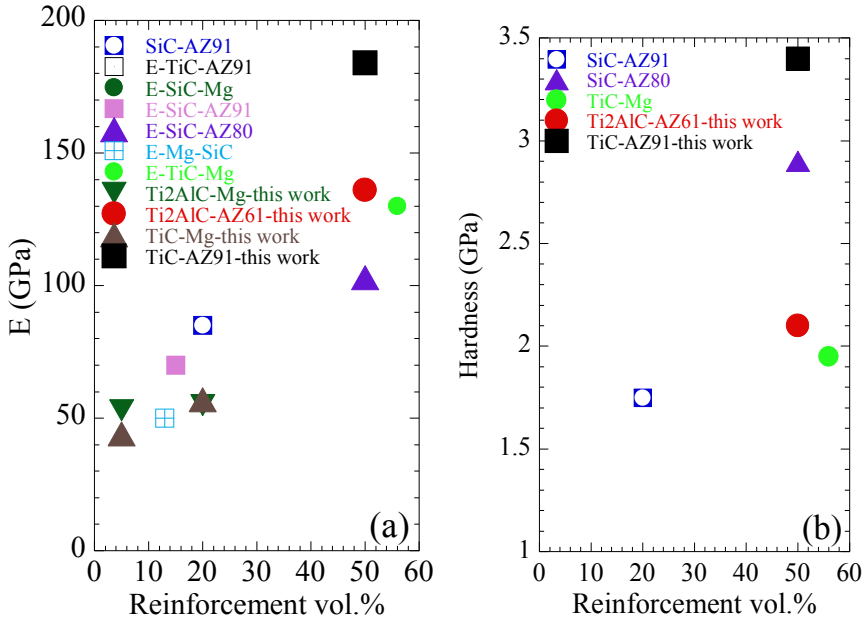

Fig. 5.16. (a) Highest elastic moduli of Mg composites reported in the literature are compared with E* of FG50-Ti_2AlC-AZ61 and FG50-TiC-AZ91 and 5 and 20 vol.% reinforcement pure Mg composites; (b) the same comparison was done for the Vickers hardness values.

Chapter 6: Energy Damping

In this chapter, the damping properties of all the composites fabricated in this study are presented and discussed. The energy dissipation is measured during cyclic compression.

6.1. Cyclic compression

At the beginning of this chapter it is useful to explain how the energy dissipation and other related parameters are measured. As described in Ch. 5, the following protocol was used for the cyclic compression experiments: Each sample was first loaded to a load corresponding to ~ 75% of its UCS for two consecutive cycles before cyclically loading it by 50 MPa decrements from the maximum load during each cycle for the 50 vol.% reinforced composites and by 30 MPa decrements for the 20 and 5 vol.% reinforced composites and the pure AZ61 alloy.

Referring to Fig. 6.1, the following procedure was followed. As a first step, the area of each stress-strain loop was measured. This area, W_d, is the energy dissipated per unit volume in each cycle. In chapter 5, E* was defined as the slope of the initial linear part. The stress at which the loading curve deviated from linear is labeled the threshold stress, σ_t. Like all other such stress-strain loops [46], at the very beginning of unloading from the maximum load in each cycle, the slope of the stress-strain curve is again equal to E*. The strain between the two parallel lines with slopes E* is the nonlinear strain, ε_{NL}. When the latter is subtracted from the total strain, ε_{tot}, the linear elastic strain, ε_{LE}, can be

calculated. The least squares fits of the entire data set – shown as the diagonal dashed lines bisecting the loops (Fig. 6.1) - yields the effective modulus, E_f.

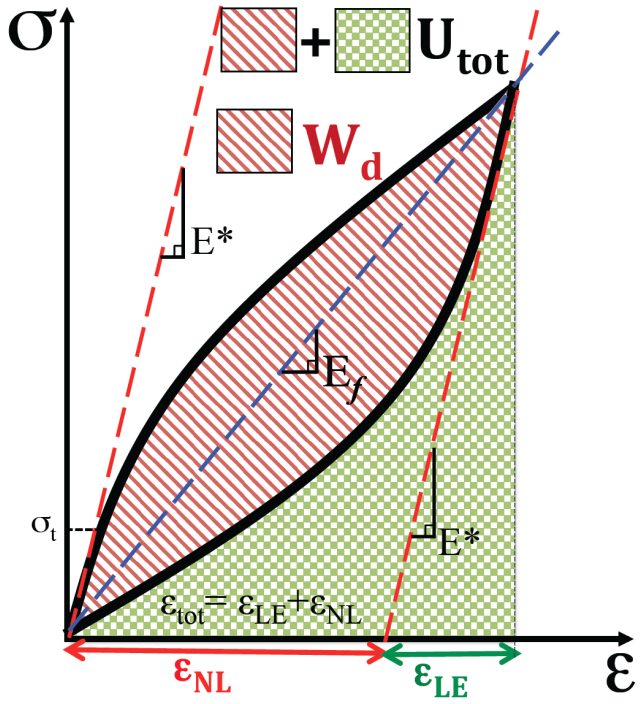

Fig. 6.1. Schematic stress-strain curve for a KNE solid where the energy dissipated per unit volume per cycle, W_d, total mechanical energy, U_{tot}, the non-linear, ε_{NL}, elastic, ε_{LE}, and total strains, ε_{tot}, threshold stress, σ_t, effective modulus, , E_f are defined.

Immediately following the decremental cyclic compression tests, and to further investigate the low cycle fatigue properties of these composites each cylinder was cyclically loaded 100 times with a strain rate of 0.01 s^{-1}, to a stress corresponding to ≤ 70% of their UCSs.

6.2. Results

6.2.1. Stress-strain loops

Figure 6.2 plots the stress-strain loops at various stresses for all the composites fabricated in this study. The loops are shifted horizontally for clarity. Clearly E_f depends on the maximum applied stress and decreases with increasing applied stress (Fig. 6.2). The average modulus, $E_{f(av)}$, - of each sample calculated by averaging all the E_f values along the entire applied stress range - is listed in Table 5.4.

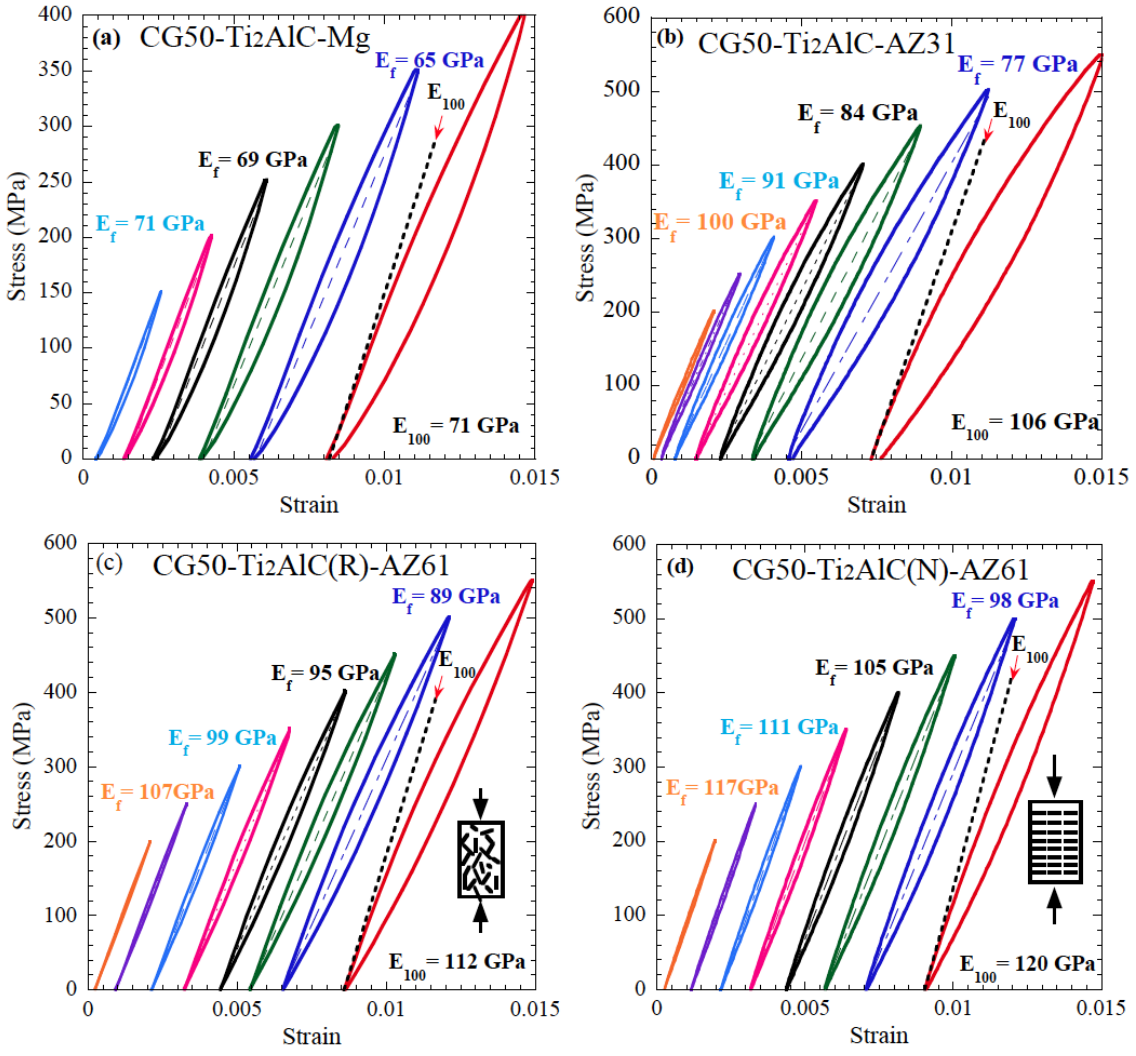

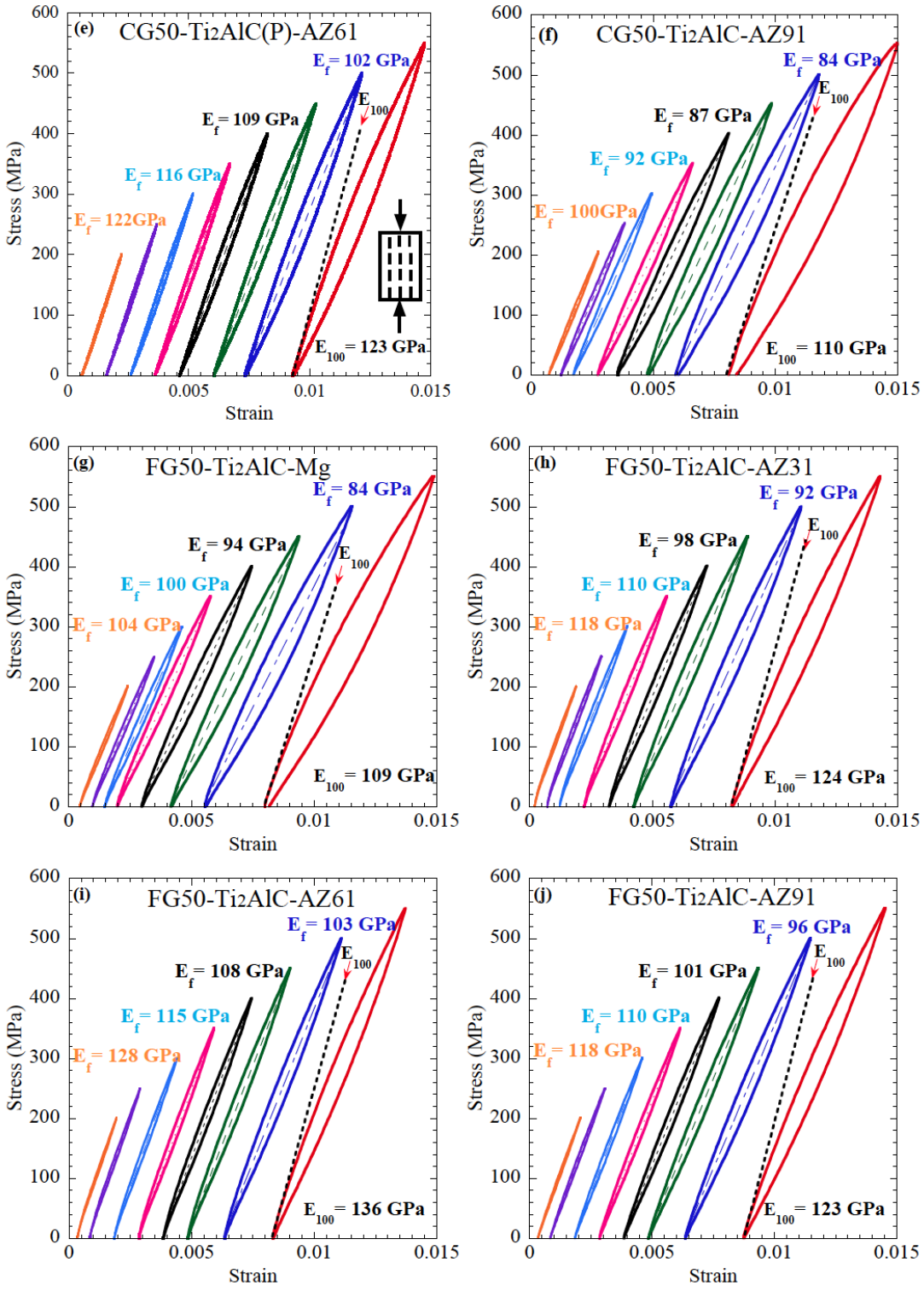
(e) CG50-Ti2AlC(P)-AZ61
Ef = 102 GPa
Ef = 109 GPa
Ef = 116 GPa
Ef = 122GPa
E100
E100 = 123 GPa
(f) CG50-Ti2AlC-AZ91
Ef = 84 GPa
Ef = 87 GPa
Ef = 92 GPa
Ef = 100GPa
E100 = 110 GPa
(g) FG50-Ti2AlC-Mg
Ef = 84 GPa
Ef = 94 GPa
Ef = 100 GPa
Ef = 104 GPa
E100 = 109 GPa
(h) FG50-Ti2AlC-AZ31
Ef = 92 GPa
Ef = 98 GPa
Ef = 110 GPa
Ef = 118 GPa
E100 = 124 GPa
(i) FG50-Ti2AlC-AZ61
Ef = 103 GPa
Ef = 108 GPa
Ef = 115 GPa
Ef = 128 GPa
E100 = 136 GPa
(j) FG50-Ti2AlC-AZ91
Ef = 96 GPa
Ef = 101 GPa
Ef = 110 GPa
Ef = 118 GPa
E100 = 123 GPa
Stress (MPa)
Strain
0
100
200
300
400
500
600
0.005
0.01
0.015

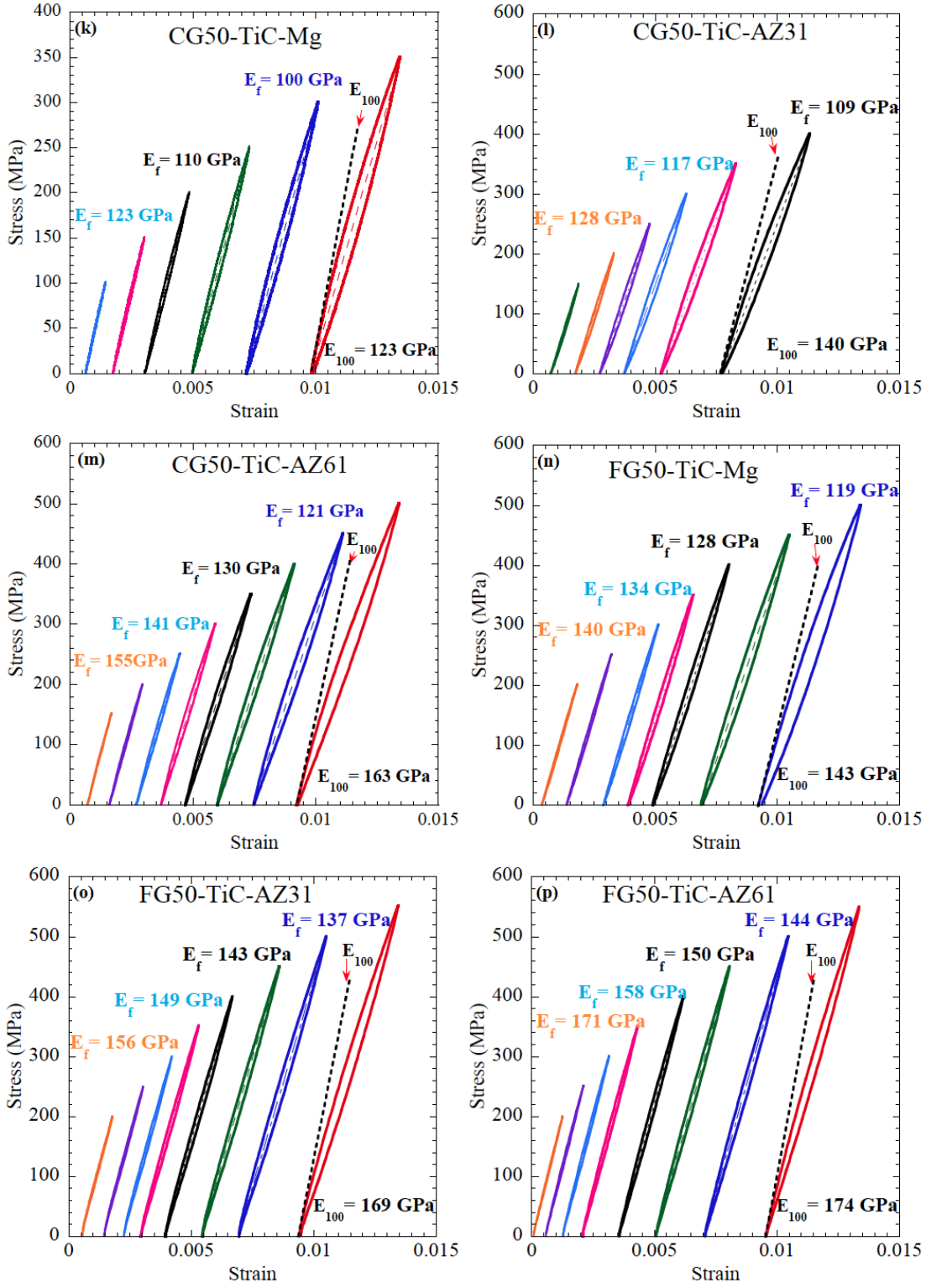
(k)
CG50-TiC-Mg
E_f = 100 GPa
E_100
E_f = 110 GPa
E_f = 123 GPa
E_100 = 123 GPa
(l)
CG50-TiC-AZ31
E_f = 109 GPa
E_100
E_f = 117 GPa
E_f = 128 GPa
E_100 = 140 GPa
(m)
CG50-TiC-AZ61
E_f = 121 GPa
E_100
E_f = 130 GPa
E_f = 141 GPa
E_f = 155GPa
E_100 = 163 GPa
(n)
FG50-TiC-Mg
E_f = 119 GPa
E_100
E_f = 128 GPa
E_f = 134 GPa
E_f = 140 GPa
E_100 = 143 GPa
(o)
FG50-TiC-AZ31
E_f = 137 GPa
E_100
E_f = 143 GPa
E_f = 149 GPa
E_f = 156 GPa
E_100 = 169 GPa
(p)
FG50-TiC-AZ61
E_f = 144 GPa
E_100
E_f = 150 GPa
E_f = 158 GPa
E_f = 171 GPa
E_100 = 174 GPa
Stress (MPa)
Strain
0
0.005
0.01
0.015

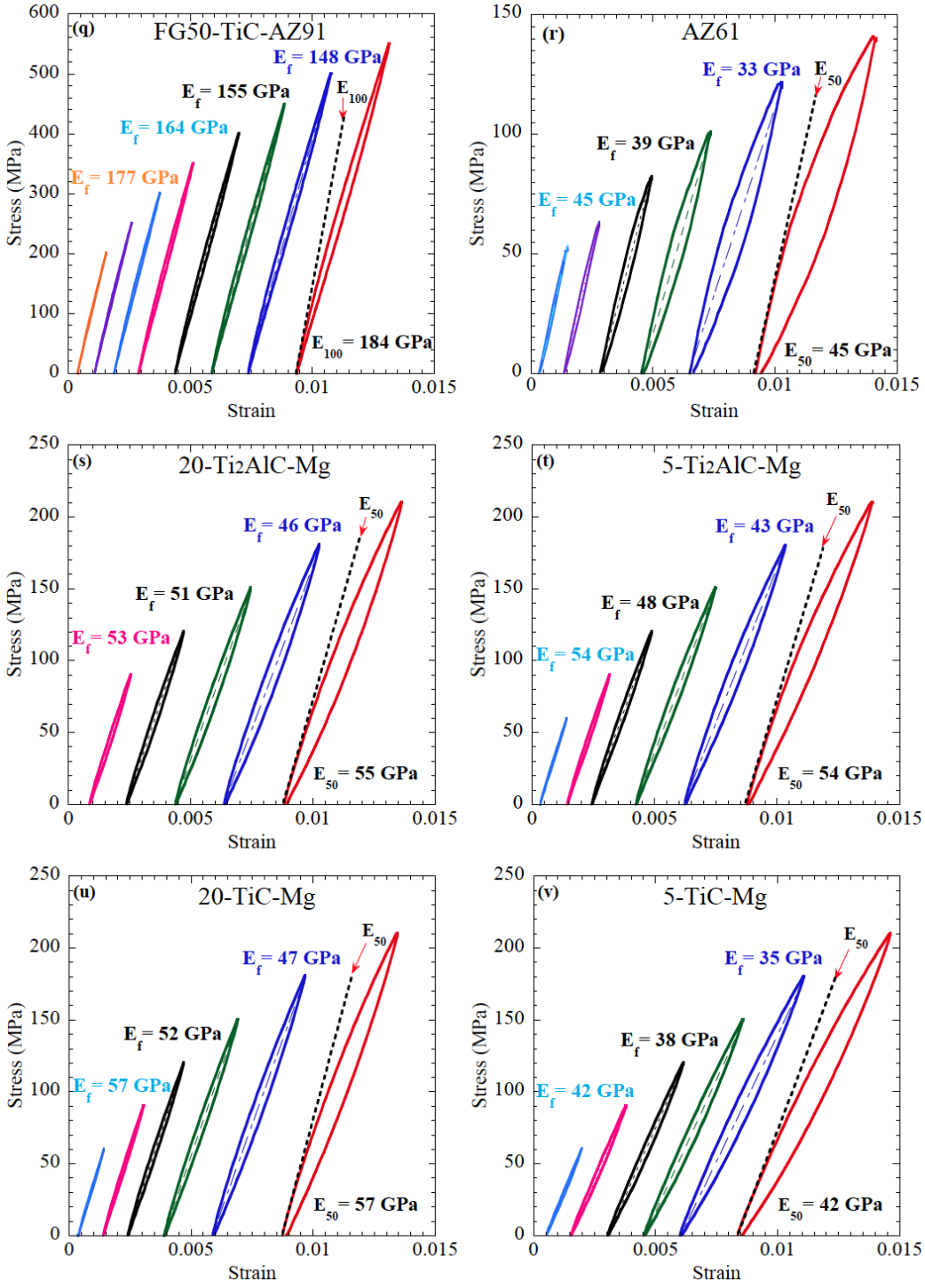

Fig. 6.2. (a) to (v) stress-strain cycles at various stresses for all the composites fabricated in this study. The curves are shifted horizontally for clarity. E_f (dashed lines inside the loops) are computed by least squares fits of the entire data set of each loop. E_{100} and E_{50} are the slopes of the stress-strain curves up to 100 MPa and 50 MPa, respectively.

6.2.2. Energy dissipation

In all the composites fabricated in this study, above σ_t, energy was dissipated during cyclic loading. The W_d values are plotted in Figs. 6.3(a) and (c).

In chapter 3, a linear correlation between W_d and σ^3 was predicted. The reasons for this statement were discussed previously. Figures 6.3(a) and (b) plot W_d, vs. σ^3 and ε_{NL} vs. σ^2 for all 50-Ti_2AlC composites, respectively. The solid lines correspond to the CG50-Ti_2AlC composite results; the dotted lines represent those for the FG50-Ti_2AlC composites.

For the sake of comparison, the W_d and ε_{NL} values of monolithic AZ61 tested herein and two bulk Ti_2AlC samples, with fine and coarse grains reported earlier [45, 62], are also plotted in Figs. 6.3(a) and (b).

At any given stress, the W_d values for the CG50-Ti_2AlC composites decrease as the matrix changes from pure Mg to AZ61 (red solid lines in Fig. 6.3(a)). The W_d values of AZ31 and AZ91 composites are almost identical and fall in between those of the Mg and AZ61matrix composites (Fig. 6.3(a)).

The same is true for the FG50-Ti_2AlC composites (Fig. 6.3(a)); the composite with the AZ61 matrix dissipates the least energy. In this series, however, the AZ91 matrix dissipates less energy than the AZ31 matrix, but both are still higher than the AZ61 matrix composite.

Figures 6.3(c) and (d) plot W_d vs. σ^3 and ε_{NL} vs. σ^2 results for both the CG50-TiC and FG50-TiC composites, depicted by solid lines and dotted lines, respectively. The same trend is observed for CG50-TiC, in which increasing the Al content of the matrix reduces W_d. However, in the case of FG50-TiC composites, the W_d values of all three Mg

alloy matrices are almost at the same level and about half of those of the FG50-TiC samples in which the matrix is pure Mg (dotted lines in Fig. 6.3(c)).

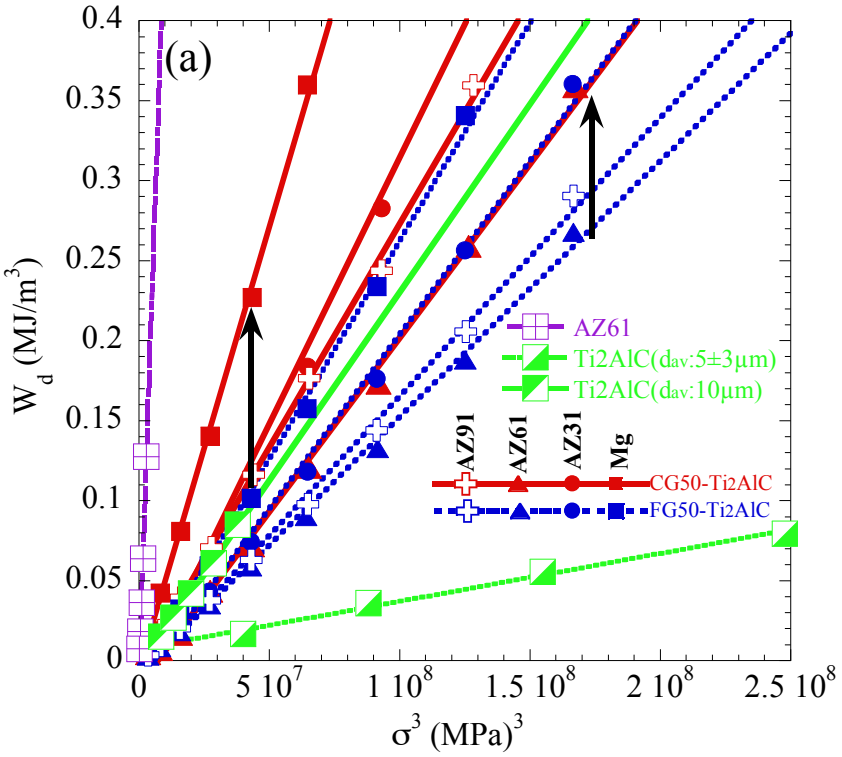

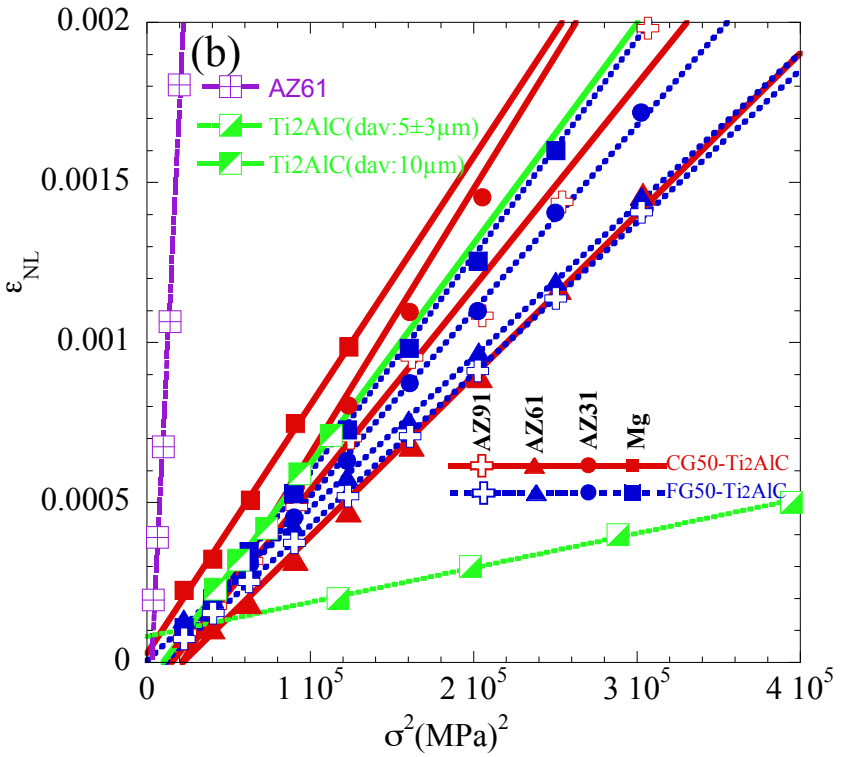

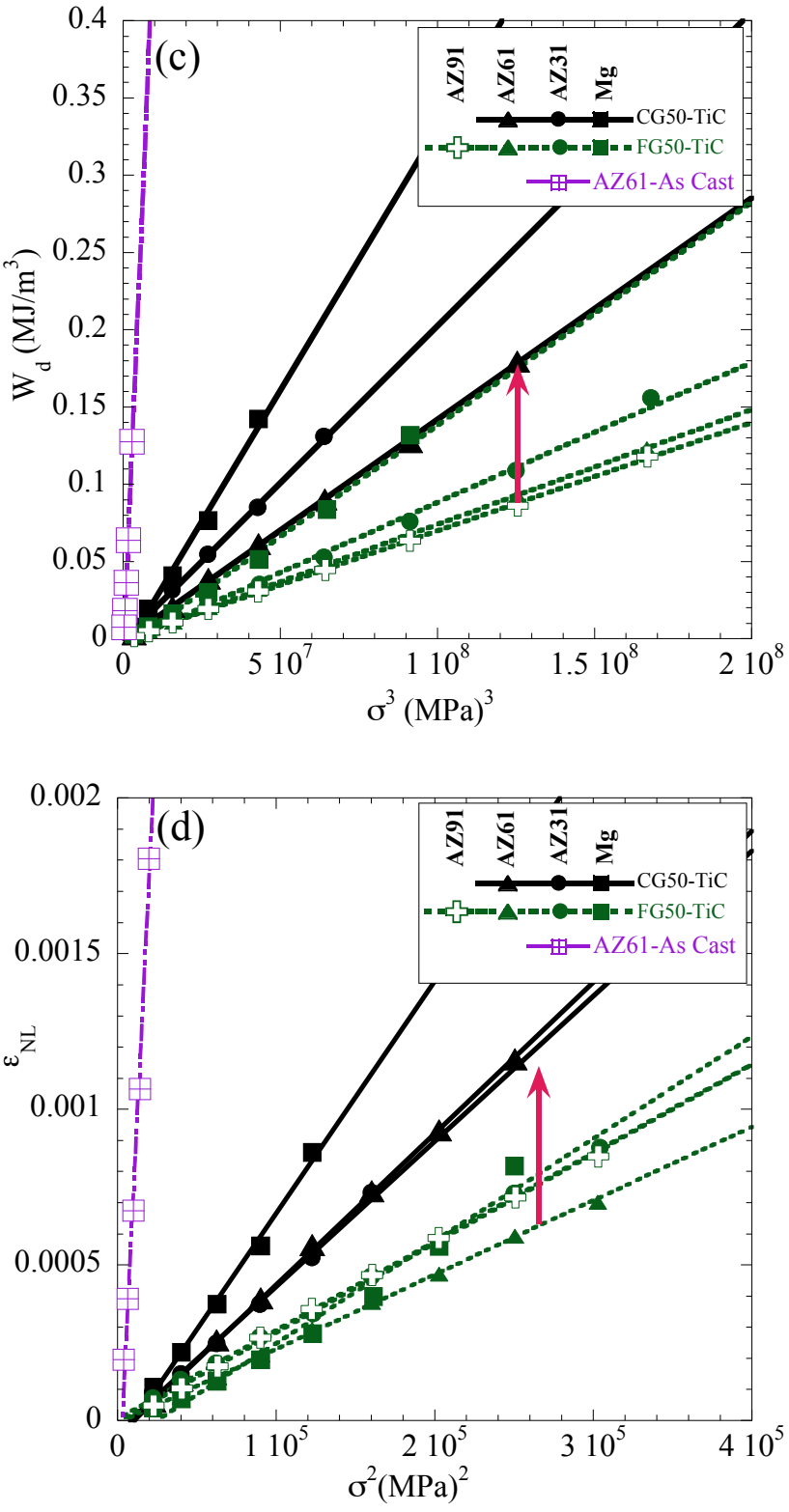

Fig. 6.3. (a) W_d vs. σ^3 and, (b) ε_{NL} vs σ^2, for all the CG50- and FG50-Ti_2AlC composites. (c) W_d vs. σ^3 and, (d) ε_{NL} vs σ^2, for all the CG50-TiC and FG50-TiC composites.

Figure 6.4 plots W_d vs. σ^3 for the 5 and 20 vol.% reinforced composites where the matrices are pure Mg. For the sake of comparison, the results of pure AZ61 and FG50-reinforced with TiC or Ti_2AlC composites with Mg matrix are shown as well.

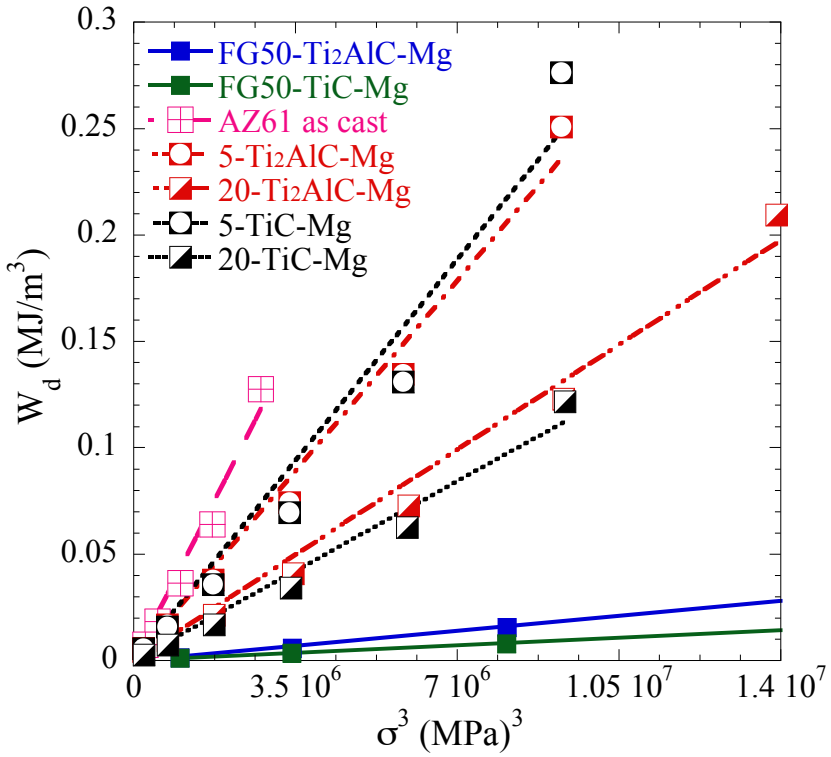

Fig. 6.4. W_d vs. σ^3 for the 20 and 5 vol.% composites, 50 vol.% composites with AZ61 matrices and monolithic AZ61.

Figure 6.5(a) compares the W_d results for the 50-Ti_2AlC-Mg composites with those of previous work fabricated by MI and HP [62]. Description of how the HP samples were fabricated can be found in chapter 2. Figure 6.5(b) also compares the W_d values for the random (R) and oriented CG50-Ti_2AlC-AZ61 samples from this work with their 50-Ti_2AlC-Mg counterparts from a previous study [62].

Figure 6.6(a) plots W_d vs. ε_{NL} for all 50 vol.% composites and the pure AZ61

tested herein. Based on Eq. 3.16 (in KNE chapter), $\frac{\partial W_d}{\partial \varepsilon_{NL}}$ was calculated after fitting a second order polynomial to the W_d vs. ε_{NL} results. The values of $\frac{\partial W_d}{\partial \varepsilon_{NL}}$ are plotted vs. applied stress in Fig. 6.6(b).

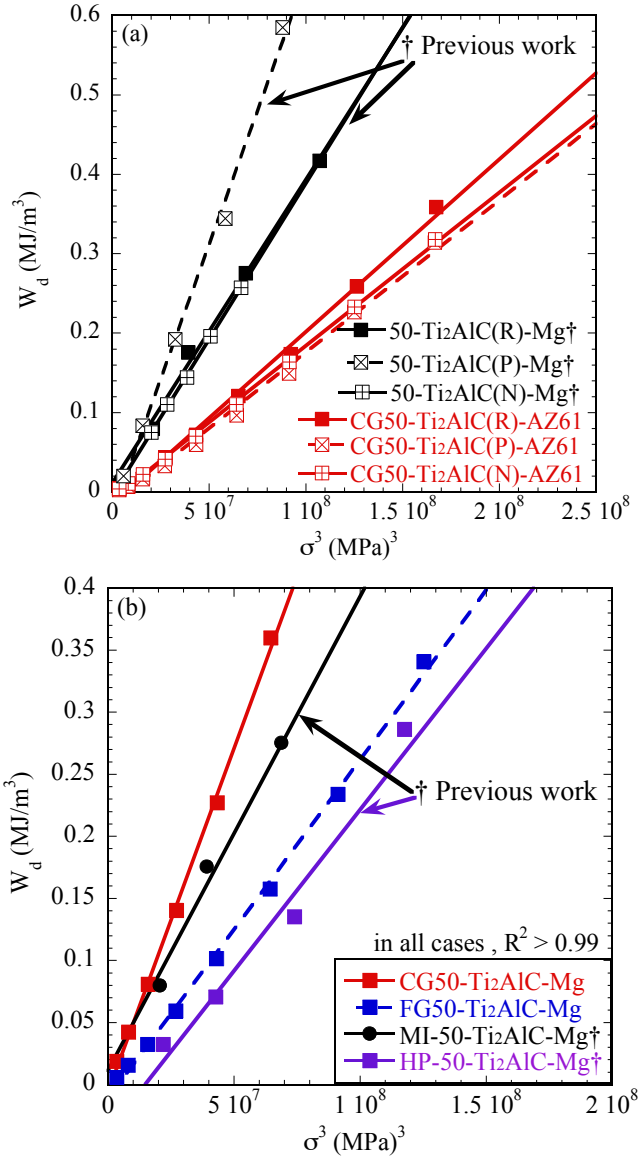

Fig. 6.5. W_d vs. σ^3 for, (a) random and oriented CG50-Ti_2AlC-AZ61 composites measured in this work compared with oriented and random Ti_2AlC-Mg composites from previous work [62]. R (random), P (parallel) and N (normal) refer to the orientation of the Ti_2AlC particles to the loading direction; (b) FG50- and CG50-Ti_2AlC-Mg in this work compared with 50-Ti_2AlC-Mg from the previous work fabricated by melt infiltration (MI) and hot pressing powder mixtures (HP) [62].

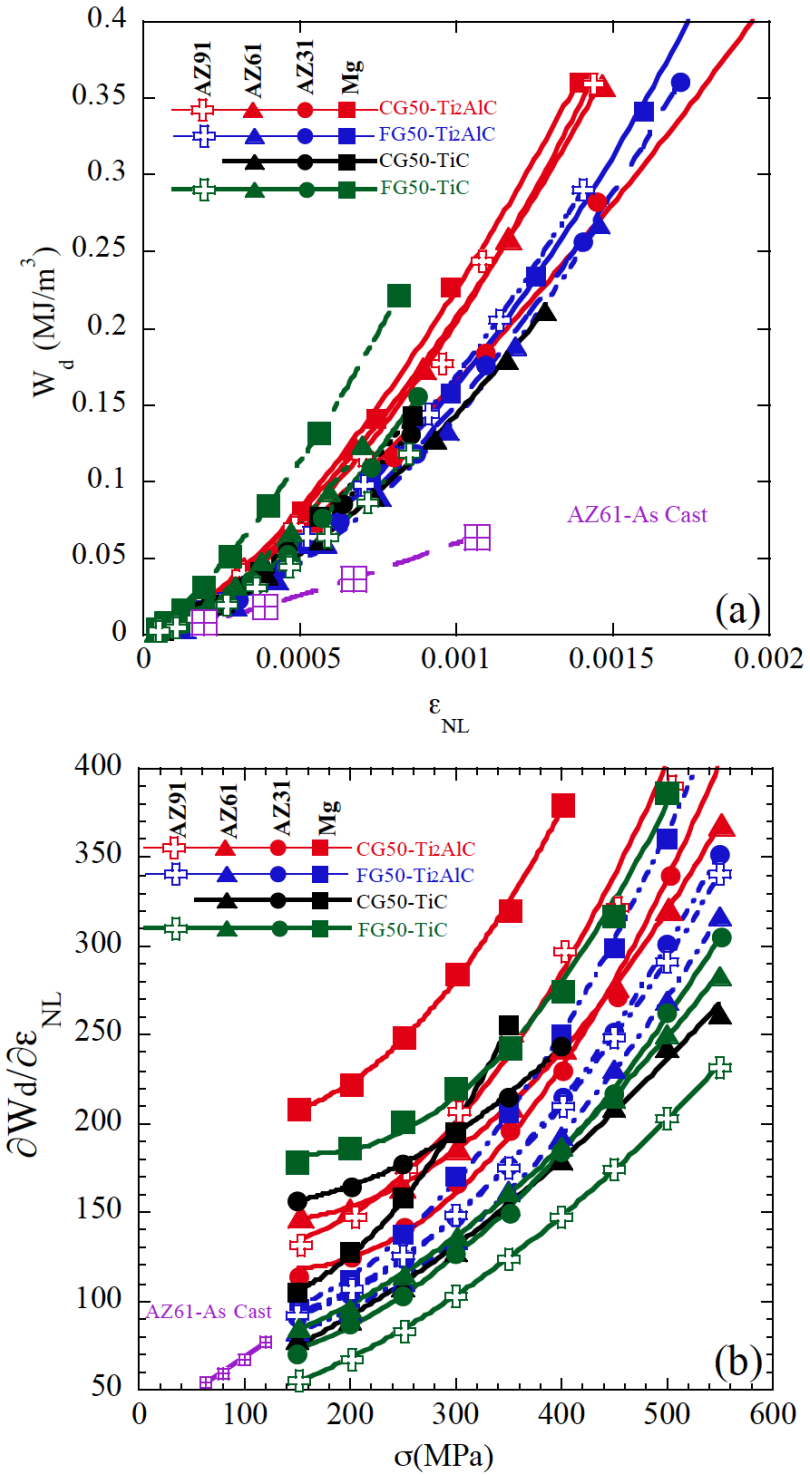

Fig. 6.6. (a) W_d vs, ε_{NL} for all the 50 vol.% reinforced composites and monolithic AZ61; (b) $\frac{\partial W_d}{\partial \varepsilon_{NL}}$ vs. σ.

Figures 6.7(a) and (b) plot the product $W_d E_{f(av)}^3$ vs. σ^3 and W_d versus ε_{tot}^3 for all 50 vol.% composites tested herein. The latter is the sum of the ε_{LE} and ε_{NL} (Fig. 6.1). All the data calculated and presented in Figs. 6.3 to 6.7 are all based on the loops shown in Fig. 6.2.

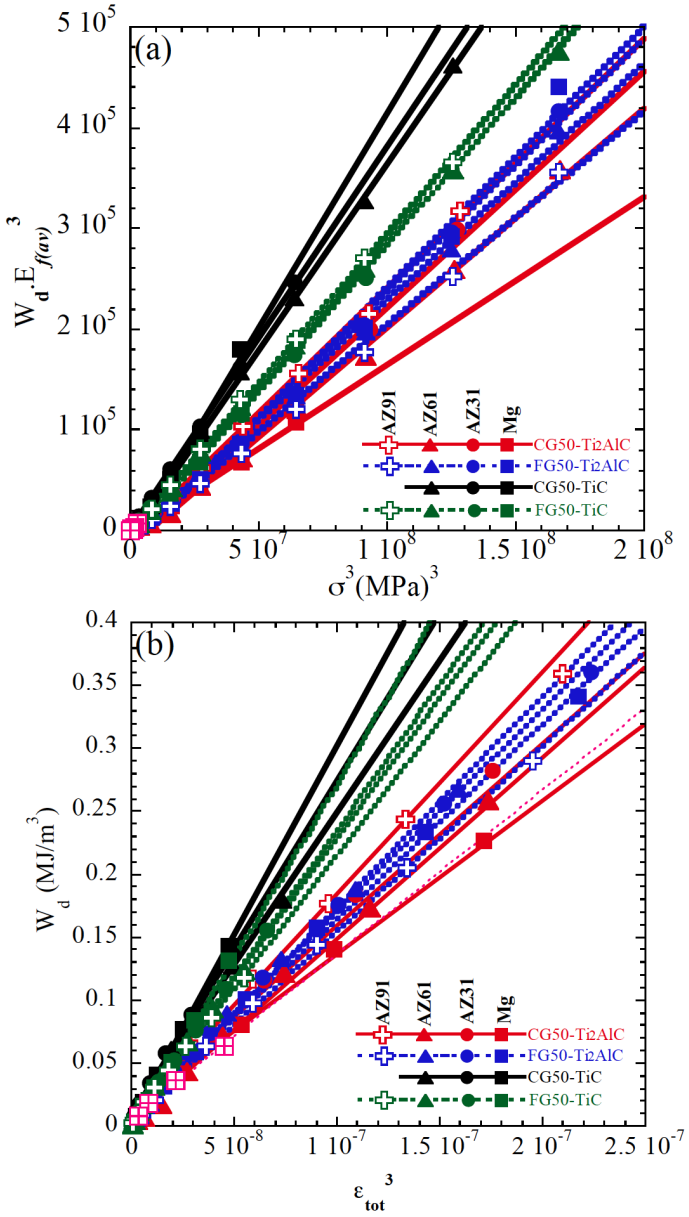

Fig. 6.7. (a) $W_d E_{f(av)}^3$ vs. σ^3, (b) W_d vs. ε_{tot}^3.

In order to achieve a better understanding of the damping properties of these composites, W_d/U_{tot} is plotted vs. applied stress for each cycle in Fig. 6.8. U_{tot} is the total energy applied on the composite and W_d is the dissipated portion of the U_{tot}, both are shown in Fig. 6.1.

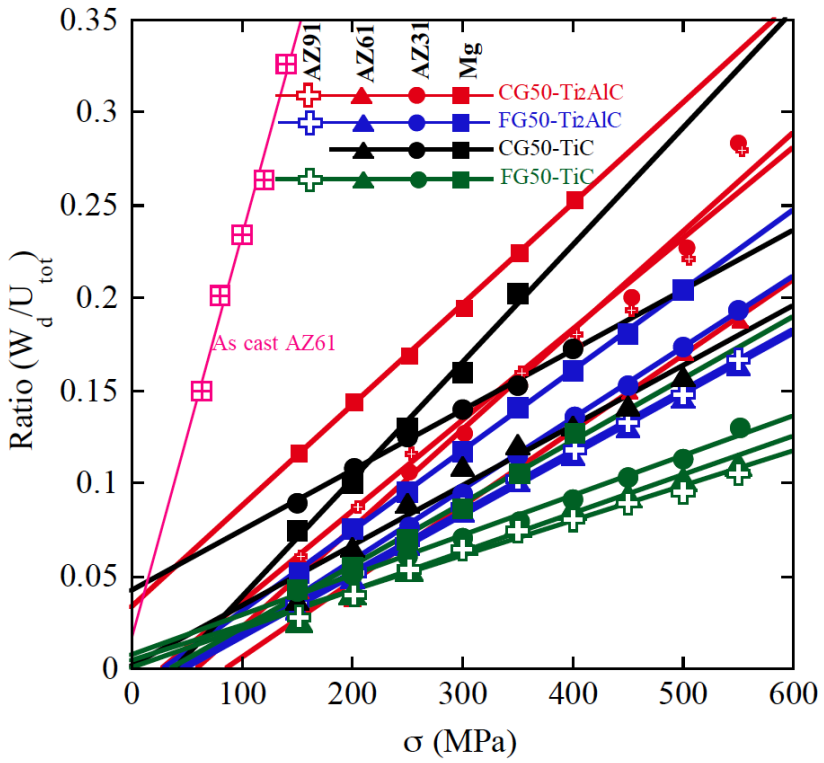

Fig. 6.8. Plot of W_d/U_{tot} ratio vs. applied stress.

6.2.3. 100 cycles of loading to a high stress

Figure 6.9(a) shows 100 cycles of compression loading to 500 MPa for the CG50-Ti_2AlC-AZ61 and CG50-TiC-AZ61 samples and to 350 MPa for CG50-Ti_2AlC-Mg and CG50-TiC-Mg samples. Note that the stress-strain loops for the latter are shifted

horizontally for clarity. The 2nd and 100th cycles of each sample are superimposed over each other and compared in Figs. 6.9(b) and (c).

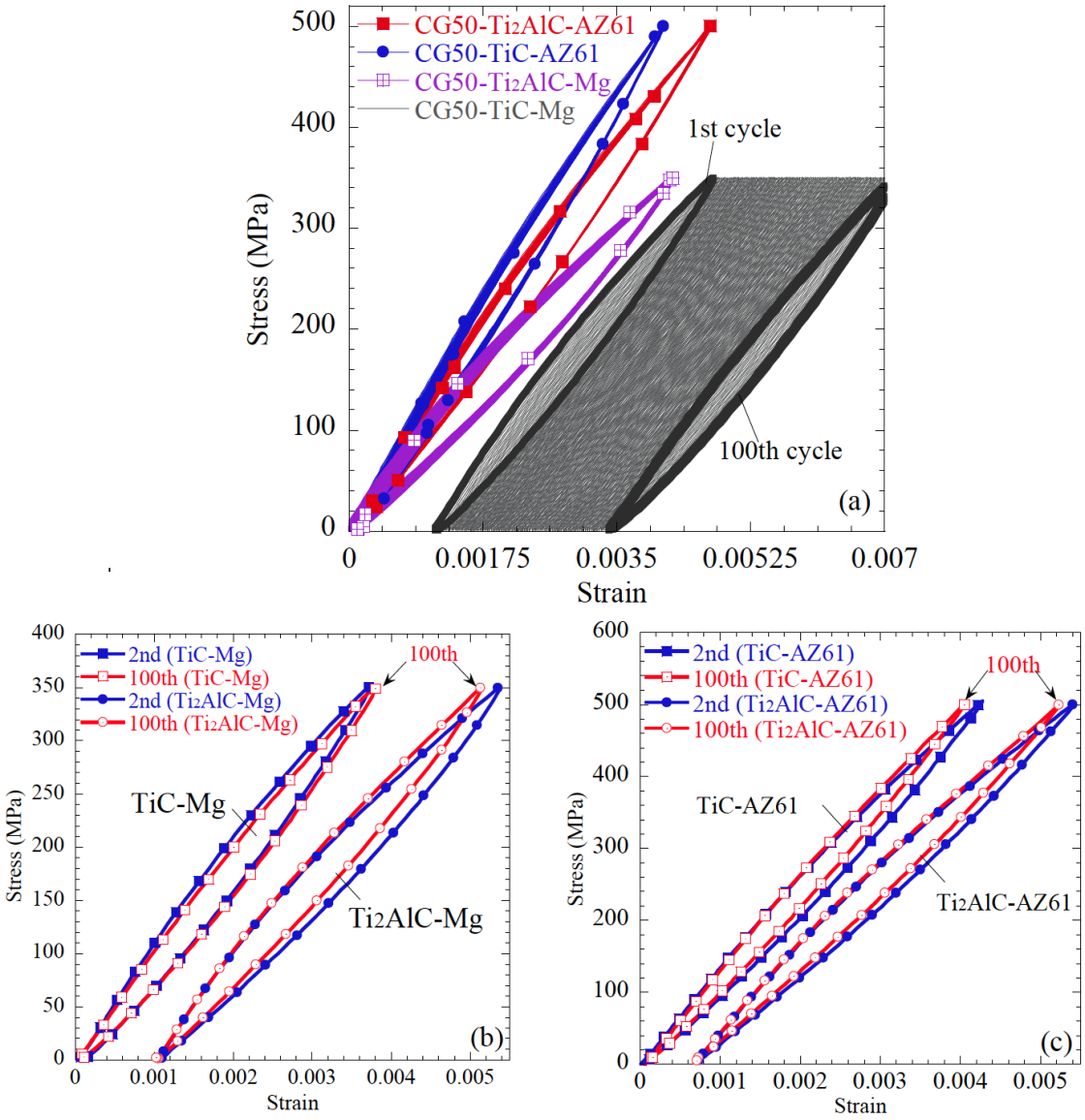

Fig. 6.9. (a) Stress-strain curves for 100 cycles of compression at a constant stress for CG50-Ti_2AlC-Mg, CG50-Ti_2AlC-AZ61, CG50-TiC-Mg and CG50-TiC-AZ61 composites. All 100 cycles for each test are shown. The CG50-TiC-Mg curves are shifted horizontally for clarity. The 2nd and 100th cycles of each test are compared for: (b) CG50-Ti_2AlC-Mg and CG50-TiC-Mg, (c) CG50-Ti_2AlC-AZ61 and CG50-TiC-AZ61 composites.

6.3. Discussion

The most important achievement of this study is the fabrication of high strength Ti_2AlC-Mg alloy composites that can dissipate up to 25% of the applied mechanical energy at stresses of the order of ≥ 400 MPa (Fig. 6.8). As discussed below, this result is mostly due to the capability of Ti_2AlC to dissipate energy at higher stresses. In the TiC composites, despite their high strengths, damping was reduced compared to the pure Mg and Ti_2AlC-Mg composites. It is important to note that the 50-Ti_2AlC-Mg composites reported herein dissipate almost twice as much energy as Mg-SiC [62] and Mg-TiC composites, with comparable mechanical and elastic properties.

Given the many variables explored herein, the effects of matrix composition, reinforcement type, reinforcement size, and reinforcement volume fraction on properties, in general, and damping in particular are discussed separately below.

6.3.1. Effect of matrix composition on damping

In general, for all four composite series, changing the matrix from pure Mg to the Mg alloys, significantly reduced W_d. This is the best seen by comparing the results - with the same color - in Figs. 6.3(a) and (c). As discussed in chapter 5, the addition of Al to the Mg matrices improved the matrix/reinforcement interfacial strengths. The results shown in Figs. 6.3(a) and (c), confirm this conclusion since stronger interfaces should yield less damping which in turn reduces W_d. The weak interface led to the highest damping for the pure Mg matrix composites. The fact that changing the matrix from either AZ31 or AZ91 to AZ61 reduces W_d, suggests that the latter form the strongest interfaces.

6.3.2. Effect of reinforcement type on damping

Given that the FG50-Ti_2AlC and FG50-TiC composites have almost the same reinforcement particle sizes, the differences between their W_d values (compare dotted lines in Figs. 6.3(a) to those in Fig. 6.3(c)) can be ascribed to the fact that Ti_2AlC itself is a high damping solid [45, 46], while TiC is not. Before making that argument, however, the following alternate ideas for the differences have to be considered:

i) Differences in dislocation densities. In theory one possible way to increase the damping capacity of a material is to increase its dislocation density [50]. However, since the CTEs of Ti_2AlC and TiC are comparable it is difficult to argue that one reinforcement results in significantly more dislocations than the other.

ii) Differences in matrix/reinforcement interfaces. In the previous chapter it was argued that the Mg/Ti_2AlC interfaces were stronger than their Mg/TiC counterparts. If that were the case, then the former composites would have been expected to dissipate less energy than the latter, which is not the case (compare W_d values in Fig. 6.3(a) with those in Fig. 6.3(b)). It follows that, here again, interfaces cannot be responsible for the differences.

The most likely explanation for the damping differences has thus be the inherent damping capacity of Ti_2AlC. As discussed previously Ti_2AlC can dissipate energy during cyclic loading [78, 109]. However, for Ti_2AlC to dissipate energy a threshold stress, σ_t, that depends on its grain size, among other factors, has to be exceeded. For example, Zhou et al. reported σ_t for bulk Ti_2AlC, with 2α of 14±7 μm, to be 180 MPa [45]. Amini et al. reported a σ_t of 226 MPa for fine-grained (2α = 5±3 μm) polycrystalline samples [62].

Based on these considerations, it follows that below the σ_t of Ti_2AlC, only the Mg-matrices should be contributing to W_d. Said otherwise, the differences in W_d values between the two families of composites should be more evident at higher applied stresses, as observed (Fig. 6.3). The W_d values of the Ti_2AlC and TiC composites are significantly different only at stresses > 200 MPa. For example, at 550 MPa, W_d of the FG50-Ti_2AlC-AZ61 composite (0.27 MJ/m^3), is about 55% higher than that of its FG50-TiC counterpart. At stresses below 200 MPa, the W_d values in the both families of composites are comparable (Fig. 6.4). As discussed in the next section, this effect is better observed when the reinforcement volume fraction, v_r, is low.

Another possible reason is that at 440 GPa, the Young's modulus of TiC is ≈ 37 % higher than that of Ti_2AlC. When the interfaces are strong, stiffer reinforcement, bear more of the stress, which reduces the stresses on the Mg matrices, which in turn, can reduce W_d.

6.3.3. Effect of reinforcement particle size on damping

In general, the presence of finer reinforcing particles can affect W_d in three major ways.

i) Effect of Ti_2AlC particle size: The W_d values for FG50-Ti_2AlC composites are lower than those of their coarse-grained (CG50) counterparts (compare solid to dotted lines in Fig. 6.3(a)).

Like Mg, the damping of Ti_2AlC is also strongly grain size dependent. For example, Zhou et al. reported W_d of monolithic Ti_2AlC with 2α (average grain thickness) of 14±7μm at 336 MPa to be 0.085 MJ/m^3 [45, 78]. However, at 0.0166 MJ/m^3, the W_d

of a fine-grained Ti_2AlC ($2\alpha = 5 \pm 3 \mu m$), at the same stress level, was reported to be 80 % lower [62]. This significant reduction can explain the smaller W_d values for the FG50-Ti_2AlC composites compared to the CG50-Ti_2AlC ones.

ii) Effect of matrix/reinforcement interfacial area. If interfacial slip is a significant contributor to damping then using finer reinforcing particles should result in an *increase* in W_d. The fact that the opposite is true is thus quite significant because it reveals that the damping sources are more within the grains than at their interfaces or grain boundaries. Said otherwise the contribution of interfacial friction to W_d, if present, must be smaller than the friction due to dislocation motion within the grains.

iii) Matrix grain size: Like the Ti_2AlC reinforcing particles, reducing the Mg grain size, should reduce matrix damping. Based on this statement, one would expect the highest damping to occur in the CG50-TiC composites, in which the average diameter of the TiC particles is 4.7 μm. However, the W_d values of the latter are comparable to the FG-Ti_2AlC composites, wherein, at 0.5 μm, the average Ti_2AlC particle size is significantly finer (compare results for CG50-TiC in Fig. 6.3(c) to FG-Ti_2AlC composites in Fig. 6.3(a)). To understand why the W_d values for the FG-Ti_2AlC composites are higher than the CG50-TiC composites, one has to again invoke the idea that the Ti_2AlC particles themselves are contributing to the damping.

6.3.4. Effect of reinforcement volume fraction

Figure 6.4 plots the W_d values for the TiC and Ti_2AlC composites as a function of v_r and matrix composition. From these results, it is clear that: i) the W_d values for $v_r = 5\%$

are higher than those for v_r = 20 % and significantly higher than those with v_r = 50 %; ii) Up to ≈ 200 MPa, and for all samples, the type of reinforcement type has little effect on W_d (Fig. 6.4). From these observations it is reasonable to conclude that at stresses of 200 MPa or lower, only the matrices are contributing to W_d. Given that the σ_t values for polycrystalline Ti_2AlC samples - whose grains were larger than the reinforcement particles used herein – were > 200 MPa, this conclusion is not too surprising [45, 62].

We note in passing, that had the un-reinforced AZ61 matrix not yielded at ≈ 220 MPa, it would have possessed the highest W_d values. Some may argue that one should simply use un-reinforced Mg for damping, since clearly the reinforcements reduce W_d. And while such an argument would be perfectly valid if a part were only subjected to low stresses, it does not hold at higher stresses.

It has been suggested that the rule of mixtures can be used to estimate the damping capacity of composites from a knowledge of the damping capacities and respective volume fractions of their individual components [53]. Such an approach cannot be used here, however, because of the strong grain size dependency of W_d in Mg and the fact that we do not know the exact grain size of Mg in the matrices. The effect of grain size is best seen in Fig. 6.4, where it is obvious that W_d of the pure Mg composite reinforced with 5 vol.% Ti_2AlC particles, is considerably lower than that of the un-reinforced AZ61. Following the rule of mixture, the addition of 5 vol.% reinforcements should not reduce the W_d by 40% as compared to pure AZ61. This can be only explained by the presence of smaller Mg grains in the composite. Furthermore, in Fig. 6.4(a), the W_d values of AZ61 and Ti_2AlC are shown, which following the rule of mixture would clearly overestimate the W_d values for the Ti_2AlC-AZ61 composite.

Based on all these considerations one can conclude that at stresses > 200 MPa, at least some of the energy dissipated in those composites is due to energy dissipation in the Ti_2AlC reinforcing particles and that the grain size of the Mg matrix also has an important effect on W_d.

6.3.5. Effect of Ti_2AlC texture

When W_d values of the random and oriented CG-Ti_2AlC-AZ61 are compared (Fig. 6.5(a)), no discernable difference was observed between the parallel, normal and random orientations of the reinforcement in the AZ61 matrix. However, in previous work, the highest W_d values were reported when the Ti_2AlC flake-like particles were aligned parallel to the loading direction (50-Ti_2AlC(P)-Mg) and W_d values in 50-Ti_2AlC(N)-Mg and 50-Ti_2AlC(R)-Mg composites were comparable (Fig. 6.5(a)) and both lower. This was explained by assuming: i) all the energy dissipation occurred in the Ti_2AlC phase, ii) Ti_2AlC dissipates energy due to the IKBs formation and annihilation upon loading and unloading and, iii) kinking is a form of buckling, which would be maximized when the basal planes are loaded parallel to the loading direction [62]. This conclusion was also made based on the idea that the Mg matrix was at the nano scale and only acted as a load transfer medium and did not contribute to W_d. The results of this study, however, reveal that not all the Mg is at nano scale and some of it does indeed contribute to W_d. Furthermore, the highest W_d values for 50-Ti_2AlC(P)-Mg composite reported previously are in contrast to the behavior of monolithic oriented Ti_2AlC in the same study. In the monolithic oriented Ti_2AlC, a sample in which grains are mostly oriented normal to the loading direction “N” dissipated more energy than one with grains

oriented along the loading direction "P" [110]. Careful examination of the stress-strain loops reported previously reveals that, in fact, the loops in 50-Ti_2AlC(P)-Mg for the 2 highest stresses are not closed (i.e. they were open) and also the loops' shape show that the sample was not perfectly aligned (See Fig. 6(b) in [62]). This might be the reason for the discrepancy.

It is important to note here that the W_d values obtained from the stress-strain loops is highly dependent on the latter's shape. From all the stress-strain curves have been acquired from macroscale cyclic compression tests over the past 10 years, it is reasonable to conclude that an accurate cyclic compression test should result in *symmetrical* stress-strain loops, similar to those shown in Fig. 6.1. If the loops are not symmetrical, it is reasonable to assume that the samples were not aligned properly or other problems exist.

To further understand if the results of this study are comparable with those previously reported, the W_d's of the CG- and FG-Ti_2AlC-Mg composites from this study are compared with those previously reported for MI-50-Ti_2AlC-Mg and HP-50-Ti_2AlC-Mg in Fig. 6.5(b). The best comparison is between the CG50- and MI50- composites, since both were fabricated using the same processing method and have almost the same reinforcement size. Both composites have comparable W_d values, which shows consistency between this and previous work. For the HPed composite in the previous work, the powder mixture was ball milled for 12 h in air, which in principal could have lead to smaller Ti_2AlC particles and also some oxidation of the Mg powders. Both of which could lead to smaller grain sizes in the composites. This might be the reason that W_d values of FG50- and HP50-Ti_2AlC are comparable (Fig. 6.5(b)).

6.4. Correlations between parameters

Over the entire stress level, W_d scales with σ^3 with correlation coefficients, R^2 of ≥ 0.99 (Figs. 6.3(a) and (c)), which is in agreement with what was concluded in chapter 3. According to Eq. 3.6 ε_{NL} should be proportional to σ^2 as observed in Figs. 6.3(b) and (d). In these composites there can be a source of damping other than Ti_2AlC and Mg matrices, which is matrix/reinforcement interface sliding. Interestingly, if the latter is a source of damping, it does not change the W_d and ε_{NL} correlations with stress in these composites. This observation is important in the sense that energy dissipation due to sliding of the microcrack surfaces might also has the same correlation with stress. In other words, W_d and ε_{NL} correlations with σ^3 and σ^2 would not lead to any conclusion about the source of damping and careful characterization is needed for this purpose.

In addition, following what was explained in the chapter 3, no linear correlation between W_d and ε_{NL} was observed (Fig. 6.6(a)).

Calculating $\frac{\partial W_d}{\partial \varepsilon_{NL}}$ and plotting it versus σ leads to a nonlinear curve with an increasing trend as shown in Fig. 6.6(b). Based on Eq. 3.16 and if damping is only due to the dislocation motion, $\frac{\partial W_d}{\partial \varepsilon_{NL}}$ should be proprtional to Ω/b and if Ω is proportional to stress, the resulting curve would be linear. This is clearly not the case for these composites, in which damping can be due to multiple sources. In other words, based on how $\frac{\partial W_d}{\partial \varepsilon_{NL}}$ changes with σ, if there is *not* a linear correlation between these two parameters, it is possible to conclude that damping is not only due to the dislocation motion. More study is needed to confirm this speculation.

Considering the scatter in W_d values for each family of composites shown in Figs. 6.3(a) and (c), if one multiplies the W_d values of each composite by $E_{f(av)}^3$, the results are interesting and each family of composites falls almost into one line as shown in Fig. 6.7(a). The reason for this observation is not clear at this time. It can be explained by the fact that multiplying $E_{f(av)}$ cubed into W_d, somehow compensates for any damping due to the differences in E and brings together all the W_d values for a family of composites.

If we divide both axis in Fig. 6.7(a) by $E_{f(av)}$ cubed, we can plot W_d versus $\left(\frac{\sigma}{E_{f(av)}}\right)^3$, in which the latter is almost the same as ε_{tot}^3. The accurate ε_{tot} for each loop can be calculated by dividing σ by E_f -not $E_{f(av)}$ - of each loop. To test this idea, W_d is plotted versus measured ε_{tot}^3 in Fig. 6.7(b) and although the results of each family of composites are not exactly overlaying each other as Fig. 6.7(a), they still lay in narrow strips. The reason for this observation is not clear at this moment; more work in needed to understand these results.

6.5. 100 cycles of loading to a high stress

Kontsos et al. reported on the fatigue behavior of Ti_2AlC-Mg composites in tension [42]. To further investigate the sources of energy dissipation and to test the interfacial strengths, select composite samples were cyclically loaded 100 times in compression. The results for the CG50-Ti_2AlC-Mg, CG50-Ti_2AlC-AZ61, CG50-TiC-Mg and CG50-TiC-AZ61 are compared in Fig. 6.9(a). With the notable exception of the CG50-Mg-TiC composite samples (both particle sizes), for all other composites, the 100 cycle stress-strain loops appeared to overlay each other with high fidelity (Fig. 6.9(a)). As shown in Figs. 6.9(b) and (c), not only was there no degradation in properties, but *cyclic*

hardening was observed in the following composites: CG50-Ti_2AlC-Mg, CG50-Ti_2AlC-AZ61 and CG50-TiC-AZ61. Based on these results it is reasonable to rule out microcracking as the main source of energy dissipation. These results provide further compelling evidence that the interfaces in these composites are relatively strong. It is worth noting in this context that the stresses to which most of these composites were loaded were of the order of ≈ 70 % of their UCS. In other words, the cycling stresses were relatively high.

In the previous chapter, it was argued that because - in the case of the CG50-Mg-TiC composites - neither matrix nor reinforcement contained Al, the interfaces were relatively weak. This conclusion is indirectly confirmed by the response of this composite composition to cyclic loading. In contrast to all Al-containing compositions, a slow accumulation of strain with each cycle was observed (see loops labeled TiC-Mg in Fig. 6.9(a)). The FG50-TiC-Mg, despite its higher strength and elastic modulus, also deformed continuously during the same 100 cycles. Together with the slow deformation, cyclic softening (Fig. 6.9(b)), was observed indicating that the Mg-TiC composite, in sharp contrast to all others, are susceptible to fatigue, presumably due the presence of weak interfaces.

Lastly in this section we note that bulk monolithic MAX phases do not show much cyclic work hardening at least up to 100 cycles [44, 78]. However, cyclic hardening in Mg and its alloys is well known [111, 112]. As a result, it is reasonable to ascribe the cyclic hardening observed in the composites (Figs. 6.9(b) and (c)) to the Mg matrices.

Finally, it is important to discuss the results obtained here from a design aspect, which depends on the application and stress levels. If high damping capacity is desired

and the design stresses are low, then pure Mg matrices can be used, provided they do not work harden and/or fatigue. For higher stresses, AZ61 matrices can be used. Using Ti_2AlC as the reinforcement increases the damping capacity regardless of the matrix. Figure 6.10 illustrates the log-log relationship between damping (loss coefficient) and Young's moduli of different solids (Ashby map [113]). Noteworthy, the composite fabricated herein, are located out of the composite envelope in the Ashby map.

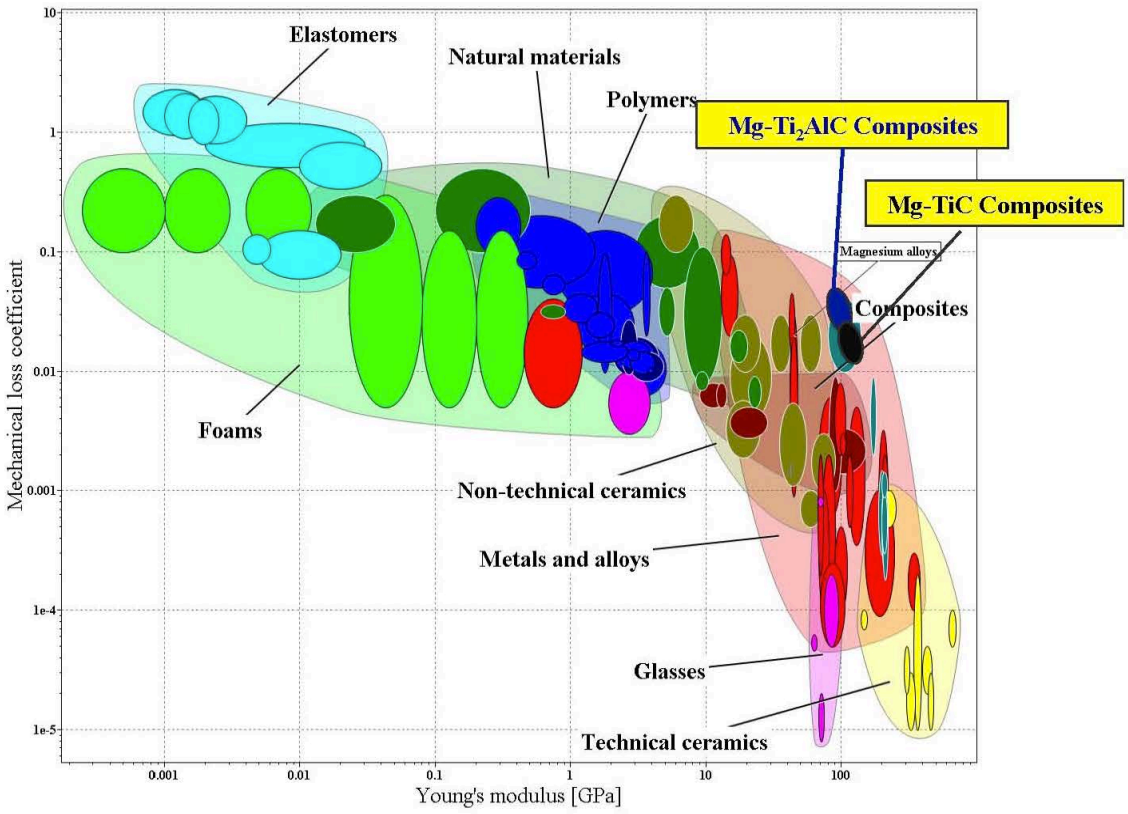

Fig. 6.10. Ashby map showing the log-log relationship between damping and Young's moduli of solids. The Ti_2AlC-Mg and TiC-Mg families of composites are shown in this map. Mechanical loss coefficient is calculated as $W_d/2\pi U_{tot}$ [113].

Chapter 7: Other Work

This chapter explores some of the effects of processing variables on these composites. All of these experiments can be the beginning of a new set of experiments, future work, that could be carried out to fully understand them.

7.1. Effect of infiltration soaking time

7.1.1. Effect of infiltration time on mechanical properties

Infiltration soaking time is the time that the temperature is held at its maximum (e.g. 750ºC for Ti_2AlC preforms). Increasing the MI time increases the time that the molten Mg alloy is in contact with the reinforcement. This, in principal, can reduce the wetting angle and also enhance chemical reactions (if any) occurring at the matrix/reinforcement interfaces. In order to investigate this effect, a CG50-Ti_2AlC-AZ61 composite, following the same processing parameters for MI, was fabricated by holding for 8 h at 750 ºC instead of 1 h. This sample will be referred to as CG50-Ti_2AlC-AZ61-8h.

The E*, $E_{f(av)}$, 0.2 % YS and UCS and V_H of this composite are compared with CG50-Ti_2AlC-AZ61 with 1 h of MI in Table 7.1. All the measured mechanical properties are almost identical; only the YS is enhanced by increasing the MI time. One interpretation is that a stronger interface forms. However, this interpretation is not correct since the other mechanical properties such as E* and $E_{f(av)}$, do not change. Given that the change in YS is small, it could simply reflect statistical variations from sample to sample.

Based on these preliminary results, it thus can be concluded that increasing the soaking time from 1 h to 8 h, does not affect the mechanical properties of Ti_2AlC reinforced composites.

This comment notwithstanding, more work is needed to confirm this conclusion. We note in passing that the fact that the mechanical properties do not vary by increasing the soaking time is in agreement with what Conteras *et al.* reported on the effect of holding time of molten Mg in contact with TiC at temperatures between 800ºC to 850ºC [26]. They reported the contact angle is reduced by increasing the holding time up to ≈ 40 to 50 min beyond which the contact angle remains constant.

Table 7.1. Effect of MI soaking time on mechanical properties. E*, $E_{f(av)}$, 0.2% YS and UCS of two CG50-Ti_2AlC-AZ61 composites, which one was held at MI temperature (750ºC) for 1 h and the other for 8 h.

Material	E^* (GPa)	$E_{f(av)}$ (GPa)	0.2%YS (MPa)	UCS (MPa)	V_H (GPa)
CG50-Ti_2AlC-AZ61-1h	112(3)	100(8)	331(6)	719(7)	2.0(1)
CG50-Ti_2AlC-AZ61-8h	112(3)	101(8)	365(5)	716(9)	2.1(1)

7.1.2. Solution of A-group element in Mg

As discussed in chapter 2, the Mg depressions in T_m and T_s reported previously in 50-Ti_2AlC-Mg composites [47] can be ascribed to the solubility of Al in the Mg matrix. The only possible way to explain the presence of Al in the matrix of Ti_2AlC-Mg composite is to assume that Al in the Ti_2AlC comes out and dissolves in the Mg matrix. Consequently, it was assumed that holding Ti_2AlC for longer times in molten Mg would

result in more Al in solution in Mg. To test this idea, Ti_2AlC powders were placed between two Mg chunks and heated for 170 h at 750 °C.

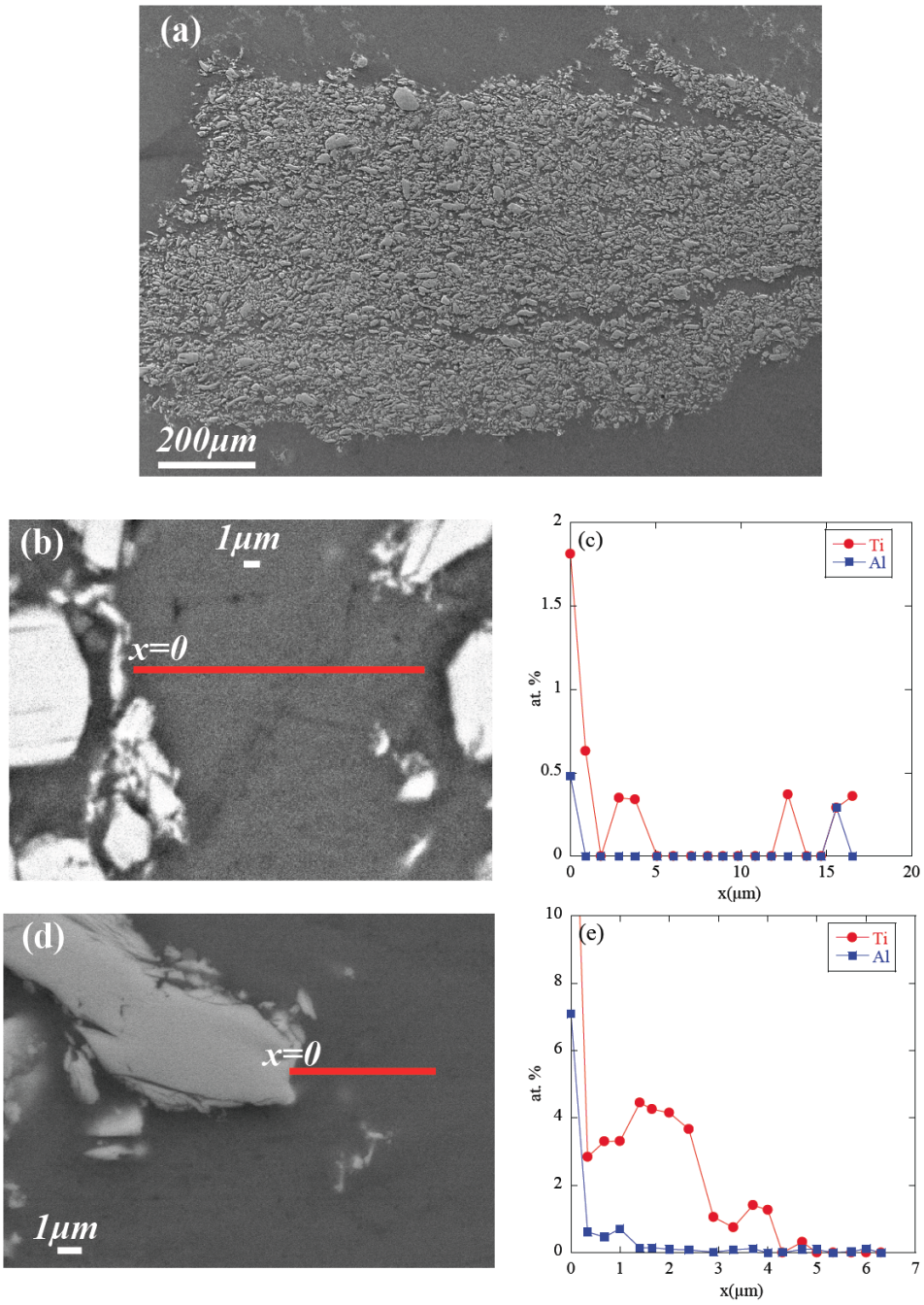

Fig. 7.1. (a) SEM image of Ti_2AlC powder soaked in Mg at 750 ºC for 170 h, (b) and (d) are the same as (a) at higher magnification, (c) and (e) EDS point scans for Al and Ti on the red lines in (b) and (d), respectively.

SEM and EDS was conducted on a polished cross section of this sample. Figure 7.1(a) shows that the Mg matrix infiltrated the Ti_2AlC powder bed. The purpose of this experiment was to allow the Al to diffuse out of the Ti_2AlC and be detected, especially in the Mg matrix between two Ti_2AlC particles or at least very close to the interface. For the sake of precision, instead of a regular EDS line scan several EDS point scans, with 1 minute scanning time, were performed on a line starting at the Mg-Ti_2AlC interface and going into the Mg matrix. Two such scans are shown in Fig. 7.1 as red lines on the SEM images. The EDS result on the closest point to Ti_2AlC in Fig. 7.1(c) (at x=0) shows 0.5 at.%, which becomes negligible afterwards. However, since Ti also was detected at this point, the simultaneous presence of Al and Ti suggests that the signal is coming from a Ti_2AlC particle close to the scanning point. The same is true for Fig. 7.1(e); in fact, the detected Ti concentration is significantly higher than Al at very point. The fact that no Al was detected on the points that Ti does not exist, reveals that Al by itself do not exist in the Mg matrix, or at least it is below the detectability of our EDS. This result is quite baffling indeed since: i) according to the Mg-Al phase diagram (Fig. 2.3(b)) Al is certainly soluble in Mg at that temperature and, ii) Al is known to easily diffuse out of the Ti_2AlC phase in molten metals, molten salts [114] and even at room temperature in HF [88]. At this time the only plausible explanation is that Mg replaces the Al in the basal planes and somehow prevents further out diffusion of the Al. This comment notwithstanding, this remains a mystery. A TEM study on Ti_2AlC grains close to the matrix might shed light on this mystery.

7.2. Effect of infiltration temperature

In order to investigate the effect of the MI temperature, a CG50-Ti_2AlC-AZ61 composite sample was fabricated via MI at 850 ºC for 1 h, which will be referred to as CG50-Ti_2AlC-AZ61-850. Table 7.2 compares the mechanical properties of the latter with the same composite which was fabricated at 750 ºC. At 663±7 MPa the UCS of the composite which was fabricated at 850 ºC was ≈ 8 % lower than that of the one MI at 750 ºC. Increasing the MI also reduced E* and $E_{f(av)}$ by almost the same percentage. As a result, it is fair to conclude that increasing the MI from 750 ºC to 850 ºC had a detrimental effect on the mechanical properties. This might be due to the increase of the chance of any reaction between Ti_2AlC and the Mg matrix (specifically the alloying elements). It is worth noting that the mechanical properties are still better than the pure Mg matrix composite fabricated at 750 ºC. More study is needed to further understand the effect of MI temperature.

Table 7.2. Effect of MI temperature on the mechanical properties, E*, $E_{f(av)}$, 0.2% YS and UCS of two CG50-Ti_2AlC-AZ61 composites, one was MI at 750ºC and the other at 850 ºC both for 1 h and CG50-Ti_2AlC-Mg MI at 750 ºC are compared.

Material	E^* (GPa)	$E_{f(av)}$ (GPa)	0.2%YS (MPa)	UCS (MPa)
CG50-Ti_2AlC-Mg	73(2)	67(4)	285(4)	600(10)
CG50-Ti_2AlC-AZ61	112(3)	100(8)	331(6)	719(7)
CG50-Ti_2AlC-AZ61-850	103(4)	90(3)	290(2)	663(7)

7.3. Effect of heat treatment

7.3.1. High temperature annealing

As mentioned in chapter 2, a side goal of this study was to investigate the physics of nc-Mg formation in the 50-Ti_2AlC-Mg composites. As one approach to do it, different high temperature annealing were preformed.

In general Mg microstructures, specifically ones with smaller grain sizes, coarsen upon annealing. Moreover, Mg-Al alloys are susceptible to heat treatment due to the variable solubility of Al in the solid state with temperature. The maximum solubility of Al in solid Mg is ~ 12.9 wt. % at the eutectic temperature of 437 ºC and reduces to ~ 2 wt.% at room temperature (Fig. 2.3(b)).

In order to investigate the effect of annealing, a CG50-Ti_2AlC-AZ61 sample with random and oriented Ti_2AlC particles was annealed at 500 ºC (≈ 84 % of T_m of Mg) for 9 h. After annealing cyclic compression tests were carried out. The first stress-strain cycles of this sample before and after annealing and their stress-strain loops are compared in Figs. 7.2(a) and (b), respectively. The differences between before and after annealing are very negligible and in the error range of our measurement. The same annealing on a 20-Ti_2AlC-Mg sample (inset in Fig. 7.2(a)) also showed no changes in the mechanical properties of these composites.

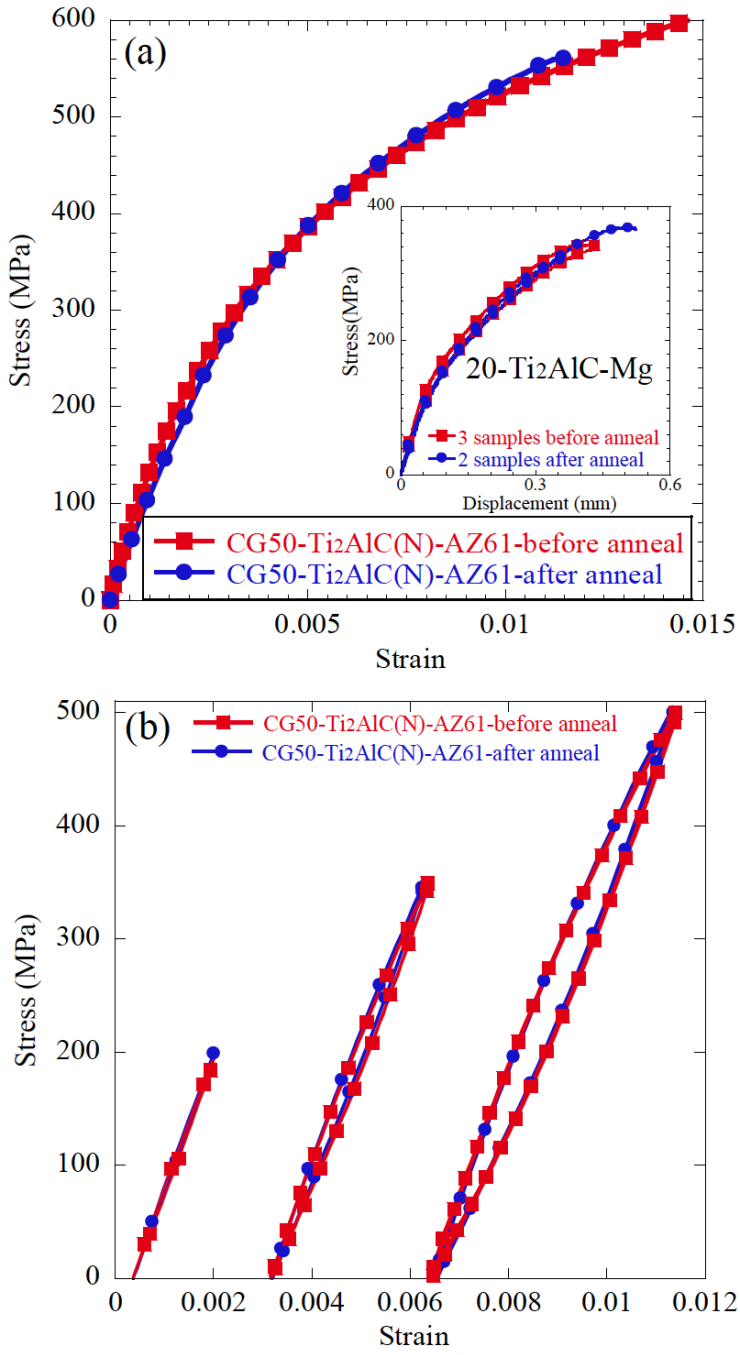

Fig. 7.2. Stress-strain compression curves of a CG50-$Ti_2AlC(N)$-AZ61 sample before and after annealing at 500 ºC for 9 h after (a) first cycle, and, (b) loops at 500 MPa, 300 MPa and 200 MPa. Loops are shifted horizontally for clarity. Inset in (a) shows first compression cycles on a 20-Ti_2AlC-Mg sample before and after annealing.

7.3.2. Aging

After it was understood that matrix composition plays a significant role in mechanical properties of these composites, some heat treatments of the composites were conducted to further understand the strengthening phenomena.

Aging in general, can create more precipitates in the matrix to further improve the strengths as a result of age hardening. In Mg containing Al alloys, age hardening is mostly related to the formation of $Mg_{17}Al_{12}$ precipitates, through a dispersion hardening process [115]. To test this idea a CG50-Ti_2AlC-AZ61 sample was aged at 200 ºC for 15 h and then tested in compression. The stress-strain curves before and after aging are compared in Fig. 7.3. Clearly, strengthening is observed, which can possibly be explained by formation of more $Mg_{17}Al_{12}$ precipitates during aging. This result suggest that at least some of the strengthening observed by increasing the Al content in the Mg matrices is due to the presence of these intermetallics. More study is needed to further understand this phenomenon.

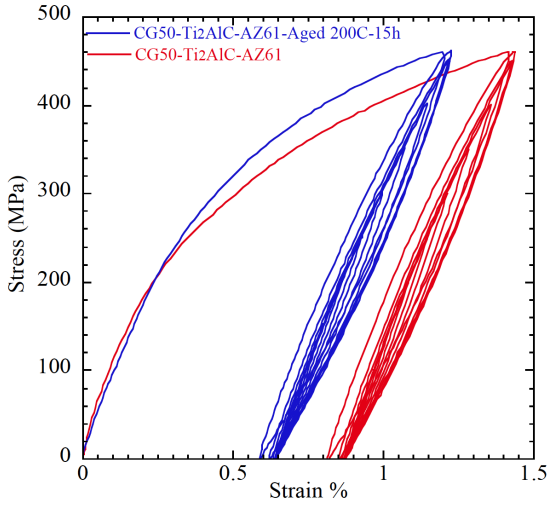

Fig. 7.3. Stress-strain curves of the CG50-Ti_2AlC-AZ61 after MI (red) and after aging at 200 ºC for 15 h (blue).

7.4. Effect of hot extrusion

To examine if it is possible to extrude the 50 vol.% carbide reinforced composites fabricated here and understand its effect on the mechanical properties, a CG50-Ti_2AlC-AZ61 composite was extruded[2], at 400 ºC with 10:1 ratio. This sample (Fig. 7.4) will henceforth referred to as CG50-Ti_2AlC-AZ61-Ex.

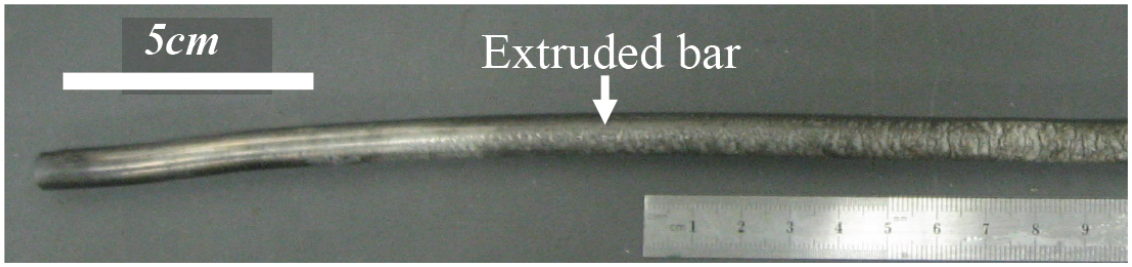

Fig. 7.4. A bar of CG50-Ti_2AlC-AZ61 composite after extrusion at 400 ºC with a 10:1 ratio.

The extruded bar was machined on a lathe to make cylinders for compression tests in the sizes used in chapter 3. The mechanical properties of the CG50-Ti_2AlC-AZ61-Ex are compared with CG50- and FG50-Ti_2AlC-AZ61 composites in Table 7.3. The E*, $E_{f(av)}$ and V_H values of the extruded sample are comparable to those of the FG50-Ti_2AlC-AZ61 sample. At 830±2 MPa, the highest UCS for a Ti_2AlC reinforced composites was measured on the extruded sample. More importantly, at 633±9 MPa the UTS of this sample is the highest value ever reported for a Mg-reinforced composite to our knowledge. The reason for the high UTS can be due to the extrusion that eliminates small pores and voids, which can be formed during MI and possibly also improving the matrix/reinforcement interface strength (Table 7.3).

[2] Hot Extrusion was done in Dr. Lavernia's lab by Dr. Troy Topping, at the University of California, Davis CA.

Cyclic compression loops of the extruded sample are shown in Fig. 7.5(a); its W_d is plotted vs. σ^3 in Fig. 7.5(b) and compared with its non-extruded counterparts. In agreement with what discussed in chapter 6, improving the elastic modulus occurs at the expense of the damping properties. In other word, stiffer composites dissipate less mechanical energy. Furthermore, the W_d of the extruded sample (coarse grained Ti_2AlC extruded composite) is similar to that of the FG50-Ti_2AlC-AZ61 (fine grain Ti_2AlC non-extruded). The reduction in W_d by extrusion can be due to various reasons. One possible explanation is that hot extrusion not only reduced the matrix grain size, but also deformed the Ti_2AlC and consequently reduced the domain size for dislocation motion. However, since AZ61 at 400 ºC is much softer than Ti_2AlC, it is very unlikely that hot extrusion of the CG-Ti_2AlC-AZ61 reduced the Ti_2AlC particle size to that of the FG-Ti_2AlC composite. This implies that it is the matrix that mostly dissipates energy and changing its grain size directly reduces W_d.

In addition, the fact that E* and $E_{f(av)}$ for these two composites are similar further confirms that it is mostly the Mg that is contributing to the plastic deformation, especially at lower stresses. It is important to note here that in both E* and E_f measurements some plastic deformation is believed to occur. The fact that E_f and W_d of these two composites are similar, is also in agreement with what is shown in chapter 6 that energy dissipation in the same family of composites depends on their elastic moduli, and W_d can be normalized by dividing it by $E_{f(av)}$ of each composite (Fig. 6.7).

The extrudability of these composites (at least of the Ti_2AlC reinforced family) with more than 50 vol.% reinforcement particles is important from a fabrication and

design point of view, in that it is possible to extrude these composites into their final shape and at the same time improve their mechanical properties.

For future work, it is worth attempting to extrude FG-50-TiC reinforced composites. If they are extrudable, then the mechanical properties most probably will also be further enhanced. Another possible study is to extrude the 20 vol.% and 5 vol.% reinforced composites, which is a necessary step to enhance their mechanical properties. In composite fabrication via powder metallurgy, a second step (such as extrusion) is almost always used to fabricate the final product.

Table 7.3. E*, $E_{f(av)}$, 0.2% YS and UCS of the CG50-Ti_2AlC-AZ61 before and after extrusion and FG50-Ti_2AlC-AZ61.

Material	E^* (GPa)	$E_{f(av)}$ (GPa)	0.2%YS (MPa)	UCS (MPa)	UTS (MPa)	V_H (GPa)
CG50-Ti_2AlC-AZ61	112(3)	100(8)	331(6)	719(7)	≈ 430(20)	2.0(1)
FG50-Ti_2AlC-AZ61	136(6)	114(4)	426(5)	760(9)	-	2.1(1)
CG50-Ti_2AlC-AZ61-Ex	133(3)	119(3)	490(12)	830(2)	633(9)	2.1(1)

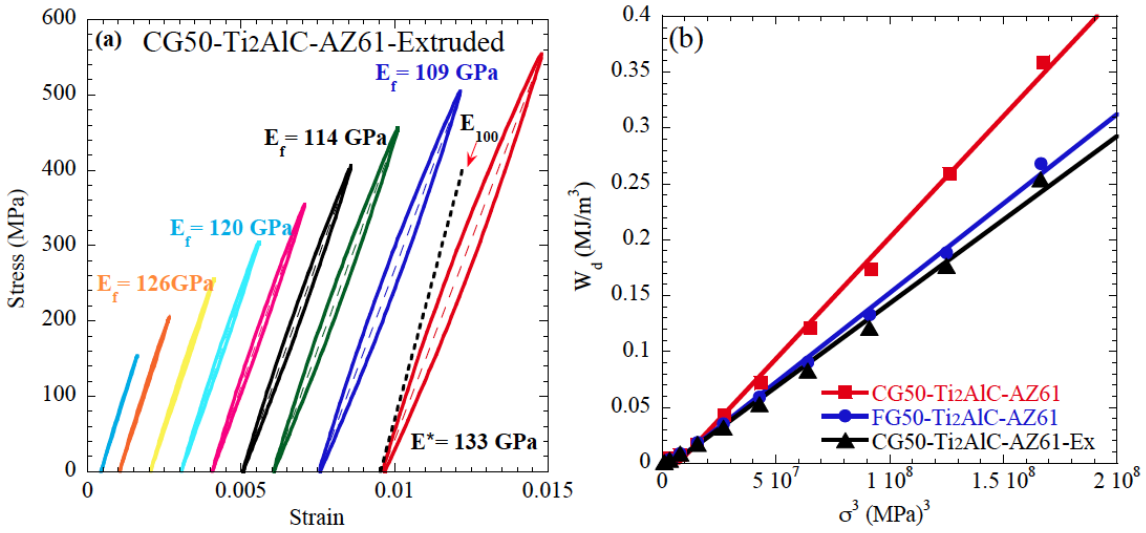

Fig. 7.5. (a) Stress-strain cycles at various stresses for CG50-Ti_2AlC-AZ61-Ex, (loops are shifted horizontally for clarity, (b) W_d vs. σ^3 of CG50-Ti_2AlC-AZ61 before and after extrusion compared with FG50-Ti_2AlC-AZ61.

7.5. Effect of MAX compositions as reinforcement

To further develop this family of composites and in order to investigate what type of MAX phases can be used to reinforce Mg and its alloys, select MAX phases were used as reinforcements and mechanically tested.

7.5.1. Ti_3SiC_2 reinforced Mg alloy composites

Previously, it was reported that using Ti_3SiC_2 as the reinforcement for the unalloyed Mg leads to a composites with low mechanical properties. At 460±10 MPa, the UCS of 50-Ti_3SiC_2-Mg was reported to be lower than that of the Ti_2AlC reinforced composites, which was explained by the lack of the nano-Mg in the matrix when Ti_3SiC_2 was used [62]. However, the results of the current study suggest that the higher strengths are mostly due to the existence of strong matrix/reinforcement interfaces. As a result, it was postulated that if a Mg-Al alloy is used as a matrix, the presence of Al in the Mg matrix could enhance the wetting and improve the interface strength. To examine this idea, an AZ61 alloy was used to fabricate 50-Ti_3SiC_2 composites, following the same MI parameters as for the Ti_2AlC composites. At 770±10 MPa, the UCS of the 50-Ti_3SiC_2-AZ61 was measured to be 40 % higher than that of the 50-Ti_3SiC_2-Mg composite. This finding is in agreement with the conclusions reached in chapter 5 about the effect of Al content on mechanical properties. Similar to the 50-TiC-Mg composite, the lack of Al in both reinforcement and matrix in the 50-Ti_3SiC_2-Mg composite leads to a weak interface. Currently, a complete study is being conducted on the fabrication and mechanical properties of 50-Ti_3SiC_2 reinforced Mg alloys composites.

7.5.2. Cr_2GeC reinforced Mg alloy composites

Based on the findings of chapter 6 that Ti_2AlC contributes to energy dissipation and following Eq. 3.8, it was postulated that using a MAX phase with a low shear modulus could lead to – all else being equal – even higher energy dissipation. At 80 GPa, the shear modulus of the Cr_2GeC is one of the lowest among all the MAX phases measured to date [34].

When a Cr_2GeC porous preform was fabricated and placed in contact with molten Mg for the purpose of MI, an exothermic reaction occurred that consumed the entire preform and the initial shape of the preform was distorted and the volume expanded. The Mg-Ge binary phase diagram is shown in Fig. 7.6. Mg_2Ge intermetallic is a compound that can form as a result of reaction between these two elements and it is reported to be exothermic [116]. The reason why this reaction does not occur for Ti_3SiC_2 is not clear at this moment. One possible explanation can be the formation of a more stable interfacial passivating layer with Si but not with Ge.

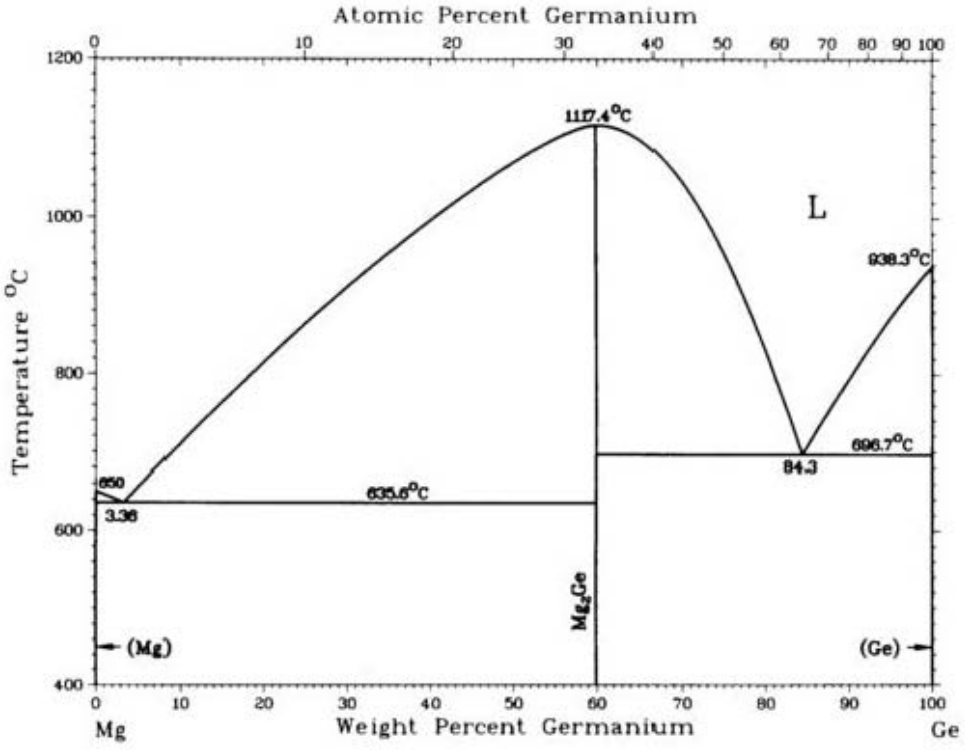

Fig. 7.6. Mg-Ge phase diagram [116].

7.5.3. Cr_2AlC reinforced Mg alloy composites

At ≈ 102 GPa, Cr_2AlC has the lowest shear modulus after Cr_2GeC in the MAX phase family. 50-Cr_2AlC-Mg and 50-Cr_2AlC-AZ61 composites are made via MI at 750 ºC and 850 ºC, respectively. The latter temperature was used for 50-Cr_2AlC-AZ61 because the first MI attempt to fabricate this composite at 750 ºC was not successful and the final sample contained many pores. The 100 ºC increase in the MI temperature, resulted in ≥ 99 % dense samples.

The first two cycles of the stress-strain tests of these two composites are compared in Fig. 7.7(a). Clearly the composite with unalloyed matrix is less ductile. Cyclic compression stress-strain loops to 300 MPa on both composites are compared in Fig. 7.7(b). Clearly, the composite with the unalloyed matrix has higher E* and $E_{f(av)}$

values (Table 7.4) than the AZ61 matrix composite. At 643 ± 20 MPa, the UCS of the 50-Cr_2AlC-Mg, was measured to be 23 % higher than 492 ± 5 MPa for the 50-Cr_2AlC-AZ61 composite. These results are in contrast to all the composites tested herein, in which changing the matrix from pure Mg to Mg alloy enhanced the elastic moduli and strengths. Previous studies showed that monolithic Cr_2AlC is not stiffer than Ti_2AlC [34]. Consequently, the fact that 50-Cr_2AlC-Mg has high E and strengths (comparable to 50-Ti_2AlC-AZ61) might be due to the strong matrix/reinforcement interface.

The lower E and strengths of the 50-Cr_2AlC-AZ61 composites compared to their pure Mg counterpart is noteworthy. It can be explained by the presence of the alloying elements in the matrix. Moreover, the 50-Cr_2AlC-AZ61 composite was fabricated at 850 ºC, which is 100 ºC higher than that of the pure Mg matrix counterpart. Higher processing temperature for Cr_2AlC reinforced composites might cause some reactions at the interface that deteriorates the mechanical properties. Further study is needed to confirm this statement.

Currently, a parallel study is being conducted to study Cr_2AlC reinforced composites with Mg, AZ31, AZ61 and AZ91 Mg alloys matrices. The preliminary results showed that in fact using Mg alloys as the matrices do not enhance the mechanical properties. Furthermore, it is shown that higher temperatures is not needed for AZ-alloys to MI into Cr_2AlC preforms and MI is possible at 750 ºC to fabricate ≥ 99 % dense composites.

Table 7.4. E^*, $E_{f(av)}$ and UCS of the 50-Cr_2AlC- composites with Mg and AZ61 matrices.

Material	E^* (GPa)	$E_{f(av)}$ (GPa)	UCS (MPa)
50-Cr_2AlC-Mg	110(2)	104(5)	643(20)
50-Cr_2AlC-AZ61	99(2)	96(3)	492(5)

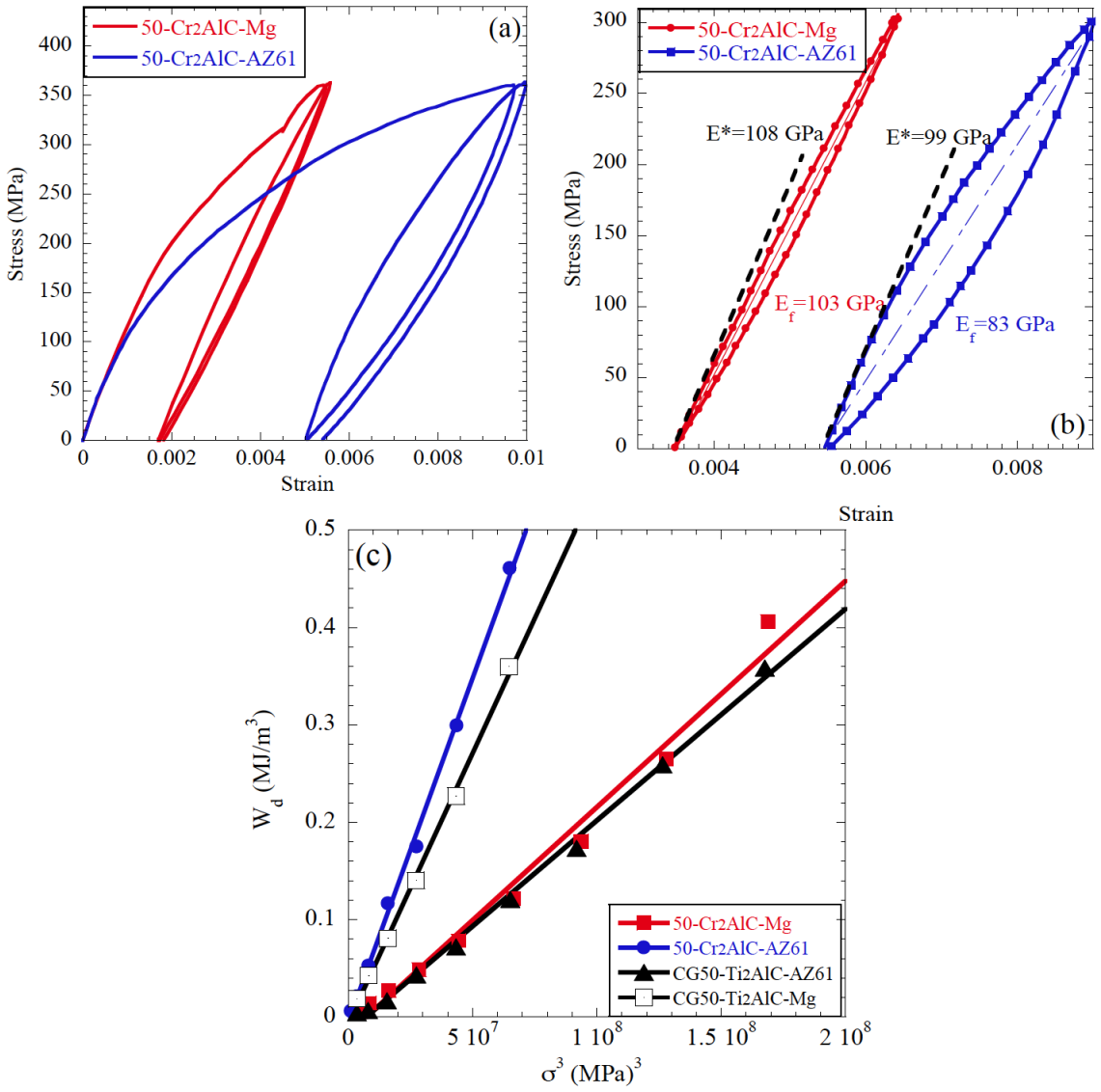

Fig. 7.7. (a) First two stress-strain compression cycles of 50-Cr_2AlC-Mg and 50-Cr_2AlC-AZ61 composites fabricated at 750 ºC and 850 ºC, respectively, (b) stress-strain loop of these two composites are compared at 300 MPa; (c) W_d vs. σ^3 of 50-Cr_2AlC-Mg and AZ61 composites are compared with their CG-$T_{i2}AlC$ counterparts.

When the W_d's of these two composites are compared with their Ti_2AlC counterparts (Fig. 7.7(c)) it is evident that the 50-Cr_2AlC-AZ61 composite dissipates more energy than the 50-Cr_2AlC-Mg composite. This observation is also the opposite of

what was observed for Ti_2AlC and TiC reinforced composites. However, it is consistent with the fact that energy dissipation on each family depends on E.

The energy dissipation of the 50-Cr_2AlC-AZ61 is even higher than that of the CG50-Ti_2AlC-Mg composite, which previously had the highest W_d values among all the composites in this study. It can be explained by the fact that in the former composite weaker interfaces led to higher energy dissipation. Moreover, it can be due to Cr_2AlC lower shear modulus that makes the W_d higher in these composite. More study is needed to further shed light on this observation.

Chapter 8: Summary and Conclusions

Magnesium and Mg-alloy composites, reinforced with 52±2 vol.% Ti_2AlC or 54±2 vol.% TiC, were fabricated using a simple melt infiltration method wherein molten Mg spontaneously flows into carbide porous preforms. The effect of reinforcing three Mg alloys - AZ31, AZ61 and AZ91 – with Ti_2AlC and TiC was explored.

At 1028±5 MPa the UCSs of a fine grain, FG, TiC-AZ61 is the highest UCS ever reported for TiC-Mg composites. The elastic modulus, at 100 MPa stress, and Vickers hardness, V_H, of this composite were measured to be 174±5 GPa and 3.4±0.3 GPa, respectively. In Ti_2AlC reinforced composites, the best mechanical properties were achieved when AZ61 was used as the matrix in FG-Ti_2AlC composites, in which the elastic modulus at 100 MPa stress, UCS and Vickers hardness were reported to be 136±6 GPa, 760±9 MPa and 2.1±1 GPa, respectively.

From the totality of our results we conclude that:

a) The presence of Al in either the matrix or reinforcement – that somehow enhances the matrix/reinforcement interface – is key to endowing these composites with the properties reported. It is speculated that the presence of Al improves the wetting TiC and Ti_2AlC by Mg, which in turn, enhances the mechanical interlocking between matrix and reinforcement. In case of the TiC-Mg composites, the total absence of Al resulted in weak interfaces that were manifested by considerably

lower moduli compared to those predicted from the ROM.

b) When Ti_2AlC is used as the reinforcement, the elastic moduli were closer to the values predicated by the ROM or the Halpin-Tsai model than the TiC composites. This observation was attributed to the formation of better matrix/reinforcement interfaces in the composites reinforced with Ti_2AlC, due to the mechanical interlocking.

c) Reducing the reinforcement particle size in both the Ti_2AlC- and TiC-composites, significantly enhanced the E*, V_H, YS and UCS values. This was attributed to a refinement of the grains in the matrices and to the presence of finer particles in the matrices.

d) The fact that 50-Ti_2AlC-AZ61 and 50-TiC-AZ61 (and 50-TiC-AZ91) composites have the best elastic and mechanical properties in each family, reveal that the optimum Al content is $\geq$ 6 wt.%. The presence of Al is believed to strengthen the matrix and also create a strong matrix/reinforcement interface. This is also consistent with the notion that the matrix grain size and the matrix/reinforcement interface strengths mostly control these properties.

e) The Ti_2AlC reinforced composites can be fabricated at 750 ºC, which is 100 ºC lower than that for TiC reinforced composites. Also, the former are slightly lighter than the latter and can be easily machined to fabricate complex parts. However, since the Ti_2AlC powders are more expensive than the TiC powders, the Ti_2AlC-composites are more expensive.

Fabrication of Mg matrix composites usually reduces its damping properties despite the fact that the elastic and mechanical properties are improved. In this work, it was shown that by using Ti_2AlC, which inherently dissipates energy, it is possible to improve the mechanical properties almost to the same as the TiC reinforced Mg composites and achieve/maintain high damping properties. It was also shown that the damping capacity of Mg-matrix composites depends on:

a) Matrix type; changing the matrix from pure Mg to AZ alloys reduces the energy dissipation which is mostly due to the smaller grain size in the Mg alloy matrices.
b) Reinforcement size; in both family of composites, reducing the reinforcement particle size lowered the energy dissipation, due to a reduction of the Mg matrix grain size. This also indicates that matrix/reinforcement interface has the least contribution in W_d.
c) Reinforcement type is effective only at stresses higher than ≈ 200 MPa. Below that stress both TiC and Ti_2AlC reinforced Mg composites have the same energy dissipation capacity. However, at higher stresses, W_d of Ti_2AlC is almost double of that of TiC reinforced composites. This is ascribed to the inherent damping capacity of Ti_2AlC beyond a threshold stress of ≈ 200 MPa.
d) Reinforcement volume fraction; since Mg has a high damping capacity, in general adding reinforcement ($v_f \geq 5$ vol.%) particles reduce its grain size, which leads to less energy dissipation. Composites with higher vol.% of the reinforcement have lower damping capacities.

Chapter 9: Appendix

This section includes the full text of three other interesting first author papers I have worked on during my PhD studies. The first two papers are on nanoindentation study and understanding the energy damping physics under nanoindentation. Although, these studies are not related to the main focus of my PhD research, they inspired me to rethink about the KNE model and led to developing new ideas on this model.
These papers include:

Nanoindentation study

A1. Reversible Dislocation Motion and Microcracking in Plastically Anisotropic Solids under Cyclic Spherical Nanoindentation (Mat. Res. Soc. Com., 2013)

A2. Spherical Nanoindentation Study of the Deformation Micromechanisms of LiTaO3 Single Crystals (J. Applied Physics, 2011).

Oxidation study

A3. On The Oxidation of Ti2GeC in Air (J. Alloys and Compounds, 2013)

A1. Reversible Dislocation Motion and Microcracking in Plastically Anisotropic Solids under Cyclic Spherical Nanoindentation

Published in: B. Anasori and M. W. Barsoum, MRS Communications, 3, 245-248 (2013). Copyright (2013) Materials Research Society (MRS).

Abstract

Recently, fully reversible dislocation motion was postulated to result in hysteretic nanoindentation load-displacement loops in plastically anisotropic solids. Since microcracking can also result in hysteretic loops, herein we define a new parameter, reversible displacement, *RD,* that can differentiate between the two. For C-plane $LiTaO_3$ surfaces and 5 other plastically anisotropic solids, the *RD* values either increase initially or remain constant with cycling. In contradistinction, for glass and A-plane ZnO, where energy dissipation is presumably due to microcracking and irreversible dislocation pileups, respectively, the *RD* values decreased continually with cycling.

A1.1. Introduction

We recently showed that many plastically anisotropic materials, in which dislocations are confined to 2-dimensions, outline fully and spontaneously reversible hysteretic stress-strain loops upon cyclic loading. We postulated that the micromechanism for this phenomenon is the formation and annihilation of multiple, co-axial parallel dislocation loops, whose shape guarantees that they only remain open when a load is applied; unloading results in their shrinkage and/or their annihilation [44, 66, 76, 78]. Over the past half dozen years we have shown that a large number of seemingly unrelated solids such as C-plane ZnO [79], $BaTiO_3$ [80], sapphire [81], $LiNbO_3$ [82], $LiTaO_3$ [83], Mg, Co, Ti, Zn [55, 57], graphite [75], mica [76, 84] and the MAX phases [78], among others trace fully reversible hysteretic stress-strain loops upon cyclic loading.

Working mostly with single crystals, we showed that when one of the aforementioned materials is indented with a spherical indenter a linear elastic regime is usually followed, in most cases, by pop-in events, that in some cases are massive [117], followed, after a few cycles, by fully and spontaneously reversible hysteretic load-displacement curves [84]. During the pop-in events, the strain energy released results in the creation of a multitude of nano-domains and, in the case of $LiNbO_3$ and $LiTaO_3$, twins [82, 83]. When the nanoindenter is reloaded into the *same* location, dislocation loops nucleate within the domains formed during the pop-ins. The reversible dislocation motion, within the loops is believed to result in the energy dissipated per unit volume per cycle, W_d. The presence of micro-domains – that play the role of grain boundaries in polycrystalline solids – that do not allow the parallel dislocation loops to dissociate into

mobile dislocation walls, MDWs, is thus essential for their reversible behavior [79, 81-83].

In our previous studies, we referred to these co-axial parallel dislocation loops as incipient kink bands, IKBs. Also, the materials that dissipated energy via this mechanism we termed kinking nonlinear elastic, KNE, solids [44, 66, 76, 78]. In sharp contradistinction to other energy dissipating mechanisms in crystalline solids, such as microcracking or phase transitions, KNE solids have excellent fatigue resistance. For example, it is possible to indent sapphire single crystals in the same location to stresses of the order of 40 GPa, 24 times and observe *no* measurable differences in the shape and/or area of the reversible load-displacement loops after the $\approx 6^{th}$ cycle [81].

The W_d values measured for $LiTaO_3$ were some of the highest of any single crystals examined so far [75, 76, 79, 81-84]. The reason for this state of affairs is believed to be the formation of twins – during the early stages of deformation and/or the pop-in events – that rotate domains into an orientation that is more amenable to reversible dislocation motion, RDM, within the basal planes [82, 83].

There are also some reports on microcracking as the origin of hysteretic load-displacement loops. Richter *et al*. ascribed the hysteretic load-displacement loops in MgO single crystals to microcracking [118]. The latter can cause some energy dissipation but typically fades with cycling. Oliver and Pharr reported hysteretic load-displacement loops during the early stages of nanoindentation in soda lime glass, which degenerated with cycling [119].

This work's main goal is to differentiate between reversible dislocation motion and other energy dissipating mechanisms, such as microcracking or irreversible dislocation pileups.

A1.2. Experimental details

To do so, two diamond hemispherical indenters with radii, R, of 5 μm and 21 μm, were loaded into the same location - on a C-plane $LiTaO_3$, a plastically anisotropic solid, and a soda-lime glass microscope slide, an amorphous material - 100 times to stresses, of the order of 6 to 9 GPa, while concomitantly recording the load-displacement curves. The loading rate/load ratio was kept constant at 0.1. To maintain contact between the indenter and the specimen each of the unloading cycles stopped at 1% of the maximum load. During some NI runs, and despite waiting for the nanoindenter to settle down, instrumental drift, both positive and negative, were observed. The origin of the instrumental drift can be the result of temperature changes during the test. This was noted despite the fact that the tests were started only when the drift was below 0.05 nm/s. Thus the maximum drift on each cycle was about ±5 nm and ±7.5 nm for 5 μm and 21 μm indenters, respectively. Needless to add, this drift can influence the load-displacement and complicate the analysis. Herein we propose a technique that can minimize the influence of drift.

A1.3. Results and discussion

Typical NI load-displacement cycles obtained when the 5 μm radius tip was indented 100 times into the same location in $LiTaO_3$ and the glass slide are shown in

Figs. A1.1(a) and (b), respectively. For the sake of clarity, only select cycles are plotted. On Fig. A1.1(a), as in all our previous work on KNE solids, the first loop is open; subsequent loops, up to cycle 6, are open, but successively less so. From the 6^{th} to $\approx$ 35^{th} cycles, the loops are closed and fully reversible. Cycling beyond 35 times, results in larger, open loops until around cycle 75, after which the loops close and become reversible again. The load-displacement plots are different on the glass sample; the first loop is open and subsequence loops are small and become smaller up to cycle 10. From the 10^{th} cycle through the end of the test (cycle 100^{th}) the loops are quite small and their areas remain more or less constant.

The first cycle load-displacement curves in both samples are quite comparable. In most of our previous NI work, to further analyze the results and differentiate between reversible dislocations motion and other reasons for energy dissipation, we converted the NI results to NI cyclic stress-strain curves. This conversion entailed some assumptions and approximations that some have questioned. Herein, to avoid this problem, we define a new parameter, viz. reversible displacement, *RD* - shown schematically in the inset in Fig. A1.1(b) - as:

$$RD = D_w - D_f$$

where D_w is the maximum width of each loop and D_f is the non-reversible displacement at the end of each cycle. It follows that *RD* is a measure of the *reversible* energy dissipation during each cycle regardless of its origin. As shown below plotting *RD* vs. cycle number is a powerful, simple and straightforward method to differentiate between these two damping phenomena.

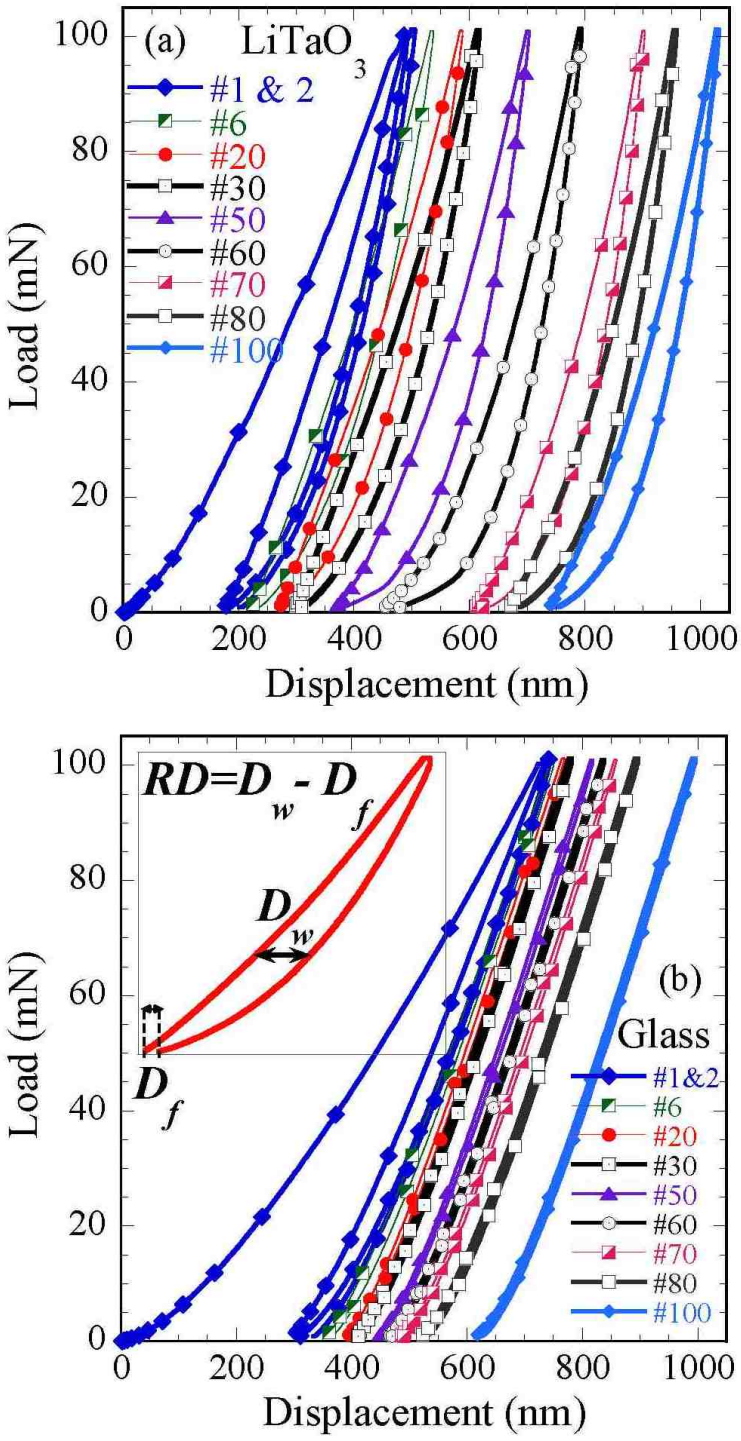

Fig. A 1.1. (a) Select NI load-displacement curves for a given location loaded 100 times to 100 mN with the 5 μm radius indenter on, a) a C-plane $LiTaO_3$ single crystal, (b) a glass slide. The top inset on (b) shows the schematic of how *RD* is calculated on each load-displacement loop.

Figure A1.2(a) plots *RD* versus cycle number for both the $LiTaO_3$ and glass samples loaded 100 times to 100 mN and 550 mN with the 5 μm and 21 μm indenters, respectively. The results on two different locations are shown for each sample and tip size. At about 13±1 nm, the *RD* on the glass slide, for the 5 μm tip, has its aximum value during cycle 2, and decreases to ≈ 3±3 nm after ≈ 10 cycles and remains constant throughout the rest of the test. For the 21 μm tip, *RD* starts around 17±1 nm, and decreases to the same minimum value (≈ 3±3 nm) as for the 5 μm tip, also after ≈ 10 cycles. In general, for both indenter sizes and for all the locations the *RD*s on the glass showed two stages: a decrease from a maximum value at the very beginning to a steady state regime after ≈ 10 cycles after which it remained constant at ≈ 3±3 nm. Note the steady state regime is achieved more or less after the same cycle numbers for both indenter sizes.

In sharp contradistinction to the glass surface, the *RD* response versus cycle number for $LiTaO_3$ for both indenter sizes in two different locations (blue and purple curves in Fig. A1.2(a)) is qualitatively and quantitatively different. Here the *RD*s start at a low value, go through a maximum around cycle 40 for the 5 μm indenter tip (blue and purple curves in center of Fig. A1.2(a)) and 10 cycles for the 21 μm indenter tip (top blue and purple curves in Fig. A1.2(a)) before gradually decreasing to the 100^{th} cycle. When the *RD*s for $LiNbO_3$ are plotted for cycles 2 to 10, a similar trend is observed (top inset in Fig. A1.2(a)).

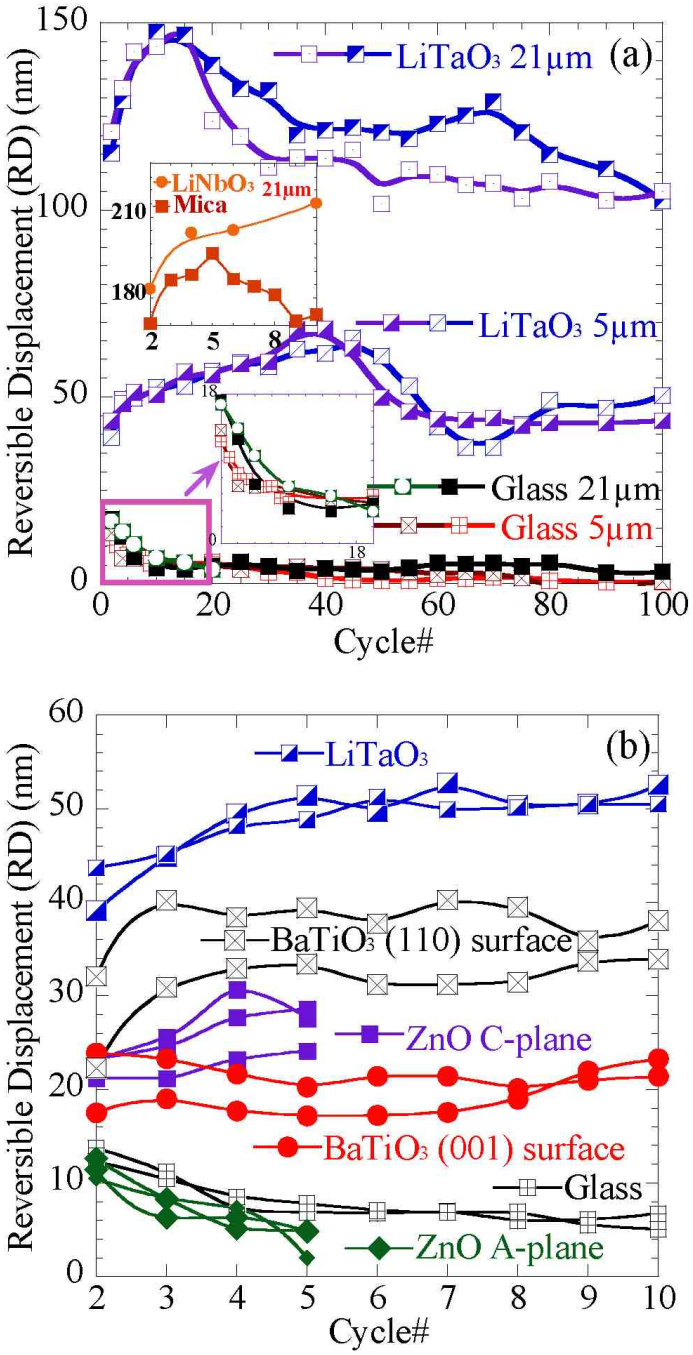

Fig. A 1.2. Reversible displacement (*RD*) versus cycle number for a) two given locations on the $LiTaO_3$ and glass samples loaded 100 times to 100 mN with the 5 mm indenter and 550mN with the 21μm indenter. The top inset shows the RD values for the $LiNbO_3$ and mica loaded 10 times to 550 mN with 21μm tip, b) up to cycle 10^{th} for two locations on $LiTaO_3$ and the glass sample indented to 100 mN with the 5 mm indenter. Also plotted are the *RD* values for A and C-plane ZnO single crystals,[79] (001) and (110) $BaTiO_3$ surfaces,[80] indented with 13.5 μm indenter.

The two diametrically opposite responses of *RD* with cycling (Fig. A1.2(a)) for the glass and $LiTaO_3$ are fully consistent with our understanding of the nature of the energy dissipated with cycling. In the glass, microcracking and the concomitant friction between the crack surfaces is the only possible energy dissipating mechanism. Since cycling would tend to wear and smooth these surfaces, it is not surprising that W_d decreases with cycling. Note that another factor could be the reduction in stress under the indenter as the microcracks increase in size with cycling. In either case, *RD decreases* with cycling. It is thus quite significant that the *RD*s for $LiTaO_3$ initially *increase* with cycling. The latter implies that the mechanism responsible the reversible displacement in $LiTaO_3$ cannot be solely due to microcracking; another mechanism, that is much more dissipative, must be invoked. Over the years we have made the case that a possible second mechanism is in the form of IKBs. The results shown in Fig. A1.2(a) support this notion. We have shown in our previous NI work that in both $LiTaO_3$ [83] and $LiNbO_3$ [82] during the pop-in stage $(10\bar{1}2)[10\bar{1}1]$ twins form. The latter rotate the basal planes in orientations that are more amenable for the nucleation and growth of IKBs that in turn result in the largest reversible NI loops we have ever measured [82, 83]. The initial increase in *RD* with cycling can thus be ascribed to this reorienation and its cyclic dependence.

Note that the conclusion that reversible dislocation motion results in hysteretic loops does not neccearily rule out microcraking. It is reasonable to assume that the reduction in *RD* past its peak values for both indenters (Fig. A1.2(a)) is related to the

nucleation and growth of microcraks. Indeed post-SEM micrographs of indented regions more often than not show a plethora of microcracks, especially after 100 cycles.

To test the general validity of this conclusion we revisited our results on the cyclic loading of $LiTaO_3$ [83], $LiNbO_3$ [82], (110) and (001) $BaTiO_3$ [80], mica [84], A and C-plane ZnO surfaces [79]. Figure A1.2(b) plots *RD* vs. cycle number for these diverse solids. The *RD* values for mica and $LiNbO_3$ are plotted in Fig. A1.2(a). Also plotted, for comparison, are the results obtained on glass obtained herein. A perusal of these results quickly establishes that with the exception of the glass and ZnO A-plane – in which the *RD*s decrease with cycle number – for all other surfaces *RD* either increase, or remain constant as in the case of the (001) $BaTiO_3$ surface with cycle number. Gratifyingly, the latter surfaces were all classified as KNE based on our analysis of their NI stress-strain curves.

The results on the ZnO A-plane are noteworthy. Based on our NI results [79] and, as importantly, those of others [120] we concluded that in this orientation *irreversible dislocation pileups* and *not* IKBs nucleated under the indenter. The latter were seen in cross-sectional transmission electron microscopy, TEM, micrographs [79, 120]. Clearly the *RD* result for this ZnO orientation is more reminiscent of the glass surface. However, in this case the energy dissipation cannot be ascribed to microcracks for the simple reason that none were observed in post-indentation SEM observations of the indentation marks [79]. This is an important result because it suggests that pileup reversibility also fades with cycling, presumably as a result of work hardening. It is worth re-emphasizing here that cracks were *not* observed when the C-plane ZnO surfaces were cyclically indented which rules out microcracking in that case.

The advantages of measuring *RD* are that only the raw load-displacement data are used. There are also some reports on measuring the full width at half maximum, FWHM, of the load-displacement loops during cyclic indentation [80, 121]. We believe *RD* is more accurate and powerful than FWHM because, a) the D_w does not always occur at half maximum, and b) during high cycle indentation tests, drift can be problematic. By subtracting the D_f from D_w the effect of drift is minimized.

A1.4. Conclusions

In conclusion herein we define a new parameter, *RD*, which is related to, and indirectly measures, the reversible deformation of a region below a spherical nanoindenter. By plotting *RD* versus the number of cycles two different responses were observed. The first was a gradual decrease in *RD* with cycling, the second was an initial gradual increase or a constancy with cycle number. The former was correlated with microcracking or irreversible dislocation pileups; the latter with reversible dislocation motion, most likely in the form of IKBs. Using this technique we re-confirmed that $LiTaO_3$, $LiNbO_3$, $BaTiO_3$, C-plane ZnO and mica single crystals are KNE solids. As importantly, we also show that the energy dissipation in glass and A-plane ZnO decrease or fade with cycling, and are thus not due to reversible dislocation motion. Finally, it is important to note that the conclusions reached herein are *not* contingent on the existence of IKBs; the conclusions reached, apply to any form of reversible dislocation motion.

A1.5. Supplementary Material

The reversible displacement, *RD*, is defined on the raw load-displacement results and is a measure of reversible energy dissipation during each cycle. D_w (nm) can be measured directly from the load-displacement curves and it is the maximum width of each loop (top inset in Fig. 1b). In almost all of the cyclic indentations that we performed, the load-displacement loops were not 100% closed. In other words, none of the load-displacement curves fully returned back to their original point. This non-reversible parameter was measured on every cycle and is labeled D_f (nm) (see top inset in Fig. 1b). D_f can be due to the plastic deformation or instrumental drift during each cycle. Regardless of its origin, by subtracting D_f from D_w, the irreversible portion of the load-displacement is removed and the remaining must be *RD*. In other words, by measuring *RD*, it is possible to focus on the reversible deformations that cause the hysteretic load-displacement loops.

SEM images of the indentation imprints of the 21 μm tip, loaded to 550 mN, after 5, 20, 40, 100 cycles into $LiTaO_3$ surfaces are shown in Figs. A1.S1a to d, respectively. From Fig. A1.S1a, it is clear that initially the cracking is minimal and the 3-fold symmetry of the $(10\bar{1}2)[10\bar{1}1]$ twins that form [83, 122] – despite the fact that the indenter tip is spherical - is obvious. With further cycling, however, the cracks grow and pile-ups around the indentation mark – and especially damage around the indentation imprint – get larger. By the 20^{th} cycle (Fig. A1.S1b), the 3-fold symmetry is less prominent, but still discernable. The twin lines also appear to be closer together after 20 cycles[83] and a damaged area is formed around the indentation mark. In the paper this damage was related to the reduction of *RD* past its peak values (cycles 10 to 20 for this

case). In other words, the reduction in *RD* was attributed to the nucleation and growth of microcracks. After 40 and 100 cycles (Figs. A1.S1c and d) the twin lines are replaced by a highly microcracked polycrystalline layer. The bottom right inset in Fig. A1.S1d shows that the single crystal is now transformed into a multitude of micrometer and sub-micrometer grains.

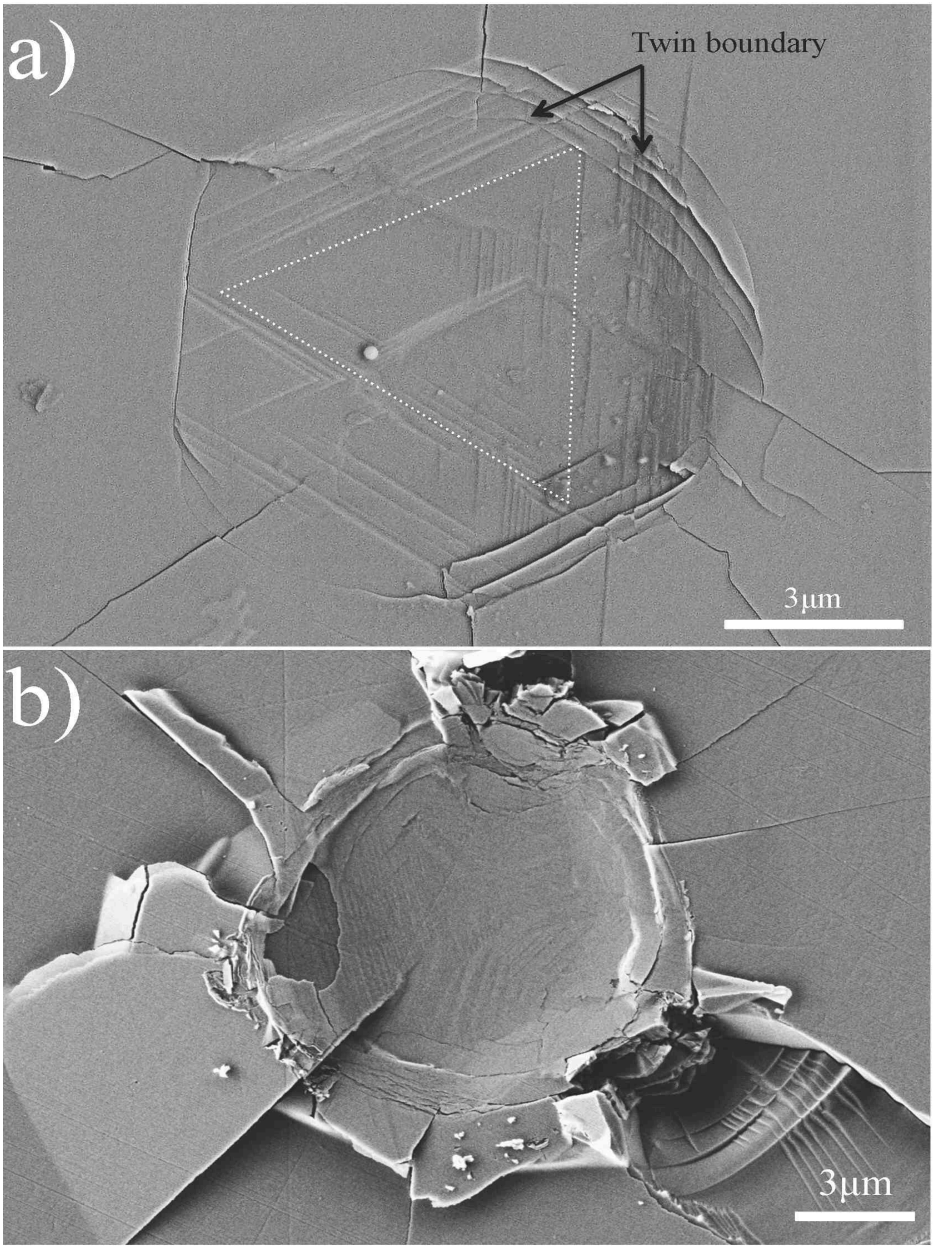

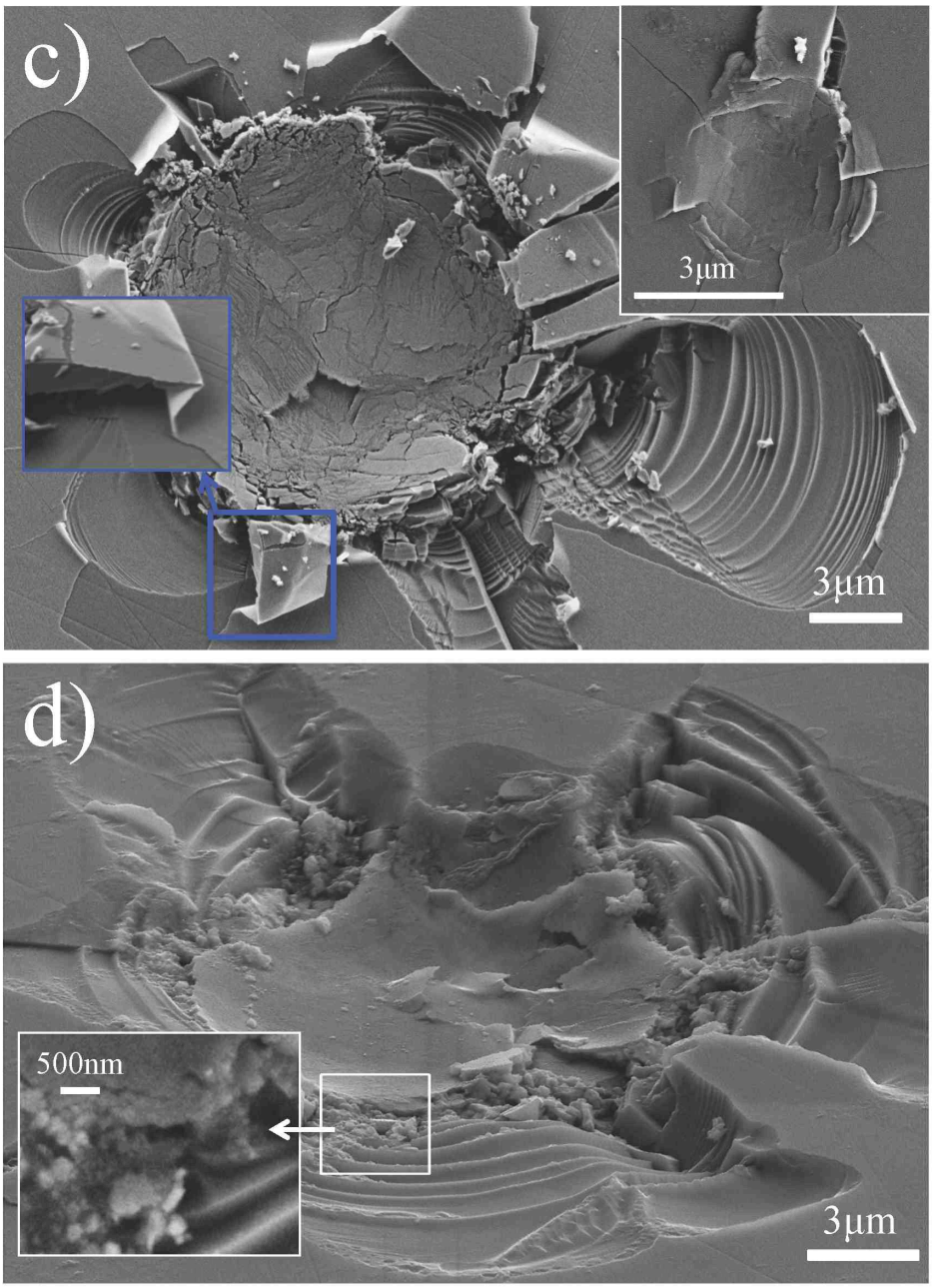

Fig. A1.S 1. SEM images of indentation marks on $LiTaO_3$ made with a 21 μm tip loaded to 550 mN, a) 5, b) 20, c) 40 and d) 100 times. The features with very sharp radii of curvature in (b) and (c) are kink boundaries. Top right inset in (c) shows the indentation mark made with a 5μm tip loaded to 100mN for 40 times. Bottom left inset in (d) shows submicron grains that formed under the nanoindenter.

Remarkably and despite the fact that the underlying imprint and its surroundings change substantively through the experiment, the *RD* values remain almost constant after cycle ≈ 20. This is an important result because it indirectly confirms that microcracks – even when present – do not greatly influence the values of *RD* or the areas of the hysteretic loops obtained. The latter are probably an order of magnitude lower than those due to reversible dislocation motion.

In the case of 5 μm indenter, the same scenario repeats. However, as mentioned in the paper, the decrease in *RD* occurs around cycle 40. The top left inset in Fig S1c shows an indentation of the 5 μm indenter loaded 40 cycles to 100 mN. Clearly, the microcracked area is smaller than that under 21 μm indenter. At this time it is reasonably well-established, that the affected zone under a spherical indenter tip, with a contact area of radius *a,* is a cylinder of height ≈ 2*a*.[123] The post-indent mark radii, *a*, for the 5 μm and 21 μm indenters were ≈ 2 and 6 μm, respectively.[83] It follows that the volume probed by the 21 μm tip is roughly 30 times larger than that of the 5 μm tip. It is again reasonable to assume that this increased volume, and the concomitant increased probability of finding defects, results in an earlier reduction in *RD* for the 21 μm tip.

A closer examination of Fig. A1.S1c shows multiple examples of areas, or features, with very sharp radii of curvature (see left inset in Fig. A1.S1c). Since such features cannot exist without a multitude of an excess of one type of dislocations, they must be kink boundaries.[81] A schematic of what we conjecture is occurring in $LiTaO_3$ under the indenter is shown in Fig. A1.S2. The formation of twins, in the very first cycle (see Fig. A1.S1a), and kink bands underneath the surface must rotate the basal planes in orientations that are more amenable to dislocation movement (Fig. A1.S2a). With further

cycling other dislocations are generated in the form of dislocation pileups and MDWs. These defects in turn continue to move and accumulate, and eventually push basal planes towards the surface (Fig. A1.S2b and c).

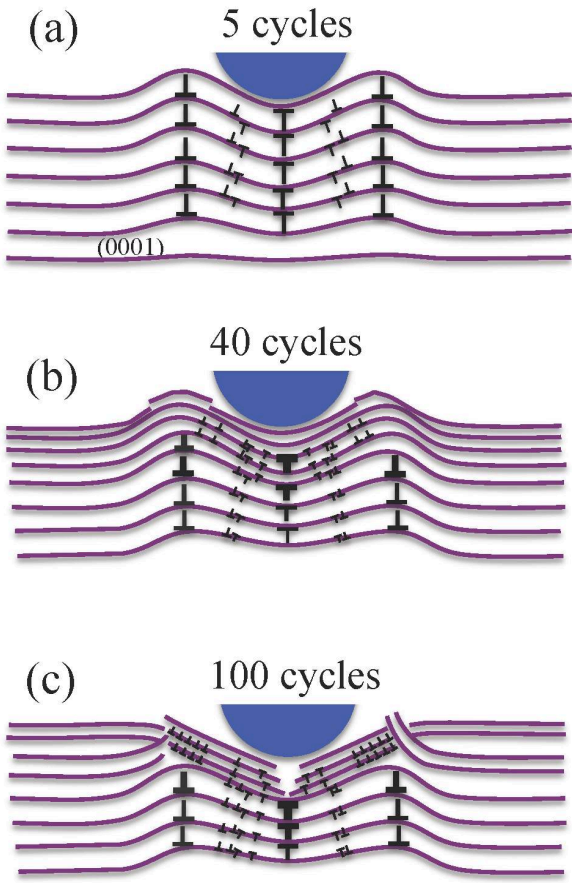

Fig. A1.S 2. The schematic of kink bands formation, dislocation movement underneath the surface after, a) 5, b) 40 and c) 100 cycles.

SEM micrographs of the glass surface indented with the 21 μm tip indenter loaded to the maximum load of our NI, viz. 550 mN, after 2, 20 and 100 cycles are shown is Figs S3a to c, respectively. These micrographs confirm that the effect of cycling on the glass surface is significantly milder than what is observed in $LiTaO_3$. For example

compare Figs. A1.S1b and Fig. A1.S3b, or Figs. A1.S1d and A1.S3c. In other words, the lack of

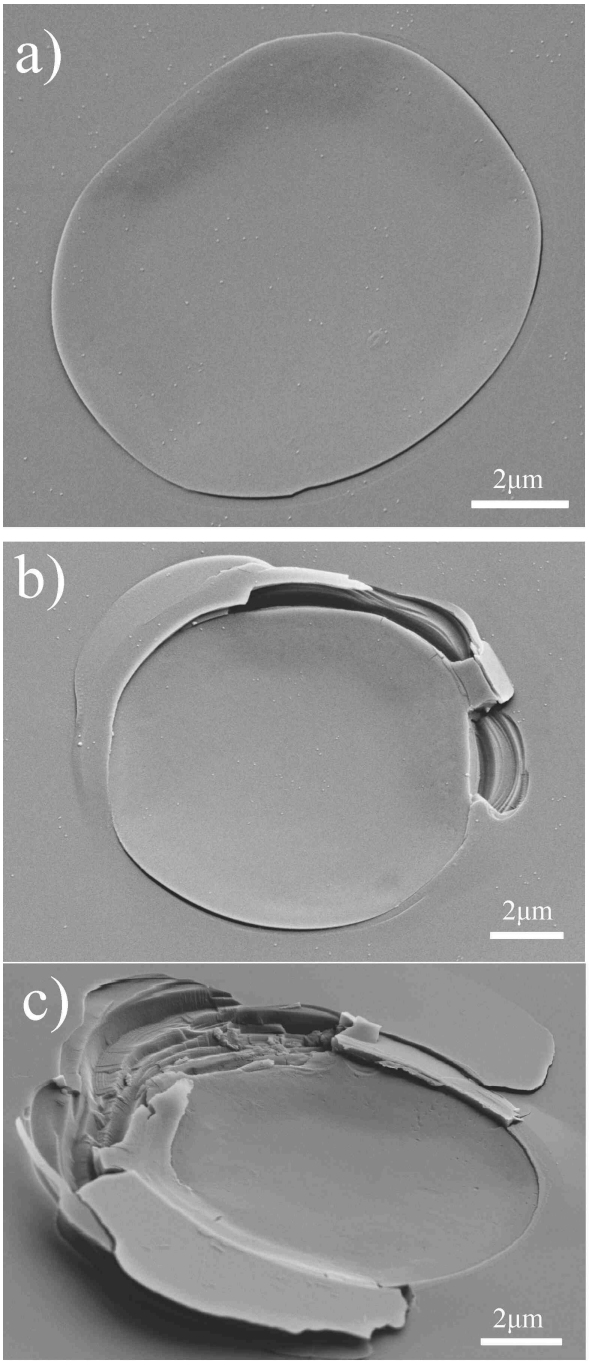

Fig. A1.S 3. SEM image of indentation mark on the glass surface made with a 21μm tip loaded to 550 mN for a) 2, b) 20 and, c) 100 cycles. No sub-micron grains in the indentation area and no damage accumulation other than some fractures around the indentation area is observed.

dislocations, results in less fatigue damage. Comparing Fig. A1.S3 with S1 clearly shows that when pure microcracking is involved, after the microcrack formation, they do not develop drastically, when the maximum load is kept constant even for 100 cycles. In addition, crack surface friction degenerated with cycling (*RD* values reaches ≈ 3±3nm after 10 cycles in the glass sample for both indenters). However, when dislocations are invloved, at low cycles a pattern of defect development can be observed by carful microscopy, and at high cycles defects development and accumulation form deeper into the bulk of the material leads to a large damaged area around the indentation mark and the *RD* values are dependent on the indenter size.

To further check our methodology, we analyzed the NI results obtained on ZnO C and A planes obtained by Basu et al.[124] The SEM micrographs, reproduced from that paper (Fig. A1.S4a and b) clearly show the total absence of microcracks. Furthermore, there was no evidence of phase transformations.[124] It follows that the major reason for the differences in the *RD* values between A and C planes (Fig. A1.2b) has to be related to the differences in dislocation arrangements/motion. In the C orienetation (Fig. A1.S4a) kink boundaries form and move away from the center of the indentation along $[11\bar{2}0]$, creating a Star of David shape on the indented surface (Fig. A1.S4a). These kink boundaries are believed to have formed as a result of the accumulation of MDWs as explained in Ref. 5. In this case, pyramidal slip bands is also activated.

However, when the A plane of ZnO are indented (Fig. A1.S4b), the basal planes are parallel to the loading direction, and the dislocations that are created at the surface irreversibly penentrate deeper into the sample and after a few cycles the region work hardens and *RD* goes to zero (Fig. A1.2b).[124]

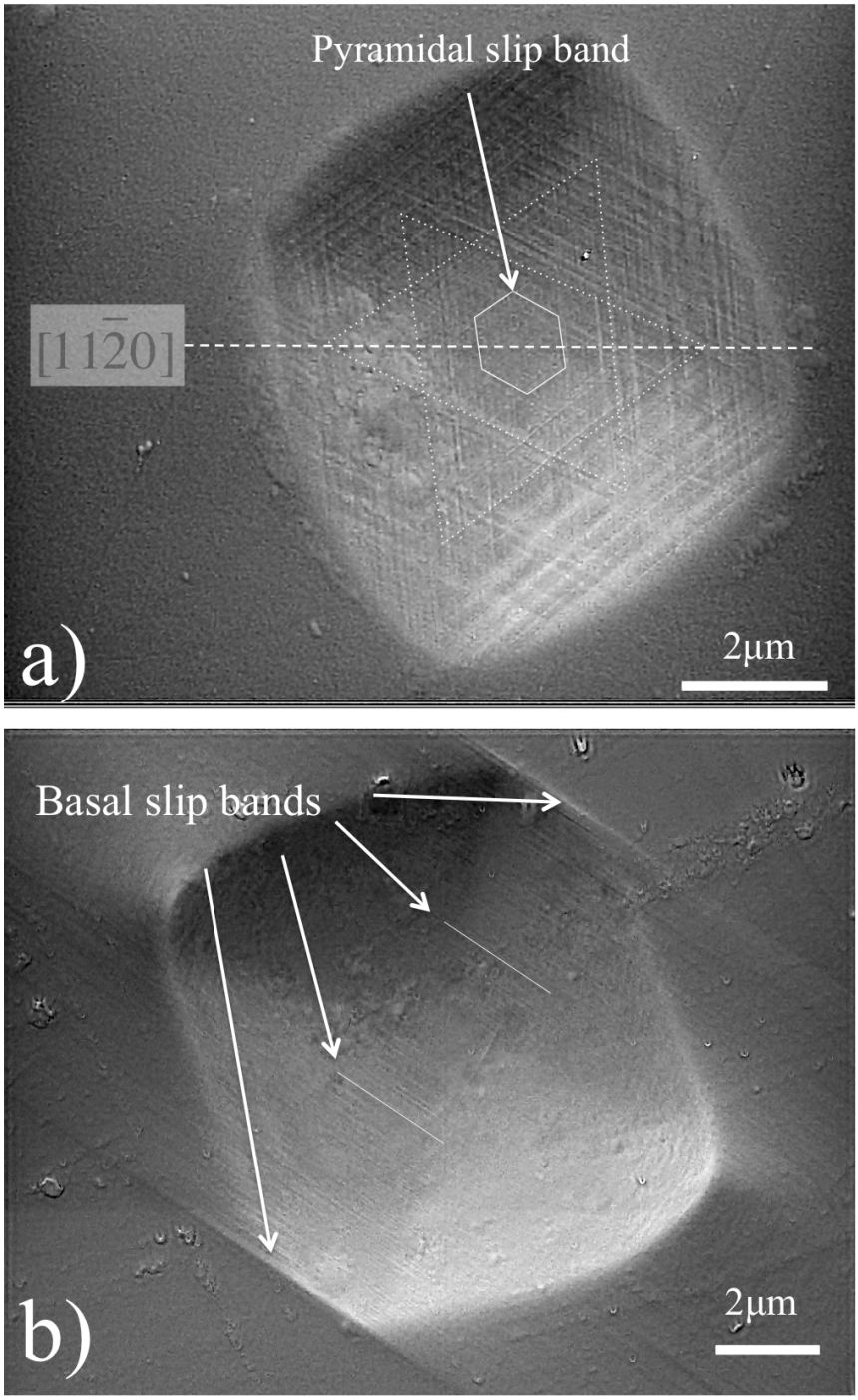

Fig. A1.S 4. SEM image of indentation mark made with a 13.5 μm tip loaded to 500mN for 5 cycles on ZnO a) C-plane and b) A-plane orientation.

It is important to note here that there are other parameters that can be the measure of energy dissipation, such as the load-displacement loop's area. However, since D_f is considered in the *RD*'s definition, it is a better measure of energy dissipation. Both *RD* and the area of the load-displacement loops for both $LiTaO_3$ and glass samples loaded 10 times to 100 mN with the 5 mm indenter are plotted in Fig. A1.S5. It is clear that comparing the area of the loops for these two samples can be confusing since they both show the same tendency. However, *RD* behavior is quite different in the two materials and is thus a better indicator of the presence or lack thereof of reversible deformation.

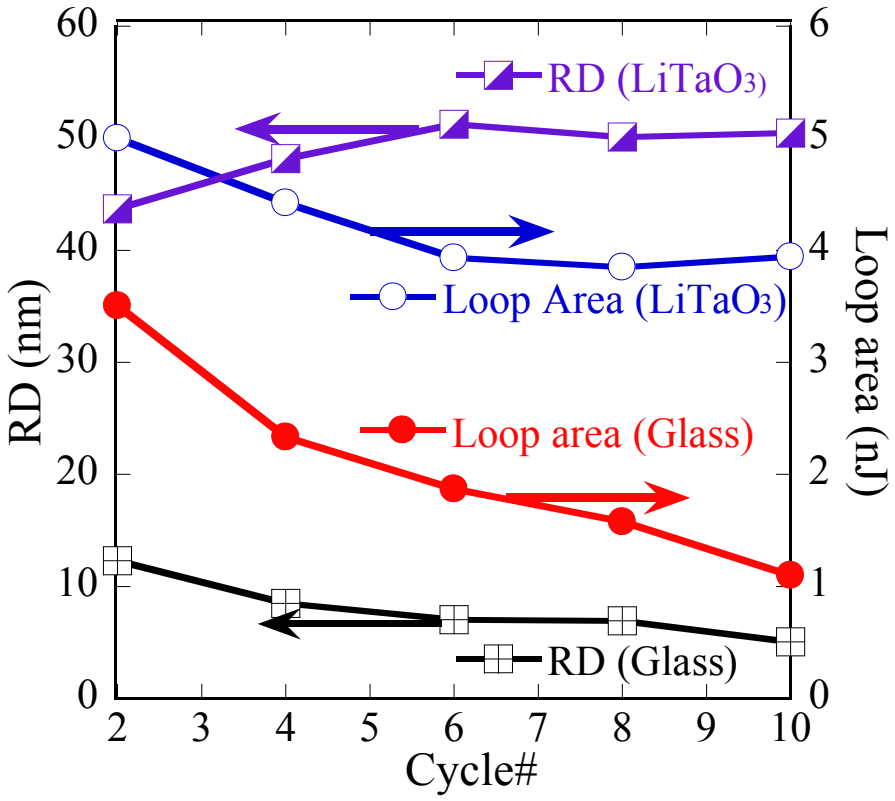

Fig. A1.S 5. Comparison of RD and area of the load-displacement loops versus cycle numbers for the $LiTaO_3$ and glass samples indented to 550mN for 10 cycles with 5µm indenter.

A2. Spherical Nanoindentation Study of the Deformation Micromechanisms of LiTaO3 Single Crystals

Published in: B. Anasori, K. E. Sickafus, I. O. Usov and M. W. Barsoum, J. App. Phys., 110 (2), 023516 (2011). Copyright (2011) American Institute of Physics.

Abstract

Herein, spherical nanoindentation (NI) was used to investigate the room temperature deformation behavior of C-plane $LiTaO_3$ single crystals loaded along the [0001] direction as a function of ion irradiation. When the NI load-displacement curves of 3 different nanoindenter radii (1.4 μm, 5 and 21 μm) were converted to NI stress-strain curves, good agreement between them was found. The surface first deforms elastically – with a Young's modulus of 205±5 GPa, calculated from the stiffness versus contact radii curves and 207±3 GPa measured using a Berkovich tip – and then plastically deforms at ≈ 6 GPa. Repeated loading, into the same location, results in large, reproducible, fully reversible, nested hysteresis loops attributed to the formation of incipient kink bands, IKBs. The latter are co-axial fully reversible dislocation loops that spontaneously shrink when the load is removed. The IKBs most probably nucleate within the $(10\bar{1}2)$ twins that form near the surface. The sharper radii resulted in twin nucleation at lower stresses. The changes in the reversible loops' shape and areas can be related to the width of the twins that form. The latter were proportional to the nanoindenter tip radii and confirmed by scanning electron microscopy and by the fact that larger threshold stresses were needed

for IKB nucleation with the smaller tip sizes. No effect of irradiation was observed on the NI response presumably because of the mildness of the irradiation damage.

A2.1. Introduction

Lithium tantalate, $LiTaO_3$, is one of the most attractive materials for nonlinear integrated optics. The properties of ferroelectric $LiTaO_3$ are similar to those of lithium niobate, $LiNbO_3$, reviewed in detail elsewhere [125, 126], with excellent nonlinear optical properties, as well as higher thresholds to photorefractive damage than $LiNbO_3$ and a lower Curie temperature [127]. The importance of $LiTaO_3$ is emerging in applications such as second-harmonic generation and optical parametric amplification/oscillation, because it can be processed to make waveguides and to engineer the nonlinearity through quasi-phase matching via periodic poling [128], offering an important alternative to $LiNbO_3$ in devices for signal processing via quadratic cascading [129]. Despite these potential applications, little work has been carried out on its mechanical behavior, especially at room temperature. Doukhan *et al.*[130] described different lattice defects in $LiTaO_3$ and concluded, not surprisingly, that it had the same twinning system as $LiNbO_3$.

Recently, we showed that the vast majority of plastically anisotropic solids with c/a ratios > 1.4, can be classified as kinking nonlinear elastic (KNE) solids [46, 76-78]. A sufficient condition for a solid to be KNE is plastic anisotropy. The signature of these solids is the formation of fully reversible, reproducible stress-strain loops during cyclic loading. The full reversibility of these loops is believed to be caused by incipient kink bands (IKBs) that are comprised of multiple, co-axial, parallel dislocation loops (Fig. 1a), which remain extended only if the load is applied; when the load is removed, they shrink,

or are annihilated altogether [66]. At high stresses, such as under a nanoindenter, the IKBs sunder and devolve, first into mobile dislocation walls, MDW's, and ultimately into kink boundaries (KBs) which are irreversible (Fig. A2.1(b)) [46, 74-76, 79, 117, 131-133]. On reloading to the same stress, IKBs nucleate in the newly created microdomains. The to-and-fro motion of the IKB dislocations, in turn, results in hysteresis and the dissipation of energy. Using this approach we showed that graphite [75], mica [76, 117], ZnO (C-orientation) [79], sapphire [132], and GaN [131] among many others are KNE solids.

Following the pioneering work of Herbert *et al.*[134] and Oliver and Pharr,[135] Suganuma [136] and Bushby [137], we developed a technique for converting spherical NI load/displacement curves to NI stress/strain curves [138, 139]. According to our technique, NI stress and strain are defined as $P/\pi a^2$ and a/R, respectively, where P, a, and R are load, contact radius and tip radius. By plotting the NI stresses and strains, more information can be gleaned from the indentation results. We applied this method to better understand the deformation behavior of a number of, oxide and nitride single crystals, such as sapphire [132], ZnO [79], $LiNbO_3$ [122], mica [76, 117], GaN [131], $BaTiO_3$ [80], and, more recently, polycrystalline Y_2O_3 [140].

Most relevant to this paper is our recent work on the nanoindentation of C-plane $LiNbO_3$ single crystals loaded along [0001] [122]. In that paper we reported an elastic modulus of 186 GPa and a Vickers microhardness of about 4.5 GPa. Cyclic loading resulted in the signature of KNE solids, viz. large, fully reversible, reproducible, hysteretic stress-strain loops. As far as we are aware, these remain the largest ever reported for crystalline solids.

Before discussing the work carried out herein it is important to summarize our IKB-based model that is, in turn, based on early work by Frank and Stroh, F&S [66]. The following is a simplified version. F&S considered an elliptic kink band, KB, with length, 2α, and width, 2β, such that α >> β (Fig. A2.1(a)) and showed that the remote shear stress, τ, needed to render such a subcritical KB unstable is given by:

$$\tau_c \approx \frac{\sigma_t}{M} \approx \sqrt{\frac{4G^2 b\gamma_c}{\pi^2 2\alpha} \ln \frac{b}{w\gamma_c}} \tag{A2.1}$$

where τ_c and σ_t are the remote critical shear and axial stresses, respectively. M is the Taylor factor relating the shear stress at the grain level to the applied stress. The maximum value of M is 2. G, b, and w are, respectively, the shear modulus, Burgers vector, and a term related to the dislocation core width [66]. If one assumes that the local stress needed to nucleate an IKB is ≈ G/35, then at 0.05 rad., the critical shear angle, γ_c, is small [66, 85].

As a first approximation, each dislocation loop (Fig. A2.1(a)) can be assumed to be comprised of two edge and two screw dislocation segments with lengths, $2\beta_x$ and $2\beta_y$, respectively. It is also assumed that when $\sigma > \sigma_t$, the IKBs grow by increasing their width, 2β, according to:

$$2\beta_x \approx \frac{2\alpha(1-\nu)}{G\gamma_c}\frac{\sigma}{M} \quad , \quad 2\beta_y \approx \frac{2\alpha}{G\gamma_c}\frac{\sigma}{M} \tag{A2.2}$$

for the edge and screw components, respectively. It follows that for $\sigma > \sigma_t$, the IKBs grow and the IKB-induced axial strain resulting from their growth is assumed to be given by [57]

$$\varepsilon_{IKB} = \frac{\Delta V.\gamma_c N_k}{k} = \frac{4\pi\alpha(\beta_x\beta_y - \beta_{xc}\beta_{yc})\gamma_c N_k}{3k} = \frac{4\pi(1-\nu)N_k\alpha^3}{3kG^2\gamma_c M^2}(\sigma^2 - \sigma_t^2) = m_1(\sigma^2 - \sigma_t^2) \tag{A2.3}$$

where m_1 is the coefficient before the term in brackets in the fourth term; N_k is the number of IKBs per unit volume; ΔV is the change in the volume kinked as the IKBs grow from a size at σ_t to their size at σ. The factor k relates the volumetric strain due to the IKBs to the axial strain along the loading direction. Experimentally, k varies from 1 to 2. For example in polycrystalline Mg it is closer to 1 [56], while in Co it is closer to 2 [55]. Reed-Hill *et al.* also assumed k = 2 when they modeled twins in Zr [141]. Herein we assumed k = 2; the implications and ramifications of this assumption are discussed below, Once m_1 is determined experimentally, if 2α can be estimated, N_k can be calculated. Note that $N_k\alpha^3$ is of the order of unity.

If Ω is the energy dissipated by a dislocation line sweeping a unit area, then the energy dissipated per cycle per unit volume, W_d, can be expressed as [57, 77]

$$W_d = 2\,\pi\left(\beta_x\beta_y - \beta_{xc}\beta_{yc}\right)N_k\,\frac{2\alpha}{D}\Omega = \frac{4\pi(1-\nu)N_k\alpha^3\Omega}{G^2 b\gamma_c M^2}\left(\sigma^2 - \sigma_t^2\right) = m_2\left(\sigma^2 - \sigma_t^2\right) \quad \text{(A2.4)}$$

which D is the distance between dislocation loops along 2α (Fig. A2.1(a)). It follows that Ω/b should be proportional, if not equal, to the critical resolved shear stress, CRSS, of an IKB dislocation loop. Combining Eqs. 3 and 4 yields:

$$W_d = 3k\,\frac{\Omega}{b}\,\varepsilon_{IKB} = \frac{m_2}{m_1}\varepsilon_{IKB} \quad \text{(A2.5)}$$

Figure 1b shows a schematic of how ε_{NL} and W_d are estimated from the NI stress-strain curves.

Assuming the IKBs to be cylinders with radii β_{av}, then the reversible dislocation density, ρ_{rev}, due to the IKBs is given by:

$$\rho_{rev} = \frac{2\pi N_k 2\alpha\beta_{av}}{D} = \frac{4\pi N_k \alpha\beta_{av}\gamma_c}{b} \quad \text{(A2.6)}$$

where β_{av} is the average of β_x and β_y.

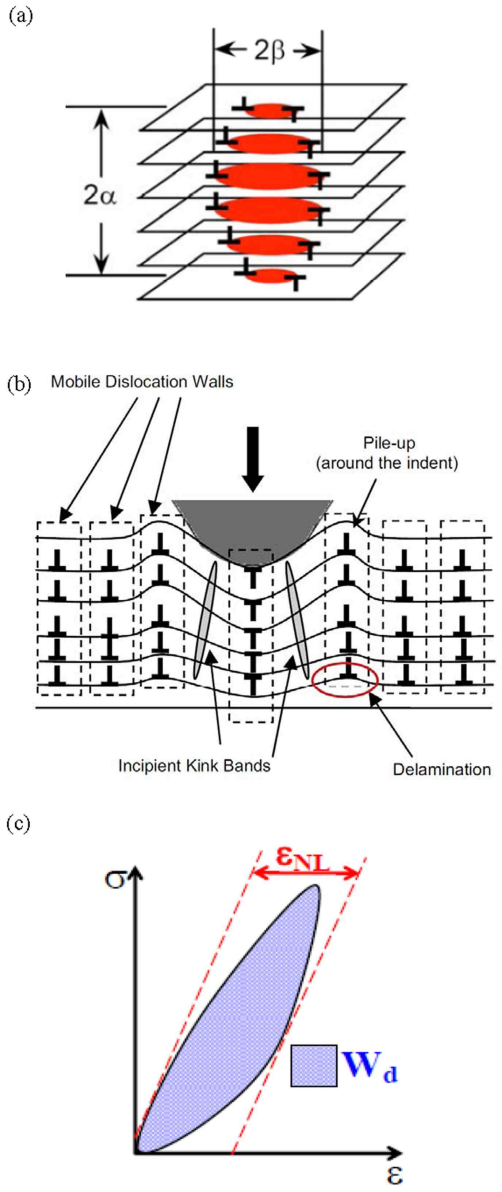

Fig. A 2.1. Schematic of, (a) dislocation loops comprising an IKB, (b) Schematic of what could be occurring below the indented surface. The emission of mobile dislocation walls that in turn form kink boundaries, are shown. Upon re-loading, the IKBs form within the kink boundaries, or twins formed during the pop-in events, (c) typical stress-strain curve for a KNE solid obtained under spherical nanoindentations, showing and the definition of non-linear strain, ε_{NL} and the energy dissipated per unit volume per cycle, W_d.

Since IKBs are comprised of dislocation loops and NI is sensitive to near surface properties, it is reasonable to assume that any process that induces near surface defects could affect the NI response of KNE solids. This is particularly true since we recently

showed that the average pop-in stresses in defective micas were significantly lower than those in less defective ones [117]. At this time it is fairly well established that irradiation of solids with light ions such as helium, He, can create a large number of defects including vacancies and interstitials, voids, dislocation loops, and He bubbles, etc. [142, 143]. On the other hand, there are some parameters, such as the material's compositional complexity, that can act to suppress the nucleation and growth of dislocation loops and voids during irradiation [144]. $LiTaO_3$ belongs to a family of oxides that possess a corundum-derivative crystal structure [145] that, because of their compositional complexity, are considered to be radiation tolerant materials. $LiTaO_3$ is the least radiation tolerant in this family of oxides and is one reason it was chosen for this work [144].

The aim of this paper is twofold. The first is to understand the deformation micro-mechanisms of C-plane $LiTaO_3$ single crystals loaded along [0001]. The second is to explore the effects of He ion irradiation on the deformation mechanisms.

A2.2. Experimental details

Two high quality, (0001) or C-plane orientation, $LiTaO_3$ single crystals were purchased (Yamaju Ceramics Co., Aichi, Japan) with both sides polished to a mirror finish.

The NI experiments were performed at room temperature with a nanoindenter (XP system, MTS Corp., Oak Ridge, TN) equipped with a continuous stiffness measurement (CSM) attachment. Three diamond hemispherical indenters with radii, R, of 21 μm, 5 μm, 1.4 μm were used. Typically, a tip was repeatedly indented in the same location, to a given load along the [0001] axis. The loading rate/load ratio was constant at 0.1. To correct for instrumental drift, the unloading segments of the sixth, and subsequent cycles,

were shifted so as to align them with the corresponding unloading segment of the previous cycles before the results were converted to NI stress-strain curves. This was carried out *if, and only if*, successive load-displacement cycles had identical areas (see below).

The load-displacement results were zero-point corrected. To determine the effective zero point, we used the method of Moseson *et al.* [138]. The latter exploits the fact that for a spherical tip, the following relationship:

$$S = 2\,E^{*}\,a \tag{A2.7}$$

where S and a harmonic contact stiffness of the surface and contact radius, respectively, holds. More details can be found in Ref. [138]. The effective modulus of the surface, E* is given by:

$$\frac{1}{E^{*}} = \frac{(1-\nu^{2})}{E} + \frac{(1-0.07^{2})}{1140} \tag{A2.8}$$

where ν and E are the Poisson's ratio and Young's moduli of the sample, respectively. The other numbers are the corresponding values for the diamond indenter tip. Poisson's ratio of $LiTaO_3$ is assumed to be 0.25 [146].

Post-indentation surface features were examined using a scanning electron microscope, SEM (Zeiss Supra 50VP, Germany). The Vickers microhardness was measured using a load of 10 N. The moduli and hardness values were also measured using a Berkovich indenter and the Oliver and Pharr method [147].

One of the $LiTaO_3$ crystals was irradiated with 2 MeV He^{+} ions at room temperature to an ion fluence of 1.67×10^{15} He/cm^2. Ion range, nuclear and electronic energy partitioning were estimated using an Lindhard–Scharff–Schiott, LSS, procedure for calculating ion stopping [148-151]. Based on LSS, the range of 2 MeV He^{+} ions in

$LiTaO_3$ was estimated to be 4.81 μm (assuming a mass density for $LiTaO_3$ of 7.41 g/cm^3).

The lattice damage was measured by Rutherford backscattering spectroscopy, RBS, in channeling mode (RBS/C) using a 2 MeV He^+ ion beam with a backscattering angle of 167^o. The ion irradiation and RBS/C analysis were carried out at the Ion Beam Materials Laboratory (IBML) at Los Alamos National Laboratory.

A2.3. Results

A2.3.1. Nanoindentation Results

Typical NI load-displacement results obtained when the 21 μm radius tip is indented into the un-irradiated sample is shown in Fig. A2.2. The corresponding results for the 5 μm tip radius indenter are shown in the bottom right inset of the same figure. The results for the irradiated samples were identical to the unirradiated samples and are not shown.

In all load-displacement plots (Fig. AB.2), the first cycle was open. After the indenter was unloaded and reloaded to the same maximum load and into the same location, the repeat cycles close and ultimately become fully reversible, and reproducible (Fig. AB.3). However, perfect reproducibility is only achieved somewhere between cycles 5 to 10 for all locations and tip sizes. The area of cycles 6 to 20 are, within the resolution limit of our NI, identical (inset in Fig. A2.3).

Typical nested loops obtained when a given location is loaded to a maximum load, unloaded and re-loaded to progressively higher loads, are shown on the loop labeled 2 in Fig. A2.3.

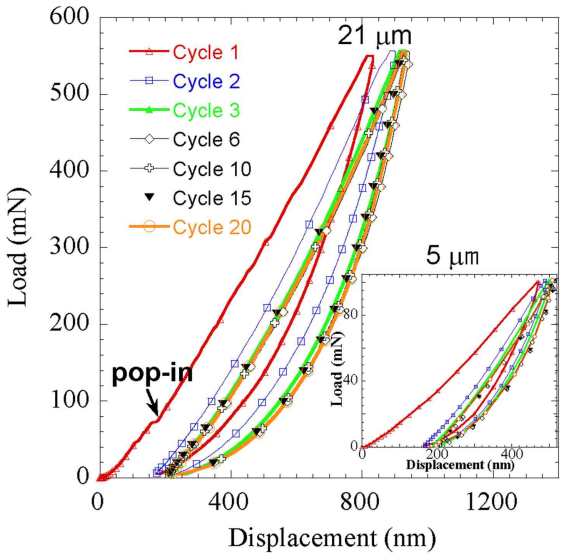

Fig. A 2.2. Typical NI load-displacement curves when an irradiated C-plane $LiTaO_3$ single crystal is loaded 20 times to 550 mN with the 21 μm radius indenter. Note presence of small pop-ins. Bottom right inset shows the same plot for the 5 μm radius tip, loaded twenty times to 100 mN. In both cases, for clarity's sake only a few cycles are plotted.

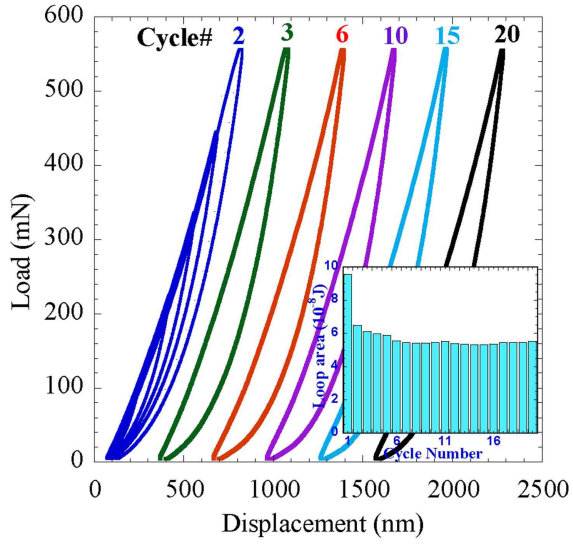

Fig. A 2.3. Load-displacement cycles 2, 3, 6, 10, 15 and 20 obtained when the 21 μm tip was indented along the [0001] into an irradiated surface. The curves were shifted to the right from their original position for clarity. Cycles 2 and 3 are open; cycles 6 to 20 are closed and equal in area. Re-loading to a lower load after loading to the maximal load always results in closed, reversible nested loops, shown for cycle 2 only. Inset plots the corresponding load-displacement loops' areas versus cycle number obtained with the 21 μm tip on an irradiated surface. After about 6 cycles, the areas are constant.

When the S vs. a results for the three radii are plotted (Fig. A2.4a) it is obvious that the relationship between the two is linear. From least squares fits of the lines and making use of Eqs. A2. 7 and A2. 8, the average Young's moduli for the 1.4 μm, 5 μm and 21 μm tips were calculated to be 206±4 GPa, 205±5 GPa and 220±5 GPa, respectively. The former two values are in excellent agreement with the moduli obtained using a Berkovich tip on the same surface, viz. 207±3 GPa.

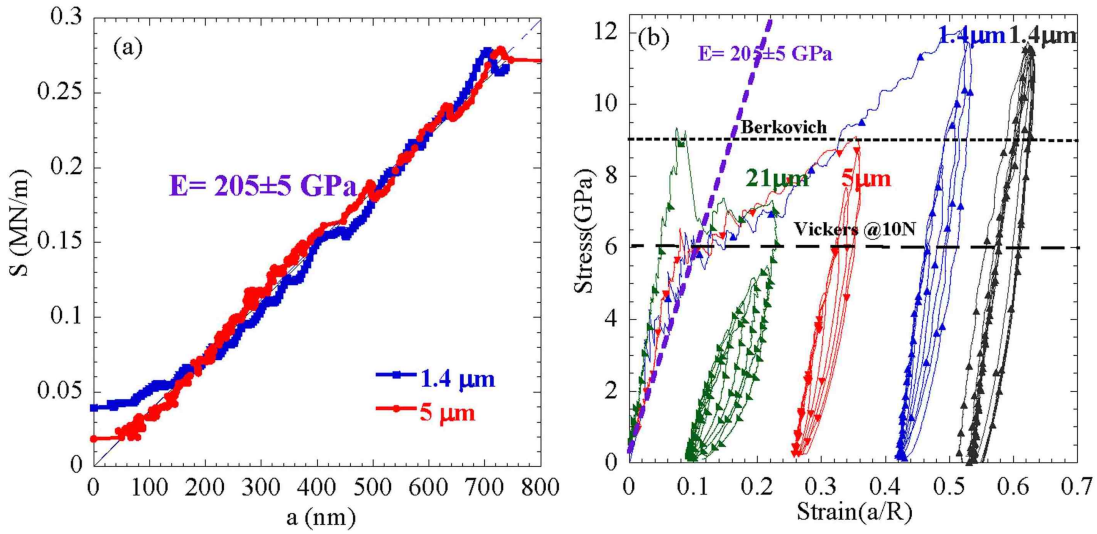

Fig. A 2.4. (a) The S vs. a curves for the 1.4 μm, 5 μm tips. (b) Typical NI stress–strain curves obtained after a given location was indented to the highest loads (550 mN for 21 μm, 100 mN for 5 μm, and 20 mN for 1.4 μm tips) for two cycles, unloaded and progressively loaded to higher stresses to obtain the nested loops (three left curves). Plot shown on extreme right shows the reproducible NI stress-strain loops for 1.4 μm indenter; it was shifted to the right from its original position for clarity. Dashed horizontal and inclined lines represent the Vickers microhardness, Berkovich hardness, and elastic moduli obtained from the S vs. a curves, respectively. Pop-ins were only observed when the 21 μm tip indenter was used.

Why E for the 21 μm tip is different is unclear at this time. One possibility for the discrepancy is that the 21 μm indenter tip may not be perfectly spherical. In the case of the 5μm and 1.4 μm indenters, the total penetration depth was kept below the spherical limit as reported by Albayrak *et al.* [152]. Regardless of the reasons for these discrepancies, they have little bearing on the conclusions reached in this work that, as shown below, rely much more on the results obtained in the plastic and/or nonlinear elastic regimes for which what occurs in the elastic regime has little influence since for all intents and purposes in the plastic regime, $h_t \approx h_c$, where h_t is the total indentation depth and h_c is the contact height.

Figure A2. 4(b) compares the stress-strain curves for the three tips. In all cases, the first cycle delineates two regimes: a linear elastic regime, followed by a plastic regime. For the 1.4 μm and 5 μm tips, the slope of the elastic regime (shown by a dashed inclined line), is consistent with the results of S vs. a plots (Fig. A2.4(a)). As noted above, the stress-strain results for the 21 μm tip indenter in the elastic regime are incorrect.

During the first cycle, in the plastic regime, the strain-hardening rate is more or less constant. More importantly, in the plastic regime, the overall shapes of the stress-strain curves are weak functions of R. Relatively, large observable pop-in events, between the elastic and plastic regimes, were *only* observed when the 21 μm tip was used.

At ≈ 6±0.5 GPa, the Vickers microhardness values (denoted by a horizontal dashed line in Fig. A2.4(b)) were measured on both un-irradiated and irradiated samples at a load of 10 N. At ≈ 9 GPa, the Berkovich hardness measured on the same surfaces is also shown as a horizontal dashed line.

In much of our work to date [75, 76, 80, 117, 122, 131, 132, 153], the deformation was initially linear, up to a pop-in stress, beyond which the deformation was plastic. As noted above, herein no pop-ins were observed for the 1.4 μm tip, and only a few for the 5 μm tip. Conversely, for the 21 μm tip, a variation in pop-in stresses was observed. The distribution of pop-in stresses can be adequately described by Weibull statistics (Fig. A2.5) and appear not to be a function of irradiation.

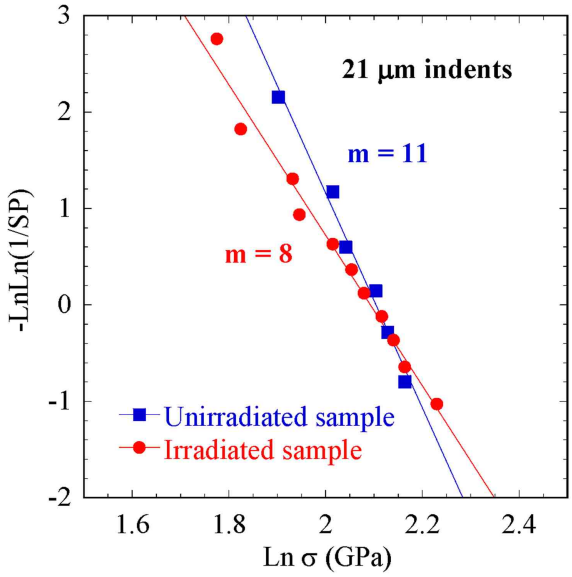

Fig. A 2.5. Plot of Weibull probabilities (SP) versus pop-in stresses (σ) for 21 μm indenter for both un-irradiated and irradiated samples. The Weibull moduli, m, are shown on the figure.

After the first cycle, two loading trajectories were followed. The first was to load the same location 20 times to the maximum load. Such experiments were carried out to investigate the reproducibility and fully reversible nature of the loops generated. Based on the results shown in Fig. A2.4(b) and the loops shown on the extreme right we conclude that these loops are highly reproducible and reversible.

The second protocol was to load the indenter to the highest load for two cycles, unload, and then reload to progressively higher loads to generate the nested loops observed in Fig. A2.4(b) [44, 77, 78, 122]. Here, as in previous work on $LiNbO_3$ [122], the shape of the loops is dependent on R. The 21 μm and 5 μm indenters yield shorter, wider loops; the 1.4 μm tip, on the other hand, results in elongated thinner loops (Fig. A2.4(b)).

All KNE solids can be characterized by three parameters, σ, ε_{NL} and W_d, all obtainable from the hysteretic stress-strain curves. At every stress, σ, W_d and ε_{NL} were estimated from the nested loops (For how ε_{NL} is defined in this work see Fig. A2.1(c)). According to Eqs. A2.4 and A2.5, W_d should scale with both σ^2 and ε_{NL} as observed in Figs. A2.6(a) and (b), respectively. The lowest correlation coefficient, θ^2, obtained from least square analysis of the results – shown in Fig. A2.6 by the solid inclined lines – is 0.97; most are > 0.98. It is obvious that the model predictions are well adhered to. The next step is to try and quantify some of the parameters to ensure that they are physically tenable. To do so the following assumptions were made: $G = c_{44} = 95$ GPa [154], $\nu = 0.25$ [146], $\gamma = 0.05$, $w = b = 0.515$ nm [155], $k = 2$ and $M = 2$. As noted above, experimentally for polycrystalline Mg, k was found to vary between 1 and 2 [56, 156, 157]. For Co, k was estimated to be 2. Reed-Hill at al. [141] assumed k = 2 for $(11\bar{2}1)$ twins in Zr. Given that the $(11\bar{2}1)$ twin is a special case of a kink boundary, for which a dislocation loop is nucleated every c-lattice parameter, i.e. D = c, it is reasonable to assume this value here as well [158]. This comment notwithstanding, the objective of this numerical exercise is not to obtain absolute and accurate values for say the CRSS's. The purpose is more to show that our model is consistent with the results obtained and can in

principle explain them without resulting in values that are not physical. This is especially true here given the very complex, non-uniform, state of stress under the nanoindenter and all the simplifying assumptions made.

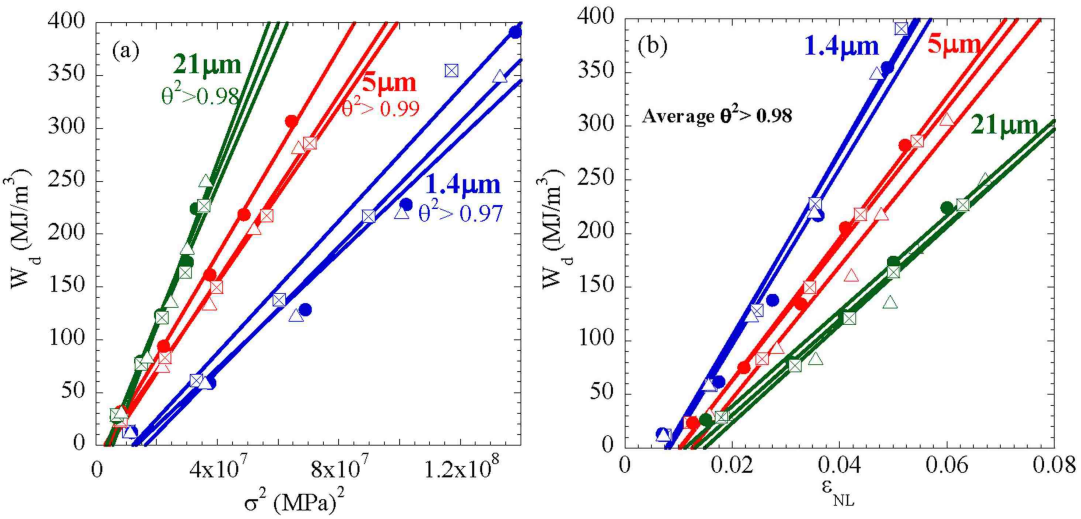

Fig. A 2.6. Plots of, (a) W_d versus σ^2 and, (b) W_d versus ε_{NL}, as a function of indenter radius. The slope dependence on the tip size is clear in (b). Each line represents a different location.

According to our model the x-axis intercepts of Fig. A2.6(a) represent the threshold stresses, σ_t needed to nucleate the IKBs. Using these σ_t values and the assumptions made above, the lengths of the IKBs, or domain sizes, 2α, can be estimated from Eq. A2.1. Once 2α is known, $2\beta_x$ and $2\beta_y$, at any σ can also be calculated from Eqs. A2.2.

According to Eq. A2.5, the slopes of the lines in Fig. A2.6(b) should be equal to $3k\Omega/b$. Assuming k= 2, Ω/b can thus be calculated. Note that according Eq. A2.5, the lines in Fig. A2.6(b) should go through the origin, when in fact they do not. The exact reason for this state of affairs is most probably due to the presence of other non-linear

reversible strains that are not due to IKBs. Such strains were observed when polycrystalline Co samples were compressed [55]. However, this discrepancy is not believed to considerably affect the slopes.

The reversible dislocation density can in turn be calculated from Eq. A2.6. The calculated values for σ_t, 2α, N_k, Ω/b, $2\beta_x$, $2\beta_y$ and σthe latter three at 5 GPa, are listed in Table A2.1.

Table A 2.1. Summary of various measured and calculated parameters as a function of R. The following was assumed: $\gamma = 0.05$, w = b = 0.515 nm, G = 96.8 GPa, $\nu = 0.25$, M = 2 and k = 2.

Tip Radius (μm)	1.4	5	21
σ_t(GPa) (From Fig. A2.6(a))	3.2 ± 0.1	2 ± 0.2	1.8 ± 0.2
2α (nm) (calculated)	114±5	292±112	361±60
$N_k\alpha^3$	0.45	0.78	1.78
$N_k(m^{-3})$	2.2×10^{21}	2.5×10^{20}	3.0×10^{20}
Ω/b (MPa)	1.3×10^3	1.1×10^3	0.7×10^3
$2\beta_x$ (nm) at 5 GPa	44 ± 2	113 ± 40	140 ± 22
$2\beta_y$ (nm) at 5 GPa	59 ± 6	151 ± 57	186 ± 31
$2\beta_y$ (nm) (Fig. A2. 7. SEM)	49 ± 5	90 ± 25	180 ± 40
ρ (m^{-2}), at 5 GPa	4×10^{15}	3×10^{15}	5×10^{16}

A2.3.2. Microstructural Observations

Despite the fact that all of the tips used were spherical, the indentation imprints in the SEM clearly exhibited three fold symmetry (Fig. A2.7). The three-fold symmetry is clearest in Figs. A2.7(b) and (c). The widths of the domains, for the 1.4 μm, 5 μm and 21 μm, shown in Figs. A2.7(a) to (d), respectively, were found to be a function of R.

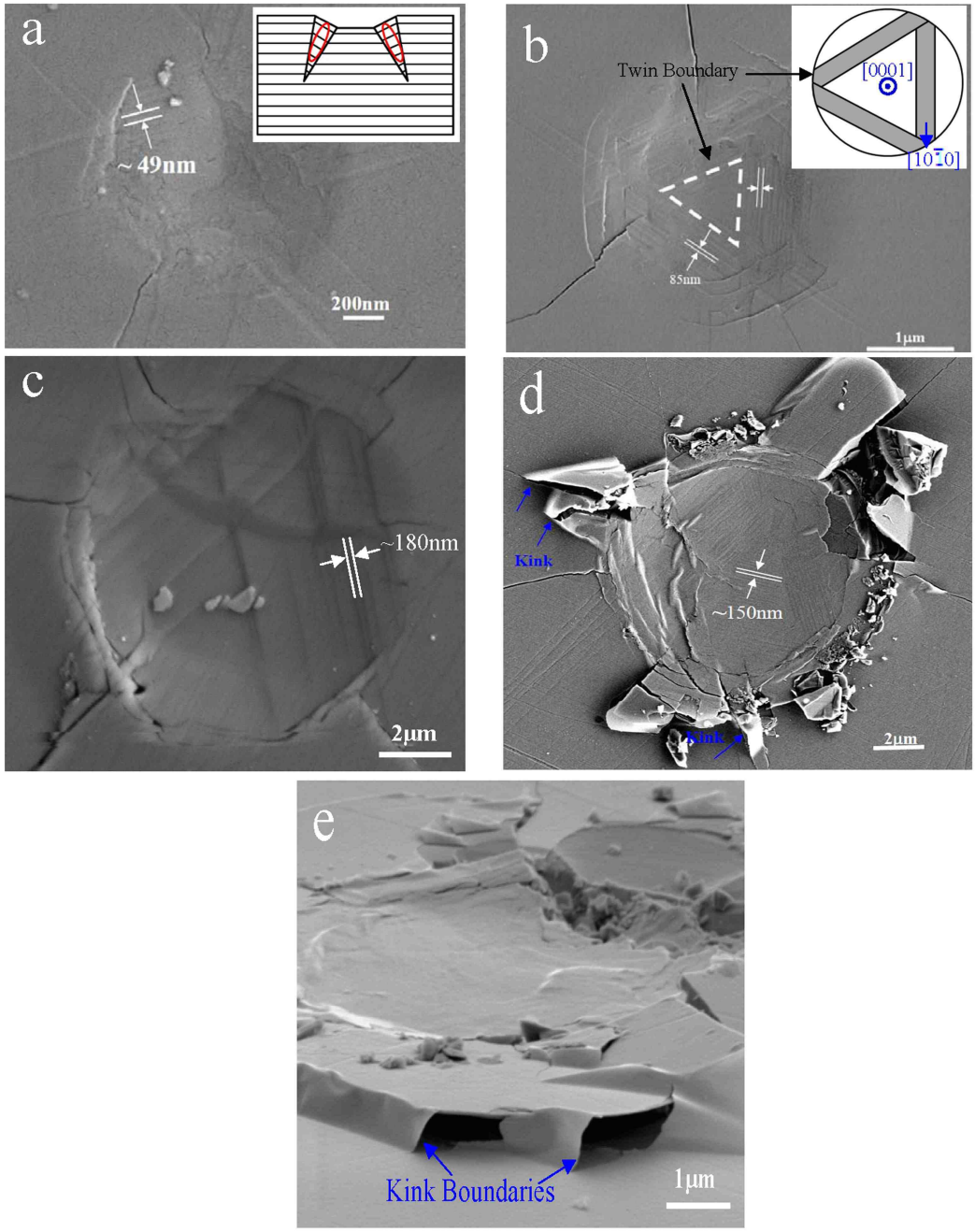

Fig. A 2.7. SEM images of NI mark on unirradiated sample made with the, a) 1.4 μm tip loaded to 20 mN after first cycle; b) 5 μm tip loaded to 100 mN after first cycle; 21 μm tip loaded to 550 mN after c) 5 cycles, d) 20 cycles; e) same as (d) but tilted 75°. Note three-fold symmetry of the linear surface features best seen in b and c. The top inset in (a) is a schematic of domains forming in the twins. Top inset in (b) shows three-fold symmetry of twins which form in $LiNbO_3$ adapted from Ref. [159]. The features with very sharp radii of curvature in (d) and (e) are kink boundaries.

A2.3.3. Irradiation Damage

Almost all of the stopping power for the 2 MeV He^+ ions in $LiTaO_3$ is attributable to electronic stopping. Nuclear stopping only plays an appreciable role near the ion end-of-range (at depths from 4.0 – 4.8 μm). The *damage energy*, ν(E), which is the fraction of the total energy (E = 2 MeV) that is consumed in *ballistic* damage events (i.e., kinematic scattering by atomic nuclei in the target) is only 0.0092 MeV, or 0.46 % of the primary ion energy.

The RBS spectra from the unirradiated and irradiated samples are shown in Fig. A2.8 and indicated that the un-irradiated sample was of a high quality. The spectrum did not change after irradiation (it was slightly higher but within the statistical error of measurements) confirming that the defect concentration in the near surface region is small and below the sensitivity level. These RBS spectra correspond to a near surface region, ~ 2 μm thick.

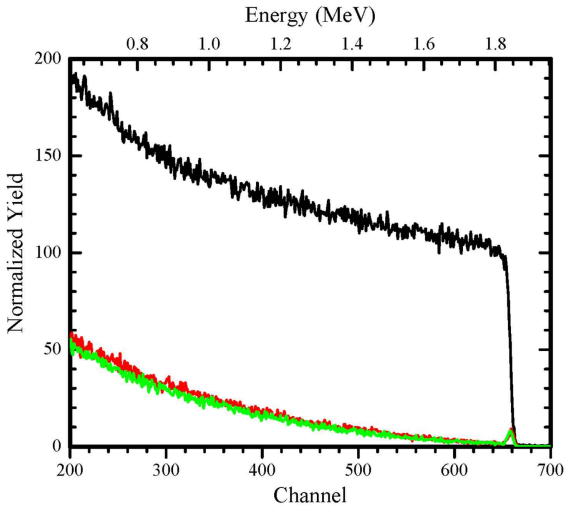

Fig. A 2.8. RBS spectra from unirradiated random (black); unirradiated aligned (red) and irradiated aligned (green). The χ_{min}=l.5% (ratio of aligned to random yield just below the surface peak) indicated very good quality of the unirradiated sample. The aligned spectrum did not change after irradiation because the concentration of defects in the near surface region is quite small.

A2.4. Discussion

Given that: a) Doukhan et al. [130] reported that $(10\bar{1}2)[10\bar{1}1]$ twins as the only deformation system in $LiTaO_3$ during compression along the c-axis, b) the twinning system in $LiTaO_3$ is identical to that of $LiNbO_3$ [130], c) The traces and steps shown in Fig. A2.7 are similar to those observed in $LiNbO_3$ [122], and, d) the three fold symmetry of the indentation marks are very similar to those reported by Park et al. in $LiNbO_3$ [159-161] (see inset in Fig. A2.7(b)), it is reasonable to conclude that the traces observed in Fig. A2.7 are due to the formation of $(10\bar{1}2)[10\bar{1}1]$ twins.

In our previous paper [122], we argued that since the loading was along [0001], the distance between the lines shown in Figs. A2.7(a), (b), (c) and (d), is the width of the domains, 2β, and not their lengths, 2α. A schematic of what we believe happens is shown in the top inset in Fig. A2.7(a). There is no reason to believe things are different here. Also, shown in Figs. A2.7(d) and 7(e) are some exceedingly sharp bends that can *only* be due to kink boundaries which is strong indirect evidence that kinking must be operative in this material.

Based on the results shown above, and those listed in Table A2.1, and by analogy with $LiNbO_3$, we conclude that $LiTaO_3$ is a KNE solid. As discussed previously [74-76, 124, 131, 132], the deformation of KNE solids under cyclic spherical NI can be explained by invoking the formation and annihilation of spontaneously reversible IKB dislocation loops.

According to the results shown in Fig. A2.3, it is obvious that after the first cycle, hysteretic loops - whose areas, W_d, get smaller until they reach a steady-state value that is no longer a function of cycling – evolve [75, 76, 78, 122, 124, 132]. These fully

reversible and reproducible loops are quite similar to those observed in other KNE solids. The different parameters, calculated from the nested loops, all yield reasonable results (Table A2.1).

The resulting reversible dislocation densities (Table A2.1) are comparable to heavily deformed metals [85] and are, again, reasonable considering they are calculated at a stress of 5 GPa [122]. It is important to note that despite the differences in the shape and size of the loops shown in the Fig. A2.4(b), at comparable stresses, ρ is a weak function of R. The importance of this conclusion lies in the fact that the crystal responds to the applied stress by forming dislocation loops, whose total lengths per unit volume, are more a function of σ than R [122]. Note this conclusion is valid for the three tip sizes even though the 2β values for the 5 μm indents do not match with those of the 1.4 and 21 μm tips.

The σ_t values shown in Table A2.1, decrease with increasing R. As postulated in our previous work [122], this is most probably due to the shrinking of domain size, 2α. For smaller R values, the domains are smaller and thus – from Eq. A2.1 - the threshold stresses should be larger, as observed (Fig. A2. 6 and Table A2.1).

When the NI stress-strain responses of the irradiated and un-irradiated surfaces are superimposed (not shown), they were, within the resolution of our experiments and experimental scatter, identical. Said otherwise, the irradiation did *not* affect the stress-strain curves either before or after the yield points.

Further evidence that the irradiation had little effect on the response is shown in Fig. A2.5. The mean and standard deviations of the pop-in stresses for the irradiated sample was 2.059±0.14; that for the un-irradiated sample was 2.205±0.09. Clearly these values

with their uncertainties overlap. It follows that the difference we see in Fig. A2.5 cannot be significant. This is especially true since taking these values at face value implies that irradiation increased the pop-in stresses, a conclusion which is difficult to reconcile with our previous work on mica that showed that the pop-in stresses deceased with defect concentration [117]. The same is true here; it is difficult to argue for a mechanism where irradiation would somehow suppress the pop-in stresses.

The reason for this state of affairs is believed to be the mild nature of the irradiation. Using a modified Kinchin-Pease equation to estimate the number of displaced atoms per incident ion [162], we find that the number of displaced atoms per ion is ~ 92 (assuming the displacement threshold energy, E_d, for all target atoms - Li, Ta, and O - is given by E_d = 40 eV which is an arbitrary assumption, often used as a reasonable guess for ceramics when there are no measured values available). The peak displacement damage dose is approximately 0.02 dpa at a target depth of ~ 4.6 μm. However, the average displacement damage dose is only about 0.001 dpa over the first 2 μm of target depth.

In summary, over the first two microns of target depth, the 2 MeV He^+ ions implanted to a fluence, $\Phi = 1.67 \times 10^{15}$ He/cm^2, produce only about one Frenkel pair per 1000 target atoms. About 99.9% of the ion stopping over this target volume is due to electronic stopping. Unless $LiTaO_3$ is highly susceptible to radiolysis (i.e., permanent atomic displacements due to electronic excitations and bond breaking), then these irradiation conditions will produce little in the way of permanent point defects or atomic disorder. This would explain why no detectable changes in mechanical properties were

observed in the NI experiments. In future experiments, ion fluences that will produce more ballistic damage over the first two microns will be used.

For reasons that are not entirely clear, twins are easier to nucleate when the sharper tips are used. This is best seen by the lack of pop-in stresses when the 1.4 and 5 μm tips are used. With the 21 μm tip, the strain energy has to reach a certain value before the twins are nucleated. This is an important observation that needs to be further looked into since it signifies that the nucleation of twins depends on more than the stress under the indenter.

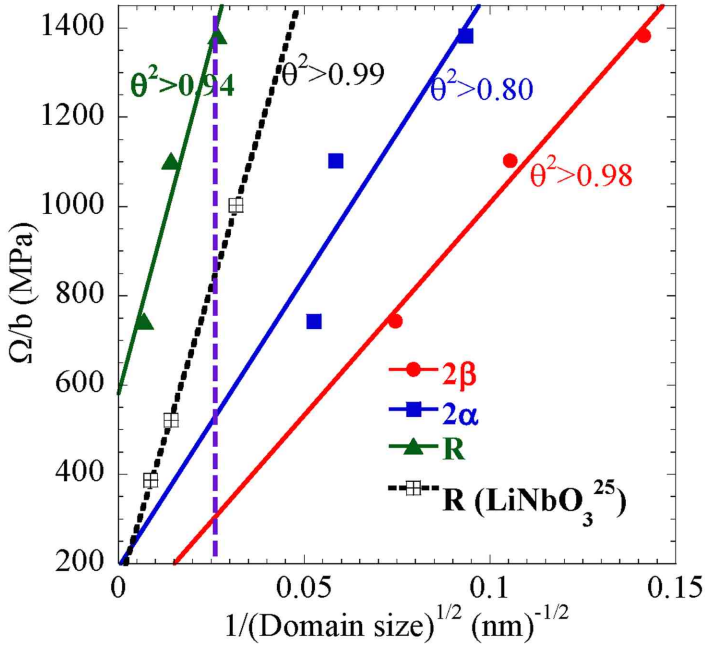

Fig. A 2.9. Hall-Petch-like correlation between the CRSS of the IKB dislocations (Ω/b) and 1/√domain size, where the domain size is assumed to be 2α, or 2β or R. The black dashed inclined line represents Ω/b vs. 1/√R for $LiNbO_3$ [122].

In our work on the MAX phases we have shown that Ω/b or the CRSS of the IKB dislocations is inversely proportional to the square root of the grain or domain size [46]. To check whether this is true here we plotted Ω/b vs. 1/√2α Fig. A2.9). A decent

correlation was found. If one plots Ω/b vs. $1/\sqrt{2}\beta$ measured directly from the SEM micrographs (see below) an even better correlation is found (Fig. A2.9). Since α is proportional to β, this correlation again is consistent with Ω/b values that follow a Hall-Petch like relationship. Lastly one can also plot Ω/b vs. $1\sqrt{R}$; again the correlation is acceptable. Note that the correlation found in Fig. A2.9 is not a result of a circular argument, since α is calculated from σ_t and the CRSSs are calculated from the totally independent measurements of W_d and ε_{NL}. The correlations between Ω/b vs. $1\sqrt{R}$ or $1/\sqrt{2}\beta$ are thus also totally independent.

When Ω/b is plotted vs. $1/\sqrt{R}$ for the $LiNbO_3$ single crystals [122], – shown as a black dashed line in Fig. A2.9 - using the methodology used herein, the correlation is once again excellent. (The calculations of Ω/b made in Ref. [122], made slightly different assumptions to reach different values of Ω/b). Not only is the correlation excellent, but the resulting line is almost parallel to that for $LiTaO_3$ (green line at extreme left in Fig. A2.9). This is an important result for the following reason: If one makes the reasonable assumption that the CRSSs of the IKB dislocations is proportional to c_{44}, then the ratio of CRSSs for $LiTaO_3$ and $LiNbO_3$ should be ≈ 1.62. Gratifyingly, the ratio of CRSSs - for a given domain size denoted by the vertical dashed line - obtained from the results shown in Fig. A2.9 is ≈ 1.6. Whether this is coincidental or not, needs more work on other crystals with different c_{44} values, but is certainly consistent with the ideas proposed herein.

Comparing both calculated and measured values for $2\beta_y$ in Table A2.1 shows that the calculated values from the model and measured values from SEM images for 1.4 μm and 21 μm are in a good agreement with each other. For reasons that are unclear, for the 5 μm

indents the calculated values differ from the measured ones. Also the calculated length of the IKBs, 2α, for 1.4 μm, 5 μm and 21 μm indents are quite reasonable and scale with the indenter radii.

Based on the totality of our results, the following scenario for what happens under the spherical NI tips can be recreated. At pop-in for the 21 μm indenter, or at the yield points for the other two tips, twins form. These twins, in turn, rotate basal planes into orientations that are more amenable for basal slip. Concomitantly, or as a result, the single crystal is fragmented into much smaller domains, with a size that scales with R. At a threshold stress - that is inversely proportional to the square root of the domain size - IKBs nucleate, within these domains. The IKBs are fully reversible and the to-and-fro motion of the IKB dislocations dissipates substantial amounts of energy.

Note that IKBs cannot form in single crystals because once they become critical they would simply run to the ends of the crystal and devolve into mobile dislocation walls [66]. Equation A2.1 – derived using a Griffith-like approach - is based on that scenario. IKBs can thus only form when there are grain, twin, or domain boundaries that confine them. During NI, these domains form during the first cycle, especially after pop-in events or yield points. It was expected that irradiation defects on the surface reduce the pop-in stress.

We note that the Vickers hardness values and the minima in the stress-strain curves after pop-ins or simply the yield points, if pop-ins are not present (Fig. A2.4(b)) are in excellent agreement. This is an important result since it indirectly confirms our methodology for converting NI load/displacement to NI stress-stain curves. The same observation was made in most of our other previous work [122, 124, 131]. The fact that

the Berkovich modulus is also in good agreement with our value is another independent confirmation for our NI methodology.

Lastly, it is worth emphasizing that given the many simplifying assumptions made in our KNE model, such as assumes a uniform uniaxial stress state, which is far from what is happening during NI, to the definition of strain to be a/R and other simplifying assumptions, the agreement between theory and experiment has to be considered excellent. One reason for this state of affairs is that the calculation of contact stresses is reasonably straightforward. Moreover, since the non-linear strains are small, the results obtained are a weak function of the exact definition of strain. These comments notwithstanding it is hereby acknowledged as noted above, that the absolute values of CRSS calculated herein have to be taken with a large grain of salt because of all the aforementioned simplifications, etc.

A2.5. Conclusions

The deformation response of C-plane $LiTaO_3$ single crystals was studied using spherical indenters with three different radii. When the load/displacement results are converted to NI stress-strain curves we conclude that

(a) During the first NI cycle two regimes are observed: a linear elastic regime, followed by a plastic regime, in which strain-hardening is observed. For the smaller tips, plastic deformation is accompanied by $(10\bar{1}2)$ twins. In the case of the 21 μm indenter the elastic regime was separated from the plastic regime by pop-ins. At the pop-ins, twins are nucleated.

(b) The elastic moduli determined from S vs. a curves of the 1.4 μm and 5 μm tips was 205±5 GPa. The corresponding Berkovich modulus is 207±3 GPa.

(c) No noticeable effect of the irradiation was observed on the NI results of the sample. The main reason for this state of affairs is believed to be the mildness of the irradiation conditions.

(d) When spherical indenters were repeatedly loaded to a given maximum load, fully reversible, reproducible hysteresis loops are obtained. The Ω/b values calculated from the model were inversely proportional to the square root of the domain size.

(e) The ratio of the CRSSs for $LiNbO_3$ and $LiTaO_3$ determined from our IKB-based microscale model were found to be roughly equal to the ratios of the shear moduli of these two compounds.

.A3. On The Oxidation of Ti_2GeC in Air

Published in: Babak Anasori, Elad N. Caspi, Yasmine Elraheb and Michel W. Barsoum, Journal of Alloys and Compounds, 580, 550-557 (2013). Copyright (2013) Elsevier.

Abstract

Herein we report on the oxidation of bulk Ti_2GeC in air in the 600°C to 800°C temperature range. At 600 ºC, and up to 500 h, the oxidation kinetics are sub-parabolic and the rutile TiO_2 layer formed is adherent and protective. At 700 ºC and 800 ºC the kinetics are parabolic up to 100 h before becoming linear. X-ray diffraction confirmed the presence of two rutile structures, TiO_2 and GeO_2, and a hexagonal GeO_2 on the oxidized surfaces. The oxidation occurs by inward diffusion of oxygen through a rutile $(Ti_{1-x}Ge_x)O_2$ solid solution with $x \leq 0.07$. Additionally, and throughout the entire temperature range studied, an oxygen-induced decomposition - occurring predominantly at the oxide/carbide interface - results in the formation of an elemental Ge-rich phase. If the rutile layer is not protective, the latter oxidizes into hexagonal GeO_2.

A3.1. Introduction

The $M_{n+1}AX_n$ (MAX) phases are layered, machinable hexagonal solids, in which nearly closed packed layers of M group elements (M represent early transition metals) interleaved with pure layers of A group elements (mostly groups 13 and 14) and X is C or N that fill the octahedral sites of M layers. More than 60 MAX phases are known to exist. These solids offer an unusual, and sometimes unique, combination of properties. Like metals, they are excellent electrical and thermal conductors [35, 40], they have superb machinability, and are damage tolerant. Like ceramics, many of them are stiff, resistant to chemical attack and some are creep and oxidation resistant [35, 40, 163].

Since this is the first report on the oxidation of Ti_2GeC, there are no previous studies with which to compare our results. However, it is instructive to review the short-term oxidation results of closely related compounds. The oxidation of Ti_3SiC_2 in air results in the formation of two layers; an inner layer comprised of titania and silica, the former in the form of rutile, and an outer layer that is pure rutile [164-166]. Sun et al. reported the oxidation kinetics to be parabolic up to 20 cycles of oxidation at 1100ºC [164]. It is also reported that oxidation kinetics of Ti_3SiC_2 at 1000ºC or higher are initially parabolic then become linear [166]. In the 1000-1300ºC temperature range Ti_2AlC shows excellent oxidation resistance due to the formation of a dense and adherent alumina layer [167-170]. However, for both Ti_3SiC_2 and Ti_2AlC, it was reported that formation of protective oxide scale is a function of purity of the samples [40, 171].

More relevant to this work is the oxidation of Ti_3GeC_2 in air in the 700 to 900 °C temperature range [172]. At 700 °C, the oxide layers were protective and the oxidation kinetics was parabolic. At 800 °C, and higher temperatures, the oxide layers were not

protective, and the kinetics were linear. In both cases the oxidation occurred by the inward diffusion of oxygen through a rutile-based $(Ti_{1-y,}Ge_y)O_2$ solid solution, with $y <$ 0.1. In addition, thin layers of solid solutions with higher volume fraction of GeO_2, as well as pores, were observed in the oxide scales. At 800 °C and higher temperatures, a layer of elemental Ge and a Ti-oxy-carbide phase were observed at the oxide/Ti_3GeC_2 interface. The most likely explanation for the presence of Ge is the thermal decomposition of Ti_3GeC_2 in the presence of oxygen. It is reasonably well established that the MAX phases do not melt but decompose peritectically into an A-group rich phase and MX (such as TiC). The peritectic decomposition temperature can be a strong function of impurities, especially oxygen [169]. A similar oxygen-induced decomposition also occurred when some of the $Ti_{n+1}AlC_n$ MAX phases were oxidized in air [169].

The purpose of this paper is to report, for the first time, on the oxidation behavior of Ti_2GeC in air in the 600 to 800 °C temperature range.

A3.2. Experimental Details

To fabricate a Ti_2GeC sample, a stoichiometric mixture of Ti, C, and Ge powders was ball milled in a plastic container with alumina balls for 24 h. The powder mixture was then placed in a graphite die, and heated under vacuum, at 5 °C/min – in a graphite heated hot press (HP; Series 3600, Centorr Vacuum Industries, Somerville, MA) – up to 900 °C and held for 1 h. The sample was then further heated at the same rate to 1200 ºC and soaked for 4 h before furnace cooled. A load corresponding to a stress of ≈ 45 MPa, was applied at 600 °C and maintained throughout the run. Rectangular specimens ≈ 4 x 4 x 10 mm^3 were cut using a diamond saw. All sides were polished down to 1200 grit SiC paper prior to carrying out the oxidation studies.

The oxidation study was carried out in air at 600 °C, 700 °C and 800 °C by placing the samples in alumina crucibles that were in turn placed in a box furnace. In order to assess the experimental error, 8 rectangular samples were used for each temperature. To measure the weight gain, the oxidation tests were interrupted and the samples were removed from the furnace at the temperature and quenched to room temperature in air. After the weight gain was measured using a balance (HRB 100, Tree Electronic Precision, China) with a resolution of 1 mg, the samples were placed back in the furnace, which was at the oxidation temperature. In other words, to quantify the oxidation kinetics all the samples were harshly thermally cycled.

In order to explore the effects of thermal cycling on the oxidation kinetics and oxide scales, one specimen was kept in the furnace at 700 °C for 170 h. Its weight gain was then compared to samples that were thermally cycled for the same total cumulative time at the same temperature.

The oxidized bulk samples were cross-sectioned, mounted and polished down to 1 μm with diamond slurries. The microstructural observations and oxide layer thicknesses estimation were carried out using a scanning electron microscope, SEM, (Zeiss Supra 50VP, Germany) equipped with an energy-dispersive spectroscope (EDS) (EDAX, Inc., Mahwah, NJ). To determine the chemical composition of the oxide layers by EDS, at least three readings were averaged for each phase or microconstituent.

X-ray diffraction (XRD) patterns from the surfaces of the as synthesized sample and oxidized samples at 600ºC for 55 h and 500 h, 700 °C for 45 h, 100 h and 340 h, and at 800 °C for 40 h and 340 h were obtained using a Rigaku diffractometer (Rigaku SmartLab, Japan), in the Bragg-Brentano configuration. The diffractograms were

collected using step scans of 0.02 in the 10°–80° 2**θ** range, with a step time of 1s. Scans were made with Cu Kα radiation (40 KV and 30 mA). The XRD beam is limited by soler collimators forming a cross-section of roughly 5 mm × 5 mm. This relatively large measured area is assumed to be representative of the oxide layer of the studied samples. The accuracy of the diffractometer in determining lattice parameters, and its instrumental peak-shape function parameters were found using Si (X-ray Diffraction Accessories, State College, PA), and LaB_6 (NIST 660B) standards.

In order to determine the nature of the different oxides formed, powdered samples were prepared by filing the Ti_2GeC sample with a diamond file. The resulting powders were then oxidized - at the same temperatures as the bulk samples - for 40 h, crushed in a mortar and pestle. XRD diffractograms of the powders were then obtained.

All diffractograms were analyzed by the Rietveld refinement method, using the FULLPROF code [90, 91]. A systematic shift of -0.06% is found in the lattice parameters' evaluation as compared to both Si and LaB_6 standards' reported value. Initial analysis indicated the presence of three oxidation products: a hexagonal GeO_2 – henceforth referred to as h-GeO_2 – and TiO_2 and GeO_2 both in the rutile structure, henceforth referred to as r-TiO_2, and r-GeO_2, respectively. For each data set a model containing r-TiO_2, r-GeO_2 and h-GeO_2 was refined. The existence of small amounts of TiC, Ge, and Ti_2GeC was also considered. The Thompson-Cox-Hastings pseudo-Voigt model was used to refine the peak-shape of each phase's reflections. Lattice strain, and particle size were also estimated assuming isotropic Lorenzian and Gaussian contributions to the peak shape function [92].

A3.3. Results

The XRD pattern of the as synthesized Ti_2GeC sample showed the existence of minor TiC, and Ge impurity phases. Rietveld refinement analysis of the data was used to estimate their quantity as 8(1) wt% and 1.0(5) wt%, respectively (Fig. A3.1(a)). SEM micrograph of the as synthesized polished surface shows uniform dispersion of these impurities in the sample (inset in Fig. 1a). Rietveld analysis of the XRD patterns of the post-oxidized samples revealed good agreement between model and measured data ($\chi^2 \sim$ 1.5 for all cases, cf. Fig. A3.1(b)).

XRD diffractograms of the oxidized bulk surfaces after 55 h and 500 h at 600 ºC, after 45 h and 340 h at 700 °C are shown in Fig. A3.2(a) and (b), respectively. Figure A3.2(c) compares the XRD diffractograms of the Ti_2GeC powders oxidized at 800 °C for 40 h to the oxidized bulk surface after 340 h at the same temperature. At all the temperatures, the presence of r-TiO_2 is unambiguous. Additionally, r-GeO_2 (argutite) and h-GeO_2 were also detected.

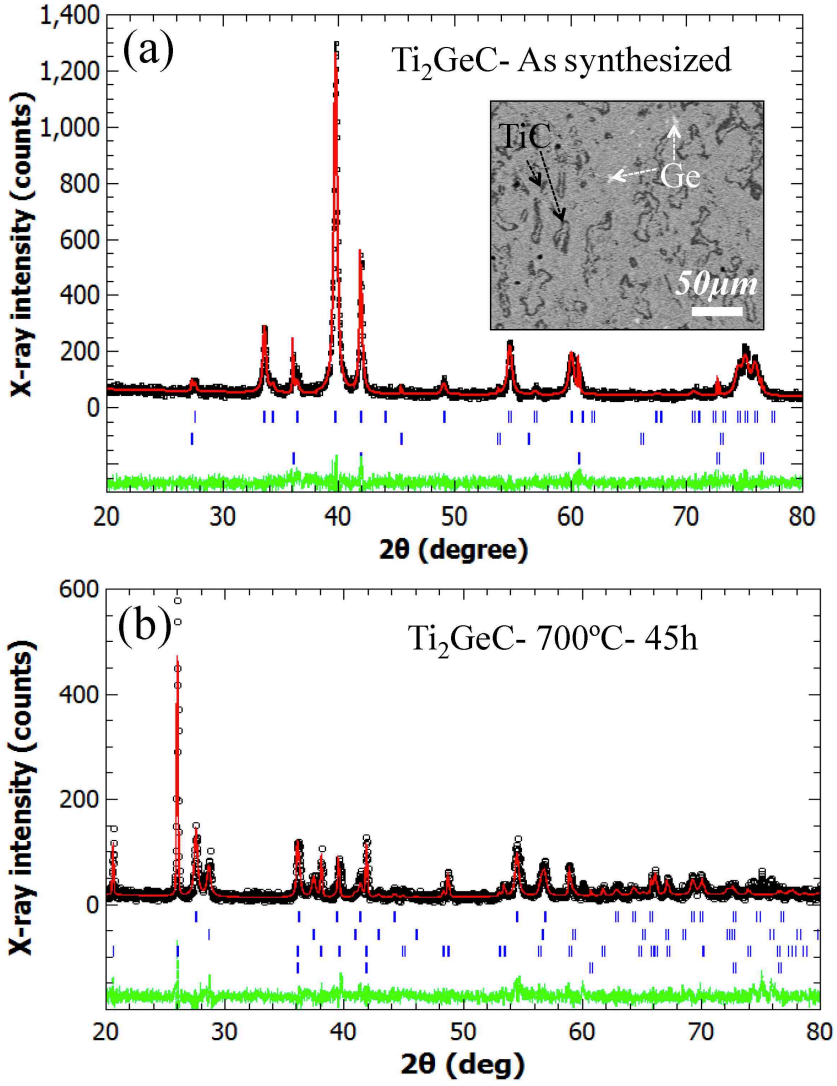

Fig. A 3.1. Rietveld analysis of the X-ray diffraction data as measured using a Rigaku SmartLab diffractometer with Cu Kα radiation of, a) the as synthesized Ti_2GeC. Open circles, solid line, and dashed line in the bottom, represent the measured data, refined model, and the difference between the two, respectively. The three rows of vertical tags represent the calculated Bragg reflections' positions of the Ti_2GeC (1st row), TiC (2nd) and Ge (3rd) phases. Top inset shows the backscattered electron SEM image of the as synthesized Ti_2GeC surface. b) the Ti_2GeC powder oxidized at 700C for 45 h. Open circles, solid line, and dashed line in the bottom, represent the measured data, refined model, and the difference between the two, respectively. The four rows of vertical tags represent the calculated Bragg reflections' positions of the r-Ti_2O (1st row), r-GeO_2 (2nd), h-GeO_2 (3rd), and TiC (4th) phases.

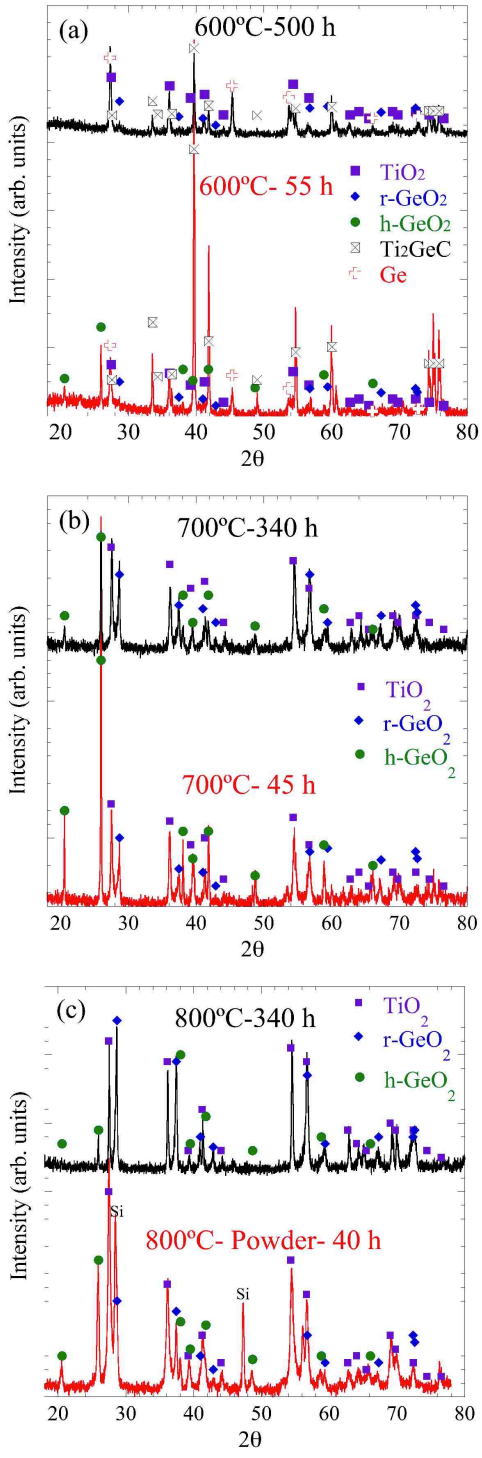

Fig. A 3.2. XRD diffractograms of bulk Ti_2AlC sample oxidized at, a) 600 ºC for 55 and 500 h, b) 700 °C for 45 and 340 h, and, c) 800ºC for 340h and powder sample oxidized at 800 °C for 40 h.

Figure A3.3 summarizes the weight percentage of 6 phases – r-TiO_2, r-GeO_2, h-GeO_2, Ti_2GeC, TiC and elemental Ge – as determined from Rietveld analysis for the different oxides. The first column in Fig. A3.3 is for the as synthesized Ti_2GeC sample prior to oxidation. Columns 2 and 3 in Fig. A3.3 are for samples oxidized at 600 ºC for 55 h and 500 h, respectively. Columns 4 to 6 are for samples oxidized at 700 °C for 40 h, 100 h and 340 h, respectively. Column 7 is for a powder oxidized at 800 °C for 40 h. The results for the last three columns were taken from an oxide layer that formed after 340 h at 800 °C. When the sample was cross-sectioned, a part of the oxide layer cleaved off, leaving a thin oxide layer on the substrate. This allowed us to obtain three different XRD diffractograms; one from the outermost layer (column 8 in Fig. A3.3), one from the surface that was adjacent to the attached layer (column 9 in Fig. A3.3), and one from the layer that was still attached to the substrate (last column in Fig. A3.3), referred to in Fig. A3.3 as top, intermediate and bottom, respectively.

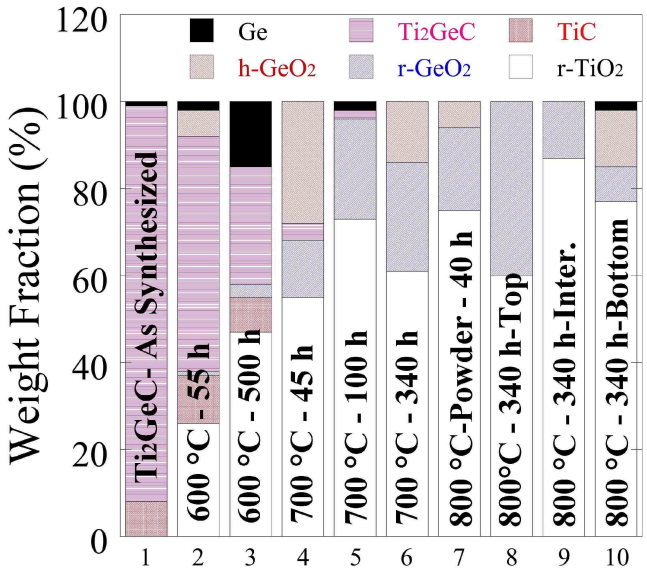

Fig. A 3.3. The Rietveld analyses results indicating the various wt. % of the different phases in the as synthesized sample and oxide layers under various conditions summarized in the vertical bars.

Rietveld analysis of the results also yielded the lattice parameters of each oxide phase (Table A3.1), their weight percentages and an estimation of their particles sizes. Notably, the r-TiO_2 (r-GeO_2) *a* and *c* lattice parameters of the 700 ^oC, and 800 ^oC oxidation samples are smaller (larger) than those previously reported for pure rutile (Table A3.1) [173, 174]. In contrast, both rutile phases' lattice parameters in the 600 ^oC oxidation samples are comparable to the previously published data for the pure phases (Table A3.1). Lastly, the Rietveld analysis also showed that the grain sizes of the r-TiO_2 and r-GeO_2 phases were of the order of 30 to 50 nm for all runs except the sample oxidized for 340 h at 800 °C. For the latter, the grain sizes of the r-TiO_2 and r-GeO_2 phases were closer to 100 nm. Also for the latter conditions, the grain size of the h-GeO_2 phase was ≈ 300 nm. In all cases the lattice strains were quite small (< 1.6%).

Table A 3.1. Summary of lattice parameters of h-GeO_2, r-GeO_2 and TiO_2 obtained from Rietveld refinement analysis of the XRD measurements of Ti_2GeC samples oxidized at 600 ºC, 700 ºC and 800 ºC. Also listed are the published lattice parameters h-GeO_2, r-GeO_2 and TiO_2. Numbers in parentheses represent the refinement (statistical) error on the last digit. The systematical error in the lattice parameters' evaluation is estimated as -0.06%.

Conditions	r-TiO_2		r-GeO_2		h-GeO_2	
	a (Å)	c (Å)	a (Å)	c (Å)	a (Å)	c (Å)
From literature	4.602(6)	2.970(4)	4.398(3)	2.8617(6)	4.9854(3)	5.6481(9)
600^{o}C – 55h	4.603(1)	2.966(2)	4.405(1)	2.857(4)	4.9826(8)	5.648(2)
600^{o}C – 500h	4.6034(6)	2.9675(5)	4.402(2)	2.861(3)	-	-
700^{o}C – 45h	4.580(1)	2.9561(7)	4.413(1)	2.8652(9)	4.984(1)	5.649(1)
700^{o}C – 100h	4.5816(5)	2.9558(4)	4.4073(6)	2.8631(5)	-	-
700^{o}C – 340h	4.577(2)	2.953(1)	4.407(2)	2.865(1)	4.986(2)	5.651(2)
800^{o}C – 40h - powder	4.576(3)	2.950(2)	4.406(3)	2.865(2)	5.008(3)	5.632(4)
800^{o}C – 340h – outermost layer (Top)	4.5736(6)	2.9505(4)	4.4086(7)	2.8639(5)	-	-
800^{o}C – 340h – adjacent to the attached layer (Intermediate)	4.584(1)	2.9560(8)	4.406(1)	2.8667(9)	-	-
800^{o}C – 340h – attached layer (Bottom)	4.586(1)	2.9572(7)	4.405(1)	2.8641(9)	4.990(1)	5.652(1)

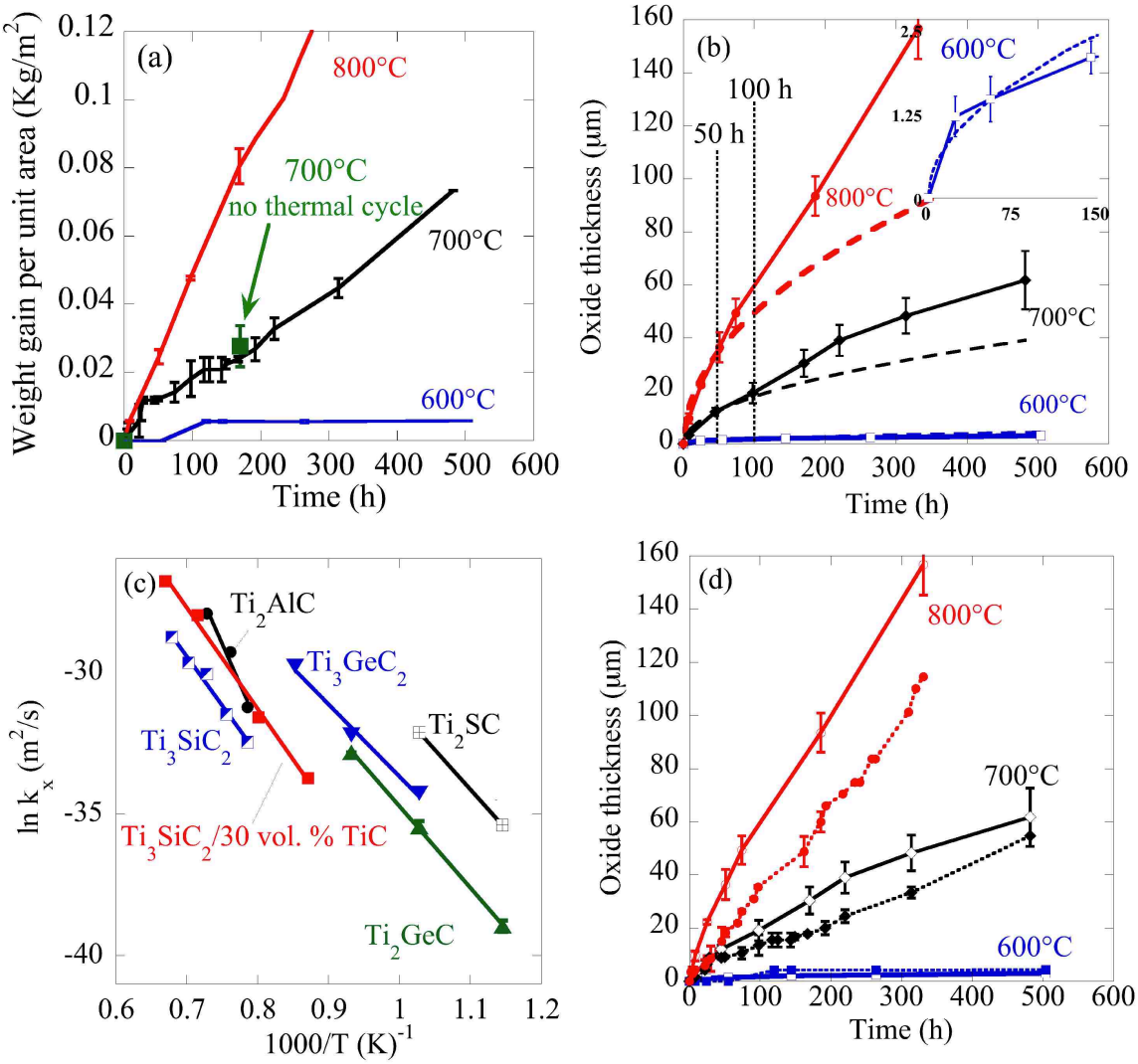

Fig. A 3.4. a) Weight gain normalized by surface area, as a function of time and temperature; b) oxide thickness as a function of time and temperature. The dashed lines represent Eq. 2 in text, plotted using k_x values obtained from least-squares fits of x^2 *vs.* t curves (not shown) at short times (t < 50 h), c) Arrhenius plot of k_x. Also shown are the results for Ti_3GeC_2 [172], Ti_2AlC [169], Ti_3SiC_2, Ti_3SiC_2– 30 vol. % TiC [166], and Ti_2SC [175] and, d) comparison of oxide thicknesses x_w (dashed lines), calculated from the weight gains assuming reaction 2 is operative and x (solid lines), directly measured in the SEM. When not shown, error bars are smaller than symbols size.

Figure A3.4a plots the weight gains per unit area of samples oxidized at 600 °C, 700 °C and 800 °C. At 600 °C no detectable weight gain was observed for the first 50 h. At t > 50 h the sample gained some weight, after which no weight gain was recorded up to 500 h. Note that the step function in weight gain simply reflects the resolution of our balance.

By increasing the temperature to 700 °C, after a relatively rapid initial weight gain (Fig. 4a), the reaction slows down up to ~ 150 h, after which the oxidation kinetics become linear. At 800 °C, the oxidation rate is quite high, suggesting that the oxide layers formed are no longer protective (Fig. A3.4a). When the normalized weight gain for the sample that was not thermally cycled at 700 °C is plotted on Fig. 4a (green square at 170 h in Fig. A3.4a) it is clear that thermal cycling did not affect the results.

The effects of time and temperature on the oxide scale thickness, x, measured directly in the SEM, are shown in Fig. A3.4b. To understand and quantify the oxidation kinetics, the following procedure, employed in several of our previous papers [169], was used. The oxide thicknesses squared, x^2, was depicted as a function of t in the range t < 50 h (not shown). A good linear correlation was found implying that:

$$x^2 = 2\,k_x\,t \qquad \text{(A3.1)}$$

where k_x is the parabolic rate constant [176]. From the slope of the lines, k_x values at 600 °C, 700 °C and 800 °C were calculated to be $1.20(6) \times 10^{-17}$, $4.0(2) \times 10^{-16}$ and $5.5(2) \times 10^{-15}$ m^2/s, respectively. The dashed lines in Fig. A3.4b correspond to those of Eq. 1, using the aforementioned k_x values. Deviations from parabolic kinetics are clearly discernible at 700 °C after 100 h and at 800 °C after 50 h.

From the Arrhenius plots of k_x (Fig. A3.4c), an activation energy of 237(7) kJ/mol is obtained. Also plotted in Fig. 4c are the k_w values for Ti_3GeC_2 calculated from the

weight gains reported by Gupta et al. [172]. Good agreement is observed between these two sets of results [172]. For further comparison, the results for the oxidation of other Ti-containing MAX phases are plotted in Fig. A3.4c [166, 175].

To shed further light on the oxidation mechanisms, the weight gain results shown in Fig. 4a were converted to oxide thicknesses, x_w, (see Appendix A) and compared to those measured in the SEM, x. The results, shown in Fig. 4d, clearly show that at 600 °C, the agreement between x_w (dashed lines in Fig. 4d) and x (solid lines in Fig. 4d) is excellent. At 700°C, the agreement is good up to t ≈ 100 h, after which $x > x_w$. At 800 °C, at all times, $x > x_w$.

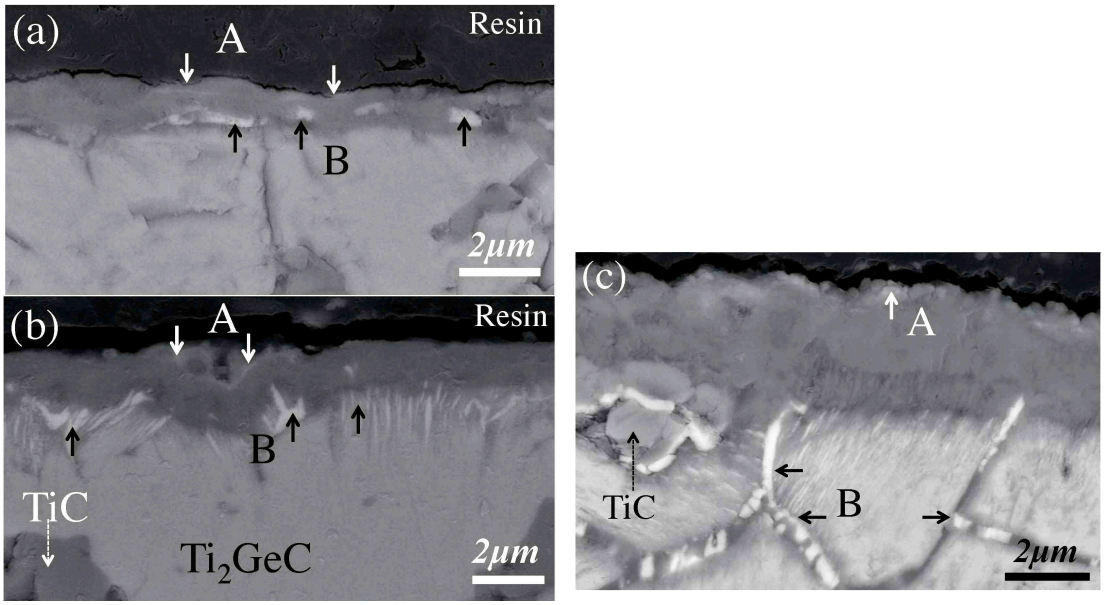

Fig. A 3.5. Backscattered electron SEM images of oxide layers formed at 600°C after, a) 24 h, b) 150 h and c) 500 h in air. Regions labeled A are GeO_2-rich oxides and regions B are oxygen poor, Ge-rich phases form as a result of decomposition of the Ti_2GeC.

The oxide layers formed at 600 °C after 24 h, 150 h and 500 h of oxidation are shown in Figs. A3.5a to c, respectively. After 24 h (Fig. A3.5a) the oxide layer is mostly comprised of r-TiO_2 (Fig. A3.3). EDS results confirmed the presence of minor amounts of Ge in the latter. Two other phases are observed in the oxide layer, both of which are brighter than r-TiO_2. The thin brighter gray regions, labeled A, which form on the outermost layer, are GeO_2-rich oxides. This layer becomes more visible with increasing time. The bright regions, labeled B, are oxygen poor, Ge-rich phases that presumably form as a result of the decomposition of the Ti_2GeC. By increasing the oxidation time to 150 h (Fig. A3.5b) the oxide layer thickness increases to ≈ 1 μm. In addition, regions with compositions similar to regions labeled B in Fig. A3.5a become more visible at the oxide/carbide interface (shown by black arrows). After 500 h of oxidation (Fig. A3.5c), the Ge content in the r-TiO_2 oxide layer decreases. In addition to the aforementioned decomposed regions, the same decomposition appears to have occurred at the grain boundaries that are in the near vicinity of the oxide layer (Fig. A3.5c). Figures A3.5a to c indicate that the oxide layers that form at 600 °C adhere well to the substrate and are apparently crack free.

Figures A3.6a to d show SEM micrographs of the oxide scales that form afer 8 h, 45 h, 100 h and 500 h of oxidation in 700 °C, respectively. At this temperature, it is again clear that Ti_2GeC decomposes at the oxide/carbide interface even at the early stages of oxidation. Further, the GeO_2-rich oxide regions, labeled A in Fig. A3.5a, are now observed within the oxide layer, as well as, at the outermost layers. The presence of meso- and micropores is also clear and their volume fraction increases with oxidation time. Multiple GeO_2-rich layers, shown by white arrows in Fig. A3.6c, are observed at t >

100 h, and striated layers are clear after 500 h of oxidation (Fig. A3.6d). The top inset in Fig. A3.6c shows the oxide scale after 170 h of oxidation at 700 °C with no thermal cycling. The same oxide regions are detected in the latter. In addition, a microcrack near the oxide/carbide interface is observed. The bottom inset in Fig. 6d, is a fractured surface of the same sample shown in Fig. 6d. Note the absence of the large corner crack observed in the micrograph of the polished sample (Fig. A3.6d).

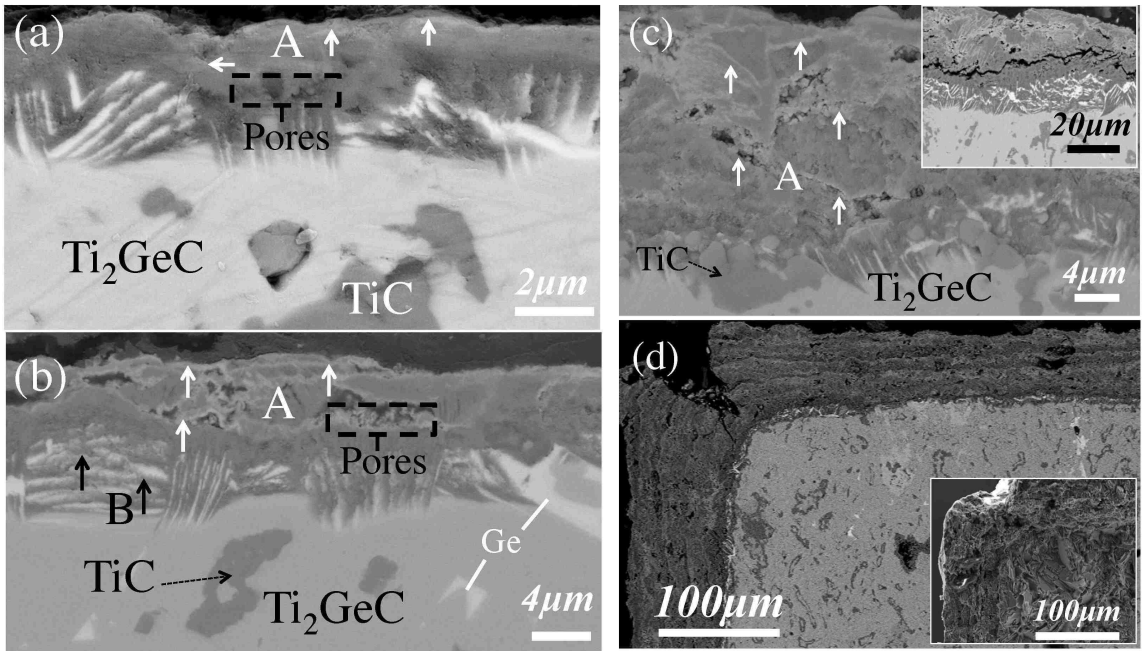

Fig. A 3.6. Backscattered electrons SEM images of oxide layers formed at 700°C after, a) 8 h, b) 45 h, c) 100 h, and, d) 500 h in air. Top inset in c shows oxidation scale of a sample oxidized 170 h in air at 700°C with no thermal cycling. Bottom inset in d shows fractured surface of the same sample shown in d. Regions labeled A are GeO_2-rich oxides and regions B are oxygen poor, Ge-rich phases form as a result of decomposition of the Ti_2GeC.

SEM micrographs of the oxide scales after 25 h and 340 h of oxidation at 800 °C are shown in Figs. A3.7a and b, respectively. EDS confirmed that the outermost layer, shown by white arrows, is a GeO_2-rich oxide layer that almost covers the entire surface. The underlying layers are presumably, a r-TiO_2 layer with some dissolved Ge, a GeO_2-rich layer, a porous r-TiO_2 based oxide layer and a decomposed region. The presence of pores and a large crack are also obvious. The latter probably formed during cross sectioning, mounting and polishing of the sample. After 340 h multiple striated oxide layers formed (Fig. A3.7b) which consisted of several layers of what was observed in Fig. 7a. After 340 h oxidation, a large corner crack was observed (Fig. A3.7b). The bottom inset in Fig. A3.7b, is a fractured surface of the same sample shown in Fig. A3.7b at higher magnification. Note the presence of nano oxide grains.

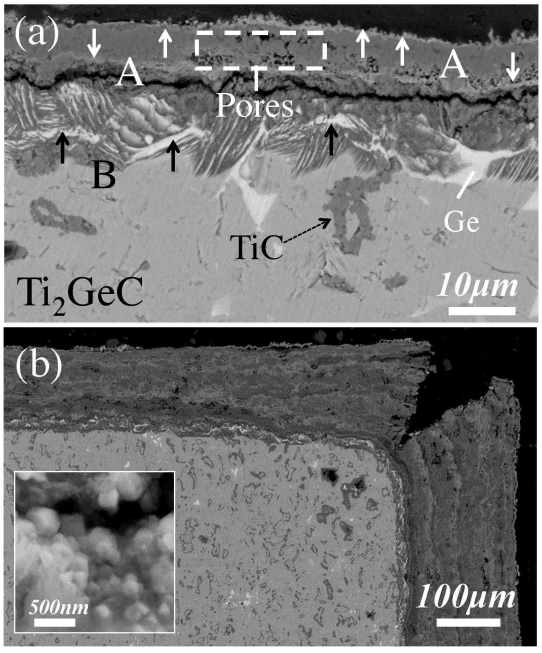

Fig. A 3.7. Backscattered electrons SEM images of oxide layers formed at 800°C after, a) 25 h and b) 340 h in air. Regions A and B are the same as what is explained on Fig. 5. Bottom inset in b shows the fractured surface of the oxide scale containing nano grains.

A3.4. Discussion

A3.4.1. Oxidation Reactions

In order to accurately discuss the XRD and EDS results it is important to consider the Cu Kα radiation penetration depth in the oxidized samples. This was calculated for the r-TiO_2 layer, the major oxide phase in all samples. Using the r-TiO_2 mass density value, 4.2 g/cm^3 [177], and the Ti, and O mass attenuation coefficient for the 8 keV Cu Kα radiation (202.3 cm^2/g, and 116.3 cm^2/g, respectively [178]) the penetration depth is estimated at 16 μm for direct angle impact on the oxide layer [178]. Then, using the measured oxide layer thickness for the different temperatures at different oxidation times (Fig. A3.4d), it is expected that information obtained from the XRD measurements that relate to the oxide layers solely comes from the sample oxidized at 700 ºC for 340 h (column 6 in Fig. A3.3), and the top oxide layer of the sample oxidized at 800 ºC for 340 h (column 8 in Fig. A3.3). Obviously, the oxidized powder refers only to the oxidized phases as well (column 7 in Fig. A3.3). In contrast, for all samples oxidized at 600 ºC (columns 2 and 3 in Fig. A3.3), and for the samples oxidized at 700 ºC for 45 h and 100 h (columns 4 and 5 in Fig. A3.3) the Cu Kα radiation is expected to penetrate beyond the oxide layer, and information obtained by XRD measurements is collected from both oxide layer and the material underneath it.

In this light, it is well understood why the Ti_2GeC phase is detected by the XRD measurements in the 600 ºC oxidized samples and in the samples oxidized at 700 ºC for 45 h and 100 h. Additionally, it is clear that the detected MAX phase content is strongly dependent of the oxide layer thickness, in strong support of it being underneath the oxide layer only (Figs. A3.3-7). Yet the most important information obtained here is the

behavior of the elemental Ge phase. Starting at ~1 wt% in the as received material the content of this phase increases upon oxidation time in a statistically significant amount (Fig. A3.3). Moreover, since this phase is not detected when the oxide layer thickness is larger than the XRD penetration depth, nor is it detected in the fully oxidized powder, it is reasonable to assume that elemental Ge is formed underneath the oxide layer. Finally, the XRD results from the 800 ºC oxidized samples strongly support this point, where elemental Ge is only detected in the bottom part, i.e. underneath the oxide layer that flacked off (columns 8-10 in Fig. A3.3). We note in passing that the estimated amount of the Ge, where it is measured underneath the oxide layer, is an under-estimation of the real amount due to the absorption of the Cu Kα radiation by the covering oxide layer.

Based on the XRD and EDS results presented above, the overall oxidation reaction of Ti_2GeC in air can be discussed in two different temperature ranges: a) 600 ºC, and b) 700 ºC and 800 ºC.

Since after oxidation at 600 °C, the lattice parameters of both r-TiO_2 and r-GeO_2 are the same as those reported in the literature for the pure phases (Table A3.1), it is assumed that no solid solution is formed and the oxidation reaction at 600 ºC can be simplified as:

$$Ti_2GeC + 4\ O_2 \rightarrow 2\ r\text{-}TiO_2 + r\text{-}GeO_2 + CO_2 \qquad (A3.2)$$

Here the oxides formed are r-TiO_2 and r-GeO_2. The reaction is simplified in that it assumes TiO_2 formed does not comprise carbon. As in all previous work on the oxidation of the MAX phases, and mainly because there is no accumulation of C at the oxide/substrate interface, C is presumed to diffuse through the oxide layers and ultimately oxidize to CO_2 [166, 169, 172, 175, 179, 180]. The fact that no solid solution

of the rutile phases are observed at this temperature is in agreement with what the TiO_2-GeO_2 binary phase diagram predicts [181].

At the oxide/Ti_2GeC interface it is reasonable to assume that the following reaction is occurring

$$Ti_2GeC + 3y/2\ O_2 \rightarrow Ti_2Ge_{1-x}C_{1-y}O_y + x\ Ge + y\ CO_2 \qquad (A3.3)$$

Here it is presumed that the O enters the 211 replacing C that diffuses through the oxide layer and is ultimately oxidized. The incorporation of O in turn, results in the decomposition of the Ti_2GeC phase forming fee Ge. Lastly, the latter is oxidized according to the following reaction:

$$2\ Ge + 2\ O_2 \rightarrow (2 - x)\ GeO_2 + x\ h\text{-}GeO\ (g) \qquad x \leq 1 \qquad (A3.4)$$

The germania that forms as a result of this reaction is h-GeO_2. In general, it has been established that normal oxidation of Ge leads to the formation of h-GeO_2. Formation of r-GeO_2 needs special conditions such as mineralizing catalysts or high pressure hydrothermal conditions [182]. It is worth noting here that elemental Ge starts oxidizing in a linear fashion at 500°C. At 550 °C, and above, Ge oxidation is controlled by diffusion of GeO away from the surface [183]. In addition, it was shown that at temperatures higher than 600 ºC, the presence of Ge next to GeO_2 can convert the latter to volatile GeO [184].

At 700 ºC and 800 ºC the overall oxidation reaction, at least initially, is given by the following simplified reaction:

$$Ti_2GeC + 4\ O_2 \rightarrow 2\ (Ti_{0.93},Ge_{0.07})O_2 + 0.9\ (Ge_{0.95},Ti_{0.05})O_2 + 0.1\ TiO_2 + CO_2 \qquad (A3.5)$$

Here the same assumptions made for the 600 ºC are applied. In addition, the solid solution compositions are assumed to be fixed and independent of oxidation temperature or time.

Concomitantly at the oxide/Ti_2GeC interface the following, again simplified, reaction is presumed to occur:

$$Ti_2GeC + 3\ O_2 \rightarrow 2\ TiO_2 + Ge + CO_2 \qquad (A3.6)$$

In the remainder of this paper we present evidence for these reactions and further discuss the oxidation kinetics.

Based on the results shown in Figs. A3.2 and 3, there is little doubt that r-TiO_2, r-GeO_2 and h-GeO_2 form as a result of oxidation. The strongest evidence for an oxygen-induced decomposition, viz. reactions A3.3 and A3.6, is the presence of elemental Ge peaks in the XRD patterns for the samples oxidized at 600 ºC for 55 h and 500 h and 700 °C for 100 h (see Fig. A3.3) and the oxide layer that remained adherent to the substrate after the 340 h run at 800 °C (last column in Fig. A3.3). As discussed in the beginning of this section, in all cases the observed amount of elemental Ge is larger than the Ge amount observed in the as received sample and beyond the statistical uncertainty. The established presence of elemental Ge underneath the oxide layer for all oxidation temperatures is strong evidence that this reaction occurs at, or near, the carbide/oxide interface, confirming the SEM observations. It is worth noting that the presence of pure Ge, TiC and Ti_2GeC in the XRD results of 600 ºC samples (columns 2 and 3 in Fig. A3.3) reveals that the rutile layer is thin enough that the Cu Kα radiation penetrated through it.

Not surprisingly, the microstructural evidence supports these conclusions. As shown in Fig. A3.5c, at longer oxidation times, the grain boundaries closer to the oxide/substrate interface decomposed and the ones far removed from the oxide/substrate interface are intact. As noted above, the MAX phases do not melt congruently but

decompose peritectically into an A-group rich phase and MX. Moreover, it is believed that the presence of oxygen and other impurities can lower their decomposition temperature [169, 172]. If indeed the decomposition is catalyzed by oxygen this result is compelling evidence for not only the inward diffusion of oxygen, but its diffusion down the grain boundaries as well.

Based on the results shown in Fig. A3.3 it is difficult to discern any trends. The most likely reason for this state of affairs is the fact that the oxide layers that form are not homogeneous, but tend to phase separate into TiO_2-rich and GeO_2-rich layers, especially at longer oxidation times. This is best seen in the results summarized in the last three columns shown in Fig. A3.3 that were all obtained from the same oxide layer, albeit at different depths. Note that both surfaces were devoid of h-GeO_2. We note in passing that this phase separation implies mobility of both Ti and Ge ions in the oxide layers formed, at least at a local level. The outermost layer was relatively rich in r-GeO_2; the intermediate one was r-TiO_2 rich. Lastly, the layer that was still adherent to the substrate (last column in Fig. A3.3), contained significant amounts of h-GeO_2 and weak Ge peaks.

The same behavior is observed after oxidation at 600 ºC. The h-GeO_2 phase was observed only at shorter oxidation time (55 h); the sample oxidized for 500 h was devoid of h-GeO2 (columns 2 and 3 in Fig. A3.3). The initial presence of h-GeO_2 can be ascribed to the oxidation of pure Ge that pre-existed in the sample and/or also as a result of the decomposition reaction A3.3. At longer time, the h-GeO_2 in the presence of pure Ge can form GeO(g) which is volatile. In addition, the oxide layer is protective and at longer time the pure Ge at the oxide/Ti_2GeC will not oxidize. This may be the reason that 15 wt.% of Ge was detected at 500 h sample.

Given the lattice parameters changes in both r-TiO_2 and r-GeO_2 at 700 ºC and 800 ºC (Table A3.1) and assuming Vegard's law is applicable, we conclude that roughly 7 at.% GeO_2 is in solid solution in the r-TiO_2 and ≈ 4.5 at.% TiO_2 is in solid solution in r-GeO_2. In agreement with the phase diagram of this system [181] and our previous work [172], these results are taken as evidence for the formation of solid solutions. Note at 600 °C, the solubility is quite small which is why reaction A3.2 does not show solid solubility as compared to reaction A3.5 that does.

Given that the h-GeO_2 forms under normal oxidation conditions and r-GeO_2 only forms under special conditions [182], as well as, our observation that the r-TiO_2 and r-GeO_2 grain sizes have similar values (< 100 nm) whereas those of h-GeO_2 are significantly larger, strongly suggest different oxidation precursors. It is thus not unreasonable to conclude that the r-GeO_2 phase forms as a result of reaction A3.2 or A3.5, while, h-GeO_2 forms as a result of the oxidation of elemental Ge.

A3.4.2. Oxidation Kinetics

Since at shorter oxidation times (< 50 h) and/or lower temperatures, the oxidation kinetics are parabolic (Fig. A3.4b), it is obvious that, at least initially, a protective layer forms. When the corresponding k_x values for the early stages of oxidation Ti_2GeC and Ti_3GeC_2 [172] are compared (Fig. A3.4c), it is reasonable to assume that the same short-term oxidation behavior is occurring in both ternaries, a not too surprising result since in both cases the same oxides form.

At this junction it is important to note that despite the fact the as synthesized sample had impurities, the oxidation kinetics at 600 °C are sub-parabolic and therefore, in

principle, Ti_2GeC can be used in air at 600 °C for extended times, despite the presence of unreacted Ge and/or Ge that resulted from decomposition of the matrix.

According to Fig. A3.4c it is also clear that the k_x values of both Ti_2GeC and Ti_3GeC_2 are about two orders of magnitude faster than those reported for other Ti-containing MAX phases [166, 169], such as Ti_2AlC and Ti_3SiC_2, but slower than Ti_2SC [175]. This is in agreement with the activation energies of these compounds. At 237(7) kJ/mol, the activation energies of the Ge-containing ternaries are larger than that of Ti_2SC [175] and smaller than those of Ti_2AlC and Ti_3SiC_2 [166]. In our previous work on the oxidation of Nb_2AlC [180] and some $Ti_{n+1}AlX_n$ phases [169] we concluded that the dissolution of aliovalent ions in the rutile affected the diffusivities of the rate limiting species, viz. the Ti and O. Herein the same argument cannot be made because Ge and Ti have the same valencies. In our paper on the oxidation of Ti_2SC [175] we ascribed the faster kinetics to the presence of parallel paths for the inward diffusion of oxygen. We make the same conjecture here. While the nature of these parallel paths is not clear at this time, as discussed below, the case can be made that one of these paths is the presence of nano- or micropores. This comment notwithstanding, such a conjecture still does not explain why the activation energies remain more or less independent of composition and/or k_x values.

A3.4.3. Evidence for, and effect of, porosity

Direct evidence for the presence of pores can be found in most SEM micrographs of the 700 ºC and 800 ºC oxide layers (e.g. see Figs. A3.6 and A3.7). Furthermore, since at 700 °C and 800 °C – but notably not at 600 °C – the oxide layer thicknesses calculated from the weight gain results (dashed lines in Fig. A3.4d) are lower than those measured

directly in the SEM (solid lines in Fig. A3.4d), we conclude that a sizable fraction of pores is present in the oxide layers at the higher temperatures. Coincidentally or not, at 700 °C, and up to about 100 h of oxidation, the agreement between x_w and x is quite good (Fig. A3.4d) suggesting that up to that time the porosity level was low. Given that it is only after 100 h that the kinetics cease to be parabolic (Fig. A3.2b), it is reasonable to conclude that the macro-porosity is responsible for the change in kinetics from parabolic to linear. Alternatively, the fact that in the presence of oxygen and Ge forms GeO at temperatures higher than 500 °C [183], may explain the change in k_x. In that respect Ge may be behaving like S in Ti_2SC [175].

At higher temperatures and/or longer times, sintering was observed at the TiO_2 regions. As a result, the top TiO_2 region in Fig. A3.7a has less porosity than the layer beneath it. In addition, the oxide layer on the long time oxidation at 800 ºC has less macro porosities than the 700 ºC one (compare Figs. A3.6d and A3.7b). The formation of striated oxide layers during the long-term oxidation of Ti_2GeC indicates that the oxidation occurs by the local outward diffusion of Ge^{+4} and Ti^{+4} ions and the inward diffusion of oxygen.

Based on the normalized weight gain of the sample which was not thermal cycled (Fig. A3.4a), it is reasonable to conclude that at least up to 700 °C and up to 10 cycles, Ti_2GeC is immune to thermal cycling. In addition, since the oxide layer at the corners of the fractured sample was not cracked (bottom inset in Fig. A3.6d) and there was a uniform oxide layer, even around the corners of the polished samples (Figs A3.6d and 7b), it is fair to assume that the large corner cracks seen in Figs. A3.6d and A3.7b were generated during sample preparation.

A3.5. Summary and Conclusions

The oxidation of Ti_2GeC in air occurs mostly by the inward diffusion of oxygen through rutile-based layers, $(Ti_x,Ge_{1-x})O_2$ with $x \leq 0.07$. At lower temperatures and shorter times, the non-reacted Ge that pre-existed in the sample and the Ge that formed as a result of the decomposition of Ti_2GeC in the presence of oxygen, oxidize to form h-GeO_2. At 600 ºC up to 500 h, the oxide layer is protective.

At 700 ºC and 800 ºC up to 100 h and 50 h, respectively, the kinetics are initially parabolic before becoming linear. The reason for this transition is believed to be the formation of pores and microcracks in the rutile layers at longer times.

Since it is only at 600 ºC that the weight gain reaches a plateau for t > 100 h, it follows that the maximum use temperature for Ti_2GeC in air would be in the vicinity of 600 ºC.

Appendix

To convert the weight gains to oxide thickness, x_w, the following assumptions were made. According to Eq. 2, oxidation of one mole of Ti_2GeC results in roughly 2 moles of TiO_2 and one mole of GeO_2. This translates to a weight gain of 0.08 kg/mole. The molar volume of fully dense TiO_2 and GeO_2 are assumed to be 19.0 and 24.6 cm^3/mole, respectively. For an area of 1 m^2, it follows that $x = 6.26 \times 10^{-5}$ m. Thus, in order to convert weight gain to x_w, the former should multiply by $6.26 \times 10^{-5}/0.08$ or 7.46×10^{-4} m/kg.

Chapter 10: References

[1] K.M. Kenyon, T.A. Holland, Excavations at Jericho, British school of archaeology in Jerusalem, 1960.
[2] T. Clyne, P. Withers, An introduction to metal matrix composites, Cambridge University Press, 1995.
[3] M. Gupta, N.M.L. Sharon, Magnesium, magnesium alloys, and magnesium composites, John Wiley & Sons, 2011.
[4] S. Amini, C. Ni, M.W. Barsoum, Processing, microstructural characterization and mechanical properties of a Ti_2AlC/nanocrystalline Mg-matrix composite. Composites Science and Technology, 69 (2009) 414-420.
[5] B.L. Mordike, T. Ebert, Magnesium: Properties — applications — potential. Materials Science and Engineering A, 302 (2001) 37-45.
[6] H. Friedrich, S. Schumann, Research for a "new age of magnesium" in the automotive industry. Journal of Materials Processing Technology, 117 (2001) 276-281.
[7] H. Furuya, N. Kogiso, S. Matunaga, K. Senda, Materials Science Forum, Trans Tech Publ, 2000, pp. 341-348.
[8] H.Z. Ye, L. Xing Yang, Review of recent studies in magnesium matrix composites. Journal of Materials Science, 39 (2004) 6153-6171.
[9] I.A. Ibrahim, F.A. Mohamed, E.J. Lavernia, Particulate reinforced metal matrix composites — a review. Journal of Materials Science, 26 (1991) 1137-1156.
[10] K. Purazrang, P. Abachi, K.U. Kainer, Mechanical behaviour of magnesium alloy MMCs produced by squeeze casting and powder metallurgical techniques. Composites Engineering, 3 (1993) 489-505.
[11] B.W. Chua, L. Lu, M.O. Lai, Influence of SiC particles on mechanical properties of Mg based composite. Composite Structures, 47 (1999) 595-601.
[12] A. Martín, J. Llorca, Mechanical behaviour and failure mechanisms of a binary Mg-6%Zn alloy reinforced with SiC particulates. Materials Science and Engineering: A, 201 (1995) 77-87.
[13] R.A. Saravanan, M.K. Surappa, Fabrication and characterisation of pure magnesium-30 vol.% SiCP particle composite. Materials Science and Engineering A, A276 (2000) 108-116.
[14] M. Zheng, K. Wu, C. Yao, Effect of interfacial reaction on mechanical behavior of SiC_w/AZ91 magnesium matrix composites. Materials Science and Engineering: A, 318 (2001) 50-56.
[15] A.R. Vaidya, J.J. Lewandowski, Effects of SiCp size and volume fraction on the high cycle fatigue behavior of AZ91D magnesium alloy composites. Materials Science and Engineering: A, 220 (1996) 85-92.

[16] M. Gupta, M.O. Lai, D. Saravanaranganathan, Synthesis, microstructure and properties characterization of disintegrated melt deposited Mg/SiC composites. Journal of Materials Science, 35 (2000) 2155-2165.
[17] S.U. Reddy, N. Srikanth, M. Gupta, S.K. Sinha, Enhancing the Properties of Magnesium using SiC Particulates in Sub-micron Length Scale. Advanced Engineering Materials, 6 (2004) 957-964.
[18] S. Ugandhar, M. Gupta, S.K. Sinha, Enhancing strength and ductility of Mg/SiC composites using recrystallization heat treatment. Composite Structures, 72 (2006) 266-272.
[19] J.-j. Wang, J.-h. Guo, L.-q. Chen, TiC/AZ91D composites fabricated by in situ reactive infiltration process and its tensile deformation. Transactions of Nonferrous Metals Society of China, 16 (2006) 892-896.
[20] L.Q. Chen, Q. Dong, M.J. Zhao, J. Bi, N. Kanetake, Synthesis of TiC/Mg composites with interpenetrating networks by in situ reactive infiltration process. Materials Science and Engineering A, 408 (2005) 125-130.
[21] A. Contreras, V.H. Lopez, E. Bedolla, Mg/TiC composites manufactured by pressureless melt infiltration. Scripta Materialia, 51 (2004) 249-253.
[22] V. Kevorkijan, S. Davor Škapin, Mg/B4C Composites with a High Volume Fraction of Fine Ceramic Reinforcement. Materials and Manufacturing Processes, 24 (2009) 1337-1340.
[23] V. Kevorkijan, Mg AZ80/SiC composite bars fabricated by infiltration of porous ceramic preforms. Metallurgical and Materials Transactions A, 35 (2004) 707-715.
[24] D.J. Lloyd, Particle reinforced aluminium and magnesium matrix composites. International Materials Reviews, 39 (1994) 1-23.
[25] P. Poddar, S. Mukherjee, K.L. Sahoo, The Microstructure and Mechanical Properties of SiC Reinforced Magnesium Based Composites by Rheocasting Process. Journal of Materials Engineering and Performance, 18 (2008) 849-855.
[26] A. Contreras, C.A. León, R.A.L. Drew, E. Bedolla, Wettability and spreading kinetics of Al and Mg on TiC. Scripta Materialia, 48 (2003) 1625-1630.
[27] W. Cao, C. Zhang, T. Fan, D.Z. Di Zhang, In Situ Synthesis and Compressive Deformation Behaviors of TiC Reinforced Magnesium Matrix Composites. Materials transactions, 49 (2008) 2686-2691.
[28] M. Shamekh, M. Pugh, M. Medraj, Understanding the reaction mechanism of in-situ synthesized (TiC–TiB2)/AZ91 magnesium matrix composites. Materials Chemistry and Physics, 135 (2012) 193-205.
[29] M. Shamekh, M. Pugh, M. Medraj, Processing and Characterization of In Situ (TiC–TiB2)p/AZ91D Magnesium Matrix Composites. Advanced Engineering Materials, 15 (2013) 708-717.
[30] D.H. Bae, M.H. Lee, K.T. Kim, W.T. Kim, D.H. Kim, Application of quasicrystalline particles as a strengthening phase in Mg–Zn–Y alloys. Journal of Alloys and Compounds, 342 (2002) 445-450.
[31] J. Koike, R. Ohyama, Geometrical criterion for the activation of prismatic slip in AZ61 Mg alloy sheets deformed at room temperature. Acta Mater, 53 (2005) 1963-1972.

[32] Y. Shimizu, S. Miki, T. Soga, I. Itoh, H. Todoroki, T. Hosono, K. Sakaki, T. Hayashi, Y.A. Kim, M. Endo, S. Morimoto, A. Koide, Multi-walled carbon nanotube-reinforced magnesium alloy composites. Scripta Materialia, 58 (2008) 267-270.
[33] M.Y. Zheng, W.C. Zhang, K. Wu, C.K. Yao, The deformation and fracture behavior of SiC_w/AZ91 magnesium matrix composite during in-situ TEM straining. Journal of Materials Science, 38 (2003) 2647-2654.
[34] M.W. Barsoum, M. Radovic, Elastic and Mechanical Properties of the MAX Phases. Annual Review of Materials Research, 41 (2011) 195-227.
[35] P. Eklund, M. Beckers, U. Jansson, H. Högberg, L. Hultman, The $M_{n+1}AX_n$ phases: Materials science and thin-film processing. Thin Solid Films, 518 (2010) 1851-1878.
[36] C. Hu, H. Zhang, F. Li, Q. Huang, Y. Bao, New phases' discovery in MAX family. International Journal of Refractory Metals and Hard Materials, 36 (2013) 300-312.
[37] M.W. Barsoum, MAX Phases: Properties of Machinable Ternary Carbides and Nitrides, John Wiley & Sons, 2013.
[38] M.W. Barsoum, T. ElRaghy, Synthesis and characterization of a remarkable ceramic: Ti_3SiC_2. J Am Ceram Soc, 79 (1996) 1953-1956.
[39] M.W. Barsoum, D. Brodkin, T. ElRaghy, Layered machinable ceramics for high temperature applications. Scripta Materialia, 36 (1997) 535-541.
[40] M.W. Barsoum, M.C. Flemings, E.J. Kramer, S. Mahajan, P. Veyssiere, Physical properties of the MAX phases. In: Encyclopedia of materials science and technology, (2006).
[41] D.J. Tallman, M. Naguib, B. Anasori, M.W. Barsoum, Tensile creep of Ti_2AlC in air in the temperature range 1000–1150°C. Scripta Materialia, 66 (2012) 805-808.
[42] A. Kontsos, T. Loutas, V. Kostopoulos, K. Hazeli, B. Anasori, M.W. Barsoum, Nanocrystalline Mg–MAX composites: Mechanical behavior characterization via acoustic emission monitoring. Acta Mater, 59 (2011) 5716-5727.
[43] M. Sundberg, G. Malmqvist, A. Magnusson, T. El-Raghy, 3rd Asian Meeting on Electroceramics (AMEC-3), 7-11 Dec. 2003, Elsevier, UK, 2004, pp. 1899-1904.
[44] M.W. Barsoum, T. Zhen, S.R. Kalidindi, M. Radovic, A. Murugaiah, Fully reversible, dislocation-based compressive deformation of Ti_3SiC_2 to 1GPa. Nature Materials, 2 (2003) 107-111.
[45] A.G. Zhou, M.W. Barsoum, Kinking nonlinear elastic deformation of Ti_3AlC_2, Ti_2AlC, $Ti_3Al(C_{0.5},N_{0.5})_2$ and $Ti_2Al(C_{0.5},N_{0.5})$. Journal of Alloys and Compounds, 498 (2010) 62-70.
[46] M.W. Barsoum, S. Basu, Kinking Nonlinear Elastic Solids, in: K.H.J. Buschow, R.W. Cahn, M.C. Flemings, B. Ilschner, E.J. Kramer, S. Mahajan, P. Veyssiere (Eds.) Encyclopedia of Materials Science and Technology, Elsevier, Oxford, 2010.
[47] S. Amini, J.M. Cordoba, L. Daemen, A.R. McGhie, C.Y. Ni, L. Hultman, M. Oden, M.W. Barsoum, On the Stability of Mg Nanograins to Coarsening after Repeated Melting. Nano Lett, 9 (2009) 3082-3086.
[48] B.D. Cullity, Elements of X-ray diffraction, 2nd edition, Addison-Wesley, London, UK, 1978.
[49] H. Baker, H. Okamoto, ASM handbook. Alloy phase diagrams, 3 (1992) 2.
[50] J. Zhang, R.J. Perez, E.J. Lavernia, Dislocation-induced damping in metal matrix composites. Journal of Materials Science, 28 (1993) 835-846.

[51] J. Zhang, R.J. Perez, C.R. Wong, E.J. Lavernia, Effects of secondary phases on the damping behaviour of metals, alloys and metal matrix composites. Materials Science and Engineering: R: Reports, 13 (1994) 325-389.
[52] R. Everett, R. Arsenault, Metal matrix composites: processing and interfaces. Academic Press, Inc, 1250 Sixth Ave, San Diego, California 92101, USA, 1991. 228, (1991).
[53] J. Zhang, R.J. Perez, E.J. Lavernia, Effect of SiC and graphite particulates on the damping behavior of metal matrix composites. Acta Metallurgica et Materialia, 42 (1994) 395-409.
[54] C. Updike, R. Bhagat, M. Pechersky, M. Amateau, The damping performance of aluminum-based composites. JOM, 42 (1990) 42-46.
[55] A.G. Zhou, D. Brown, S. Vogel, O. Yeheskel, M.W. Barsoum, On the kinking nonlinear elastic deformation of cobalt. Materials Science and Engineering A, 527 (2010) 4664-4673.
[56] A.G. Zhou, M.W. Barsoum, Kinking Nonlinear Elasticity and the Deformation of Magnesium. Metall Mater Trans A, 40A (2009) 1741-1756.
[57] A.G. Zhou, S. Basu, M.W. Barsoum, Kinking nonlinear elasticity, damping and microyielding of hexagonal close-packed metals. Acta Mater, 56 (2008) 60-67.
[58] D.W. James, High damping metals for engineering applications. Materials Science and Engineering, 4 (1969) 1-8.
[59] X.S. Hu, Y.K. Zhang, M.Y. Zheng, K. Wu, A study of damping capacities in pure Mg and Mg–Ni alloys. Scripta Materialia, 52 (2005) 1141-1145.
[60] J. Gu, X. Zhang, Y. Qiu, M. Gu, Damping behaviors of magnesium matrix composites reinforced with Cu-coated and uncoated SiC particulates. Composites Science and Technology, 65 (2005) 1736-1742.
[61] R. Schaller, Metal matrix composites, a smart choice for high damping materials. Journal of Alloys and Compounds, 355 (2003) 131-135.
[62] S. Amini, M.W. Barsoum, On the effect of texture on the mechanical and damping properties of nanocrystalline Mg-matrix composites reinforced with MAX phases. Materials Science and Engineering A, 527 (2010) 3707-3718.
[63] O. Mügge, On slip and related phenomena in crystals. Neues Fahr. F. Miner, 7 (1898) 71-158.
[64] E. Orowan, A type of plastic deformation new in metals. Nature, 149 (1942) 643-644.
[65] J.B. Hess, C.S. Barrett, Structure and nature of kink bands in zinc. American Institute of Mining and Metallurgical Engineers -- Journal of Metals, 1 (1949) 599-606.
[66] F.C. Frank, A.N. Stroh, On the Theory of Kinking. Proceedings of the Physical Society, **65** (1952) 811-821
[67] J.J. Gilman, Mechanism of ortho kink-band formation in compressed zinc monocrystals. Journal of Metals, 6 (1954) 621-629.
[68] J. Roberts, N. Brown, Microstrain in zinc single crystals. TRANSACTIONS OF THE AMERICAN INSTITUTE OF MINING AND METALLURGICAL ENGINEERS, 218 (1960) 454-463.
[69] M.W. Barsoum, D. Brodkin, T. El-Raghy, Layered machinable ceramics for high temperature applications. Scripta Materialia, 36 (1997) 535-541.

[70] T. El-Raghy, A. Zavaliangos, M.W. Barsoum, S.R. Kalidindi, Damage mechanisms around hardness indentations in Ti3SiC2. J Am Ceram Soc, 80 (1997) 513-516.
[71] M.W. Barsoum, T. El-Raghy, Room-temperature ductile carbides. Metall Mater Trans A, 30 (1999) 363-369.
[72] M.W. Barsoum, L. Farber, T. El-Raghy, Dislocations, kink bands, and room-temperature plasticity of Ti3SiC2. Metallurgical and Materials Transactions A, 30 (1999) 1727-1738.
[73] L. Farber, L. Levin, M.W. Barsoum, High-resolution transmission electron microscopy study of a low-angle boundary in plastically deformed Ti_3SiC_2. Philosophical Magazine Letters, 79 (1999) 163-170.
[74] A. Murugaiah, M.W. Barsoum, S.R. Kalidindi, T. Zhen, Spherical nanoindentations and kink bands in Ti_3SiC_2. Journal of Materials Research, 19 (2004) 1139-1148.
[75] M.W. Barsoum, A. Murugaiah, S.R. Kalidindi, T. Zhen, Y. Gogotsi, Kink bands, nonlinear elasticity and nanoindentations in graphite. Carbon, 42 (2004) 1435-1445.
[76] M.W. Barsoum, A. Murugaiah, S.R. Kalidindi, T. Zhen, Kinking nonlinear elastic solids, nanoindentations, and geology. Phys Rev Lett, 92 (2004) 255508.
[77] M.W. Barsoum, T. Zhen, A. Zhou, S. Basu, S.R. Kalidindi, Microscale modeling of kinking nonlinear elastic solids. Phys Rev B, 71 (2005) 134101.
[78] A.G. Zhou, M.W. Barsoum, S. Basu, S.R. Kalidindi, T. El-Raghy, Incipient and regular kink bands in fully dense and 10 vol.% porous Ti2AlC. Acta Materialia, 54 (2006) 1631-1639.
[79] S. Basu, M.W. Barsoum, Deformation micromechanisms of ZnO single crystals as determined from spherical nanoindentation stress-strain curves. J. Mater. Res., 22 (2007) 2470-2477.
[80] R. Buchs, S. Basu, O.A. Elshrief, R. Coward, M.W. Barsoum, Spherical nanoindentation and Vickers microhardness study of the deformation of poled BaTiO3 single crystals. Journal of Applied Physics, 105 (2009).
[81] S. Basu, M.W. Barsoum, S.R. Kalidindi, Sapphire: A kinking nonlinear elastic solid. Journal of Applied Physics, 99 (2006).
[82] S. Basu, A.G. Zhou, M.W. Barsoum, Reversible dislocation motion under contact loading in LiNbO3 single crystal. J. Mater. Res., 23 (2008) 1334-1338.
[83] B. Anasori, K.E. Sickafus, I.O. Usov, M.W. Barsoum, Spherical nanoindentation study of the deformation micromechanisms of LiTaO3 single crystals J. Appl. Phys., 110 (2011) 023516.
[84] S. Basu, M.W. Barsoum, On Spherical Nanoindentations, Kinking Nonlinear Elasticity of Mica Single Crystals and Their Geological Implications. J. Struct. Geology, 31, (2009) 791–801.
[85] D. Hull, D.J. Bacon, Introduction to Dislocations, 1965.
[86] G.E. Dieter, Mechanical Metallurgy, McGraw-Hill, USA, 1986.
[87] L. Sun, R.H. Wagoner, Complex unloading behavior: Nature of the deformation and its consistent constitutive representation. International Journal of Plasticity, 27 (2011) 1126-1144.

[88] M. Naguib, M. Kurtoglu, V. Presser, J. Lu, J. Niu, M. Heon, L. Hultman, Y. Gogotsi, M.W. Barsoum, Two-Dimensional Nanocrystals Produced by Exfoliation of Ti3AlC2. Advanced Materials, 23 (2011) 4248-4253.
[89] A. Murugaiah, A. Souchet, T. El-Raghy, M. Radovic, M. Sundberg, M.W. Barsoum, Tape Casting, Pressureless Sintering, and Grain Growth in Ti_3SiC_2 Compacts. J Am Ceram Soc, 87 (2004) 550-556.
[90] H.M. Rietveld, A profile refinement method for nuclear and magnetic structures. Journal of Applied Crystallography, 2 (1969) 65-71.
[91] J. Rodríguez-Carvajal, Recent advances in magnetic structure determination by neutron powder diffraction. Physica B: Condensed Matter, 192 (1993) 55-69.
[92] J. Rodriguez-Carvajal, M.T. Fernandez-Diaz, J.L. Martinez, Neutron diffraction study on structural and magnetic properties of La2NiO4. Journal of Physics: Condensed Matter, 3 (1991) 3215-3234.
[93] C. Berthold, A. Bjeoumikhov, L. Brügemann, Fast XRD2 Microdiffraction with Focusing X-Ray Microlenses. Particle & Particle Systems Characterization, 26 (2009) 107-111.
[94] M.W. Barsoum, The $M_{N+1}AX_N$ phases: A new class of solids: Thermodynamically stable nanolaminates. Progress in Solid State Chemistry, 28 (2000) 201-281.
[95] W. Jeitschko, H. Nowotny, F. Benesovsky, Kohlenstoffhaltige ternäre Verbindungen (H-Phase). Monatshefte für Chemie / Chemical Monthly, 94 (1963) 672-676.
[96] J.C. Halpin, Primer on composite materials analysis, 2nd, rev. / edition ed., Technomic Pub. Co. , Lancaster, PA, 1992.
[97] M.W. Barsoum, T. El-Raghy, The MAX phases: Unique new carbide and nitride materials: Tertiary ceramics are soft and machinable, yet heat-tolerant, strong and lighweight. American Scientist, 89 (2001) 334-343.
[98] G.S. Ansell, F.V. Lenel, Criteria for yielding of dispersion-strengthened alloys. Acta Metall Mater, 8 (1960) 612-616.
[99] H.O. Pierson, Handbook of Refractory Carbides and Nitrides: Properties, Characteristics and Applications, Noyes Publications, Westwood, New Jersey, 1996.
[100] M. Barsoum, T. El-Raghy, M. Ali, Processing and characterization of Ti_2AlC, Ti_2AlN and $Ti_2AlC_{0.5}N_{0.5}$. Metallurgical and Materials Transactions A, 31 (2000) 1857-1865.
[101] R.J. Arsenault, M. Taya, Thermal residual stress in metal matrix composite. Acta Metall Mater, 35 (1987) 651-659.
[102] R.O. Elliott, C.P. Kempter, Thermal Expansion of Some Transition Metal Carbides. The Journal of Physical Chemistry, 62 (1958) 630-631.
[103] F. Mestral, F. Thevenot, Ceramic composites: TiB_2-TiC-SiC. Journal of Materials Science, 26 (1991) 5547-5560.
[104] M. Taya, R.J. Arsenault, Metal Matrix Composites: Thermomechanical Behaviour, Pergamon Press, , Oxford, 1989.
[105] J. Huang, T. Arbel, L. Ligeski, J. McCaffrey, S. Kulkarni, J. Jones, T. Pollock, R. Decker, S. LeBeau1, in: A.e. al (Ed.) Magnesium Technology 2010, Warrendale, PA, 2010, pp. 489-493.

[106] M. Radovic, M.W. Barsoum, T. El-Raghy, J. Seidensticker, S. Wiederhorn, Tensile properties of Ti_3SiC_2 in the 25–1300°C temperature range. Acta Mater, 48 (2000) 453-459.
[107] B. Anasori, S. Amini, V. Presser, M.W. Barsoum, TMS Conference, Mg Technology 2011, San Diego, CA., 2011.
[108] B. Anasori, M.W. Barsoum, On the Effect of Ti_2AlC on the Formation of Thermally Stable Mg Nano Grains, Magnesium Technology 2012, John Wiley & Sons, Inc., 2012, pp. 409-412.
[109] T. Zhen, M.W. Barsoum, S.R. Kalidindi, Effects of temperature, strain rate and grain size on the compressive properties of Ti3SiC2. Acta Mater, 53 (2005) 4163-4171.
[110] S. Amini, Department of Materials Science and Engineering Drexel University, Philadelphia, 2009.
[111] J. Zhang, Q. Yu, Y. Jiang, Q. Li, An experimental study of cyclic deformation of extruded AZ61A magnesium alloy. International Journal of Plasticity, 27 (2011) 768-787.
[112] R. Stevenson, J.B.V. Sande, The cyclic deformation of magnesium single crystals. Acta Metall Mater, 22 (1974) 1079-1086.
[113] M.F. Ashby, On the Engineering Properties of Materials. Acta Metall Mater, 37 (1989) 1273-1293.
[114] M. Naguib, V. Presser, D. Tallman, J. Lu, L. Hultman, Y. Gogotsi, M.W. Barsoum, On the Topotactic Transformation of Ti2AlC into a Ti–C–O–F Cubic Phase by Heating in Molten Lithium Fluoride in Air. J Am Ceram Soc, 94 (2011) 4556-4561.
[115] C.H. Cáceres, C.J. Davidson, J.R. Griffiths, C.L. Newton, Effects of solidification rate and ageing on the microstructure and mechanical properties of AZ91 alloy. Materials Science and Engineering: A, 325 (2002) 344-355.
[116] H. Kroemer, G.F. Day, R.D. Fairman, J. Kinoshita, Preparation and some Properties of Mg2Ge Single Crystals and of Mg2Ge p‐n Junctions. Journal of Applied Physics, 36 (1965) 2461-2470.
[117] S. Basu, A. Zhou, M.W. Barsoum, On spherical nanoindentations, kinking nonlinear elasticity of mica single crystals and their geological implications. Journal of Structural Geology, 31 (2009) 791-801.
[118] A. Richter, B. Wolf, M. Nowicki, R. Smith, I.O. Usov, J.A. Valdez, K. Sickafus, Multi-cycling nanoindentation in MgO single crystals before and after ion irradiation. Journal of Physics D-Applied Physics, 39 (2006) 3342-3349.
[119] W.C. Oliver, G.M. Pharr, Improved technique for determining hardness and elastic modulus using load and displacement sensing indentation experiments. Journal of Materials Research, 7 (1992) 1564-1583.
[120] V.A. Coleman, J.E. Bradby, C. Jagadish, M.R. Phillips, A Comparison of the Mechanical Properties and the Impact of Contact Induced Damage in a- and c- Axis ZnO Single Crystals. MRS Online Proceedings Library, 957 (2006) 0957-K0907-0917.
[121] T. Saraswati, T. Sritharan, S. Mhaisalkar, C.D. Breach, F. Wulff, Cyclic loading as an extended nanoindentation technique. Materials Science and Engineering: A, 423 (2006) 14-18.

[122] S. Basu, A.G. Zhou, M.W. Barsoum, Reversible dislocation motion under contact loading in LiNbO3 single crystal. Journal of Materials Research, 23 (2008) 1334-1338.
[123] A.C. Fischer-Cripps, Introduction to Contact Mechanics, 2 ed., Springer-Verlag, New York, 2000.
[124] S. Basu, M.W. Barsoum, Deformation micromechanisms of ZnO single crystals as determined from spherical nanoindentation stress-strain curves. Journal of Materials Research, 22 (2007) 2470-2477.
[125] E.D. Palik, Handbook of Optical Constants of Solids. *Handbook of Optical Constants of Solids* (San Diego, CA: Academic), 3 (1998) 777-805.
[126] V. G. Dmitriev, G. G. Gurzadyan, D.N. Nikogosyan, Handbook of Nonlinear Optical Crystals, Springer, New York, 1999.
[127] G.D.B. A. Ashkin, J. M. Dziedzic, R. G. Smith Optically-induced refractive index inhomogeneities in LiNbO3 and LiTaO3. *Appl. Phys. Lett*, 9 (1966) 72-74.
[128] K. Mizuuchi, K. Yamamoto, T. Taniuchi, FABRICATION OF 1ST-ORDER PERIODICALLY DOMAIN-INVERTED STRUCTURE IN LITAO3. *Appl. Phys. Lett*, 59 (1991) 1538-1540.
[129] G. Assanto, G. Stegeman, M. Sheikbahae, E. Vanstryland, ALL-OPTICAL SWITCHING DEVICES BASED ON LARGE NONLINEAR PHASE-SHIFTS FROM 2ND HARMONIC-GENERATION. *Appl. Phys. Lett*, 62 (1993) 1323-1325.
[130] J. C. Doukhan, P. Cordier, N. Doukhan, Lattice Defects in Lithium Tantalate. *43rd Annual Synposium on Frequency Control* (1989) 497-508.
[131] S. Basu, M.W. Barsoum, A.D. Williams, T.D. Moustakas, Spherical nanoindentation and deformation mechanisms in freestanding GaN films. Journal of Applied Physics, 101 (2007).
[132] S. Basu, M.W. Barsoum, S.R. Kalidindi, Sapphire: A kinking nonlinear elastic solid. Journal of Applied Physics, 99 (2006) 063501.
[133] B.J. Kooi, R.J. Poppen, N.J.M. Carvalho, J.T.M. De Hosson, M.W. Barsoum, Ti3SiC2: A damage tolerant ceramic studied with nano-indentations and transmission electron microscopy. Acta Mater, 51 (2003) 2859-2872.
[134] E.G. Herbert, G.M. Pharr, W.C. Oliver, B.N. Lucas, J.L. Hay, 28th International Conference on Metallurgia, April 30, 2001 - May 30, 2001, Elsevier, San Diego, CA, United states, 2001, pp. 331-335.
[135] W.C. Oliver, G.M. Pharr, Measurement of hardness and elastic modulus by instrumented indentation: Advances in understanding and refinements to methodology. Journal of Materials Research, 19 (2004) 3-20.
[136] M. Suganuma, M.V. Swain, Simple method and critical comparison of frame compliance and indenter area function for nanoindentation. Journal of Materials Research, 19 (2004) 3490-3502.
[137] A.J. Bushby, Nano-indentation using spherical indenters. Non-Destructive Testing and Evaluation, 17 (2001) 213-234.
[138] A.J. Moseson, S. Basu, M.W. Barsoum, Determination of the effective zero point of contact for spherical nanoindentation. Journal of Materials Research, 23 (2008) 204-209.
[139] S. Basu, A. Moseson, M.W. Barsoum, On the Determination of Indentation Stress-Strain Curves Using Spherical Indenters. J. Mater. Res., **21**, (2006) 2628-2637.

[140] O. Yeheskel, I.C. Albayrak, B. Anasori, M.W. Barsoum, Mechanical and elastic properties of fine-grained polycrystalline scandia and erbia as determined by indentation techniques. Journal of the European Ceramic Society, 31 (2011) 1703-1712.
[141] R.E. Reed-Hill, E.P. Dahlberg, W.A. Slippy, Jr., Some anelastic effects in zirconium at room temperature resulting from prestrain at 77K. Transactions of the Metallurgical Society of AIME, 233 (1965) 1766-1771.
[142] N. Li, M.S. Martin, O. Anderoglu, A. Misra, L. Shao, H. Wang, X. Zhang, He ion irradiation damage in Al/Nb multilayers. Journal of Applied Physics, 105 (2009).
[143] H. Trinkaus, W.G. Wolfer, CONDITIONS FOR DISLOCATION LOOP PUNCHING BY HELIUM BUBBLES. Journal of Nuclear Materials, 122 (1984) 552-557.
[144] J.N. Mitchell, R. Devanathan, N. Yu, K.E. Sickafus, C.J. Wetteland, V. Gopalan, M.A. Nastasi, K.J. McClellan, Radiation effects in corundum structure derivatives. Nuclear Instruments & Methods in Physics Research Section B-Beam Interactions with Materials and Atoms, 141 (1998) 461-466.
[145] C.J. Wetteland, K.E. Sickafus, V. Gopalan, J.N. Mitchell, T. Hartmann, M.A. Nastasi, C.J. Maggiore, J.R. Tesmer, T.E. Mitchell, Radiation damage effects in ferroelectric LiTaO3 single crystals. Materials Research Society Symposium, 504 (1999).
[146] J. Li, X.M. Zhou, W.J. Zhu, F.Q. Jing, A shock-induced phase transformation in a LiTaO3 crystal. Journal of Applied Physics, 102 (2007).
[147] W.C. Oliver, G.M. Pharr, Measurement of hardness and elastic modulus by instrumented indentation: advances in understanding and refinements to methodology. Journal of Materials Research, 19 (2004) 3-20.
[148] J. Lindhard, V. Nielsen, M. Scharff, Approximation method in classical scattering by screened coulomb fields (notes on atomic collisions, I). Kongelige Danske Videnskabernes Selskab, Matematisk-Fysiske Meddelelser, 36 (1968) 32 pp.
[149] J. Lindhard, M. Scharff, H.E. Schiott, Range concepts and heavy ion ranges. Notes on atomic collisions. II. Kongelige Danske Videnskabernes Selskab, Matematisk-Fysiske Meddelelser, 33 (1963) 39 pp.
[150] J. Lindhard, V. Nielsen, M. Scharff, P.V. Thomsen, Integral Equations Governing Radiation Effects (Notes on Atomic Collisions, III). Mat. Fys. Medd. Dan. Vid. Selsk., 33 (1963) 1-42.
[151] J. Lindhard, M. Scharff, Energy Dissipation by Ions in the kev Region. Physical Review, 124 (1961) 128.
[152] I.C. Albayrak, S. Basu, A. Sakulich, O. Yeheskel, M.W. Barsoum, Elastic and Mechanical Properties of Polycrystalline Transparent Yttria as Determined by Indentation Techniques. J Am Ceram Soc, 93 (2010) 2028-2034.
[153] M.W. Barsoum, M. Radovic, T. Zhen, P. Finkel, S.R. Kalidindi, Dynamic elastic hysteretic solids and dislocations. Phys Rev Lett, 94 (2005) -.
[154] J.G. Gualtieri, J.A. Kosinski, A. Ballato, PIEZOELECTRIC MATERIALS FOR ACOUSTIC-WAVE APPLICATIONS. Ieee Transactions on Ultrasonics Ferroelectrics and Frequency Control, 41 (1994) 53-59.
[155] V. Bornand, P. Papet, E. Philippot, Deposition of LiTaO3 thin films by pyrosol process. Thin Solid Films, 304 (1997) 239-244.

[156] D.W. Brown, S.R. Agnew, S.P. Abeln, W.R. Blumenthal, M.A.M. Bourke, M.C. Mataya, C.N. Tome, S.C. Vogel, The role of texture, temperature, and strain rate in the activity of deformation twinning, in: P.V. Houtte, L. Kestens (Eds.) Icotom 14: Textures of Materials, Pts 1and 2, 2005, pp. 1037-1042.
[157] B. Clausen, C.N. Tome, D.W. Brown, S.R. Agnew, Reorientation and stress relaxation due to twinning: modeling and experimental characterization for Mg. Acta Mater, 56 (2008) 2456-2468.
[158] E.J. Freise, A. Kelly, Twinning in graphite. Proceedings of the Royal Society of London, Series A (Mathematical and Physical Sciences), 264 (1961) 269-276.
[159] B.M. Park, K. Kitamura, Y. Furukawa, 9th International Meeting on Ferroelectricity. IMF-9, 24-29 Aug. 1997, Korean Phys. Soc, South Korea, 1998, pp. 789-792.
[160] B.M. Park, K. Kitamura, K. Terabe, Y. Furukawa, Y. Ji, E. Suzuki, Mechanical twinning in stoichiometric lithium niobate single crystal. Journal of Crystal Growth, 180 (1997) 101-104.
[161] B.M. Park, K. Kitamura, Y. Furukawa, J. Yangyang, Relation between mechanical twinning and cracking in stoichiometric lithium niobate single crystals. J Am Ceram Soc, 80 (1997) 2689-2692.
[162] M.J. Norgett, M.T. Robinson, I.M. Torrens, PROPOSED METHOD OF CALCULATING DISPLACEMENT DOSE RATES. Nuclear Engineering and Design, 33 (1975) 50-54.
[163] X.H. Wang, Y.C. Zhou, Layered Machinable and Electrically Conductive Ti2AlC and Ti3AlC2 Ceramics: a Review. Journal of Materials Science & Technology, 26 (2010) 385-416.
[164] Z. Sun, Y. Zhou, M. Li, Cyclic-Oxidation Behavior of Ti3SiC2-Base Material at 1100°C. Oxidation of Metals, 57 (2002) 379-394.
[165] D.B. Lee, S.W. Park, Oxidation of Ti3SiC2 between 900 and 1200 °C in Air. Oxidation of Metals, 67 (2007) 51-66.
[166] M.W. Barsoum, L.H. Ho-Duc, M. Radovic, T. El-Raghy, Long time oxidation study of Ti_3SiC_2,Ti_3SiC_2/SiC, and Ti_3SiC_2/TiC composites in air. J Electrochem Soc, 150 (2003) B166-B175.
[167] S. Basu, N. Obando, A. Gowdy, I. Karaman, M. Radovic, Long-Term Oxidation of Ti2AlC in Air and Water Vapor at 1000-1300 degrees C Temperature Range (vol 159, pg C90, 2012). J Electrochem Soc, 159 (2012) S9-S9.
[168] J.W. Byeon, J. Liu, M. Hopkins, W. Fischer, N. Garimella, K.B. Park, M.P. Brady, M. Radovic, T. El-Raghy, Y.H. Sohn, Microstructure and Residual Stress of Alumina Scale Formed on Ti2AlC at High Temperature in Air. Oxidation of Metals, 68 (2007) 97-111.
[169] M.W. Barsoum, N. Tzenov, A. Procopio, T. El-Raghy, M. Ali, Oxidation of Tin+1AlXn (n=1-3 and X=C, N): II. Experimental results. J Electrochem Soc, 148 (2001) 551-562.
[170] M. Sundberg, G. Malmqvist, A. Magnusson, T. El-Raghy, Alumina forming high temperature silicides and carbides. Ceramics International, 30 (2004) 1899-1904.
[171] Y. Zhou, H. Zhang, M. Liu, J. Wang, Y. Bao, Preparation of TiC free Ti_3SiC_2 with improved oxidation resistance by substitution of Si with Al. Materials Research Innovations, 8 (2004) 97-102.

[172] S. Gupta, A. Ganguly, D. Filimonov, M.W. Barsoum, High-temperature oxidation of Ti3GeC2 and Ti3Ge0.5Si0.5C2 in air. J Electrochem Soc, 153 (2006) 61-68.
[173] Y. Kudoh, H. Takeda, H. Arashi, In situ determination of crystal structure for high pressure phase of ZrO 2 using a diamond anvil and single crystal X-ray diffraction method. Physics and Chemistry of Minerals, 13 (1986) 233-237.
[174] Z. Johan, E. Oudin, P. Picot, Analogues germanifères et gallifères des silicates et oxydes dans les gisements de zinc des Pyrénées centrales, France; argutite et carboirite, deux nouvelles espèces minérales. TMPM Tschermaks Petr. Mitt., 31 (1983) 97-119.
[175] S. Amini, A.R. McGhie, M.W. Barsoum, Isothermal Oxidation of Ti_2SC in Air. J Electrochem Soc, 156 (2009) P101-P106.
[176] M.W. Barsoum, Fundamentals of Ceramics, Institute of Physics, Bristol, 2003.
[177] M.E. Straumanis, T. Ejima, W.J. James, The TiO2 phase explored by the lattice constant and density method. Acta Crystallographica, 14 (1961) 493-497.
[178] J.H. Hubbell, S.M. Seltzer, Report NISTIR-5632 (National Institute of Standards and Technology, 1995), http://physics.nist.gov/xaamdi.
[179] M.W. Barsoum, T. ElRaghy, L.U.J.T. Ogbuji, Oxidation of Ti_3SiC_2 in air. J Electrochem Soc, 144 (1997) 2508-2516.
[180] I. Salama, T. El-Raghy, M.W. Barsoum, Oxidation of Nb2AlC and (Ti,Nb)2AlC in air. J Electrochem Soc, 150 (2003) 152-158.
[181] E.M. Levin, C.R. Robbins, H.F. McMurdie, Phase Diagrams for Ceramists, American Ceramic Society, Columbus, OH, 1964.
[182] M.M. Faktor, J.I. Carasso, Tetragonal Germanium Dioxide and Equilibria in the Ge‐O‐H System. J Electrochem Soc, 112 (1965) 817-822.
[183] J.T. Law, P.S. Meigs, Rates of Oxidation of Germanium. J Electrochem Soc, 104 (1957) 154-159.
[184] K. Kita, C.H. Lee, T. Nishimura, K. Nagashio, A. Toriumi, Control of Properties of GeO2 Films and Ge/GeO2 Interfaces by the Suppression of GeO Volatilization. ECS Transactions, 19 (2009) 101-116.

VITA

Babak Anasori

Education

Ph.D., Materials Science and Engineering, Drexel University, Philadelphia, PA **2014**

M.Sc., Materials Science and Engineering, University of Tehran, Tehran, Iran **2007**

B.Sc., Materials Science and Engineering, Sharif University of Technology, Tehran, Iran **2004**

Awards and Honors

First Place and People's Choice Award, NSF and Science Visualization Challenge **2014**
International Science & Engineering Visualization Challenge, National Science Foundation (**NSF**) and Journal Science, The award was highlighted in **Science**, Vol. 343 pp. 602-603 (2014).

Doctoral Research Excellence Award, Drexel University, Philadelphia, PA **2014**

Teaching Achievement Award, the highest award for a TA in Drexel University, Philadelphia **2014**

Graduate Excellence in Materials Science (GEMS) Award, Diamond Award **2012**
American Ceramics Society (ACerS).

People's Choice Award, NSF and Science Visualization Challenge **2012**
International Science & Engineering Visualization Challenge, National Science Foundation (**NSF**) and Journal Science, The award was highlighted in **Science**, Vol. 335 pp. 526-527 (2012). News about this award was also appeared on National Geographic, BBC, MSNBC, Washington Post, Wired, Russian News.

Best Junior Researcher Award **2011**
Nanomaterials Symposium, The Minerals, Metals & Materials Society (TMS), San Diego, CA.

George Hill Jr. Fellowship award, **2013**
Awarded to graduate students with academic excellence, Drexel University, Philadelphia

Continuing Teaching Excellence Award, Drexel University, Philadelphia, PA **2013**
Teaching Excellence Award, Highly Commended, Drexel University, Philadelphia, PA **2012**

Roland B. Snow Award for **Best of the Show** **2013**
First Place in Scanning Electron microscopy category
American Ceramic society (ACerS) Ceramographic Exhibit, MS&T 2013, Montreal, QC, Canada

Roland B. Snow Award for **Best of the Show** **2012**
First Place in Scanning Electron microscopy category
American Ceramic society (ACerS) Ceramographic Exhibit, MS&T 2012, Pittsburgh, PA

Research Day Award, Poster presentation **2014**
Drexel University, Philadelphia, PA

First place in "Class 4 Scanning Electron Microscopy" **2013**
International Metallographic Contest (IMC 2013), International Metallographic Society, an affiliate of ASM International

Best Student Presentation, Second Place **2011**
in AIAA- Greater Philadelphia Regional Aerospace Eng. and Tech. Symposium, Newtown, PA.

Second Place in "**Science as Art**" competition **2012**
Materials Research Society (MRS) fall meeting, Boston, MA.

Cover Story, Nano Today, Vol 9, No. 2, April **2014**

Cover Story, Materials Today, Vol 17, No. 5 **2014**

Cover Story, Nano Today, Vol 7, No. 1, February **2012**

Cover Story, Advanced Materials, Vol. 23, No. 37, October 4 **2011**

Cover Story, **Nanotech Insight**, Vol. 2, Issue 4, October **2011**

Cover Story, Chemical & Engineering News, Vol. 90, Issue 41, October **2012**

Front-page Story, The Philadelphia Inquirer, February 13 **2012**

Video Story, Inside Science TV, **2012**
Sponsored by **American Institute of Physics**, August 30
(http://www.insidescience.org/?q=content/nanomaterials-energy-efficiency/777)

First place in "Class 4 Scanning Electron Microscopy" **2012**
Third place in "Class 11 Digital Microscopy Artistic"
International Metallographic Contest, International Metallographic Society, an affiliate of ASM International

Second place & **Third place** in Graduate Research Photo Contest **2012**
Drexel University, Philadelphia, PA

Poster Award, MS&T 2011 **2011**
in Acta Materialia Gold Medal Symposium honoring Dr. Narayan, MS&T 2011, Columbus, OH

Second Place, Scanning Electron Microscopy **2011**
Ceramographic Exhibit by American Ceramic Society held in MS&T 2011, Columbus, OH.

Finalist, Science as Art competition, MRS fall Meeting, Boston, MA. **2011**

First place in "Class 11 Digital Microscopy Artistic" **2011**
First place in "Class 9 Artistic Microscopy - Black and White Only"
Second place in "Class 4 Scanning Electron Microscopy"
International Metallographic Contest, International Metallographic Society, an affiliate of ASM International

Finalist, NSF and Science Visualization Challenge **2011**
International Science & Engineering Visualization Challenge, National Science Foundation (**NSF**) and **Journal Science**.

Electron Microscopy Images Featured on: **2011-2014**

2012 Calendar, American Physical Society (APS),

MRS Bulletin, Image gallery, February 2012

2011 & 2012 & 2013& 2014 calendars, Drexel Nanotechnology Institute (DNI),

Homepage rotation image on **American Physical Society (APS) website** (www.aps.org), 2011

2011 & 2014 calendars, Carl Zeiss Company.

Finalist, Science as Art competition, MRS fall Meeting, Boston, MA. **2010**

7th among 134 images, Carl Zeiss nano-contest **2010**

First Place Winner, CRF Image Competition, College of Engineering, Drexel University. **2010**

Travel Awards, Graduate Division, Drexel University, Philadelphia, PA **2010-2011**

30th among nearly 4000 Mat. Sci. and Eng. Graduates in National Entrance Exam **2004**

1st with distinction among all Graduates of Khaatam College. **1999**

2nd with distinction among all Graduates of Sadr College. **1998**

Research Appointments

Doctoral Fellow - Drexel University; Philadelphia, PA **2009-2014**
Research Experiences:
Fabrication & Characterization of MAXMETs: Metal Matrix Composites Reinforced with MAX Phases
Fabrication & Characterization of MAX Phases: Ternary Carbides and Nitrides.
Nanoindentation Studies on Deformation Mechanisms of HCP Single Crystals.
Creep Studies of MAXMETs and MAX Phases
Oxidation Studies of ternary carbides;

Instrument Manager, Nanoindenter **Jan 2013-Present**
Centralized Research Facility (CRF), Drexel University, Philadelphia, PA

Failure Analysis Scientist, **2013-2014**
Aluminum-lithium Alloys, Federal Aviation Administration (FAA) and Drexel University; Philadelphia, PA

R&D Engineer, Aluminat Co. Tehran; Iran **2007-2008**
Modification and Optimization of Casting, Extrusion and Heat Treatment of Aluminum Alloys.

Project Director, Naab Co. Tehran, Iran (Part time) **2004**
Directing the Complete Research of Investment Casting and its Benefits.

Project Director; Shahid Hossein Zadeh Electroplating Co. Tehran, Iran (Part time) **2003**
Directing the Effect of Various Alloy Elements on Chromizing

Characterization Techniques

Transmission Electron Microscopy (JEOL JEM-2010F)
Scanning Electron Microscopy (Supra 50, Zeiss)
Focused Ion Beam (FEI Strata DB235)
X-Ray Diffractometer (Siemens D50 and Rigaku SmartLab)
Differential Scanning Calorimetry (TA Q2000)
Nanoindentation (Nanoindenter XP)
Mechanical testing: Room and high temperature tensile and compression (MTS 810 - Instron 5600, 8800)
Vickers, Brinell indentation (LECO-M400)
Light Microscopy (Olympus, PMG3)

Publications

1. **B. Anasori,** E. N. Caspi, M. W. Barsoum, "Fabrication and Mechanical Properties of Pressureless Melt Infiltrated Magnesium Alloy Composites Reinforced with TiC and Ti_2AlC Particles", Materials Science and Engineering A (2014).
2. **B. Anasori**, M. W. Barsoum: "Reversible Dislocation Motion and Microcracking in Plastically Anisotropic Solids under Cyclic Spherical Nanoindentation", MRS Communications, 3, 245-248 (2013).
3. **B. Anasori**, M. Beidaghi, Y. Gogotsi, "Graphene – transition metal oxide hybrid materials", Materials Today, 17, 253-254 (2014).
4. **B. Anasori**, Y. Elraheb, E. N. Caspi, M. W. Barsoum, "On the Cyclic Oxidation of Ti_2GeC in Air", Journal of Alloys and Compounds, 580, 550-557 (2013).
5. **B. Anasori**, F. Saillot, D. Stanley, J. Awerbuch, T. Tan: "Fatigue Crack Growth in Aluminum Lithium Riveted Lap Joints", Procedia Engineering, 74, 413-416, 2014
6. E. N. Caspi, M. Shamma, **B. Anasori**, B. Clausen, D. W. Brown, S. C. Vogel, V. Presser, S. Amini, O. Yeheskel and M. W. Barsoum, "In situ Neutron Diffraction Evidence For Incipient Kink Bands in Highly Textured Polycrystalline Ti_2AlC Samples", (under review, Acta Materialia).
7. H. Gong, B. Anasori, C. R. Dennison, K. Wang, E. C. Kumbur, R. Strich, J. G. Zhou, "Fabrication, biodegradation behavior and cytotoxicity of Mg-nanodiamond composites for implant application", (under review, Journal of Materials Science: Materials in Medicine).
8. D. J. Tallman, **B. Anasori**, M. W. Barsoum, "A Critical Review of the Oxidation of Ti_2AlC, Ti_3AlC_2 and Cr_2AlC in Air", Mater. Research letters, 1, 115-125 (2013).
9. **B. Anasori**, M. W. Barsoum: "Energy Dissipation in Mg Alloy Composites Reinforced with TiC or Ti_2AlC Particulates", (submitted).
10. J. Griggs, **B. Anasori**, G. Bentzel, G. A. Vetterick, M. L. Taheri, M. W. Barsoum: "Reversible Plasticity of Magnesium Single Crystals under Cyclic Nanoindentation", (ready for submission).
11. A. Mockute, J. Lu, E. J. Moon, M. Yang, **B. Anasori**, S. J. May, M. W. Barsoum, J. Rosen: "Solid solubility and magnetism upon Mn incorporation in bulk Cr_2AlC and Cr_2GaC MAX phases", Materials Research Letters (2014).
12. D. J. Tallman, M. Naguib, **B. Anasori**, M. W. Barsoum, "Tensile Creep of Ti_2AlC in Air in the 1000-1150 °C Temperature Range", Scripta Mater. 66, 805–808 (2012).

13. **B. Anasori,** M. W. Barsoum, "On the Effect of Ti_2AlC on the Fabrication of Extraordinary Thermally Stable Mg Nano Grains", Magnesium Technology 2012, John Wiley & Sons, Inc. New York.
14. S. Basu, O.A. Elshrief, R. Coward, **B. Anasori**, M.W. Barsoum, "Microscale deformation of (001) and (100) rutile single crystals under spherical nanoindentation", J. Mater. Res., 27, 1, 53-63 (2012).
15. **B. Anasori**, K. E. Sickafus, Igor O. Usov, M. W. Barsoum, "Spherical nanoindentation study of the deformation micromechanisms of LiTaO3 single crystals ". J. App. Phys., 110 (2), 023516 (2011).
16. **B. Anasori**, S. Amini, V. Presser, M. W. Barsoum, "Nanocrystalline Mg-Matrix Composites with Ultrahigh Damping Properties", Magnesium Technology 2011, John Wiley & Sons, Inc. New York, 463-468.
17. A. Kontsos, T. Loutas, V. Kostopoulos, K. Hazeli, **B. Anasori**, M. W. Barsoum. "Nanocrystalline Mg-MAX composites: Mechanical behavior characterization via acoustic emission monitoring", Acta Materialia. 59 (14), 5716-5727 (2011).
18. O. Yeheskel, I. C. Albayrak, **B. Anasori**, M. W. Barsoum, "Mechanical and Elastic Properties of Fine-grained Polycrystalline Scandia and Erbia as Determined by Indentation Techniques", Journal of the European Ceramic Society, 31 (9), 1703-1712 (2011).

Conference Presentations

1. **B. Anasori**, F. Saillot, D. Stanley, K. Stonaker, J. G. Bakuckas, J. Awerbuch, T. Tan: "Reconstruction of fatigue crack growth of aluminum lithium riveted lap joints", **AA&S** 2014, Baltimore, MD, **April 2014**
2. **B. Anasori**, M. W. Barsoum, "Reversible Dislocation Motion and Microcracking in Plastically Anisotropic Solids under Cyclic Spherical Nanoindentation", **MRS Fall Meeting**, Boston, MA, **December 2013**.
3. **B. Anasori**, M. W. Barsoum, "Effect of alloying and interfaces on the mechanical properties of nano-grained Mg-Ti_2AlC composites", **TMS** 2013 Annual Conference, San Antonio, FL, **March 2013.**
4. **B. Anasori**, M. W. Barsoum, "Nano-grained Mg Composites Reinforced with MAX Phases", **MRS Fall Meeting**, Boston, MA, **November 2012**.
5. **B. Anasori**, M. Agne, M. W. Barsoum, "Thermally stable Nano-grain Mg Composites Reinforced with MAX Phases", **MS&T** Conference, Pittsburgh, PA, **October 2012.**
6. **B. Anasori**, M. W. Barsoum, "Microcracking and Reversible Dislocation Motion in Plastically Anisotropic Solids Under Cyclic Spherical Nanoindentation", **Nano Measure Symposium**, Stanford, CA, **June 2012**.
7. **B. Anasori**, M. W. Barsoum, "On the Effect of Ti_2AlC on the Formation of Thermally Stable Mg Nano Grains", **TMS** 2012 Annual Conference, Orlando, FL, **March 2012.**
8. **B. Anasori,** M. W. Barsoum, "Investigation of the Formation and Extraordinary Thermal Stability of Mg Nano-grains in Ti2AlC-Mg Composites", **MS&T** Conference, Columbus, OH, **October 2011.**
9. **B. Anasori**, K. E. Sickafus, I. O. Usov, M. W. Barsoum, "Spherical Nanoindentation and Kinking Non-linear Elasticity of LiTaO3 Single Crystals", **MS&T** Conference, Columbus, OH, **October 2011.**
10. **B. Anasori**, A. Kontsos, K. Hazeli ,M. W. Barsoum, "Mechanical Properties of Nanocrystalline Mg-Matrix Composites Reinforced with Ti2AlC", **ASME** Applied Mech. and Mat. Conf., Chicago, IL, **May 2011**.
11. **B. Anasori**, M. W. Barsoum, "Extraordinary Thermally Stable Nanocrystalline Mg-matrix Composites with Ultrahigh Damping Properties" **AIAA** Greater Philadelphia Regional Aerospace Engineering and Technology Symposium, Newtown, PA, **April 2011**.

12. **B. Anasori**, S. Amini, V. Presser, M. W. Barsoum, "Effect of Reinforcement Volume Fraction on the Properties of Nanocrystalline Mg Matrix Composite Reinforced with Ti2AlC", **TMS** Annual Conference, San Diego, CA, **February 2011**.
13. **B. Anasori**, S. Amini, V. Presser, M. W. Barsoum, "Nanocrystalline Mg-Matrix Composites with Ultrahigh Damping Properties", **TMS** Annual Conference, San Diego, CA, **February 2011**.
14. S. Amini, M. W. Barsoum, **B. Anasori**, "Thermal Stability and Effect of Texture on Ultrahigh Damping of Nanocrystalline Mg-Matrix Composites Reinforced with MAX Phases", **ACERS** Conference, Daytona Beach, FL, **January 2011.**
15. **B. Anasori,** Y. Elraheb, M. W. Barsoum, "Isothermal Oxidation of Ti2GeC in Air", **ACERS** Conference, Daytona Beach, FL, **January 2011.**
16. S. Amini, **B. Anasori**, J. M. C. Gallego, A. R. McGhie, C. Ni, L. Hultman, M. W. Barsoum, "Mechanical Properties and Kinking Non-Linear Elasticity of Nano Crystalline Mg-Matrix Composites Reinforced with MAX Phases", **MS&T** Conference, Houston, TX, **October 2010.**
17. **B. Anasori**, S. Amini, M. W. Barsoum, "Thermal Stability of Nanocrystalline Mg-Matrix Composites Reinforced with MAX Phases", **MS&T** Conference, Houston, TX, **October 2010.**
18. **B. Anasori**, S. Amini, J. M. C. Gallego, A. R. McGhie, C. Ni, L. Hultman, M. W. Barsoum, "On the Thermal Stability of Nanocrystallin Mg-matrix Composites reinforced with MAX Phases", **NATAS** Annual Conference, Philadelphia, PA, **August 2010.**
19. **B. Anasori**, S. Amini, M. W. Barsoum, "On the Stability of Mg Nanograins to Coarsening after Repeated Melting", **TAFDV** Spring Symposium, Philadelphia, PA, **March 2010**.

Teaching Experience

Teaching Certificate **2012**
Teaching assistant workshop and creation of teaching portfolio, Drexel University, Philadelphia, PA

Teaching Assistant and Recitation Instructor, (5 terms) **2010-2013**
Introduction to Materials Science; Undergraduate course, Drexel University, Philadelphia, PA (≈ 500 students register each term in this course. Each recitation class has about 30 students. Also, I held review lectures for the entire ≈ 500 students. Overall rating by the students for four consecutive terms: 4.86±0.06 out of 5)

Nanoindentation Lab Instructor, **2012-2013**
ASM Materials camp, Drexel University, Philadelphia, PA

Scanning Electron Microscopy (SEM) Lab Instructor, **2012**
ASM Materials camp, Drexel University, Philadelphia, PA

Ceramic Lab Instructor, (5 summer sessions) **2009-2013**
MATE 100, Materials two-day course, Drexel University, Philadelphia, PA

Ceramic Lab Instructor, (5 1-day events) **2009-2013**
ASM Materials camp, Drexel University, Philadelphia, PA

Physics Teacher, **2000-2004**
Khaatam High school; Tehran, Iran

Private Tutor, **1999-2005**
Teaching high school students in physics and chemistry and mathematic, Tehran, Iran.